UNIVERSITY OF COPENHAGEN

FACULTY OF SCIENCE
NIELS BOHR INSTITUTE

Ph.D. Thesis

José Enedilton Medeiros Pereira

Hydrogen Bond Dynamics in Bioactive Molecules by Neutron Scattering and Density Functional Theory

Ph.D. Thesis

Hydrogen Bond Dynamics in Bioactive Molecules by Neutron Scattering and Density Functional Theory

José Enedilton Medeiros Pereira

A thesis submitted in fulfilment of the requirements for Ph.D. degree

University of Copenhagen

Faculty of Science

Niels Bohr Institute

Copenhagen - Denmark

Supervisor: Heloisa Nunes Bordallo

January 2018

Abstract

This thesis presents results on hydrogen dynamics in different systems of molecules with biological properties, analyzed using a combination of neutron spectroscopy and density function calculations (DFT). These investigations are further supported by calorimetric studies, structural analysis and Raman spectroscopy. The principle aim of the studies carried out during the 3 years of this project was to widen the applications of neutron techniques in the study of molecules of biological interest.

To this end, the evolution of the hydrogen bonds in deuterated crystalline D-Alanine ($C_3D_7NO_2$) as a function of temperature was studied using neutron powder diffraction, polarized Raman scattering and *ab initio* calculations of the harmonic vibrational frequencies. The findings using this approach produced one publication in IUCrJ, appended as Paper 1 of this thesis. The results show changes in the number of vibrational modes as a function of temperature caused by dissimilarities in the structural properties of D-Alanine compared to enantiomeric form L-Alanine.

Another subject of the study was the analysis of the antipsychotics drugs haloperidol ($C_{21}H_{23}ClFNO_2$), aripiprazole ($C_{23}H_{27}Cl_2N_3O_2$), and quetiapine hemifumarate ($C_{21}H_{25}N_3O_2S \cdot 0.5C_4H_4O_4$), chosen based on similarities in their structures and function. The aims were to look for any relationship between the crystalline stability and dynamics of these molecules and to add such information to molecular dynamics simulations. To this end, inelastic neutron scattering measurements were supported by density functional theory calculations, while conformational transformations and the purity of the samples were determined from X-rays and calorimetric studies. The outcome of this work resulted in Paper 2, also appended to the thesis, which is currently in preparation for journal submission.

Considering that neutron spectroscopy is highly sensitive to identifying hydrogen in biological samples, studies of the hydrogen mobility within innate and demineralized human dentine were performed combining the elastic fixed window approach and thermal analysis. This work sought to gather additional information on the states of water within the dental hard tissues. Our findings support the idea that hydroxyapatite protects the collagen in innate dentine. Demineralized dentine, on the other hand, acts as a sponge where free, bulk-like water

is trapped. This research resulted in a BSc thesis that I co-supervised and in Paper 3 (appended) that is under peer review in The Journal of Dental Research.

Analysis of the dynamics of the Hepatitis B surface antigen (HBsAg) encapsulated in the mesostructured porous silicate Santa Barbara Amorphous (SBA-15) was also carried out, using calorimetric studies combined with quasi-elastic neutron scattering and the elastic fixed window approach. These very preliminary findings cast light on the behavior of the distribution of HBsAg within the SBA-15 structure. The main results are presented in Paper 4 (appended), submitted to the Special Topics (ST) issue on the theme "Physics Inspired by Living Matter: Dynamics, Topology and Functionality" of the 2017 Geilo School in the European Physical Journal (EPJ).

The final scientific contribution presented in this thesis is a book chapter that summarizes results from neutron powder diffraction and inelastic neutron scattering on different crystalline amino acids, such as L-alanine ($C_3H_7NO_2$), L-valine ($C_5H_{11}NO_2$) and L-leucine ($C_3H_7NO_2$). The main outcome of this book chapter is a summary of how small variations in the hydrogen bond network correlate to conformation changes in these structures.

Resume

I denne afhandling præsentereres resultater med fokus på hydrogendynamik i forskellige molekylære systemer med biologiske egenskaber. Resultaterne er analyseret ved at kombinere neutronspektroskopi og densitetsfunktionsberegninger (DFT). Disse resultater er yderligere understøttet af undersøgelser fra kalorimetriske analyser, strukturanalyse og Raman-spektroskopi. Hovedformålet med analyserne, der er blevet udført de sidste 3 år, er at udvide anvendelses metoderne af neutronsprednings teknikker i studiet af molekyler i biologisk interesse studier.

Til dette formål blev udviklingen af hydrogenbindingerne som funktion af temperatur i deutereret krystallinsk D-Alanin ($C_3D_7NO_2$) undersøgt med neutronpulverdiffraktion, polariseret Raman-spredning og ab initio-beregninger af de harmoniske vibrationelle frekvenser. Resultaterne fra denne analyse resulterede i en publikation i IUCrJ; Papir 1 i denne afhandling. Resultaterne viser ændringer i antallet af vibrationsformer som funktion af temperatur. Disse forskelle er forårsaget af forskelle D-Alanins strukturelle egenskaber, sammenlignet med spejlbilledisomerer fra L-Alanin.

Et andet emne i afhandlingen er analysen af antipsykotiske lægemidler, haloperidol ($C_{21}H_{23}ClFNO_2$), aripiprazol ($C_{23}H_{27}Cl_2N_3O_2$) og quetiapinhemifumarat ($C_{21}H_{25}N_3O_2S \cdot 0.5C_4H_4O_4$) Disse antipsykotiske lægemidler er valgt ud fra lighederne i deres strukturer og funktion. Formålet med denne analyse var at undersøge forhold mellem den krystallinske stabilitet og dynamikken i molekylerne, og derefter at bruge resultaterne til molekylære dynamik simuleringer. Til dette formål blev uelastiske neutronspredning malinger, understøttet af DFT-beregninger, udført og kombineret med kalorimetriske undersøgelser der viser konformationelle transformationer og renheden af prøverne. Resultatet fra dette arbejde resulterede i papir 2, der også er vedlagt afhandlingen, og som skal indsendes til review så hurtigt som muligt.

Neutronspektroskopi er yderst velegnet til at identificere hydrogen i biologiske prøver, og derfor blev der udført analyser af hydrogenmobilitet inden for naturligt og demineraliseret humant dentin. Ydermere blev neutronspektroskopi kombinereret med elastic fixed window metode og kalorimetriske analyser. Formålet med dette arbejde var at indsamle yderligere oplysninger om tilstanden af vand inden for det dentale hårde væv. Vores resultater understøtter

ideen om, at hydroxyapatit beskytter kollagenet i det nartuligt medfødt dentin. Demineraliseret dentin fungerer derimod som en svamp, hvor frit, bulk vand er fanget. Denne forskning resulterede i en bachelorafhandling, som jeg co-supervised, og i Paper 3, der er under peer review i "The Journal of Dental Research".

Endelig blev dynamikken af Hepatitis B-overfladeantigenet (HBsAg) indkapslet i det mesostrukturerede porøse silicat Santa Barbara Amorphous (SBA-15) analyseret med kalorimetriske undersøgelser, kombineret med kvasi-elastisk neutronspredning (QENS) og elastic fixed window metode (EFW) tilgang. Disse foreløbige resultater skildrede opførelsen af fordelingen af (HBsAg) inden for SBA-15-strukturen. Hovedresultaterne er præsenteret i papir 4, indsendt til Special Topics (ST) under temaet for Geilo School 2017 i European Physical Journal (EPJ).

Det sidste videnskabelige bidrag, der fremlægges i denne afhandling, er et bogkapitel, som opsummerer resultaterne fra neutronpulverdiffraktion og inelastisk neutron-spredning på forskellige aminosyrer, såsom for eksempel L-alanin ($C_3H_7NO_2$), L-valin ($C_5H_{11}NO_2$) og L-leucin ($C_3H_7NO_2$) krystaller. Her understreges resuméet vedrørende, hvordan små variationer i hydrogenbindingsnetværket korrelerer med ændringerne i formen på den dertilhørende makromolekyle strukturer.

Acknowledgments

First, I would like to thank my supervisor Heloisa N. Bordallo for her support, friendship, guidance and for accepting to develop this project with me.

I also would like to thank Dr. Paulo de Tarso, for the support and help in the development of my PhD project.

I would like to thank my collaborators for the productive discussions and all local contacts for the help received in performing of the experiments.

A thanks goes to Anton Stampfl, Garry McIntyre and Nicolas De Souza for all support received during my six months internship at the Australian Nuclear Science and Technology Organisation (ANSTO).

I am especially grateful to Eveline for be with me in my more difficult and stressful periods during the last seven years.

A big thanks goes to my friends Gadelha and Aldilene, people that help me a lot, before and until this last moment in my PhD in professional and personal aspects.

I would like to thank my colleagues and friends: Éverton, Marcella, Martin, Murillo, Sergey, Simon, Sotiri for their scientific input and help during this work.

I would like to thank everyone that directly or indirectly have contributed to have this thesis completed.

Finally, I would like to thank my parents, Mano and Fátima, for the unlimited support and positivity as well as my brothers and family.

Curriculum Vitae

Jose Enedilton Medeiros Pereira

Born in Ceará, Brazil | On 23.02.1987 | Telephone: +45 53 37 72 33

e-mail: jose.enedilton@nbi.ku.dk; pereira.jose0001@gmail.com

Education:

2015 –   PhD in physics at The Niels Bohr Institute - University of Copenhagen.

2012 – 2014   Master degree in Physics at the Universidade Federal do Ceará.

2008 – 2012   Bachelor degree in Physics at the Universidade Federal do Ceará.

2008 – 2011   Regular Training in English (Hours: 462h), Municipal Research Institute Administration and Human Resources, IMPARH, Fortaleza, Brazil.

Complementary Education:

2017   Advanced Presentation Techniques, University of Copenhagen (Denmark).

2016   Erice School "Neutron Science and Instrumentation", II course: "Designing and Building a Neutron Instrument"- XIV School of Neutron Scattering "Francesco Paolo Ricci" (SoNS) (Italy).

2016   Academic Writing, University of Copenhagen (Denmark).

2015   5th Annual Niels Bohr International Academy Workshop on ESS Science: Condensed Matter Theory and Advanced Software, Copenhagen (Denmark).

2015   Advanced Measuring Techniques for DSC/DTA, TGA and Combined Systems (STA) and Evolved Gas Analysis (EGA) offered by NETZSCH-Gerätebau GmbH in Copenhagen.

2015   Mantid Training Courses, held at the Rutherford Appleton Laboratory (United Kingdom).

2015   19th Jülich Centre for Neutron Science – Neutron Scattering (JCNS), held in Jülich and Munich (Germany).

Pedagogical Skills:

2017	Teaching Assistant in the course: NFYK12004U - Applications of X-ray and Neutron Scattering in Biology, Chemistry and Physics.
2016	Co-supervised three MSc students in the course: NFYK15011U - From Idea To Result.
2016	Co-supervised the BSc student Alexander Kjello Lauritsen. Currently MSc at the Niels Bohr Institute.
2016	Introduction to University Pedagogy, University of Copenhagen (Denmark).

Personal Fellowships

2017	Travel Grant from the NNSP Soft-Bio network (10000 NOK).
2015 – 2018	Brazilian Government Science without Borders (SwB) PhD. Fellowship.
2012 – 2014	Brazilian Government M.Sc. Fellowship. Awarded to excellent young scientists.

Experience:

2016	Internship at the Australian Nuclear Science and Technology Organisation (ANSTO). During the six months of my change of scientific environment, I acted as local contact or as support for the main local contact (Dr. Anton Stampfl) in the instrument TAIPAN.
2015 – 2018	Responsible for the thermal analyses laboratory at the X-ray and Neutron Science group at the Niels Bohr Institute – University of Copenhagen.

Research Skills:

- Broad experience in neutron time-of-flight spectroscopy:
    - Institut Laue-Langevin-ILL (France) using the direct time of flight spectrometer IN6.
    - Rutherford Appleton Laboratory (United Kingdom) using the indirect time of flight spectrometer TOSCA.
    - Paul Scherrer Institute-PSI (Switzerland), Australian Nuclear Science and Technology Organisation – ANSTO (Australia) and at the Spallation Neutron

Source – SNS (USA) using the backscattering spectrometers MARS, EMU and BASIS, respectively.
- ANSTO using the Be-Filter spectrometer TAIPAN.

- Data treatment of inelastic neutron scattering data, including *ab initio* calculations:
  - Large Array Manipulation Program – LAMP; Manipulation and Analysis Toolkit for Instrument Data - Mantid Project; aCLIMAX software; Gaussian09 software.

- Broad knowledge in Raman scattering, Infrared spectroscopy and crystal growth
  - Experience in Raman Scattering measurements (T64000 spectrometer of Jobin-Yvon) at the Universidade Federal do Ceará (Brazil) and at The University of New South Wales – Sydney (Australia).

- Extended knowledge in thermal analysis (DSC, TGA-FTIR).
  - Experience in thermogravimetric analysis measurements, using the instrument PERSEUS TG 209 F1 Libra from NETZSCH coupled with a Fourier transform infrared spectrometer by BRUKER Optics Inc. (TGA-FTIR) and Differential Scanning Calorimetry (DSC) measurements, using a NETZSCH DSC 214 *Polyma.*

- Knowledge in Rietveld analysis, Origin pro lab, Peak fit as a tool of data analysis.

Conferences:

- Oral presentations

2017   Hydrogen bonds in enantiomers: The alanine paradigm – International Conference on Neutron Scattering 2017 (ICNS 2017), Daejeon (Korea).

2017   Hydrogen bond dynamics in antipsychotics by neutron spectroscopy and density functional theory – MLZ conference: Neutrons for Health 2017, Bad Reichenhall (Germany).

2017   Hydrogen bond dynamics, conformational flexibility and polymorphism in antipsychotics - The Annual Condensed Matter and Materials Meeting 2017, Wagga Wagga (Australia).

- Posters

2015   Hydrogen bond dynamics, conformational flexibility and polymorphism in antipsychotics - 6th European Conference on Neutron Scattering (ECNS 2015), Zaragoza (Spain).

2015   Understanding structure and dynamics of complex systems using scattering techniques – DANSCATT Meeting 2015, Aarhus, (Denmark).

Publications:

- Articles

   J. E. M. Pereira, Juergen Eckert, Svemir Rudić, Dehong Yu, Richard Mole, Nikolaos Tsapatsaris and Heloisa N. Bordallo. Hydrogen bond dynamics and conformational flexibility in antipsychotics. *In preparation.*

   M. K. Rasmussen, **J. E. M. Pereira**, M.C. Berg, G. N. Iles, N. H. Jalarvo, V. F. Botosso, O. A. Sant'Anna, M. C. A. Fantini, H. N. Bordallo. Dynamics of encapsulated hepatitis B surface antigen: A combined neutron spectroscopy and thermo-analysis study. *Under review.*

   A. K. Lauritsen, **J. E. M. Pereira**, F. Juranyi, H. N. Bordallo, L. Larsen, A. R. Benetti; Probing water mobility in human dentine using neutron spectroscopy; Journal of Dental Research. *Under review.*

   E. A. Belo, **J. E. M. Pereira**, P. T. C. Freire, D. N. Argyriou, J. Eckert, and H. N. Bordallo, "Hydrogen bonds in crystalline D -alanine: diffraction and spectroscopic evidence for differences between enantiomers," *IUCrJ*, vol. 5, no. 1, pp. 6–12, Jan. 2018. DOI: 10.1107/S2052252517015573.

- Book chapter

   P. T. C. Freire, **J. E. M. Pereira**, and H. N. Bordallo, "Application of Neutron Scattering in Amino Acid Crystals – Structural and Dynamical Information," in *Neutron Scattering*, InTech, 2016), DOI: 10.5772/62198.

Language:

Portuguese: Native

English: Good

Spanish: Basic knowledge

Publications and Author Contributions

Paper 1: E. A. Belo, <u>J. E. M. Pereira</u>, P. T. C. Freire, D. N. Argyriou, J. Eckert, and H. N. Bordallo, "Hydrogen bonds in crystalline D -alanine: diffraction and spectroscopic evidence for differences between enantiomers," *IUCrJ*, vol. 5, no. 1, pp. 6–12, Jan. 2018. DOI: 10.1107/S2052252517015573.

Author contribution: In this publication, I performed density functional theory calculations (DFT) in the fully hydrogenated D-Alanine using the software *Gaussian09* taking as initial structure data from the atomic coordinates of the D-Ala at 280 K. I also made all figures presented in the manuscript. Furthermore, I actively participated in the analysis and interpretation of the calculated and experimental Raman and neutron powder diffraction data as well as in writing the manuscript. In addition, I keenly discussed with all co-authors during the extensive review process of the manuscript.

Paper 2: <u>J. E. M. Pereira</u>, Juergen Eckert, Svemir Rudić, Dehong Yu, Richard Mole, Nikolaos Tsapatsaris and Heloisa N. Bordallo. Hydrogen bond dynamics and conformational flexibility in antipsychotics. *In preparation*

Author contribution: I performed the thermo-analysis experiments, which included differential scanning calorimetry (DSC) and the thermogravimetric analysis coupled to infrared spectroscopy (TGA-FTIR). In addition, I analyzed and interpreted the data from inelastic neutron scattering (INS) experiments, collected using the spectrometers PELICAN and TOSCA located at the Australian Nuclear Science and Technology Organisation - ANSTO (Australia) and at the ISIS Neutron and Muon Source at the Rutherford Appleton Laboratory (United Kingdom). I also performed density functional theory calculations (DFT) in the single molecules structure of the studied samples using the software *Gaussian09*. I wrote the manuscript, with considerable input of all co-authors and made the final figures. I expect to submit this manuscript before my thesis defense.

Paper 3: A. K. Lauritsen, <u>J. E. M. Pereira</u>, F. Juranyi, H. N. Bordallo, L. Larsen, A. R. Benetti; Probing water mobility in human dentine using neutron spectroscopy; Journal of Dental Research. *Under review*.

Author contributions: I supervised the first author of this manuscript, A. K. Lauritsen, during his BSc project. Therefore, I guided the student as well as performed the inelastic neutron scattering experiment using the elastic fixed window (EFW) approach at the Paul Scherrer Institut - PSI (Switzerland) using the backscattering spectrometer MARS. Other aspects of this research involved collecting differential scanning calorimetry (DSC) and thermogravimetric analysis coupled to infrared spectroscopy (TGA-FTIR) measurements and careful preparation of the samples. For the thermal analysis, together with my student, we performed a series of preliminary measurements in order to define the protocol used in the final calorimetric measurements. Finally, Alexander and I did the data analysis and the final figures of the submitted manuscript. In addition, I discussed the results with the co-authors as well as participated in the reviewing process of the manuscript.

Paper 4: M. K. Rasmussen, J. E. M. Pereira, M.C. Berg, G. N. Iles, N. H. Jalarvo, V. F. Botosso, O. A. Sant'Anna, M. C. A. Fantini, H. N. Bordallo. Dynamics of encapsulated hepatitis B surface antigen: A combined neutron spectroscopy and thermo-analysis study. *Under review.*

Author contribution: During the process of acquiring the data for this submitted publication, I carried out inelastic neutron scattering using the elastic fixed window (EFW) approach at the Australian Nuclear Science and Technology Organisation - ANSTO (Australia) using the backscattering spectrometer EMU. Furthermore, I discussed the ensemble of the results with all co-authors as well as participated in writing the manuscript.

Book Chapter: P. T. C. Freire, J. E. M. Pereira, and H. N. Bordallo, "Application of Neutron Scattering in Amino Acid Crystals – Structural and Dynamical Information," in *Neutron Scattering*, InTech, 2016), DOI: 10.5772/62198.

Author contribution: I wrote Section 3 of this book chapter. This part involves the basic theory of neutron scattering needed for the comprehension of our extensive work in amino acids. This part of my work was very important, as during the process of writing this section, I did an extensive literature research on neutron scattering concepts, which introduced me to the fundamental aspects of neutron scattering process, and mainly to the description in how the neutron interacts with matter. This knowledge was important for the understanding and analyses of the data collected during the projects developed in my Ph.D.

Contents

Chapter 1

Introduction

Neutron spectroscopy is one of the most powerful and versatile experimental techniques to study structure and dynamics of materials that contain hydrogen atoms. This type of information can be difficult to observe by other probes, including X-ray diffraction, nuclear magnetic resonance (NMR), optical microscopy, and various spectroscopies, either because hydrogen atoms only scatter X-radiation weakly or because the motions of interest are outside the time window probed by the more accessible spectroscopic techniques, including NMR. With this in mind, the focus of this thesis was to further our understanding of the hydrogen dynamics in molecules with biological properties and increased complexity. Thus, amino acids, antipsychotics drugs, water mobility in human dentine as well as analysis of the dynamics of the Hepatitis B surface antigen (HBsAg) encapsulated in Santa Barbara Amorphous (SBA-15) mesostructured porous silicate were investigated.

In Chapter 2, an overview of the relevant concepts regarding the techniques used in the studies performed for this thesis is given, with a particular attention to neutron spectroscopy.

Chapter 3 is dedicated to the study of the D-alanine amino acid. Amino acids are fundamental molecules in life that can be found in two enantiomers: L and D-forms, except for glycine with its chiral centre on the α-carbon. The interest in these molecules comes from the following facts:

(i)   although progress in analytical chemical tools has now established that considerable amounts of D-amino acids are also found in higher mammals including humans [1];

(ii)   D-Amino acids are now increasingly recognized as physiologically active molecules as well as potential biomarkers [2].

Remarkably, very few studies have been devoted to the understanding of their solid-state properties. Most reports do not find any difference in their properties when compared to the opposite chiral counterpart, as one would expect, except, of course, in experiments where the chiral character is relevant [3], [4]. However, some papers [5]–[7] have described possible phase transitions in single crystals of D-Alanine (D-Ala) based on observed differences between crystalline D-Ala and L-alanine (hereafter L-Ala) as a function of temperature.

Consequently, in order to verify possible differences in the hydrogen bound network in crystalline D-Ala and L-Ala, we have carried out a study using neutron powder diffraction, polarized Raman scattering and *ab initio* calculations of harmonic vibrational frequencies in D-Ala. The results are shown in Paper 1; the aim of this study was to explore how and if variations in the hydrogen bond network correlates to conformation changes in enantiomorphic structures. A similar approach, used in previous studies on other amino acids, such as L-alanine ($C_3H_7NO_2$), L-valine ($C_5H_{11}NO_2$) and L-leucine ($C_3H_7NO_2$), resulted in a book chapter reviewing all results, presented in Chapter 7 of this thesis and in the appendix.

Other project developed during this thesis was dedicated to study of the hydrogen dynamics in three antipsychotic drugs: haloperidol ($C_{21}H_{23}ClFNO_2$), aripiprazole ($C_{23}H_{27}Cl_2N_3O_2$) and quetiapine hemifumarate ($C_{21}H_{25}N_3O_2S \cdot 0.5C_4H_4O_4$). These drugs, present a wide range of undesirable side effects, which are related to their function and delivery method. Pharmaceutical companies, however, appear to have withheld significant information on these types of drugs because of their commercial significance; the market for antipsychotic drugs is valued at USD 11.7 billion in 2015 [8]. Another important factor to take into account regarding the way of action of these drugs is the flexibility of the protein-ligand complex, which is a crucial aspect of protein structure and function [9]. As it is apparent that there is a general lack of understanding of the conformational habit of these molecules, with this study we aimed are to explore any relationship between the crystalline stability and dynamics on these molecules. To achieve our goal, we have carried out inelastic neutron scattering (INS) measurements combined with density functional theory (DFT) calculations supported by thermal analysis. While conformational transformations and the purity of the samples was verified based on the calorimetric studies, a relatively good agreement between the calculated and experimental spectra allowed for the assignment of the vibrational modes, resulting mostly from the hydrogen atoms. The results of this project are discussed in detail on Chapter 4, Paper 2 and its supplementary information.

Chapter 5 presents results on hydrogen mobility within innate and demineralized human dentine, the material that makes up the bulk of our teeth. It has a tubular structure created by the collagen network and is comprised of three main components: water, protein and hydroxyapatite ($HCa_5P_3O_{13}$). Therefore, in dentistry it is highly interesting to understand the physical properties of this material, as this can enable progress in the field of dental resins, normally used to make fillings in cavities. In order to obtain information on water mobility inside the samples and how this affects the dentine structure measurements using neutron spectroscopy and thermal analyses were performed. The final results of this project are given on Paper 3 and its supplementary information.

Very preliminary results on the dynamic of encapsulated Hepatitis B surface Antigen (HBsAg) using neutron spectroscopy are presented in Chapter 6 and Paper 4 in this thesis. The main motivations for this work were:

(1) Hepatitis B is a disease which attacks the liver and the best way to prevent is by vaccination, however;

(2) oral delivery of hepatitis B vaccine containing the Hepatitis B surface Antigen (HBsAg) can offer significant benefits over injections, such as less side effects and better immunological response [10]. Santa Barbara Amorphous (SBA-15), a mesostructured porous silicate, has shown to protect the vaccine from gastric acid, making oral delivery possible [10], therefore it is not clear how the vaccine is confined in the SBA-15 structure;

(3) can we use neutrons to observe how encapsulation modifies the dynamics of the water (salt solution) hydrating the protein?

Thus, aiming to understand the interactions in this encapsulation process of the HBsAg by SBA-15, were carried out experiments using calorimetric studies combined with quasi-elastic neutron scattering (QENS) and the elastic fixed window (EFW) approach. Our initial findings indicate that in the timescale accessible by the used spectrometers, the vaccine in salt solution is immobilized or covered by the inner structure of the mesoporous SBA-15. This is evidenced by the values of the diffusion coefficient and residence time obtained.

Finally, Chapter 8 summarized the main results of each project and gives perspectives for future work to be carried out in order to clarify some points of interest that were left to be answered after this thesis.

<div align="right">

Chapter 2

</div>

Brief Overview of the Experimental Techniques

This chapter is devoted to introducing the basic concepts of the experimental techniques used during this thesis. Here a brief introduction to the relevant concepts of neutron scattering, density functional theory (DFT) and thermal analysis are given. The description of the different neutron instruments used during the development of this thesis will be presented together with the description of the individual papers.

2.1 Basics of Neutron Scattering and Density Functional Theory

Postulated by Rutherford in 1920 and discovered by J. Chadwick in 1932, neutrons are non-charged subatomic particles with mass rather close to that of the proton, $m_n = 1.675 \cdot 10^{-27}$ kg, magnetic moment equals to - 1.913 μ_b, and a nuclear spin $s = \frac{1}{2}$. These properties are important and unique for developing the theory of neutron scattering [11].

Neutrons can be described using either classical mechanics, with momentum $\vec{p} = m\vec{v}$, where m is the neutron mass and $\vec{v}$ is its velocity, or as a wave, with momentum $\vec{p} = \hbar\vec{k}$, with $|\vec{k}| = \frac{2\pi}{\lambda}|\mathrm{k}|$ defining the wave vector of the neutron and λ its associated wavelength. This implies that neutron scattering processes are based on the analysis of momentum and energy transfer, which may occur due to the interactions between neutrons and matter. The momentum transfer vector or scattering vector, $\vec{Q}$, illustrated in Figure 1, is defined as the vector difference between the incoming and scattered wave vectors as:
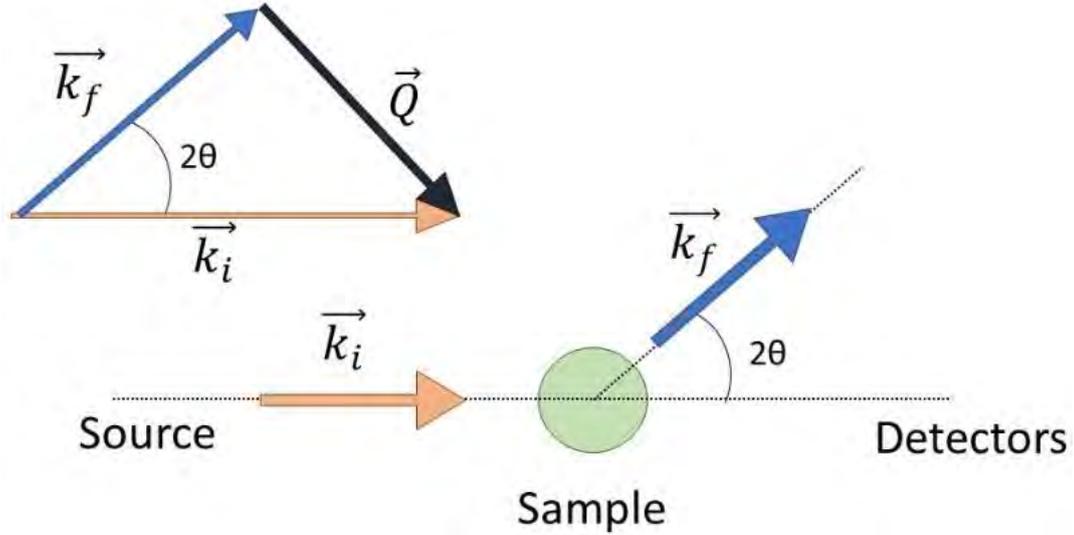
Figure 1 Basic principle of a typical inelastic neutron scattering experiment, where incident neutrons with $\vec{k_i}$ wave vector are scattered from a sample with a wave vector equals to $\vec{k_f}$. These scattered neutrons are then detected at an angle 2θ, The momentum transfer $\vec{Q}$, is given by $\vec{Q} = \vec{k_i} - \vec{k_f}$. During an elastic neutron scattering experiment $\vec{k_i} = \vec{k_f}$.

$$\vec{Q} = \vec{k_i} - \vec{k_f}, \tag{2.1}$$

while the variation in the neutron momentum is given by:

$$\hbar\vec{Q} = \hbar(\vec{k_i} - \vec{k_f}), \tag{2.2}$$

the corresponding neutron energy E can be described as:

$$E = \frac{p^2}{2m} = \frac{1}{2}mv^2 = \frac{h^2}{2m\lambda^2} = \frac{\hbar^2 k^2}{2m}, \tag{2.3}$$

where $h = 2\pi\hbar = 6.626.10^{-34}$J·s is the Planck's constant. Thus, variation of the energy ($\hbar\omega$) measured in a neutron scattering experiment is given by:

$$\hbar\omega = E_i - E_f = \frac{\hbar^2}{2m}(k_i^2 - k_f^2). \tag{2.4}$$

Classified after their energy, Table 1 [12], neutrons can be called hot, thermal or cold when their average energy corresponds to about k_BT with average temperatures around 2000 K, 300 K or 25 K, respectively. Since neutrons are non-charged particles, their interactions with matter, both nuclear and magnetic are short range; therefore, neutrons can penetrate deeply into matter. This enables us to study the structure and dynamics of materials under very precise

environmental conditions such as pH, extreme pressure, controlled temperature, hydration conditions or under application of electric or magnetic field.

Table 1 Neutron classification considering their energy range and corresponding temperature and wavelength.

	Hot	Thermal	Cold
Temperature T (K)	1000 – 6000	60 – 1000	1 – 120
Energy E (meV)	100 – 500	5 – 100	0.1 – 10
Wavelength λ (Å)	1 – 0.4	0.4 - 1	30 - 3

During the scattering process, elastic scattering occurs when the variation of energy between neutron and the sample is zero, $\hbar\omega = 0 \Rightarrow k_i = k_f$. On the other hand, when this variation is different from zero, the scattering processes is called inelastic. If, $\hbar\omega < 0 \Rightarrow k_i < k_f$, energy is transferred from the sample to the neutron, resulting in neutron energy gain by phonon absorption; in an analogy to Raman scattering, this is called the anti-Stokes side. When, $\hbar\omega > 0 \Rightarrow k_i > k_f$, energy is transferred from the neutron to the sample resulting in neutron energy loss through the creation of a phonon, this is called the Stokes side. A special case occurs when $\hbar\omega \approx 0$, an inelastic neutron scattering with ω centred around zero ($\omega = 0$), this is the so-called quasi-elastic neutron scattering (QENS), which is better described in Section 2.1.3. The neutron scattering process is illustrated in Figure 2.
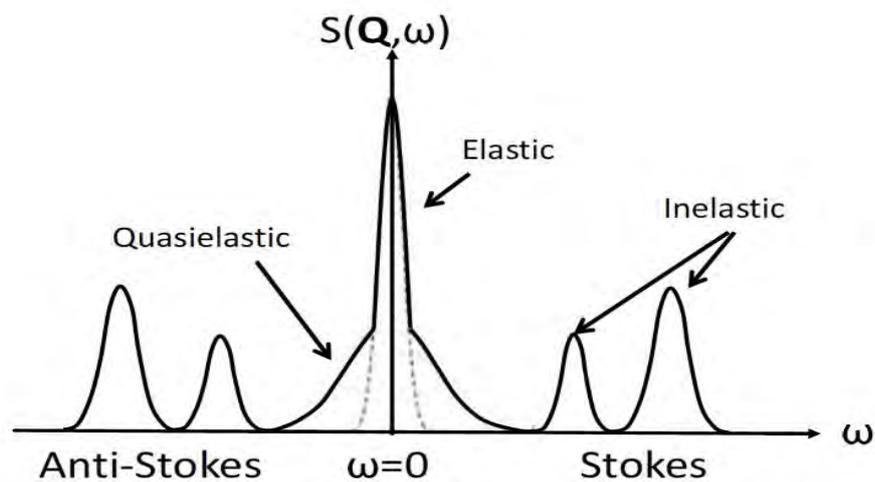

Figure 2 Elastic and quasi-elastic scattering are both centered at ω = 0. For ω > 0, the sample gains energy from the neutron by entering an excited state and creating a phonon, this is the Stokes side of the spectrum. For ω < 0, the sample loses energy to the neutron, which absorbs a phonon, this is the anti-Stokes side of the spectrum. The relative intensities are arbitrary.

2.1.1 Scattering Length and the Neutron Cross Section

In all neutron scattering experiments, after interacting with a nucleus of a single fixed atom, the scattered neutron wave is isotropic, and can be described as:

$$\psi_1 = \frac{b}{r} e^{i\vec{k}_1 \vec{r}}, \tag{2.5}$$

where, **r** is the distance between the nucleus and a detector, and the amount *b*, which has the dimensions of length, defines the scattering ability of the atomic nucleus. It may be regarded as a real and known constant for a given nucleus or isotope [13]. The neutron scattering length, *b,* depends sensitively on the details of the nuclear interaction. Thus, it has a specific value for each nucleus, due to variations of nuclear spin direction with time, differences between isotopes and elements. The scattering length cannot be calculated but can be determined experimentally. A table with the scattering length values for each atom and its isotopes can be found in the literature, for example, in the Neutron Data Booklet [12].

The precision and quality of a scattering experiment is directly associated to the number of neutrons scattered by a sample and subsequently detected, and therefore depends on the strength of the neutron source [14]. The flux Φ of a neutron beam is defined as:

$$\Phi = \frac{n}{s}, \tag{2.6}$$

where *n* is the quantity of neutrons colliding on a target surface per second and *s* is the surface area perpendicular to the neutron beam direction. Using Eq. (2.6) we can define the neutron scattering cross section, σ, as the number of neutrons either absorbed or scattered each second by the sample over the total flux Φ.

$$\sigma = \frac{neutrons\ per\ second}{\Phi}, \tag{2.7}$$

σ has dimension of area and is expressed in *barns*, $1barn = 10^{-24} cm^2$. Considering the scattering of the neutrons in all directions, the surface area perpendicular to the neutron beam is the total solid angle *4π*. Thus, total scattering cross section can then be written as:

$$\sigma = 4\pi b^2, \tag{2.8}$$

In the scattering process, the neutron does not interact uniformly with the all atoms from the sample. This happens due differences related to isotope types as well as to the spin direction of the neutron compared to the spin direction of the atom. Thus, we can define two different type of scattering lengths, the coherent scattering length (b_{coh}), and the incoherent scattering length, (b_{inc}). The coherent scattering length is the mean of the scattering lengths, $\langle b \rangle$, and is related to the scattering from the same or different atoms at distinct times. It is defined as:

$$\langle b \rangle = \sum_i c_i b_i , \tag{2.9}$$

where c_i is the fractional concentration of nuclei with scattering b_i. Consequently, the coherent scattering cross section can be written as:

$$\sigma_{coh} = 4\pi \langle b \rangle^2 . \tag{2.10}$$

The incoherent scattering length is the deviation from the average scattering length from the same atom at different times, and is given by:

$$b_{inc} = \sqrt{\langle b^2 \rangle - \langle b \rangle^2} , \tag{2.11}$$

so, the incoherent scattering cross section is:

$$\sigma_{inc} = 4\pi (\langle b^2 \rangle - \langle b \rangle^2) . \tag{2.12}$$

In general, coherent scattering is associated with the determination of the sample structure minimizing the incoherent contribution to the differential cross section, while incoherent scattering is used mostly for the study of dynamics of atoms and molecules [15], [16]. The probability of interactions between the neutrons and the atoms is a characteristic of each isotope and described by coherent and incoherent cross sections (σ_{coh} and σ_{inc}), as shown in Table 2. The cross section is related to the coherent (b_{coh}) and incoherent (b_{inc}) scattering length by Eq. (2.8). The high σ_{inc} value of ^{1}H in comparison to other elements allows for an easier assignment of the vibrations related to hydrogen atoms. On the other, the high value of the coherent cross section of [2]D when compared to ^{1}H allows to locate the hydrogen atom by using deuteration. This fact is widely exploited by exchanging protons with deuterons to mark

different components of the samples/molecules under investigation. This is the so-called contrast matching. For instance, by selectively deuterating the hydrogen groups in L-alanine ($C_3H_7NO_2$) it was possible to separate the vibration originating either from the NH_3 or the CH_3 moieties, as illustrated in Figure 3, adapted from [17]. These properties are important for the studies performed in this thesis.

Table 2 Coherent (σ_{coh}) and incoherent (σ_{inc}) cross-sections in 10^{-24} cm^2 for selected elements and isotopes [12].

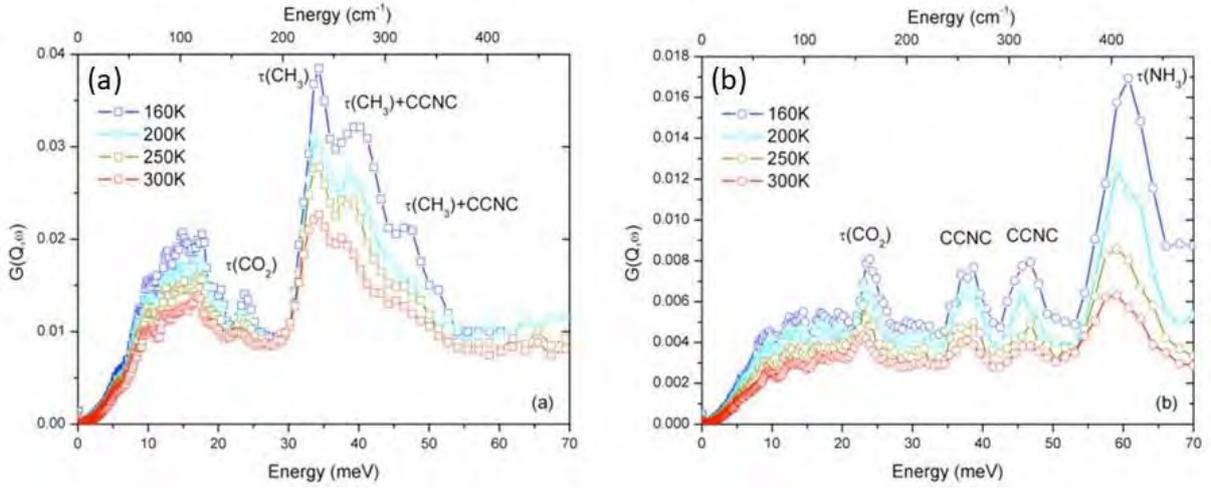|	^{1}H	^{2}D	C	O	N	Cl
σ_{coh}	1.76	5.59	5.55	4.23	11.0	11.5
σ_{inc}	80.27	2.05	<0.01	<0.01	0.50	5.30

Figure 3 Inelastic neutron scattering spectra at various temperatures for (a) $C_2H_4(ND_2)CO_2D$ (Ala-ND₃) and (b) $C_2D_4(NH_2)CO_2H$ (Ala-CD₄) obtained using the spectrometer NEAT located in Berlin, Germany.

In a typical neutron experiment the collected information is related to the partial differential cross-section, $d^2\sigma/(d\Omega d\omega)$, given by Eq. (2.13), according to Ref. [18].

$$\frac{d^2\sigma}{d\Omega d\omega} = \frac{\sigma_{coh}}{4\pi\hbar}\frac{k_f}{k_i}S_{coh}(\vec{Q},\omega) + \frac{\sigma_{inc}}{4\pi\hbar}\frac{k_f}{k_i}S_{inc}(\vec{Q},\omega), \qquad (2.13)$$

where, $S_{coh}(\vec{Q},\omega)$ and $S_{inc}(\vec{Q},\omega)$ are the coherent and incoherent scattering functions. These functions are Fourier transformations of the van Hove correlation functions $G(\vec{r},t)$, which can be described as the probability for an atom at the origin at time 0, to also be found within the unit volume at a position $\vec{r}$ at a time t.

Van Hove's correlation functions can be divided into two parts: a distinct part, $G_d(\vec{r}, t)$ and a self part, $G_s(\vec{r}, t)$. The distinct part $G_d(\vec{r}, t)$ gives the probability of finding at $\vec{r}$ and at time t, an atom that is distinct from the one found at the origin at time 0; and the self part deals with situations where the same atom located at the origin at time 0 is found at position $\vec{r}$ at time t. $G_d(\vec{r}, t)$ is related to $S_{coh}(\vec{Q}, \omega)$, while $G_s(\vec{r}, t)$ with $S_{inc}(\vec{Q}, \omega)$ [19].

2.1.2 Inelastic and Quasi-Elastic Neutron Scattering

As shown in the Table 2, different elements have distinct values for the coherent and incoherent scattering lengths. In this work, the studied materials are hydrogenous systems, and as for the hydrogen $\sigma_{inc} \gg \sigma_{coh}$, we can consider that in a inelastic neutron scattering study the contribution from the coherent scattering is negligible compared to the incoherent scattering. This justifies the use of neutron spectroscopy as the main tool to study hydrogen dynamics in different structures. Therefore, considering only the incoherent part of Eq. (2.13) and the self part, $G_s(\vec{r}, t)$, of the van Hove correlation function. The self part can be divided in the two parts [16].

$$G_s(\vec{r}, t) = G_s(\vec{r}, \infty) + G_s^{'}(\vec{r}, t), \tag{2.14}$$

where the first term is the value of the correlation function at very long times, $(t \to \infty)$. The Fourier transformation in both space and time domains lead to the incoherent scattering function, which is separated into elastic and inelastic components given by:

$$S_{inc}(\vec{Q}, \omega) = S_{inc}^{el}(\vec{Q}, \omega)\delta(\omega) + S_{inc}^{in}(\vec{Q}, \omega). \tag{2.15}$$

From Eq. (2.15), we observe that, as already shown in Figure 2, the scattering function can be separated into a purely elastic component and an inelastic component. The inelastic part can in turn be further divided into a purely inelastic scattering part, produced by vibrational motions, and a quasi-elastic contribution, resulting from atomic translational and rotational motions. These are the so-called inelastic neutron scattering (INS) and quasi-elastic neutron scattering (QENS). Considering that the different contributions happen in different time scales, each scattering functions can be described independently from each other, and the total scattering function is a convolution of the scattering functions attributed to each motion [20]. Consequently, the contributions from single particle motions, $S_{inc}(\vec{Q}, \omega)$, takes the form:

$$S_{inc}(\vec{Q}, \omega) = S_{inc}^{trans}(\vec{Q}, \omega) \otimes S_{inc}^{rot}(\vec{Q}, \omega) \otimes S_{inc}^{vib}(\vec{Q}, \omega). \tag{2.16}$$

The terms in equation (2.16) describe contributions from the translational, rotational and vibrational modes, respectively.

Now I will focus on the description of inelastic neutron scattering and how the combination of this experimental technique to density functional theory (DFT) was useful to the development of this thesis. A more detailed discussion of Equation 2.16 is given in Section 2.1.4.

2.1.3 Inelastic Neutron Scattering and Density Functional Theory Calculations

The main characteristic of an inelastic neutron scattering (INS) measurement is the determination of characteristic frequencies of the atomic motions in a given material. Similar to other spectroscopic techniques, the results are basically a spectrum formed by several peaks, which broaden with increasing temperature due to the Debye-Waller factor. INS however, offers a unique advantage that cannot be achieved by other widely used optic spectroscopies techniques, like Infrared and Raman:

1. INS has no selection rules due the nature of the interaction between the probe and the sample (neutron-nucleus interaction). Thus, in principle all transitions are observable;

2. due the large H-cross section, INS is extremely useful for looking hydrogen motions [21];

3. the INS amplitude is proportional the motion and the scattering cross section of the atoms involved.

These properties make INS an extraordinary test bed for the quality of *ab initio* calculation of vibrations in molecules [22], which are applied to characterize and/or predict materials properties, and also used for the simulation of process in materials [23].

Density functional theory (DFT) calculation is mainly applied for understanding electronic, structural and vibrational properties of large molecular systems. A force constant refinement method, based on the INS vibrational frequencies, is briefly described in Figure 4, adapted from [21].

The combination of INS to DFT calculations was used in this thesis during the development of papers 1 and 2. Details are given in Chapters 3 and 4, respectively.
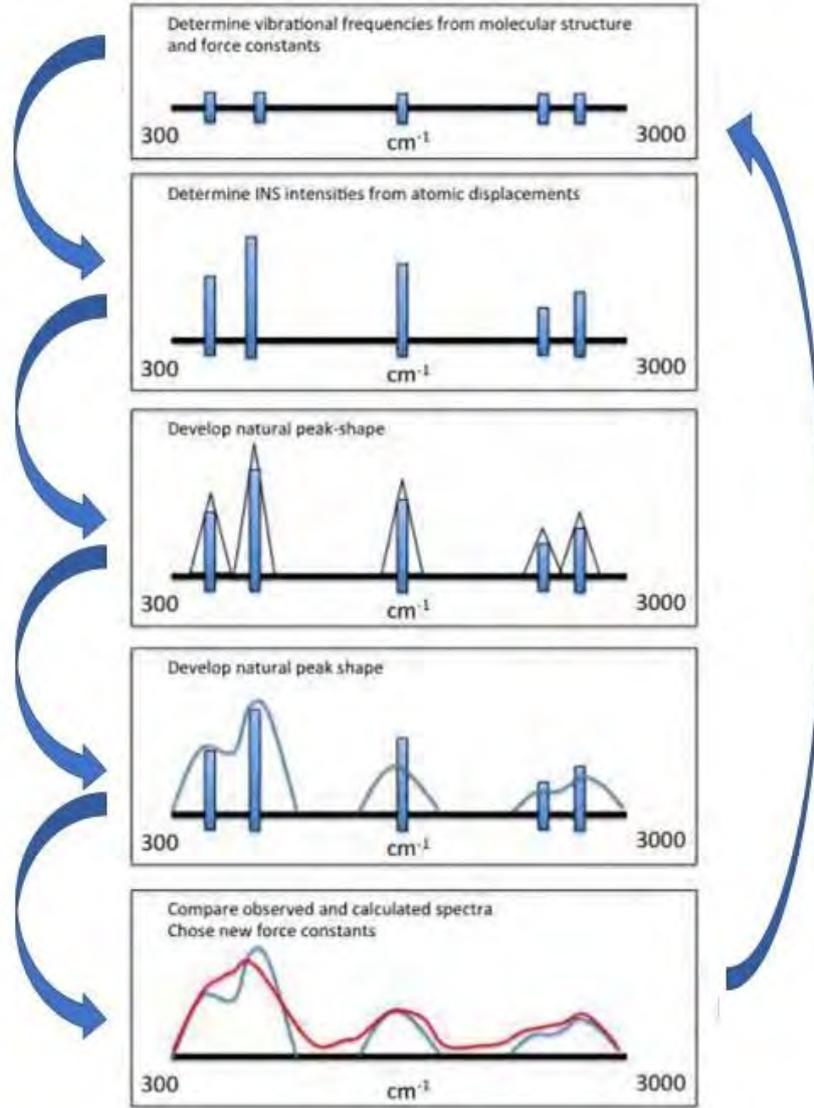
Figure 4 Schematic of the theoretical INS spectrum based on DFT method used in this thesis as a support for the INS data interpretation.

I turn now to a brief discussion of QENS and the EFW approach.

2.1.4 Quasi-Elastic Neutron Scattering - QENS

In a QENS spectrum, the vibrational contribution, $S_{inc}^{vib}(\vec{Q}, \omega)$, will mainly contribute to the background. Thus, in the Equation 2.16, it can be simply substituted with an attenuation term such as the Debye–Waller factor [16]. As a result, the incoherent scattering function can be re-written as:

$$S_{inc}(\vec{Q}, \omega) = e^{-\langle u(t)^2 \rangle Q^2/3} \left[S_{inc}^{trans}(\vec{Q}, \omega) \otimes S_{inc}^{rot}(\vec{Q}, \omega) \right]. \tag{2.17}$$

The translational contribution, important for dispersed molecules, can be described by an

isotropic continuous translation diffusion model, where $S_{inc}^{trans}(\vec{Q},\omega)$ is a Lorentzian function:

$$S_{inc}^{trans}(\vec{Q},\omega) = \frac{1}{\pi}\frac{DQ^2}{(DQ^2)^2 + \omega^2},\tag{2.18}$$

where DQ^2 is the half-width at half-maximum (HWHM) Γ of the Lorentzian curve, and D is the translational diffusion coefficient [19], described as:

$$D = \frac{\langle l^2 \rangle}{6\tau},\tag{2.19}$$

$$\Gamma = DQ^2.\tag{2.20}$$

where l is the distance that the particle travel during the time τ. From Eq. (2.19) and (2.20), we can conclude that, for continuous diffusion Γ and Q^2 are linearly dependent.

In the case of *bulk water*, the motions of the water molecules occur by finite jumps, thus DQ^2 is insufficient to describe the diffusion. The Singwi and Sjölander [24] model is then the best choice, where Γ is defined as:

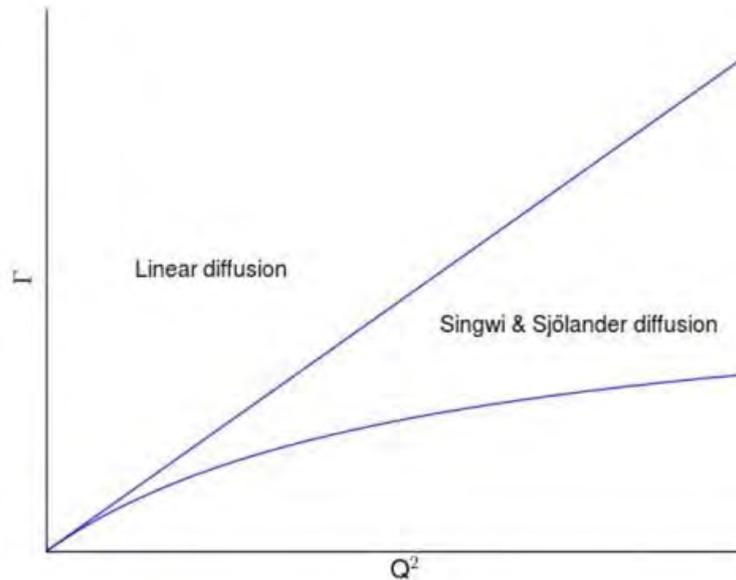$$\Gamma = \frac{DQ^2}{DQ_\tau^2 + 1}.\tag{2.21}$$

Figure 5 Representations of the linear and Singwi-Sjölander diffusion models.

On the other hand, the rotational scattering function, $S_{inc}^{rot}(\vec{Q},\omega)$, is normally well described using the Sears model [25], in which the rotational motion is assumed to be confined

on the surface of a sphere with radius *a,* and reorientations of atoms in a molecule by small random angle changes are considered. The function then becomes:

$$S_{inc}^{rot}(\vec{Q}, \omega), = A_0(Q_a)\delta(\omega) + \sum_{l=1}^{\infty} A_l(Q_a)\frac{1}{\pi}\frac{\tau_l}{1 + \omega^2\tau^2}, \qquad (2.22)$$

where, $A_0(Q_a)$ is the elastic structure factor, $A_l(Q_a)$ is the quasi-elastic structure factor and τ_l is the rotational residence time. The relaxation time τ_l describes the half-width half-maximum (HWHM) of the Lorentzians. Only a finite number of the Bessel functions will contribute to the signal over the entire Q-range accessible at an instrument, thus, the Sears expansion can be approximated to a finite series of Lorentzians. Therefore, in practice the collected data can be described by one or two Lorentzians [26]. Quasi-elastic signal originating from water hydrating on encapsulated protein was analysed in Paper 4.

2.1.5 Elastic Fixed Window Approach - EFW

The elastic fixed window (EFW) approach provides the evolution of the intensity of the elastic line $S_{el}(\vec{Q}, \omega \approx 0)$, as a function of temperature. Increasing the temperature, more vibrations in the sample are activated due the thermal activation, in consequence the elastic intensity of the scattered neutrons decreases. If this evolution deviates from the expect Debye-Waller effect, we have an indication of some type of (diffusive) motion faster than the instrumental time resolution and thus visible within the resolution of the spectrometer. Moreover, it also provides a measure of the time- averaged spatial distribution of the protons. By analyzing these changes, it is possible for instance to determine the onset of the molecular mobility by noting points of inflexions in the elastic scattering response activated at different temperatures. This approach was used in Papers 3 and 4.
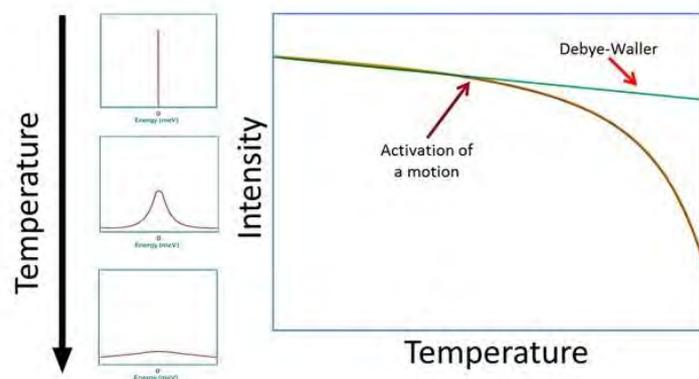

Figure 6 Illustration of the elastic fixed window (EFW) approach. The elastic intensity decreases if the dynamic scattering increases.

2.2 Thermal Analysis

Thermal analysis covers a group of methods in which physical or chemical properties of a substance or reaction products are measured as a function of time or temperature, while the temperature of the sample under a specific atmosphere, is submitted to a controlled programming. These methods find applications in quality control and research of industrial products such as polymers, pharmaceuticals, clays, minerals, metals and alloys [27].

2.1.1 Differential Scanning Calorimetry - DSC

Differential scanning calorimetry (DSC) is a thermal technique that measures the difference in the amount of energy delivered to a test substance and to a reference material, as a function of temperature or time, while both are subject to a controlled temperature programming.

Physical-chemical changes in the sample in which heat exchange occurs, such as: melting, crystallization or glass transition, more heat (endothermic event) or less heat (exothermic event) is needed to maintain the same temperature between the substance and the reference material. From DSC measurements, we obtain a curve that relates the rate of heat flux delivered to the sample as a function of temperature and time. Valuable information can be obtained by analyzing the generated curve, as the area of a peak in a DSC graph is directly proportional to the enthalpy variation of the event, see Figure 7 adapted from [28]. Consequently, we can use DSC to calculate heat capacity, thermal conductivity, purity, phase
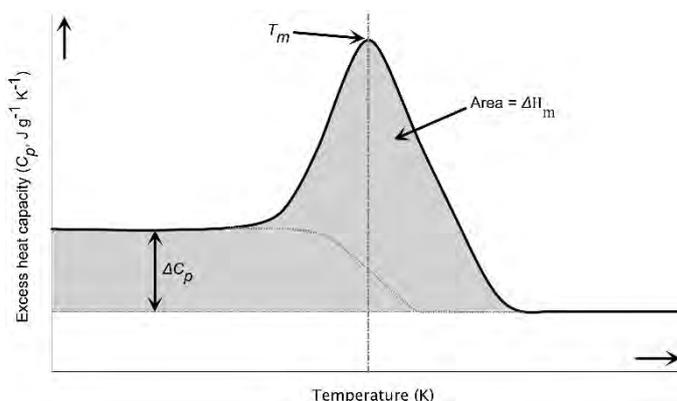

Figure 7 Example of differential scanning calorimetry (DSC) analysis. T_m corresponds to the lower critical solution temperature (LCST), ΔH_m is the enthalpy changes at the midpoint of the collapse transition, i.e., when $T \sim T_m$ and ΔC_p is the heat capacity change.

diagrams, enthalpy of transitions, crystallinity degree, melting point [29]. Here this technique was applied to obtain the results reported in papers 2 and 3, described in the Chapters 4 and 5.

DSC data presented in this thesis were collected at University of Copenhagen, using a NETZSCH DSC 214 *Polyma* in samples sealed in aluminum crucibles, placed in a nitrogen atmosphere purged at 40 *ml/min*. An empty crucible was used as reference material. The instrument was calibrated with indium as a standard. In Figure 8, a diagram of the heat-flux cell (adapted from [30]).
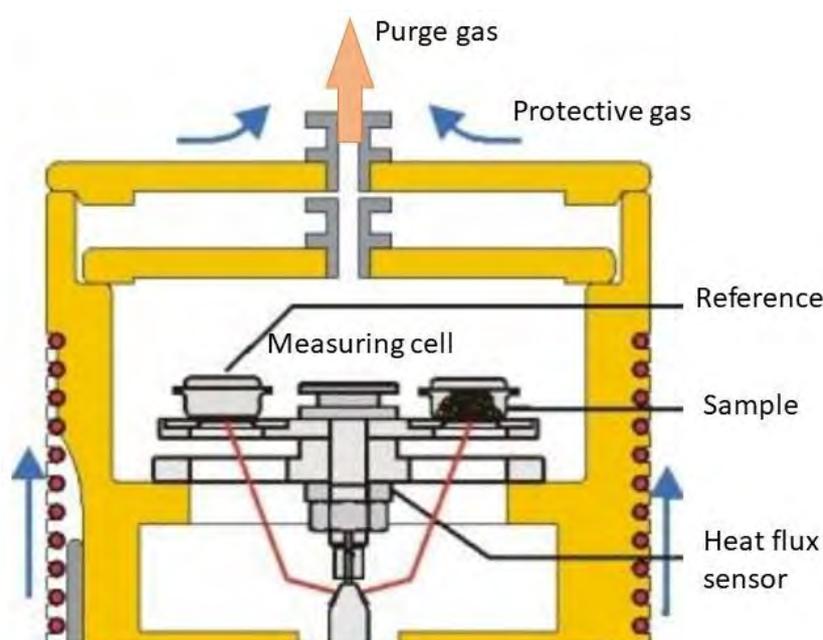

Figure 8 Layout of a measuring cell into a DSC instrument. Reference and sample crucibles are placed in the heat flux sensor. The difference in the energy necessary for keeping both crucibles at the same temperature, during a heating or cooling process, is the measured quantity.

2.1.2 Thermogravimetric Analysis Coupled to Infrared Spectroscopy – TGA-FTIR

Thermogravimetric analysis (TGA) studies the variation of mass occurring in a sample due to physical or chemical transformations as a function of time or temperature, using either a constant heating rate (kinetic measurements), or a constant temperature (isothermal measurements). The mass or fraction of the mass of a substance is continuously measured, and the information obtained is represented on a thermal decomposition curve or thermogram. see Figure 9. The main items measured are: evaporation, sublimation, decomposition, dehydration, oxidation, reduction and adsorption of gas [27], [31].

An interesting strategy is to couple a Fourier Transformed Infrared (FTIR) spectrometer to the TGA instrument. Infrared spectroscopy depends of the interaction between the infrared
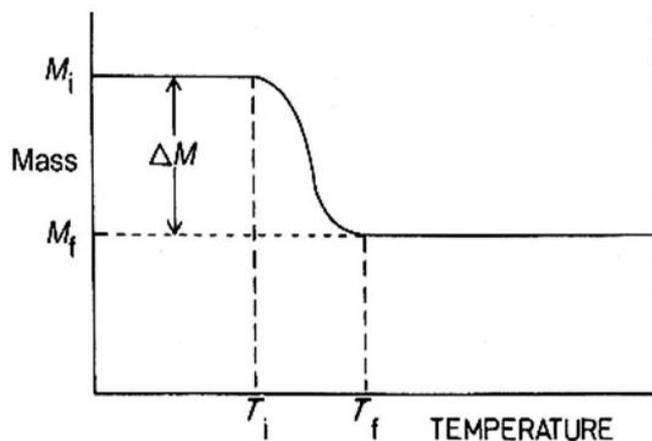
Figure 9 Schematic for a single step decomposition reaction.

radiation with the vibrating moments dipoles of the molecules, except to homonuclear diatomic molecules. Thus, an absorption spectrum from the released gases of the sample during the TGA measurement can be collected, allowing the identification of the decomposing components of a material [32]. This approach was used in Papers 2, 3 and 4, discussed in detail in Chapters 4, 5 and 6.

All the TGA-FTIR experiments used in this thesis were performed at the University of Copenhagen, using a NETZSCH TGA 209 F1 Libra instrument equipped with a FTIR spectrometer from Bruker Optics. Figure 10, illustrates the instrument used as well as shows a schematic view of the main components. This figure was adapted from [33].
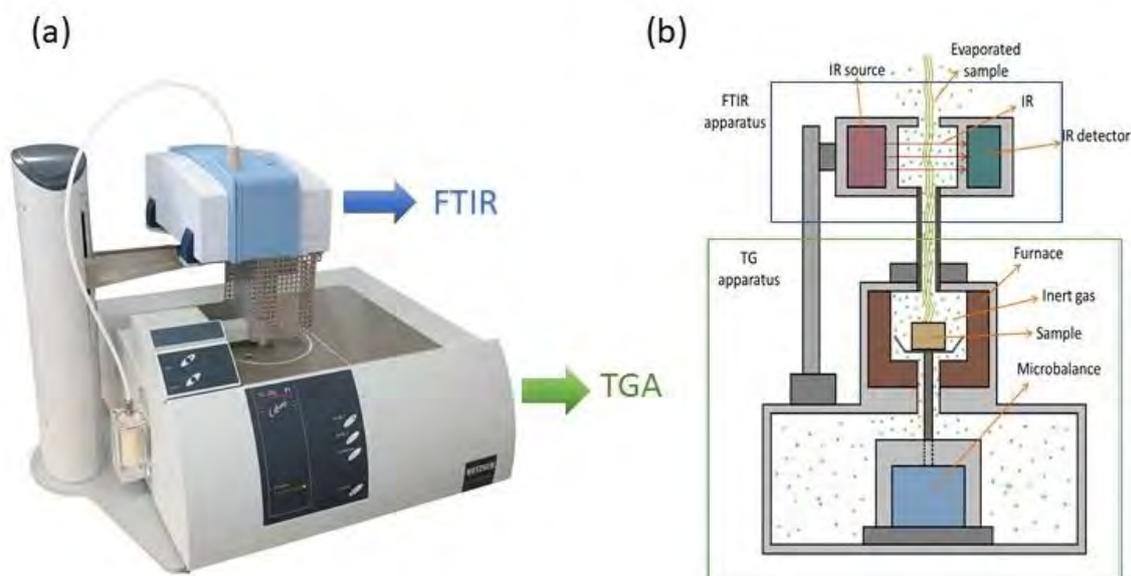

Figure 10 (a) Instrument used for performing the TGA-FTIR measurements. (b) Schematic view of the main components of the apparatus.

Paper 1 - Hydrogen bonds in crystalline D -alanine: diffraction and spectroscopic evidence for differences between enantiomers
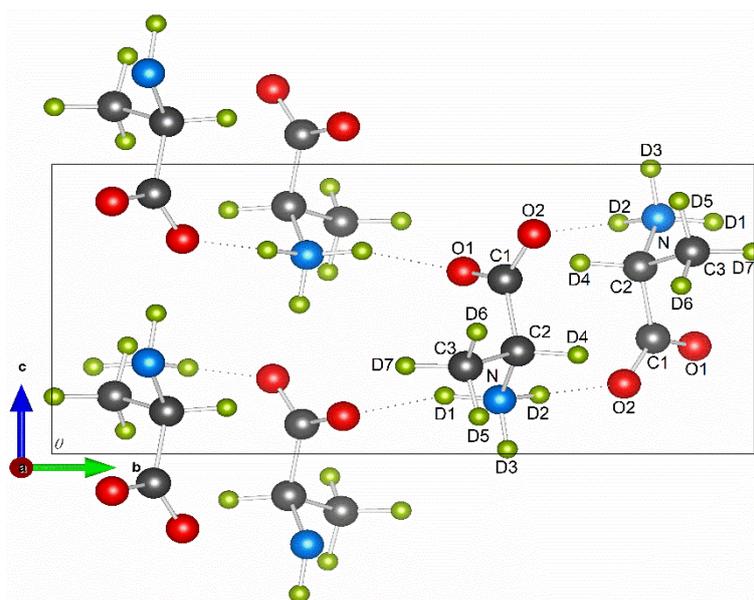

Figure 11 Crystal structure of fully deuterated D-alanine (D-Ala, C_3D_7NO) projected onto the ab-plane with atoms labelled as in Ref. Destro *et al*., 1988. The C atoms are shown in grey, the O atoms in red, the N in blue and the D atoms in green.

In this paper, we were able to connect the results from structural and dynamic studies of D-alanine (D-Ala, $C_3D_7NO_2$) using neutron powder diffraction (NPD), polarized Raman scattering (RS) and density functional theory (DFT) calculations of harmonic vibrational frequencies. The observed behavior of D-alanine at low temperature and calculated data were compared with previous studies in the enantiomer form, L-alanine (L-Ala). As a result, we

were able to show that the temperature dependencies of the ND_3 bond lengths in D-alanine are notably dissimilar compared with its enantiomer form, L-alanine. This was ascribed to slight differences in crystal packing in the two forms of alanine that is not evident in the average crystal structure. This study also demonstrated that the particular arrangement of hydrogen bonds observed in D-alanine induces distinct dynamics, which culminates in the observation of additional Raman modes.

The influence of temperature in the structure of fully deuterated D-Ala was obtained by means of neutron powder diffraction (NPD). These data were collected using the high-resolution two-axis diffractometer D2B located at Institut Laue-Langevin-ILL (France), by other members of the group. The diffractometer D2B was designed to achieve high resolution and high flux. This instrument allows an accurate determination of lattice constants and internal atomic coordinates, and consequently for the observation of subtle structural changes. It is particularly well-suited for Rietveld refinements [34].

The NPD data presented in Paper 1 were collected using a wavelength of 1.594 A° in small temperature intervals between 4 and 280 K, and were analysed using the GSAS suite of programs [35]. A schematic view of the diffractometer D2B is presented in Figure 12, adapted from [34].
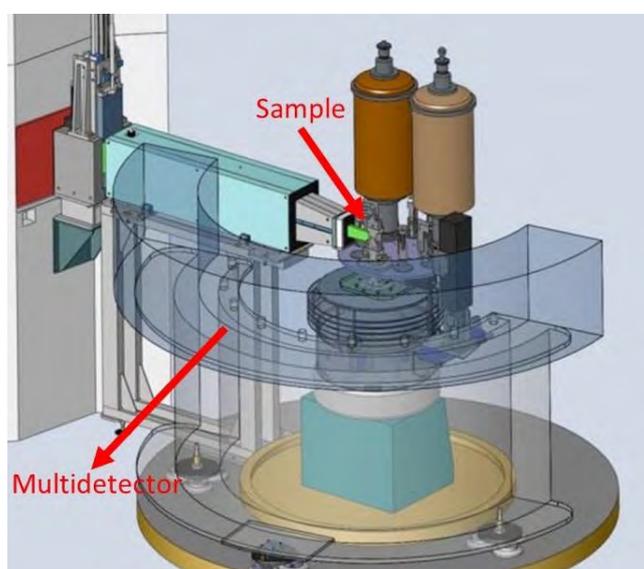

Figure 12 A schematic view of the diffractometer D2B located at Institut Laue-Langevin-ILL (France).

Polarized Raman spectroscopy (RS) data collection was performed on a hydrogenated D-Ala single crystal ($C_3H_7NO_2$) using a Horiba T64000 triple spectrometer, equipped to a liquid nitrogen cooling charge-coupled-device (CCD) detector, coupled to an Olympus BX 40 microscope to focalize the sample. Six different scattering geometries, *z(xx)z, x(yy)x, y(zz)y,*

x(yz)x, y(xz)y, z(xy)z were analysed in the interval of temperature from 20 K to 295 K. The measurements were carried out at Universidade Federal do Ceará (Brazil) by the co-authors. Figure 13 shows a photograph of the instrument.

Figure 13 Picture of the Horiba T64000 triple spectrometer used for polarized Raman measurements located at Universidade Federal do Ceará (Brazil).

In RS, a single frequency of radiation, provided by a laser, is used to irradiate the sample, which is scattered by the molecules. It is a form of vibrational spectroscopy, much like infrared (IR), where the IR bands arise from a change in the dipole moment of a molecule, due to the interaction between the incident light with the molecule. In the case of RS, however the interaction between the probe and the sample that gives rise to the Raman bands occurs due to the variation of the induced dipole moment in the molecule by the electric field from the incident radiation. The incident photon induces a polarization in the cloud of electrons around the nuclei to form a short-lived state called "virtual state", this state is not stable, thus the photon is re-radiated. If the re-radiated photon has the same energy of the incident photon, the scattering process is elastic, defined as Rayleigh scattering. In an inelastic process, the energy of the scattered photon is different of the incident photon by one vibrational unit, providing structural information of the molecule. These processes are illustrated in Figure 14 [36]–[38]. Certain vibrations that are allowed in Raman are forbidden in IR, whereas other vibrations may be observed by both techniques although at significantly different intensities, thus these techniques can be thought of as complementary.

Ab initio calculations of harmonic vibrational frequencies were carried out to assist with the analysis of the vibrational spectra. The Raman spectrum on gas-phase, using as reference
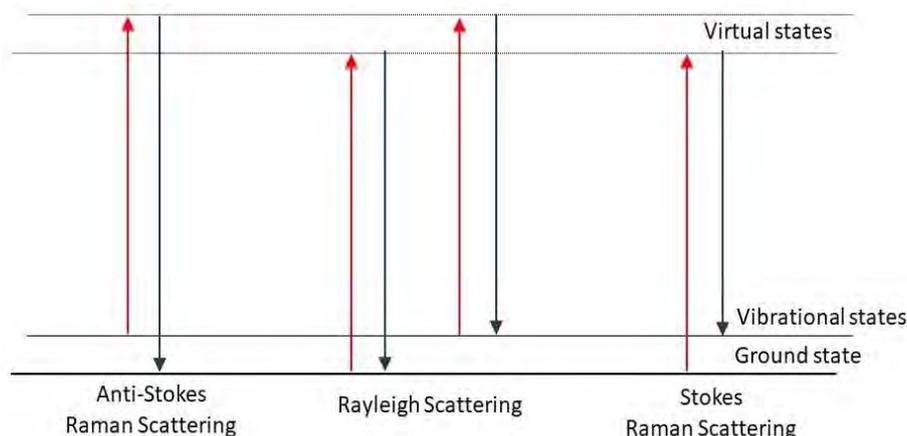
Figure 14 Schematic of the Rayleigh and Raman scattering processes.

the obtained atomic coordinates of the D-Ala at 280 K, was calculated with the software Gaussian09 [39]. Gaussian is an electronic structure program that predicts the energies, molecular structures, vibrational frequencies and molecular properties of molecules and reactions in a wide variety of chemical environment.

This data was also used as an input to aCLIMAX [22] software, to generate the corresponding INS spectra. Additionally, vibrational frequencies of crystalline D-Ala and the enantiomer form L- Alanine, were obtained by periodic calculations with the *Vienna Ab initio Simulation Package* (VASP) [40]. VASP is a complex package used for performing *ab initio* quantum-mechanical molecular dynamics (MD) simulations using pseudopotentials or the projector-augmented wave method and a plane wave basis set. To get an overview of the size of a system that can be accurately modeled using these computational approaches, we refer to Figure 15, adapted from [41].
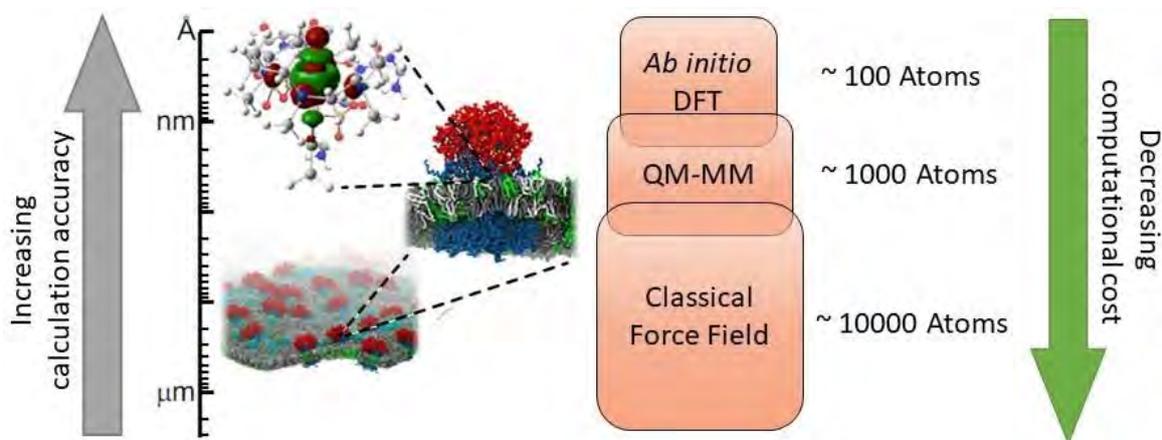

Figure 15 Computational methods and corresponding multiscale approaches. Accuracy and computational cost are higher in quantum computations of molecular systems on the atomic scale, while decrease in the description of sites in microscopic scales using classical force fields.

Based in the ensemble of our results, we found that the reorientation of the NH_3^+ group in D-Ala induces modification of the $N - H \cdots O$ hydrogen bonds between two neighbouring molecules. Differently from L-Ala, a new Raman active mode for D-Ala is observed at 468 cm^{-1} below 200 K. In addition, NPD results show that the temperature dependence of the $N - D$ covalent bonds in D-Ala and L-Ala are quite different.

To conclude, our work indicates that both L-Ala and D-Ala undergo micro-conformation transitions due to a subtle rearrangement of the hydrogen-bond network, which is manifested in the local symmetry but not the average structure of the crystal. The paper is attached to the thesis in the appendix.

Chapter 4

Paper 2 - Hydrogen bond dynamics and conformational flexibility in antipsychotics

In this project, three different antipsychotics, haloperidol ($C_{21}H_{23}ClFNO_2$), aripiprazole ($C_{23}H_{27}Cl_2N_3O_2$) and quetiapine hemifumarate ($C_{21}H_{25}N_3O_2S \cdot 0.5C_4H_4O_4$), were investigated. Their schematic structures are depicted in Figure 16. Our main objectives with this work were (i) to explore the relationship between the crystalline stability and the dynamics of these molecules and (ii) to add such information to molecular dynamics simulations of the docking process, which currently only account for flexibility of the receptor.
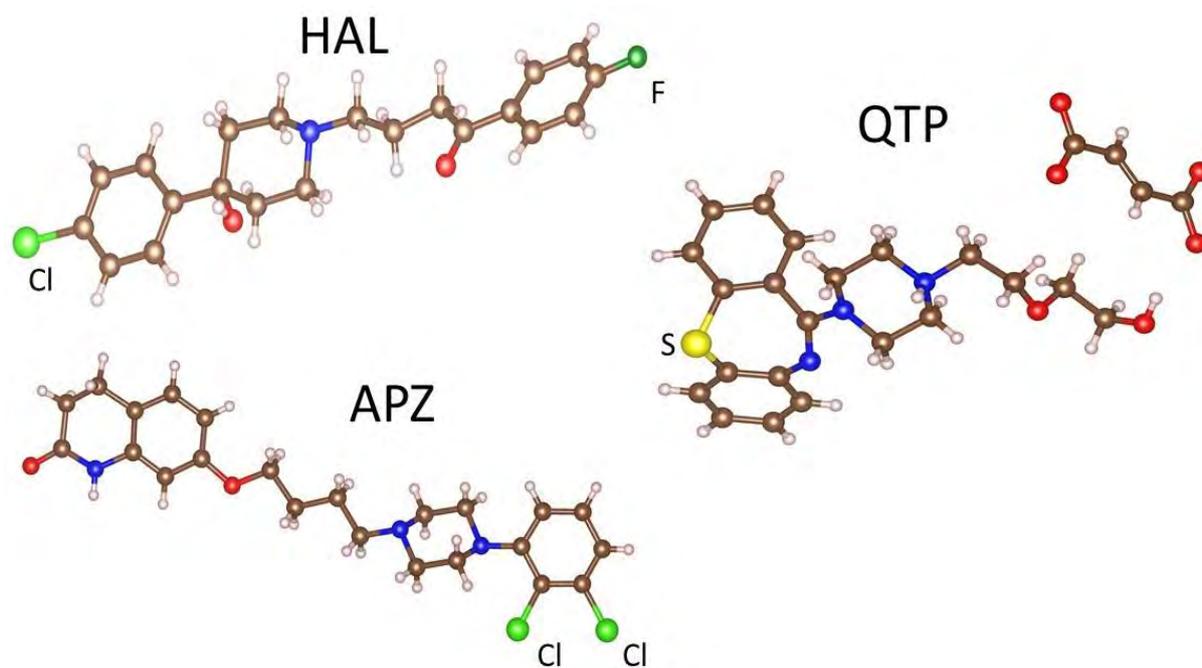

Figure 16 Molecular structure for haloperidol (HAL), aripiprazole (APZ) and quetiapine hemifumarate (QTP).

To this end, first the powder samples of haloperidol (HAL), aripiprazole (APZ) and quetiapine hemifumarate (QTP) had their molecular structures confirmed by X-rays powder diffraction (XRPD), a widely technique used to identify structures as it allows for good spacial resolution and fast measurements. The XRPD measurements were performed at Chemistry Department - University of Copenhagen, using a Bruker D8 Advance diffractometer with Cu Kα radiation (1.5418 Å) in θ/θ geometry.

Following this initial check, calorimetric studies were performed using DSC and TGA-FTIR, at the University of Copenhagen. As these techniques allow to observe changes that a variation of temperature, by a constant heating process, induce in a material, it is possible to establish the temperature range in which it has fixed and constant chemical composition, or the temperature in which they begin to decompose, or to follow the progress of dehydration reactions (loss of moisture) as well as to verify the melting point. Thus, these results gave us a complete picture of the thermal effects on the crystalline stability of these selected drugs.

DSC measurements were performed on samples sealed in aluminum crucibles, placed in a nitrogen atmosphere purged at 40 ml/min. An empty crucible was used as reference material. The instrument was calibrated with indium as a standard. Different heating rates between 2 and 15°C/min were used for all samples. The samples of HAL and APZ were heated in the interval between room temperature (RT) 25 °C and 180 °C, while the data for QTP were collected up to a temperature of 300 °C. In the TGA-FTIR experiments, the samples were placed in an aluminum oxide crucible and heated from RT to 300 °C at a constant heating rate of 10°C/min, under nitrogen gas flow of 20 ml/min. Simultaneously, spectra of the evolved gases were recorded every 3 °C to facilitate the understanding of the decomposition process. Figure 17 presents the results for the calorimetric studies.

After being sure of the structure and purity of our samples, the dynamics of polycrystalline antipsychotic compounds were further studied by INS vibrational spectroscopy using two spectrometers: PELICAN, a direct time-of-flight spectrometer located at the Australian Nuclear Science and Technology Organisation - ANSTO (Australia) [42], and TOSCA, an inverse geometry time-of-flight spectrometer located at the ISIS Neutron and Muon Source - Rutherford Appleton Laboratory (United Kingdom) [43].

Direct time-of-flight spectrometers, such as PELICAN, use a monochromatic neutron pulse E_i to exchange energy with the sample and then the flight-time of the scattered neutrons
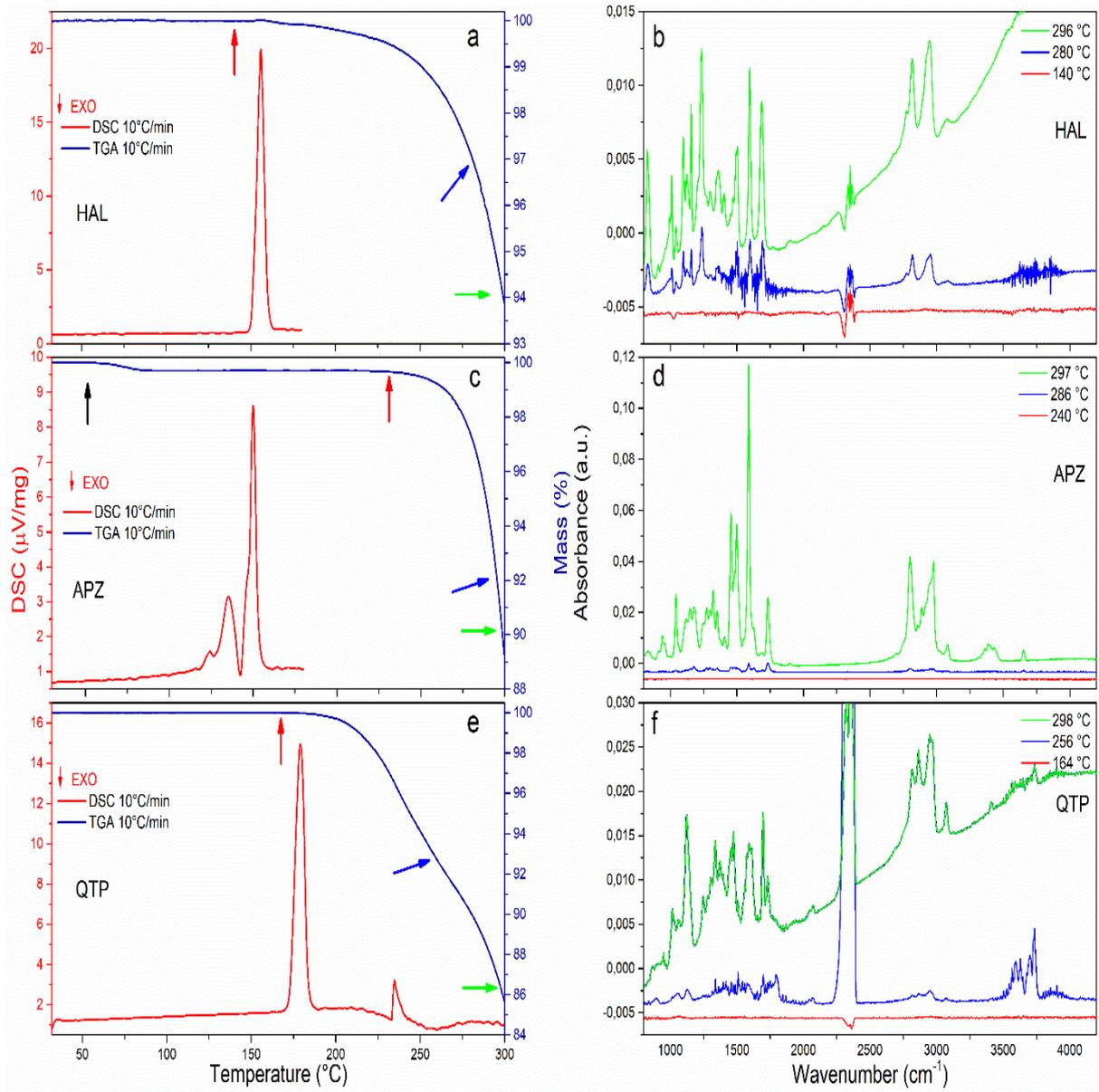
Figure 17 TGA-FTIR and DSC results. The left side of the figure shows the TGA and DSC curves while in the right side shows the FTIR collected during the heating process in the TGA. The arrows in the right side correspond the specific temperature present in the respective FTIR data. The black arrow in (b) indicates the dehydration process described in the text and associated to vibrational modes observed between 120 to 140 °C.

to determine the final energy E_f. The monochromatization of the beam is realized with a crystal followed by Fermi-choppers. The desired wavelength, λ, is selected by the Fermi-choppers according to the condition:

$$\lambda = \frac{h\tau}{mL},$$

(4.1)

where m is the neutron, h is Planck's constant, L is the distance between the choppers and τ is the calculated time-of-flight. The time at which the monochromatic pulse arrives at the sample

is known, thus the energy of the scattered neutrons is obtained from the flight-time of the neutrons from the sample to the detectors [44]. A schematic is shown in Figure 18 adapted from [45].
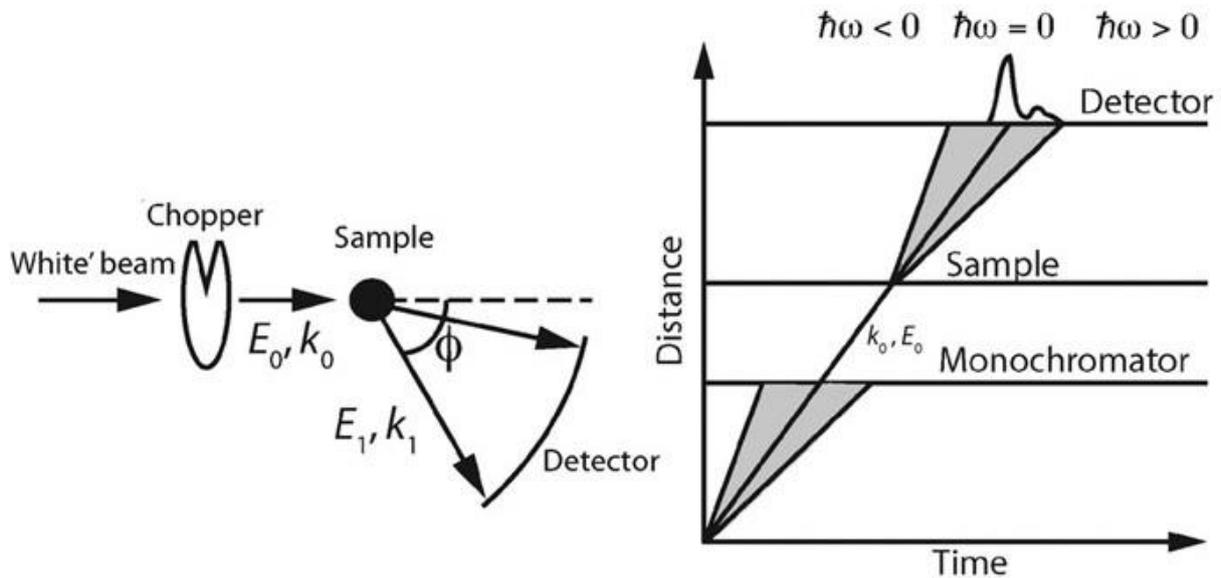

Figure 18 Schematic of a direct-geometry neutron spectrometer together with its corresponding distance–time diagrams for single pulses of neutrons.

In Figure 19 adapted from [46], a graphic representation of the kinematic region (between the red (lower) and blue (upper) parabolas) for incident neutron energy E_i=1μeV clearly shows that, a direct geometry instruments give us broader information on the neutron energy gain of the neutron or energy gain of the sample, i.e. the anti-Stokes side of the spectra.
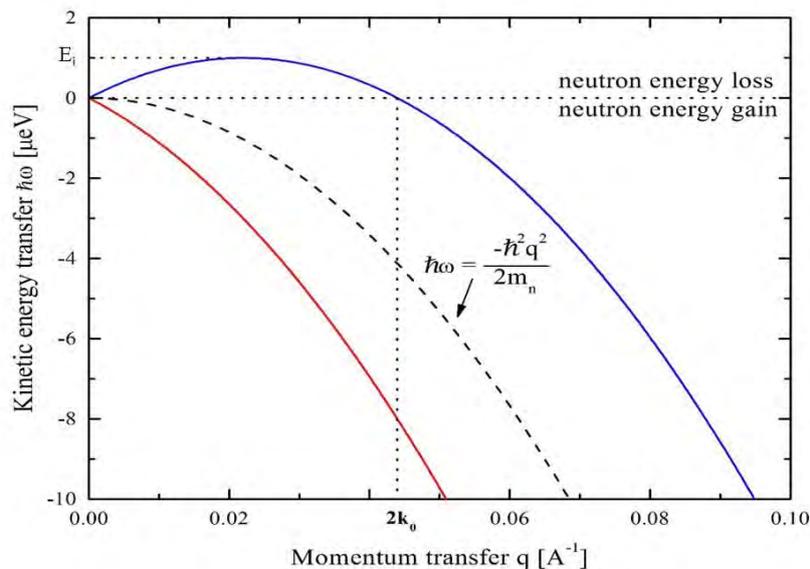

Figure 19 Graphic representation of the kinematic region (between the red (lower) and blue (upper) parabolas) for incident neutron energy E_i=1μeV.

In the case of the inverse geometry time-of flight spectrometer located in spallation source as is the case of TOSCA, the neutrons are produced already produced in pulses, therefore in principle, there is no need for a chopper. Usually the incident energy is measured by the time-of-flight and the final energy is kept constant by a set of analyzer crystals. A schematic is shown in Figure 20, adapted from [45].
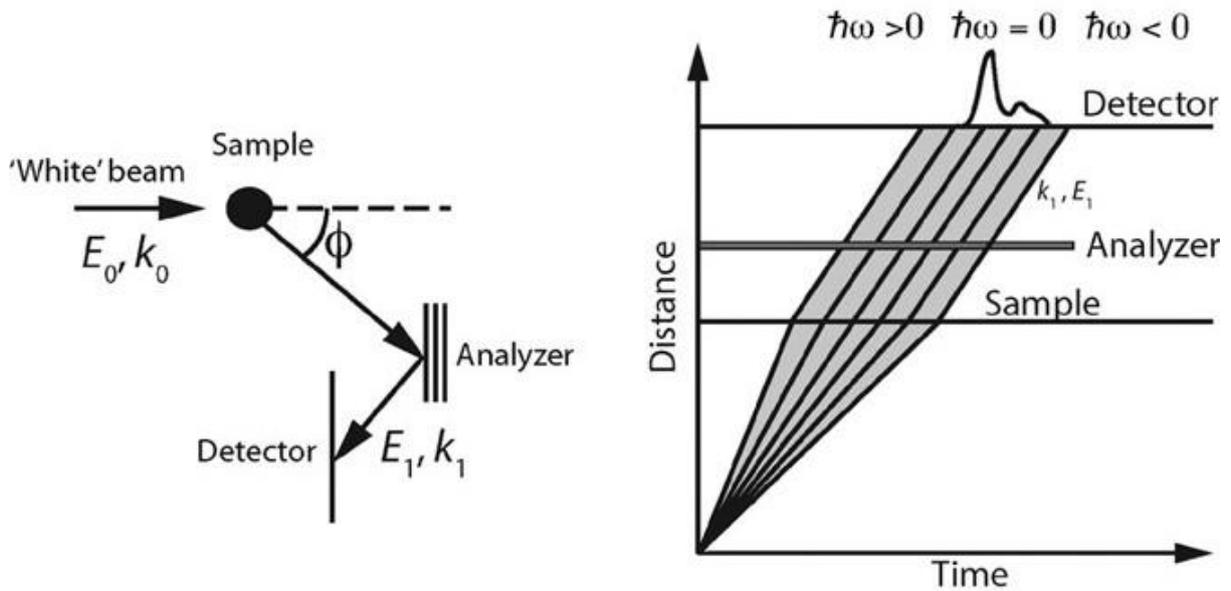

Figure 20 Schematic of an inverse-geometry neutron spectrometer located in a spallation source together with its corresponding distance–time diagrams for single pulses of neutrons.

With all this information in mind, we have used PELICAN with an incident wavelength of 4.72 Å and an instrumental resolution of $\Delta E= 1200$ µeV, to (i) access the vibrational motions in the antipsychotic molecules in the energy range $0 – 40$ meV ($0 - 322$ cm^{-1}) and (ii) check the dynamical behavior of the different local motions occurring the observation time covered by the instrument by analyzing the evolution of the quasi-elastic scattered intensity.

Data were then collected at temperatures of 60 K, 100 K, 150 K, 200 K, 250 K and 300 K and processed using the Large Array Manipulation Program (LAMP) [47]. The spectra were first normalized to a vanadium standard to account for detectors efficiency, followed by subtraction of the spectrum of an empty sample holder to correct for background. Finally, the spectra were converted to the incoherent dynamic structure factor, $S(Q, \omega)$, where Q is the magnitude of the scattering wave vector and ω is the energy transfer.

No quasi-elastic broadening was observed, thus indicating that no relaxation processes is thermally activated in the samples within the observation time window of 60 *ps* covered by the spectrometer.

As S(Q, ω), is dominated by vibrational motions of the hydrogen atoms and it is also correlated the generalized density of state GDOS, $G(\hat{\theta}, \omega)$, the information contained in S(Q, ω) was converted as follows:

$$G(\hat{\theta}, \omega) = \frac{S(\hat{\theta}, \omega)}{Q^2(\hat{\theta}, \omega)} B(\omega, T), \tag{4.2}$$

where $\hat{\theta}$ refers to the averaged scattering angle and $S(\hat{\theta}, \omega)$ is the scattering vector, which is calculated at each energy transfer for the averaged scattering angle as:

$$S(\hat{\theta}, \omega) = \frac{1}{N_D} \sum_i S_i(\theta_i, \omega), \tag{4.3}$$

obtained by summing the signal from the first to the last detector considered, with θ_i being the angle corresponding to each detector. N_D is the total number of detectors.

$$B(\omega, T) = \hbar\omega(1 - e^{-\hbar\omega/kT}), \tag{4.4}$$

is a function accounting for the population of the vibrational modes with temperature, *T* [48]. Thus, the temperature dependence of the GDOS will give rise to broadening in the harmonic motions of the molecular groups in HAL, APZ and QTP. Note that in the case of direct geometry instruments, $\hbar\omega$ is negative as the energy transfer is from the sample to the neutron (anti-Stokes or down scattering or neutron energy gain), as discussed earlier. This implies that at lower temperature the bands in the inelastic spectrum have intensities proportional to the Boltzmann factors and therefore vanish on cooling.

TOSCA, on the other hand, as an inverse geometry time-of-flight spectrometer allows for observing vibrational spectra in the neutron energy loss, or energy gain of the sample, i.e. the Stokes side of the spectra. The instrument covers the entire frequency range for molecular vibrations. Therefore, to minimize the broadening effects cause by thermal activation on the vibrational modes, INS spectra for all samples were recorded at 10 K and converted to the scattering law, S(Q, ω) using standard programs.

Periodic calculations on crystalline antipsychotics were performed using VASP, previously described in Chapter 3. The atomic coordinates were optimized with the unit cell fixed at the experimental values [49]–[51], followed by harmonic frequency calculations. The

resulting vibrational amplitudes and frequencies were used to derive a simulated INS spectrum with the aCLIMAX software [22].

Comparisons of the experimental INS spectra for HAL, APZ and QTP with those calculated by DFT were initially intended to provide information about the flexibility of the molecular groups in each sample and to connect this flexibility to the stability of the crystalline structures. This task, i.e. the assignment of the main vibrational bands in the INS originating from large amplitude motions of the H-atoms, was achieved by visualizing the molecular vibrations of the modes obtained by VASP using Jmol software [52]. In Figure 21, the experimental results obtained using PELICAN (top) and TOSCA (middle) are compared to the DFT calculations (bottom) for QTP. However, while performing this task, a number of points were carefully considered:

(i)   The spectra have a relatively complex and structureless nature resulting from the low symmetry of this molecule, however the calculation does not seem to miss any observed feature.

(ii)   Most of the intensity in the analyzed region from 0 to 40 meV (0 to 322 cm^{-1}) is due to mixed external motions of the molecule in the lattice, making the disentanglement of the low-frequency modes very difficult.

(iii)   Thus, even if the agreement between calculated and experimental data is sufficiently good, only few vibrational features can be unambiguously assigned.

With this in mind, when assigning the most intense modes obtained in the calculated spectra, marked with blue arrow for QTP and red arrow for HAL, see Figure 22, we can conclude that:

(i)   In HAL the main mode at 8 meV can be described as displacements of the H-atoms in the aromatic rings (hidroxyclorophenilpiperidino and fluorophenyl), while most of the low frequencies modes arise from deformations of the alkyl group connecting the hydrophobic and hydrophilic heads.

(ii)   In APZ, in the analysed range all modes seem to have similar intensities, indicating similar contribution of the hydrogen atoms to the normal mode eigenvector, and consequently that we are observing collective motions dominated by displacements of the piperazine and quinoline rings along the chain.

(iii)   In QTP the most intense modes at 7, 16 and 20 meV can be described as deformations from the aromatic rings

This approach, i.e. the combination of INS and DFT calculations, can be valuable for drug design as it can provide insight on how a starting molecule can change to another due to the flexibility of the hydrogen atoms, and thus how these changes allow the drug to fit into flexible receptors. The paper with supplementary information with these results is given in the appendix.

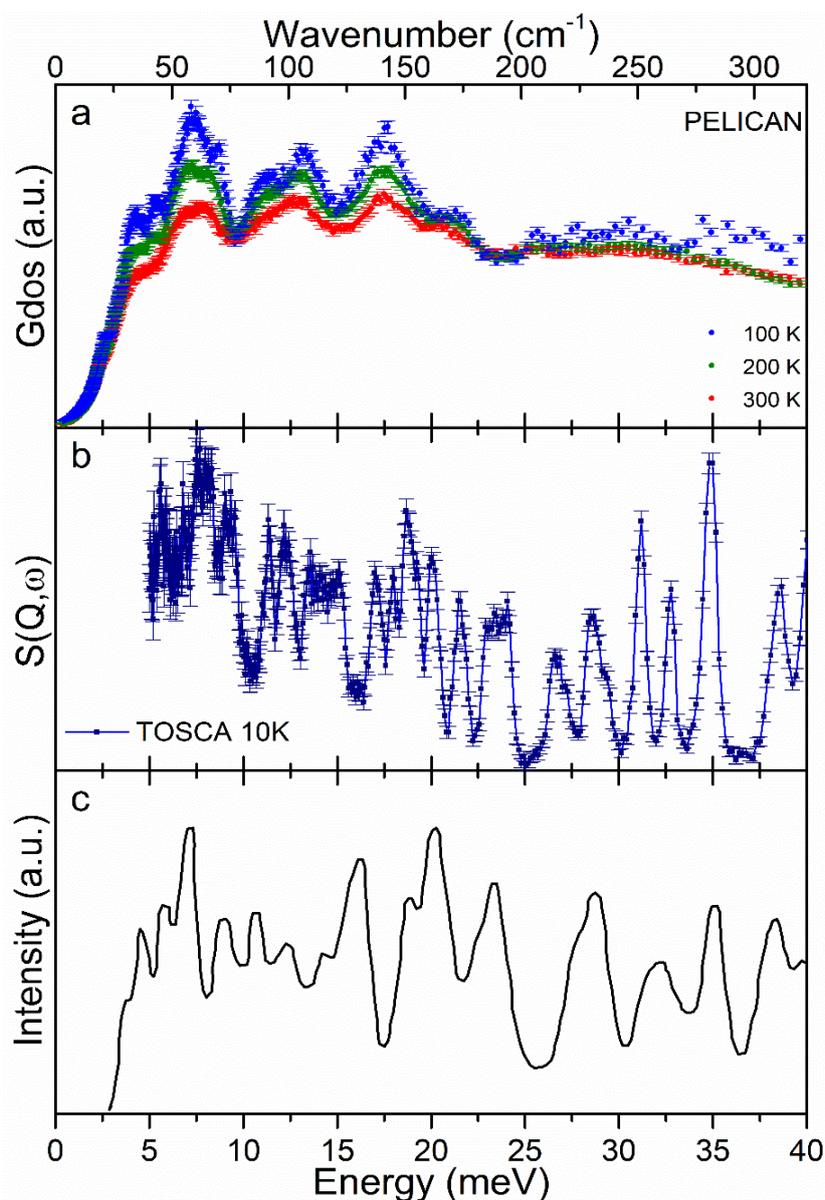**Figure 21** Experimental and calculated INS data for QTP ($C_{21}H_{25}N_3O_2S \cdot 0.5C_4H_4O_4$). (a) Experimental INS data obtained using the spectrometer PELICAN at different temperatures. (b) Experimental INS data from the spectrometer TOSCA obtained at 10 K. (c) Calculated INS spectra obtained using the VASP software.
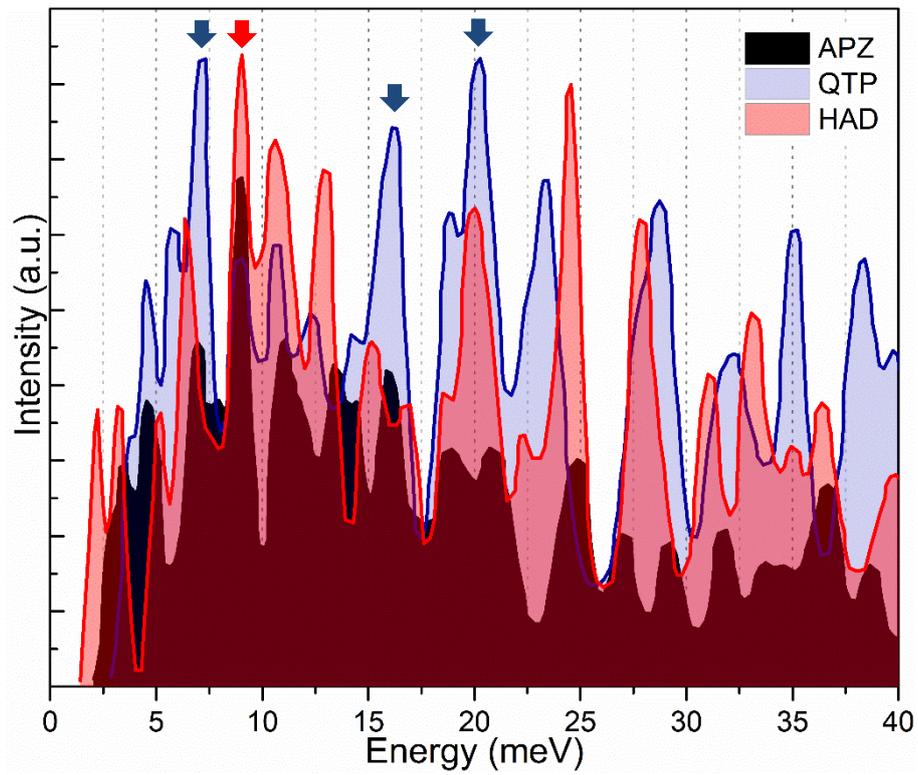
Figure 22 Calculated INS using the VASP software. APZ in black, QTP in blue and HAD in red.

Chapter 5

Paper 3 - Probing water mobility in human dentine using neutron spectroscopy

During this work, we investigated the hydrogen mobility within innate and demineralized human dentine, which was analysed by combining neutron spectroscopy and thermal analysis methods. The results were first presented by A. K. Lauritsen in his BSc thesis, which I co-supervised in 2016. Afterwards, new measurements were performed, and a paper was submitted to Journal of Dental Research. The attached paper is now under a second review, where the highlighted in yellow indicates changes to the original version.

Dentine is the material that makes up the bulk of human teeth. It has a tubular structure created by the collagen network. It is comprised of three main components: water, protein and hydroxyapatite ($HCa_5P_3O_{13}$). Water within dentine may exist in different states: 1) an almost free state, also known as bulk-like water; 2) adsorbed to the surface, named loosely bound water; and 3) as structural water, also called tightly bound water. These different states of water in dentin are related to variations in mass loss as a function of temperature, pressure [53] or dehydration methods [54]. Furthermore, these different water states are likely to be influenced by acid-etching the dentine prior to bonding, a pretreatment required for traditional adhesive dental materials. Therefore, understanding the changing states of water within demineralized dentine may help optimize bonding to this tissue.

In order to perform these experiments, two slices from seventeen human molars anonymous donors were used. The teeth were sectioned using a diamond disc refrigerated by water (Accutom, Stuers, Denmark) at the Department of Odontology ate the University of Copenhagen. All slices were stored in 0.5% chloramine to prevent microbial growth and rinsed

in deionized water immediately before the experiments. To get information from the same biological material, one slice from each tooth (n=17) was immersed in 10% phosphoric acid (pH 1.0) under mechanical agitation during 4 days and is hereon referred to as demineralized dentine. The demineralized dentine was then completely rinsed and immersed in deionized water for 24 h under mechanical agitation at 300 rpm. The remaining dentine slices (n=17), referred to as dentine herafter, remained untreated. From each sample (dentine and demineralized dentine), 16 slices were analysed using neutron spectroscopy, while 1 slices was used for thermal analysis. A schematic of the sample preparation is shown in figure 23.
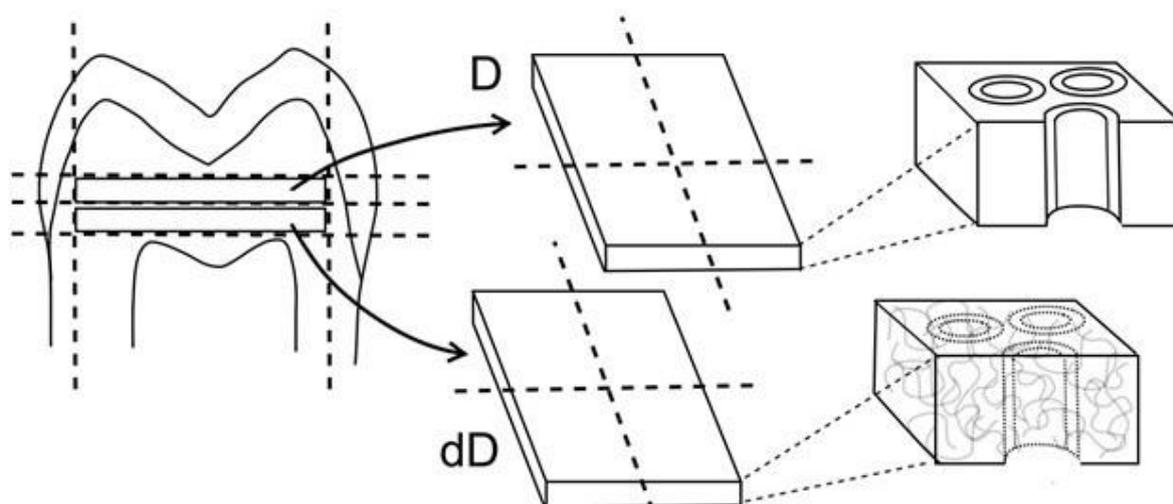

Figure 23 Schematic of the sample preparation. From each tooth 2 dentine slices were obtained, namely dentine (D) and demineralized dentine (dD). To the right are enlarged cuts of the dentine showing the schematic tubular structure in the samples, including the exposed collagen in dD.

DSC and TGA-FTIR measurements were performed at the University of Copenhagen, in order to better understand the denaturation and the subsequent decomposition of the protein, as well as decomposition of the hydroxyapatite, as a function of tissue mineralization.

Two slices from the same tooth were scratched with a sharp blade followed by breaking each slice using tweezers in 4 equal parts, see Figure 24. In the case of the demineralized dentin, as the sample was very soft, only the blade was used. Since it was possible to measure only 2 parts simultaneously after cutting, the other parts remained immersed in water until the time of the measurement. All samples were dried using paper towels immediately before the experiments to minimize observation of surface water.
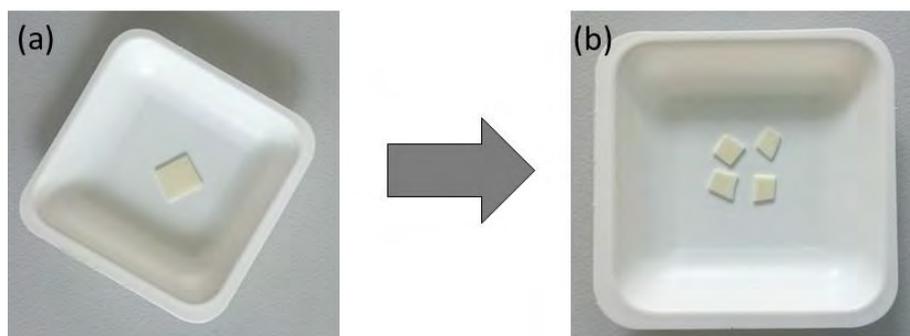
Figure 24 Photograph of the sample used for the calorimetric measurements. (a) Slice of a dentine sample. (b) Slice of a dentine sample after the cutting process.

Based on the results presented in A. K. Lauritsen thesis, the best conditions for the thermal analysis measurements were determined. Therefore, all DSC experiments started at 20 °C and the samples, placed in a sealed aluminum crucible, were heated to 500 °C at 5 °C/min under a nitrogen atmosphere purged at 40 ml/min. As reference material an empty crucible was measured under the same conditions. The instrument was calibrated with indium as a standard. In the case of the TGA-FTIR measurements, the samples were placed in an aluminum oxide crucible, and kept under an isotherm at 20 °C during 5 min, in order to stabilize the initial environment. Afterwards the samples were heated a rate of 5 °C/min to 600 °C under nitrogen gas flow of 20 ml/min. A new FTIR spectrum of the evolved gases was recorded for every 3
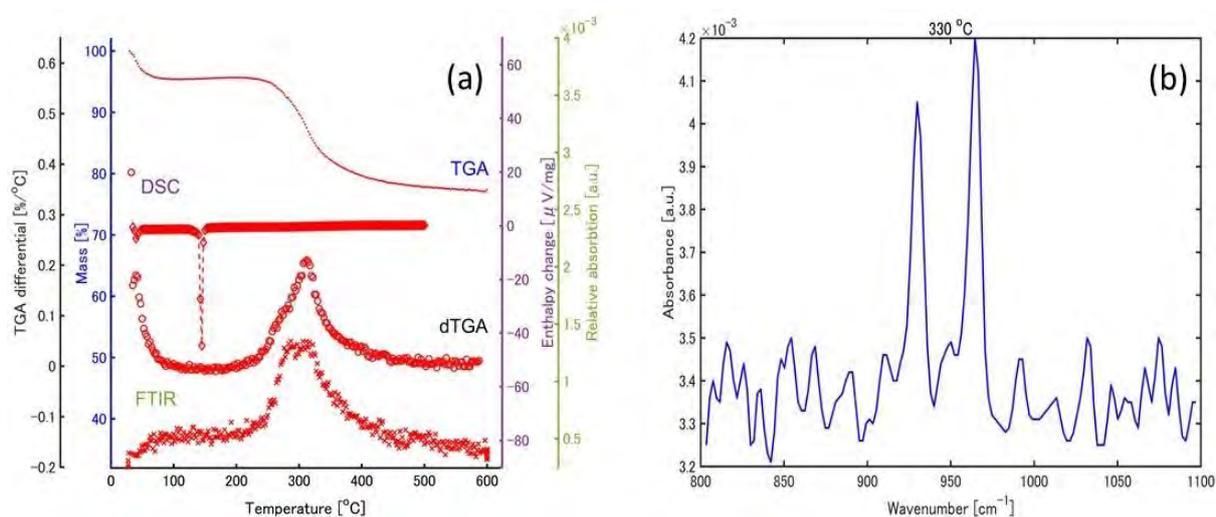
Figure 25 (a) Representative curves from demineralized dentine plotted as a function of temperature. 1) Results from the TGA are expressed as percentage mass; the dTGA, is defined as the negative of the differential of the TGA curve and is expressed as percentage mass per degree of temperature increase; and the FTIR curve represents the relative absorbance, defined as the ratio between the maximum peak intensity and the mean value of the spectral background, in arbitrary units. 2) Calorimetry (DSC) data is expressed as enthalpy change in voltage per mass. (b) Absorbance spectrum from a demineralized dentine sample at 330 °C between 800 and 1100 cm^{-1}. Note here the peaks associated to the vibration of phosphorous at 940 and 960 cm⁻¹.

degrees of data collection, thus facilitating the understanding of the decomposition process. As we were dealing with biological samples, to verify the reproducibility of the results all measurements were taken in either duplicate (for the paper) or in triplicated (for the thesis).

Figure 25 presents the result obtained for demineralized dentine. One of the main findings from the thermal analysis was that collagen denaturation occurs at low temperature in demineralized dentin. As the temperature increases second mass loss, corresponding to a peak in the dTGA curve at $T_{deg} = 330$ ºC is observed. Analysis of the FTIR-TGA spectrum at selected temperatures shows the appearance of a vibration at 960 cm^{-1}, ascribed to a symmetric stretch of P-O [55] and a second vibrational mode at ~940 cm^{-1}, related to phosphonate bands [56]. The presence of the P-O stretch in the demineralized sample implies that using 10% phosphoric acid for 4 days does not completely solubilize all hydroxyapatite crystallites. This contradicts previous work [54] and shows that the flexural method alone is not enough to confirm the complete demineralization of dentine.

Additionally, the EFW approach was used to study the hydrogen dynamics of water and hydroxyl groups in both samples. Figure 26 shows a photograph of the sample used in the experiment mounted inside a flat aluminium sample holder.

The EFW data between 2 and 300 K were collected using the inverted geometry time-of-flight backscattering spectrometer MARS (Mica Analyzer high-Resolution Spectrometer) at the Paul Scherrer Institute - PSI (Switzerland), SINQ spallation source, in Switzerland, between 2 K (He temperature) and 300 K (27 °C). Using a wavelength of 6.66 Å corresponding to an elastic resolution of ~13 μeV [57].

Figure 26 Picture of the dentin slices used for experiment carried out on the backscattering MARS at PSI, Switzerland.

A backscattering spectrometer uses a geometrical condition to achieve its high resolution. The energy transfer between the neutron and the sample is observed by varying the incident neutron energy E_i, while keeping the final energy E_f fixed. The variation in incident neutron energy, E_i comes by Doppler shifting the neutron wavelength. The beam hits first the sample and the neutrons are then scattered towards the analyzers. These are supposed to scatter the neutrons back in a Bragg angle. Differentiating Bragg's law ($\lambda = 2d \sin\theta$) we have:

$$\frac{\Delta\lambda}{\lambda} = \frac{\Delta d}{d} + \cot(\theta)\,\Delta\theta, \qquad (5.1)$$

where d crystal analyzer lattice spacing, λ is the neutron wavelength, and θ is the scattering angle. With this technique we can achieve an energy resolution as high as FWHM $\approx 0.1\ \mu eV -$ 3.5 μeV. The right side of the Eq. 5.1 becomes very small when the Bragg angle is close to 90°, thus the wavelength band broadening of the neutrons detected is minimized [16]. A schematic view of the MARS spectrometer is presented in Figure 27, adapted from [57].
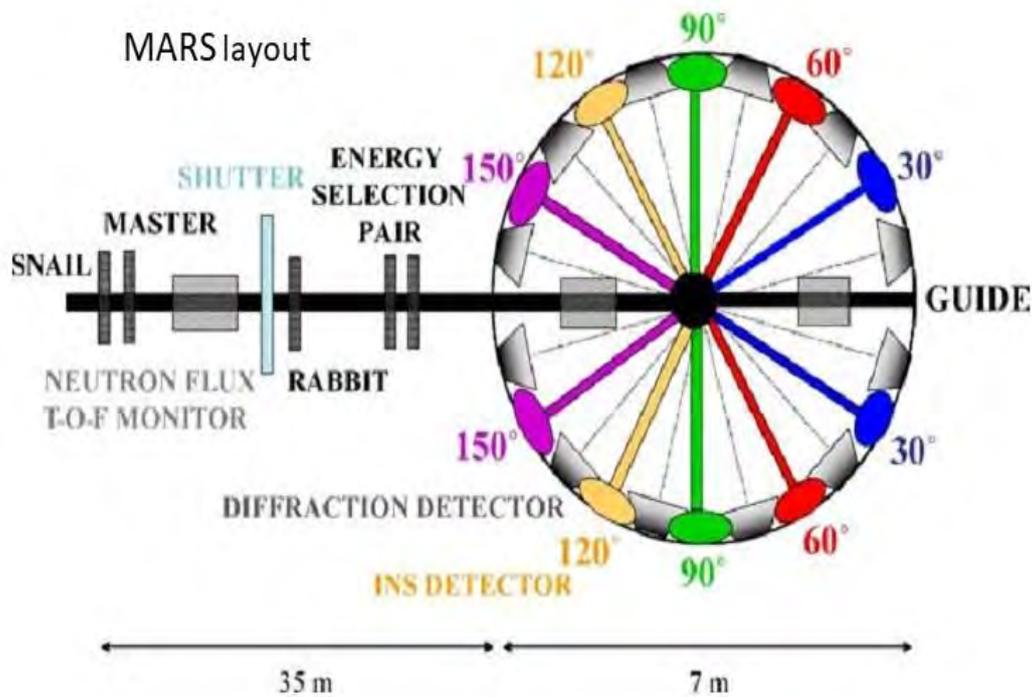
Figure 27 Schematic view of the backscattering spectrometer MARS, located at PSI (Switzerland).

As in neutron spectroscopy the signal of the hydrogen dominates, any changes in the measured intensity observed in the EFW scan are directly related to structural changes in the hydrogenous moieties. The mineral content does not scatter strongly and therefore cannot account for the observed changes. Therefore, by combining neutron spectroscopy with the

calorimetric data, our findings support the idea that hydroxyapatite protects the collagen in innate dentine. Demineralized dentine, on the other hand, acts as a sponge where free, bulk-like water is trapped.

Chapter 6

Paper 4 - Dynamics of encapsulated hepatitis B surface antigen: a combined neutron spectroscopy and thermo-analysis study

Oral delivery of hepatitis B vaccine containing the Hepatitis B surface Antigen (HBsAg) are expected to improve the efficiency of hepatitis B vaccination and lessen side effects from injection vaccination. To this end, macro and ordered mesoporous silicate SBA-15 has showed to be promising. However, little is known how it protects the antigen. Imaging studies, however, have indicated that HBsAg agglomerates in branching structures inside the grains and/or the macropores of the SBA-15 [58].

Aiming to disentangle the dynamic of the protein confined within different pore sizes of SBA-15, TGA-FTIR combined with QENS data and EFW approach were used to study hepatitis B surface antigen (HBsAg) encapsulated by Santa Barbara Amorphous (SBA-15), hereafter SBA-15+HBsAg. These very initial results are presented in Paper 4 given in the appendix.

However, before the proceeding with the experimental details, it is important to give more information on this complex system. HBsAg is used for vaccination against hepatitis B as well as to diagnose hepatitis B infection in humans. The surface antigen contributes in the formation of distinct types of particles, which can be found in the blood serum of an infected individual. A type of HBsAg particle envelops the infectious 42 nm hepatitis B virus. Another type is the rod-shaped particle of only HBsAg with a diameter of 22 nm, and get another type of particle consisting only of HBsAg also with 22 nm [59]. The latter is used for vaccination.

SBA-15 is a hexagonal ordered mesoporous silica that has an effective immunological response as adjuvant, Figure 28, adapted from [58]. Moreover, SBA-15 protects the vaccine from gastric acid, making oral delivery possible [60]. This type of encapsulation also facilitates storage at room temperature. The latter is an advantage as the vaccine must be stored at 4°C to be effective. However, the HBsAg protein, used in the Hepatitis B vaccine, is apparently too large to fit inside the less than 2 nm micropores and 10 nm mesopores present in the SBA-15 structure raising the question of how SBA- 15 can protect the antigen. Does confinement of
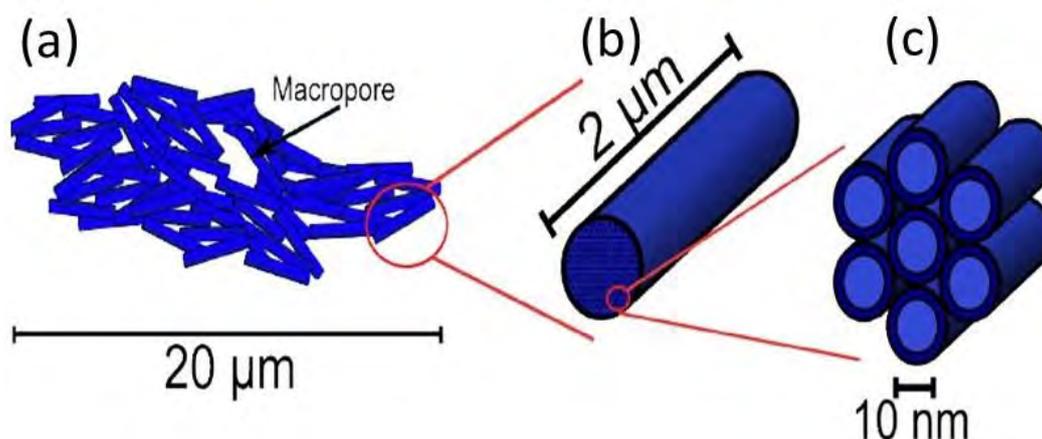

Figure 28 Illustration of SBA-15. (a) SBA-15 macropores in the 20 μm particle, (b) 2 μm rod-shaped subunit and in (c) 10nm hexagonal ordered mesopores.

HBsAg results in interactions between this antigen and the adjuvant? The aim of this work was to shed light on these questions.

The experimental procedure to analyze such a complex system was as follows. SBA-15 industrially produced by the company Cristalia, São Paulo, Brazil was used to encapsulate HBsAg with the ratio 1 SBA-15 : 5 HBsAg, by researchers at the Butatan Institute, Brazil. The encapsulation was performed by initially mixing 250 mg of SBA-15 with 500 mL of a solution that consisted of a 0.5 mg/mL HBsAg in a phosphate buffered saline solution (PBS, 10mM Na_2HPO_4 solution) buffer solution with pH 7.4, and then supplied with extra PBS solution to obtain the 500 mL volume, this sample was used as reference to observe what happens when the protein in incorporated p(1 SBA-15 :1 HBsAg). By changing the volume of the initial HBsAg solution, adding PBS solution, the mass ratio of HBsAg to SBA-15 was varied, while the amount of PBS salt was maintained. The samples were labelled as: SBA-15+PBS for the sample reference, and SBA-15+HBsAg for the sample with vaccine (SBA-15+PBS+HBsAg) [58].

TGA-FTIR measurements were performed at the University of Copenhagen, to determine and characterize the decomposing substances upon heating the samples, the mass loss and the chemical composition of the released gases. The samples were placed in an aluminum oxide crucible, heated at a rate of 10 °C/min to 600 °C under nitrogen gas flow of 20 ml/min. A new FTIR spectrum of the evolved gases was recorded for every 3 degrees of data collection.

Neutron spectroscopy data were obtained using the backscattering spectrometer EMU and BASIS, located at Australian Nuclear Science and Technology Organisation – ANSTO (Australia) and at the Spallation Neutron Source – SNS (USA), respectively. A briefly explanation about the backscattering spectrometer basic mode of action was given in the Chapter 5.

EMU is a reactor based cold-neutron backscattering spectrometer with Si (111) crystal analyzer, characterized by an energy resolution in the order of 1.1 μeV (FWHM) at the elastic line, for a total energy transfer range of ±28 μeV, across an elastic momentum transfer range spanning ~0.1 to 1.95 Å^{-1} [61]. The instrument is illustrated in Figure 29, adapted from [62]. BASIS is a spallation source backscattering spectrometer that also uses Si (111) crystals for analyzing the neutron beam with incident λ centered at 6.4 Å. The energy transfer, ΔE, ranges from -150 μeV to +150 μeV with an energy resolution of ΔE = 3.5 μeV at FWHM. The detectors cover an elastic Q-range of 0.1 Å^{-1} to 2 Å^{-1} [63]. Both spectrometers are suitable for study diffusing water molecules or yet larger molecules like polymers or biological molecules.
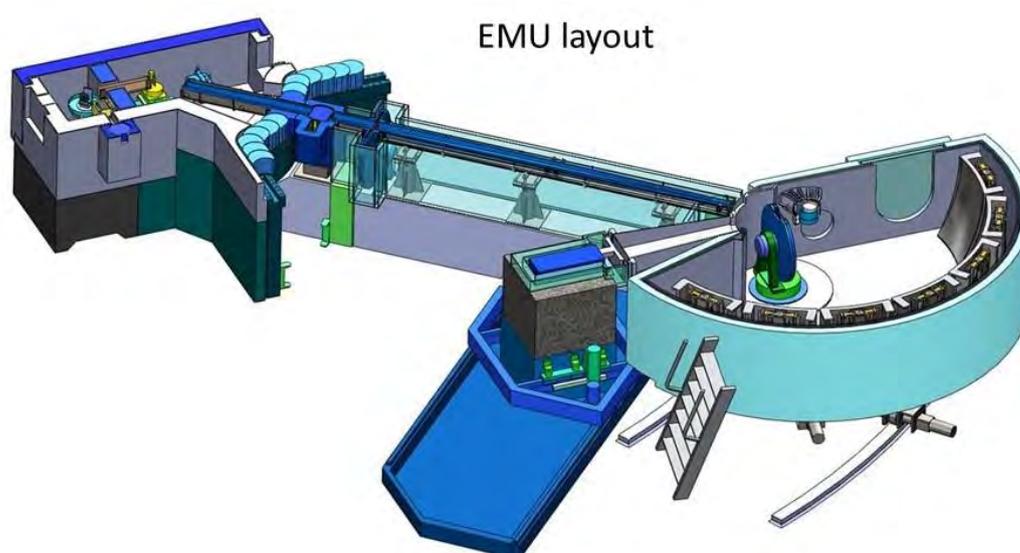

Figure 29 Schematic view of the reactor based cold-neutron backscattering spectrometer EMU, located at Australian Nuclear Science and Technology Organisation – ANSTO (Australia).

EMU was used to collect EFW data on heating from 20 K to 300 K. The powder sample was placed in an aluminum sachet inside the annular cylindrical sample holders. See Figure 30.

Figure 30 Pictures of mounting process of the sample for the measurement at EMU.

QENS data was obtained using the instrument BASIS, by the instrument responsible, in order to probe the confined water dynamics using the same samples at 310 K, i.e. body temperature. The BASIS tank is illustrated in Figure 31, adapted from [63].
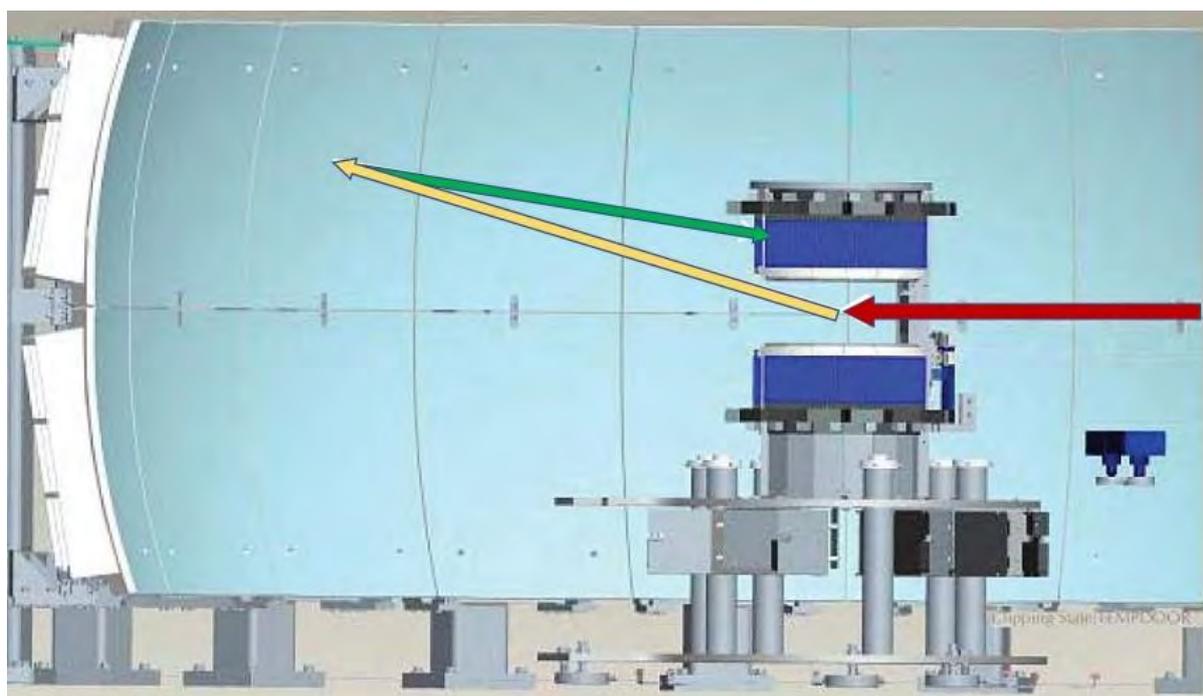
Figure 31 Schematic view of the BASIS tank. Red arrow is the incident neutron that is scattered by the sample at the center yellow arrow, then Bragg-reflected by Si (111) analyser crystal, and finally intercepted by a detector, green arrow.

The main conclusion of this manuscript was that in the *ns* timescale the vaccine in salt solution is immobilized or covered by the inner structure of the mesoporous SBA-15. This is clearly reflected by the values of the diffusion coefficient and residence time, and consequently by the mean jump lenght obtained using the Singwi and Sjölander model.

Table 3 Diffusion coefficient D_t and residence time τ_0 and distance l obtained using the Singwi and Sjölander model for the confined water in SBA-15+PBS and SBA-15+HBsAg.

Sample	$D_t(10^{-9}m^2/s)$	$\tau_0(ps)$	$l(\text{Å})$
SBA-15+PBS	0.8 ± 0.3	24 ± 3	3.4
SBA-15+HBsAg	0.37 ± 0.06	20 ± 3	2.1

Chapter 7

Book Chapter - Application of neutron scattering in amino acid crystals – structural and dynamical information

This book chapter helped me (and hopefully the general reader) in the understanding of the fundamental concepts regarding the neutron scattering process. Section 3, the one I wrote, introduces the basic concepts of neutron diffraction and inelastic neutron scattering, a powerful technique to investigate several materials, among them, amino acid crystals. The book chapter itself summarizes how small variations in the hydrogen bond network correlates to conformation changes in the on aliphatic amino acids L-alanine ($C_3H_7NO_2$), L-valine ($C_5H_{11}NO_2$) and L-leucine ($C_3H_7NO_2$) crystals. Selected main findings reported in this book chapter are:

- NPD and INS are powerful techniques to investigate amino acid crystals. From these studies the possibility to correlate small variations of the network of hydrogen bonds to conformation changes in the amino acid molecules was discussed.

- L-leucine, presents only one polymorph at room temperature, but undergoes phase transitions at low and high temperatures. The new phases were analyzed and insights about the conformation of the molecules were attained.

- L-valine by comparison between RS and INS to identify infrared active modes responsible for the phase transition undergone by the crystal at approximately 120 K.

- Fully deuterated sample of L-alanine present a structural phase transition at ~ 170 K, that can be related to the Ubbelohde effect, or in other words different dimensions of the hydrogen bonds stabilize differently the deuterated and the non-deuterated crystals.

Chapter 8

Conclusions and Final Comments

In this chapter, I will first summarize the main conclusions of each publication that made the body of this thesis - the papers themselves can be found in the appendix – and subsequently give a brief overview of possible ways to continue these researches.

In Paper 1, we studied hydrogen bonds in deuterated crystalline D-Alanine (D-Ala, $C_3D_7NO_2$). Our results demonstrated that the reorientation of the NH_3^+ group in D-Ala induces modification of the $N - H \cdots O$ hydrogen bonds between two neighbouring molecules. A new Raman active mode in D-Ala was observed at 468 cm^{-1} below 200 K. This mode is not observed in the enantiomer form, L-Ala. Based on neutron powder diffraction results, we showed that the temperature dependence of the $N - D$ covalent bonds in D-Ala and L-Ala are quite different. Thus, this work shows that both L-Ala and D-Ala undergo micro-conformation transitions due to a subtle rearrangement of the hydrogen-bond network, which is manifested in the local symmetry but not in the average structure of the crystal. In the analysed samples, L-Ala and D-Ala, these transitions are dissimilar.

In paper 2, a comparison between the experimental inelastic neutron scattering (INS) spectra for haloperidol ($C_{21}H_{23}ClFNO_2$), aripiprazole ($C_{23}H_{27}Cl_2N_3O_2$) and quetiapine hemifumarate ($C_{21}H_{25}N_3O_2S \cdot 0.5C_4H_4O_4$) and their calculated spectra, by density functional theory provided information about the flexibility of the molecular groups in each sample. The normal modes observed in HAL at low frequencies, 8 meV, come from displacements of the H in the rings and the majority of the low frequencies groups/modes are assigned to deformations of the alkyl group connecting the hydrophobic and hydrophilic heads. In APZ, however, the modes are assigned to collective motions dominated by displacements of the piperazine and quinoline rings. In QTP, the vibrational modes around 7, 16 and 20 meV reflect deformations from the aromatic structure. These results shed light on the flexibility of the structure in each drug. This is a valuable information that can enhance the level of accuracy in

molecular dynamics simulations, which is becoming a routine tool for drug discovery. However, in most cases, this approach only accounts for the flexibility of the receptor.

In paper 3, differences in the enthalpy observed in the DSC curves obtained for dentine and demineralized dentine are related to collagen denaturation either stabilized or not by the mineral phase in the tooth. Furthermore, TGA-FTIR experiments show a clear difference in the shape of the relative absorbance when comparing mineralized and demineralized dentine. The presence of P-O stretching in the FTIR spectra obtained from the demineralized dentine shows that etching with 10% phosphoric acid for 4 days does not completely solubilize all hydroxyapatite crystals. Based on neutron spectroscopy studies, we were able to conclude that that hydroxyapatite protects the collagen in innate dentine, while in demineralized dentine, it acts as a sponge where free bulk-like water is trapped.

In paper 4, TGA-FTIR results indicate that the surface antigen HBsAg is confined in two different environments in the bi-modal silicate SBA-15. The majority, which degrades at 300 °C, is present in the larger macropores (20μm) of SBA-15 and a smaller amount is most likely attached to the entrance of the mesopores (2μm) and starts degrading at 800 °C. The diffusion coefficient shows that, when compared to bulk-water, the water in the SBA-15+PBS solution is slowed down by a factor close to 3, whereas when introducing the antigen to the solution and then to the SBA-15 (SBA-15+PBS+HBsAg), the diffusion coefficient is slowed down by a factor 6. However, the mean jump lengths are similar, indicating that hydrogen in SBA-15+PBS+HBsAg and SBA-15+PBS are confined in similar conditions, in agreement with the Master thesis of Martin K. Rasmussen [58].

The results present in this thesis open different research opportunities. Here I name only a few related to the main research areas in which I was involved during my PhD:

(i) new studies aiming to compare the evolution of the H-bonds lengths by thermal effect in enantiomeric forms of different amino acids, in order to verify if they present dissimilarities, would be of great interest;

(ii) from paper 2, a new perspective would be to perform the same type of analysis in the polymorphic forms of the same drugs and compare how the changes in the structure affects the flexibility of the molecules in relation to the forms studied in this project;

(iii) to get a more accurate information the dentin samples which come from different donors, analyzing a higher number of samples might be provide more reliable information using the same techniques employed in Paper 3

Bibliography

[1]   S. Karakawa, K. Shimbo, N. Yamada, T. Mizukoshi, H. Miyano, M. Mita, W. Lindner, and K. Hamase, "Simultaneous analysis of D-alanine, D-aspartic acid, and D-serine using chiral high-performance liquid chromatography-tandem mass spectrometry and its application to the rat plasma and tissues.," *J. Pharm. Biomed. Anal.*, vol. 115, pp. 123–129, 2015.

[2]   T. Kimura, K. Hamase, Y. Miyoshi, R. Yamamoto, K. Yasuda, M. Mita, H. Rakugi, T. Hayashi, and Y. Isaka, "Chiral amino acid metabolomics for novel biomarker screening in the prognosis of chronic kidney disease.," *Sci. Rep.*, vol. 6, no. October 2015, p. 26137, 2016.

[3]   A. Ganesan, M. J. Brunger, and F. Wang, "A study of aliphatic amino acids using simulated vibrational circular dichroism and Raman optical activity spectra," *Eur. Phys. J. D*, vol. 67, no. 11, p. 229, Nov. 2013.

[4]   K. Ishikawa, Y. Terasawa, M. Tanaka, and T. Asahi, "Accurate measurement of the optical activity of alanine crystals and the determination of their absolute chirality," *J. Phys. Chem. Solids*, vol. 104, pp. 257–266, 2017.

[5]   C. H. Wang and R. D. Storms, "Raman Study of Hydrogen Bonding and Long-Wavelength Lattice Modes in an L-Alanine Single Crystal," *J. Chem. Phys.*, vol. 55, no. 10, p. 5110, 1971.

[6]   W. Wang, F. Yi, Y. Ni, Z. Zhao, X. Jin, and Y. Tang, "Parity Violation of Electroweak Force in Phase Transitions of Single Crystals of D- and L-Alanine and Valine," *J. Biol. Phys.*, vol. 26, no. 1, pp. 51–65, 2000.

[7]   W. Wang, W. Min, F. Bai, L. Sun, F. Yi, Z. Wang, C. Yan, Y. Ni, and Z. Zhao, "Temperature-dependent magnetic susceptibilities study on parity-violating phase transition of d- and l-alanine crystals," *Tetrahedron: Asymmetry*, vol. 13, no. 22, pp. 2427–2432, Nov. 2002.

[8]   "Antipsychotic Drugs Market Size & Share | Industry Report, 2014-2025." [Online]. Available: http://www.grandviewresearch.com/industry-

analysis/antipsychotic-drugs-market. [Accessed: 20-Nov-2017].

[9]   M. L. Teodoro, G. N. Phillips, and L. E. Kavraki, "Understanding Protein Flexibility through Dimensionality Reduction," *J. Comput. Biol.*, vol. 10, pp. 3–4, 2003.

[10]   L. Wang and R. L. Coppel, "Oral vaccine delivery: can it protect against non-mucosal pathogens?," *Expert Rev. Vaccines*, vol. 7, no. 6, pp. 729–738, Aug. 2008.

[11]   S. W. Lovesey, *Theory of neutron scattering from condensed matter*. Clarendon, 1986.

[12]   A. J. Dianoux, G. H. Lander, and Institut Laue-Langevin., *Neutron data booklet*. Old City, 2003.

[13]   J. Fitter, T. Gutberlet, and J. Katsaras, *Neutron scattering in biology : techniques and applications*. Springer, 2006.

[14]   T. Report, D. Richter, and T. Springer, "A twenty years forward look at neutron scattering facilities in the OECD countries and Russia," *Forum Am. Bar Assoc.*, pp. 1–53.

[15]   G. L. Squires, *Introduction to the Theory of Thermal Neutron Scattering*. Cambridge: Cambridge University Press, 2012.

[16]   M. Bée, *Quasielastic neutron scattering : principles and applications in solid state chemistry, biology, and materials science*. Adam Hilger, 1988.

[17]   J. M. de Souza, P. T. C. Freire, D. N. Argyriou, J. A. Stride, M. BarthÃ¨s, W. Kalceff, and H. N. Bordallo, "Raman and Neutron Scattering Study of Partially Deuterated L-Alanine: Evidence of a Solid-Solid Phase Transition," *ChemPhysChem*, vol. 10, no. 18, pp. 3337–3343, Dec. 2009.

[18]   R. Hempelmann, *Quasielastic Neutron Scattering and Solid State Diffusion*. Oxford University Press, 2000.

[19]   G. H. Vineyard, "Scattering of slow neutrons by a liquid," *Phys. Rev.*, vol. 110, no. 5, pp. 999–1010, 1958.

[20]   M. L. Martins, W. P. Gates, L. Michot, E. Ferrage, V. Marry, and H. N. Bordallo, "Neutron scattering, a powerful tool to study clay minerals," *Applied Clay Science*, vol. 96. Elsevier, pp. 22–35, 01-Jul-2014.

[21] G. J. Kearley, "The application of normal coordinate analysis to INS spectra," *Spectrochim. Acta Part A Mol. Spectrosc.*, vol. 48, no. 3, pp. 349–362, Mar. 1992.

[22] A. J. Ramirez-Cuesta, "aCLIMAX 4.0.1, the new version of the software for analyzing and interpreting INS spectra," *Comput. Phys. Commun.*, vol. 157, no. 3, pp. 226–238, 2004.

[23] J. Hafner, "Ab-initio simulations of materials using VASP: Density-functional theory and beyond," *J. Comput. Chem.*, vol. 29, no. 13, pp. 2044–2078, Oct. 2008.

[24] K. S. Singwi and A. Sjölander, "Diffusive Motions in Water and Cold Neutron Scattering," *Phys. Rev.*, vol. 119, no. 3, pp. 863–871, Aug. 1960.

[25] V. F. Sears, "Theory of Cold Neutron Scattering by Homonuclear Diatomic Liquids: II. Hindered Rotation," *Can. J. Phys.*, vol. 44, no. 6, pp. 1299–1311, Jun. 1966.

[26] M. C. Bellissent-Funel, S. H. Chen, and J. M. Zanotti, "Single-particle dynamics of water molecules in confined space," *Phys. Rev. E*, vol. 51, no. 5, pp. 4558–4569, May 1995.

[27] D. A. Skoog, F. J. Holler, and S. R. Crouch, *Principles of Instrumental Analysis*, 7th ed. Cengage Learning, 2017.

[28] C. Fuciños, P. Fuciños, M. Míguez, I. Katime, L. M. Pastrana, and M. L. Rúa, "Temperature- and pH-Sensitive Nanohydrogels of Poly(N-Isopropylacrylamide) for Food Packaging Applications: Modelling the Swelling-Collapse Behaviour," *PLoS One*, vol. 9, no. 2, p. e87190, Feb. 2014.

[29] M. Ionashiro, *Giolito: Fundamentos da Termogravimetria e Análise Térmica Diferencial e Calorimetria Exploratória Diferencial*, 1st ed. São Paulo: Giz editorial, 2005.

[30] NETZCH, "DSC 214 Polyma - NETZSCH Analyzing & Testing." [Online]. Available: https://www.netzsch-thermal-analysis.com/us/products-solutions/differential-scanning-calorimetry/dsc-214-polyma/. [Accessed: 11-Jan-2018].

[31] M. E. Brown, "Thermogravimetry (TG)," in *Introduction to Thermal Analysis*, Dordrecht: Springer Netherlands, 1988, pp. 7–22.

[32] P. R. Griffiths and J. A. de Haseth, *Fourier Transform Infrared Spectrometry*. Hoboken, NJ, USA: John Wiley & Sons, Inc., 2007.

[33] "TG 209 F1 Libra® - NETZSCH Analyzing & Testing." [Online]. Available: https://www.netzsch-thermal-analysis.com/us/products-solutions/thermogravimetric-analysis/tg-209-f1-libra/. [Accessed: 11-Jan-2018].

[34] "Instrument Layout." [Online]. Available: https://www.ill.eu/instruments-support/instruments-groups/instruments/d2b/description/instrument-layout/. [Accessed: 10-Jan-2018].

[35] A. C. Larson and R. B. Von Dreele, "General Structure Analysis System (GSAS)." Los Alamos National Laboratory Report LAUR (1994), pp. 86–748, 1994.

[36] B. Schrader, *Infrared and Raman Spectroscopy*. Weinheim, Germany: Wiley-VCH Verlag GmbH, 1995.

[37] O. Sala, *Fundamentos da Espectroscopia Raman e no Infravermelho*. UNESP, 1996.

[38] E. Smith and G. Dent, *Modern Raman Spectroscopy - A Practical Approach*. Chichester, UK: John Wiley & Sons, Ltd, 2004.

[39] M. J. . Frisch, G. W. . Trucks, H. B. . Schlegel, G. E. . Scuseria, M. A. . Robb, J. R. . Cheeseman, G. . Scalmani, V. . Barone, B. . Mennucci, G. A. . Petersson, H. . Nakatsuji, M. . Caricato, X. . Li, H. P. . Hratchian, A. F. . Izmaylov, J. . Bloino, G. . Zheng, and D. J. Sonnenb, "Gaussian09." Gaussian, Inc., Wallingford CT, 2009.

[40] G. Kresse and J. Furthmüller, "Efficient iterative schemes for ab initio total-energy calculations using a plane-wave basis set," *Phys. Rev. B*, vol. 54, no. 16, pp. 11169–11186, 1996.

[41] H. I. Ingolfsson, C. Arnarez, X. Periole, and S. J. Marrink, "Computational 'microscopy of cellular membranes," *J. Cell Sci.*, vol. 129, no. 2, pp. 257–268, Jan. 2016.

[42] D. Yu, R. Mole, T. Noakes, S. Kennedy, and R. Robinson, "Pelican – a Time of Flight Cold Neutron Polarization Analysis Spectrometer at OPAL," *J. Phys. Soc. Jpn*, vol. 82, 2012.

[43] D. Colognesi, M. Celli, F. Cilloco, R. J. Newport, S. F. Parker, V. Rossi-Albertini, F.

Sacchetti, J. Tomkinson, and M. Zoppi, "TOSCA neutron spectrometer: The final configuration," *Appl. Phys. A Mater. Sci. Process.*, vol. 74, no. SUPPL.I, pp. 64–66, 2002.

[44] G. J. Kearley, "Instrumentation for neutron spectroscopy," *Spectrochim. Acta Part A Mol. Spectrosc.*, vol. 48, no. 3, pp. 285–291, 1992.

[45] M. Karlsson, "Proton dynamics in oxides: insight into the mechanics of proton conduction from quasielastic neutron scattering," *Phys. Chem. Chem. Phys.*, vol. 17, no. 1, pp. 26–38, Dec. 2015.

[46] S. Döge, C. Herold, S. Müller, C. Morkel, E. Gutsmiedl, P. Geltenbort, T. Lauer, P. Fierlinger, W. Petry, and P. Böni, "Scattering cross sections of liquid deuterium for ultracold neutrons: Experimental results and a calculation model," *Phys. Rev. B*, vol. 91, no. 21, p. 214309, Nov. 2015.

[47] D. Richard, M. Ferrand, and G. J. Kearley, "Analysis and visualisation of neutron-scattering data," *J. Neutron Res.*, vol. 4, no. 1, pp. 33–39, Dec. 1996.

[48] S. Rols, H. Jobic, and H. Schober, "Monitoring molecular motion in nano-porous solids," *Comptes Rendus Phys.*, vol. 8, no. 7–8, pp. 777–788, Sep. 2007.

[49] D. E. Braun, T. Gelbrich, V. Kahlenberg, R. Tessadri, J. Wieser, and U. J. Griesser, "Conformational polymorphism in aripiprazole: Preparation, stability and structure of five modifications," *J. Pharm. Sci.*, vol. 98, no. 6, pp. 2010–2026, 2009.

[50] K. Ravikumar, B. Sridhar, IUCr, C. J., D. J., R. F. C., W. S., C. M. O., and J. N. D., "Quetiapine hemifumarate," *Acta Crystallogr. Sect. E Struct. Reports Online*, vol. 61, no. 10, pp. o3245–o3248, Oct. 2005.

[51] M. D. Prasanna and T. N. G. Row, "Weak interactions involving organic fluorine: analysis of structural motifs in Flunazirine and Haloperidol," *J. Mol. Struct.*, vol. 562, no. 1–3, pp. 55–61, May 2001.

[52] "Jmol: an open-source Java viewer for chemical structures in 3D. http://www.jmol.org/." .

[53] J. J. Lim and A. R. Liboff, "Thermogravimetric Analysis of Dentin," *J. Dent. Res.*, vol. 51, no. 2, pp. 509–514, Mar. 1972.

[54]   K. A. Agee, A. Prakki, T. Abu-Haimed, G. H. Naguib, M. A. Nawareg, A. Tezvergil-Mutluay, D. L. S. Scheffel, C. Chen, S. S. Jang, H. Hwang, M. Brackett, G. Gregoire, F. R. Tay, L. Breschi, and D. H. Pashley, "Water distribution in dentin matrices: Bound vs. unbound water," *Dent. Mater.*, vol. 31, no. 3, pp. 205–216, 2015.

[55]   D. M. Wieliczka, P. Spencer, and M. B. Kruger, "Raman Mapping of the Dentin/Adhesive Interface," *Appl. Spectrosc.*, vol. 50, no. 12, pp. 1500–1504, Dec. 1996.

[56]   L. Daasch and D. Smith, "Infrared Spectra of Phosphorus Compounds," *Anal. Chem.*, vol. 23, no. 6, pp. 853–868, Jun. 1951.

[57]   P. Tregenna-Piggott, F. Juranyi, and P. Allenspach, "Introducing the inverted-geometry time-of-flight backscattering instrument, MARS at SINQ," *J. Neutron Res.*, vol. 16, no. 1, pp. 1–12, Mar. 2008.

[58]   M. K. Rasmussen, "Physical characterizationof a new oral delivery vehicle for Hepatitis B and diphtheria vaccination," University of Copenhagen, 2017.

[59]   I. Berkower, A. Spadaccini, H. Chen, D. Al-Awadi, J. Muller, Y. Gao, D. Feigelstock, K. Virnik, and Y. Ni, "Hepatitis B Virus Surface Antigen Assembly Function Persists when Entire Transmembrane Domains 1 and 3 Are Replaced by a Heterologous Transmembrane Sequence," *J. Virol.*, vol. 85, no. 5, pp. 2439–2448, 2011.

[60]   K. Scaramuzzi, G. D. Tanaka, F. M. Neto, P. R. A. F. Garcia, J. J. M. Gabrili, D. C. A. Oliveira, D. V Tambourgi, J. S. Mussalem, D. Paixão-Cavalcante, M. T. D'Azeredo Orlando, V. F. Botosso, C. L. P. Oliveira, M. C. A. Fantini, and O. A. Sant'Anna, "Nanostructured SBA-15 silica: An effective protective vehicle to oral hepatitis B vaccine immunization," *Nanomedicine Nanotechnology, Biol. Med.*, vol. 12, no. 8, pp. 2241–2250, Nov. 2016.

[61]   N. R. de Souza, A. Klapproth, and G. N. Iles, "EMU: High-Resolution Backscattering Spectrometer at ANSTO," *Neutron News*, vol. 27, no. 2, pp. 20–21, Apr. 2016.

[62]   "Emu   -   ANSTO."   [Online].   Available: http://www.ansto.gov.au/ResearchHub/OurInfrastructure/ACNS/Facilities/Instruments/Emu/index.htm. [Accessed: 17-Jan-2018].

[63]   E. Mamontov and K. W. Herwig, "A time-of-flight backscattering spectrometer at the Spallation Neutron Source, BASIS," *Rev. Sci. Instrum.*, vol. 82, no. 8, pp. 4732806–85109, 2011.

Appendix

Publications

Paper 1

E. A. Belo, J. E. M. Pereira, P. T. C. Freire, D. N. Argyriou, J. Eckert, and H. N. Bordallo, "Hydrogen bonds in crystalline D -alanine: diffraction and spectroscopic evidence for differences between enantiomers," *IUCrJ*, vol. 5, no. 1, pp. 6–12, Jan. 2018. DOI: 10.1107/S2052252517015573.

Hydrogen bonds in crystalline D-alanine: diffraction and spectroscopic evidence for differences between enantiomers

Ezequiel A. Belo,[a,b] Jose E. M. Pereira,[c] Paulo T. C. Freire,[b] Dimitri N. Argyriou,[d] Juergen Eckert[e,f] and Heloisa N. Bordallo[c,e]*

[a]Faculdade de Física, Universidade Federal do Pará, Belém, Pará, Brazil, [b]Departamento de Física, Universidade Federal do Ceará, Fortaleza, Ceará, Brazil, [c]Niels Bohr Institute, University of Copenhagen, Universitetsparken 5, Copenhagen, 2100, Denmark, [d]European Spallation Source, 176, SE-221 00 Lund, Sweden, [e]Department of Chemistry, University of South Florida, 4202 East Fowler Ave, Tampa, FL 33620, USA, and [f]Theoretical Division, Los Alamos National Laboratory, Los Alamos, NM 87545, USA. *Correspondence e-mail: bordallo@nbi.ku.dk

Enantiomeric amino acids have specific physiological functions in complex biological systems. Systematic studies focusing on the solid-state properties of D-amino acids are, however, still limited. To shed light on this field, structural and spectroscopic studies of D-alanine using neutron powder diffraction, polarized Raman scattering and *ab initio* calculations of harmonic vibrational frequencies were carried out. Clear changes in the number of vibrational modes are observed as a function of temperature, which can be directly connected to variations of the N—D bond lengths. These results reveal dissimilarities in the structural properties of D-alanine compared with L-alanine.

1. Introduction

It is well known that chirality plays a fundamental role in the bioactivity of molecules taking part in vital functions of living organisms. Amino acids are fundamental molecules of life and can, except for glycine, be found in enantiomeric L- and D-forms with their chiral centres on the α-carbon. Moreover, progress in analytical chemical tools has now established that considerable amounts of D-amino acids are also found in higher mammals including humans (Karakawa *et al.*, 2015). Their distribution and regulation are different from those of the L-forms. It is well known that D-alanine (D-Ala), D-serine (D-Ser) and D-aspartic acid (D-Asp) can be viewed as the main targets for physiological functions and the diagnosis of various diseases, such as chronic kidney disease, endocrine glands disorders, and schizophrenia (Hamase *et al.*, 2002).

Although D-amino acids are now increasingly recognized as physiologically active molecules, as well as potential biomarkers (Kimura *et al.*, 2016), remarkably few studies have been devoted to the understanding of their solid-state properties. As anticipated, most reports do not find any difference in their properties when compared with their chiral counterpart, except in experiments where the chiral character is relevant (Ganesan *et al.*, 2013; Ishikawa *et al.*, 2017). Nevertheless, a number of papers from W. Wang's group (Wang *et al.*, 2000, 2002) have described possible phase transitions in single crystals of D-Ala based on observed differences between crystalline D-Ala and L-alanine (hereafter L-Ala) as a function of temperature. These differences were related to the parity violation energy difference (PVED), which has been searched for in chiral molecules since its conjecture by A. Salam in 1992 (Salam, 1992). However, no evidence for this theory has been
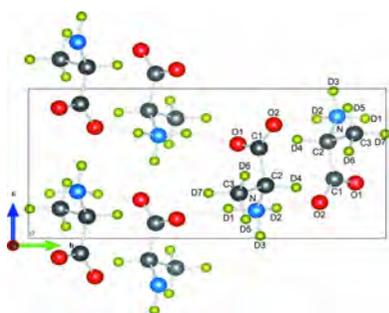
obtained to date. For instance, Sullivan *et al.* (2003) have re-examined these measurements, and as well carried out X-ray diffraction and ^{13}C solid-state NMR in both enantiomers of alanine between room temperature and about 250 K, and found no anomalous behaviour. Along these lines Wilson *et al.* (2005) have further investigated the crystal structures of hydrogenated L-Ala (at 295 and 60 K) and D-Ala (at 300, 295, 260, 250, 240 and 60 K) using single-crystal neutron diffraction. Once more, no clear structural changes were found, which could have supported the anomalies observed in the bulk measurements, and in turn be indicative of the observable effect of PVED.

Careful scrutiny of the results reported in Wilson *et al.* (2005), however, led us to realise that changes in the N—H covalent bond distances as a function of temperature in D-Ala appeared to be different from those observed for L-Ala. The data for fully hydrogenated single-crystal results from Wilson *et al.* (2005) are given as supplementary information (Fig. S1). Data obtained by Lehmann *et al.* (1972) and Destro *et al.* (2008) for L-Ala are also reported. These findings as well as the biological relevance of D-Ala gave rise to the investigations reported in this paper. Here the structural stability of fully deuterated D-Ala was analysed by means of neutron powder diffraction (NPD), while the dynamics of hydrogenated D-Ala were analysed using single-crystal polarized Raman spectroscopy (RS).

Herein we report on a number of differences in the dynamical behaviour of D-Ala compared with L-Ala, the most remarkable being the observation of new Raman active modes in the *A*- and *B*-irreducible representations of the factor group D_2 below 160 and 260 K, respectively. These findings together with the neutron powder diffraction and density-functional-theory-based methods (DFT) results show that small differ-

ences in the crystal packing, which were previously disregarded (Wilson *et al.*, 2005), can indeed induce different rearrangements of the NH_3^+ group in D-Ala and L-Ala. We note that the macroscopic symmetry of the crystal is nevertheless preserved.

2. Experimental details

Polarized Raman spectra were collected on hydrogenated $C_3H_7NO_2$ single crystals obtained by a slow evaporation technique from the preparation of saturated solutions using the solubility curve of D-Ala (Dalton & Schmidt, 1933). Crystals of a few millimetres in size were obtained by this method, powered again and reutilized for preparation of new saturated solutions. This process was repeated three times in order to obtain crystals with higher quality. The crystals were polished and cut into three parallelepipeds with approximately 90 mm^3 volume, such that each has *a*, *b* and *c* crystallographic axes perpendicular to the corresponding faces. The 514 nm line of an argon ion laser operating with an output power of 250 mW along with a detection system (Horiba T64000 triple spectrometer) coupled to a liquid nitrogen cooling charge-coupled-device (CCD) detector was used to collect the data. The samples were mounted in a cryogenic helium closed-cycle system where the temperature could be varied continuously from 295 K to 20 K and maintained constant within ± 0.5 K. Six different scattering geometries, $x(yy)x$, $y(zz)y$, $z(xx)z$, $x(yz)x$, $y(xz)y$, $z(xy)z$, were analysed in the backscattering geometry.

Neutron powder diffraction (NPD) measurements on the fully deuterated D-Ala, $C_3D_7NO_2$, purchased from Cambridge Isotope Laboratories and used without further treatment, were performed on the D2B diffractometer located at the ILL. Data were collected at a wavelength of 1.594 Å in small temperature intervals between 4 and 280 K. This instrument is well suited for an accurate determination of lattice constants, the internal atomic coordinates and a refinement of crystal structure with high resolution. The temperature-dependent powder diffraction data were analysed using the crystallographic model of Destro *et al.* (1988) as initial input with the *GSAS* suite of programs (Larson & Von Dreele, 1994). The labelling scheme of the atoms is shown in Fig. 1. Atomic positions were refined together with lattice constants, isotropic atomic displacement parameters and instrumental peak shape parameters. Special attention was paid to modelling of the background, as the thermal diffuse scattering contribution is significant.

Two types of *ab initio* calculations of harmonic vibrational frequencies were carried out to assist with the analysis of the vibrational spectra. The Raman spectrum was calculated for the isolated molecule using *Gaussian*09 (Frisch *et al.*, 2009), using as reference the atomic coordinates of the D-Ala at 280 K. The structure was optimized using the polarized continuum model (PCM) of the self-consistent reaction field (SCRF) theory together with the DFT B3LYP level of theory using a 6–311++$G(d,p)$ basis set. Vibrational frequencies of crystalline D-Ala were obtained by periodic calculations on a
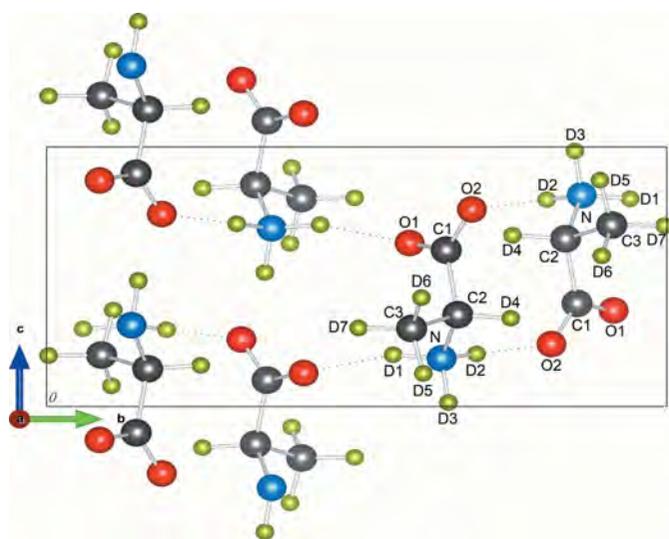

Figure 1
Crystal structure of fully deuterated D-alanine (D-Ala, C_3D_7NO) projected onto the *ab* plane with atoms labelled as in Destro *et al.* (1988). The C atoms are shown in grey, O atoms in red, N in blue and D atoms in green.

$2 \times 1 \times 2$ supercell of the alanine crystals with the *Vienna Ab initio Simulation Package* (VASP) (Kresse & Furthmüller, 1996), using the Perdew–Burke–Ernzerhof (PBE) functional along with Vanderbilt ultrasoft pseudopotentials (Perdew *et al.*, 1996) with a plane wave kinetic energy cutoff of 450 meV. A $4 \times 4 \times 4$ Monkhorst–Pack mesh of k points (Monkhorst & Pack, 1976) was used to further improve agreement at lower frequencies. This methodology was first applied to optimize the positions of the atoms within the $2 \times 1 \times 2$ supercell. The optimized atomic positions were in turn used to calculate the harmonic frequencies and atomic vibrational amplitudes in the enantiomers for computing the INS spectra, including folding with the experimental resolution function using the program *aClimax* (Ramirez-Cuesta, 2004).

3. Results and discussion

3.1. Raman scattering: anomalies in the lattice modes of hydrogenated D-Ala

In this section we will discuss the Raman spectra of D-Ala between 30 and 180 cm^{-1} for six different scattering geometries [$z(xx)z$, $x(yy)x$, $y(zz)y$, $x(yz)x$, $y(xz)y$, $z(xy)z$] and between 200 and 600 cm^{-1} in the $x(yy)x$, $y(zz)y$ geometries as a function of temperature. Frequency changes in the low spectral region will give insight into deformation of the crystalline lattice, while in the medium region of the spectrum we can follow the evolution of the NH$_3^+$ group, which in L-Ala appears at around 480 cm^{-1} (Susi & Byler, 1980; Bordallo *et al.*, 1997; Zhang *et al.*, 2015).

According to a group theory analysis, the D-Ala crystal possesses 153 optical modes divided into the irreducible representations of D_2 factor group as $39\,A + 38\,B_1 + 38\,B_2 + 38\,B_3$ of which 132 modes are internal modes and 21 modes are external, distributed into 12 librations and 9 translations. Modes observed in the Raman spectra of $z(xx)z$, $x(yy)x$, $y(zz)y$

scattering geometries are non-polar representing the Raman tensor components α_{xx}, α_{yy} and α_{zz}. From the theoretical group analysis, six Raman active modes are expected at low wavenumbers, divided into three translational (T) and three librational (L) modes. L-modes, in particular, can be understood as hindered rotations about three perpendicular axes u, v and w, where u is nearly parallel to the crystal c axis (where a chain of hydrogen bonds links adjacent molecules), v is parallel to the long molecular axis and w is defined as perpendicular to the plane of the molecule (Loh, 1975; Crowell & Chronister, 1993). The two modes of lowest energy, at ~40 and 48 cm^{-1}, observed in almost all scattering geometries, are assigned to w-axis librations (Loh, 1975; Crowell & Chronister, 1993).

Initially, we discuss the temperature-dependent Raman spectra of D-Ala for the $x(yy)x$ scattering geometry (A irreducible representation of the factor group D_2) shown in Fig. 2(a). In this figure it is important to consider the behaviour of the bands at 41 and 48 cm^{-1}, indicated by arrows, which present a notable change of intensity at low temperatures. Interestingly, in the spectrum recorded at room temperature the intensity of the band at 41 cm^{-1} is greater than the intensity of the band at 48 cm^{-1}, while in the spectrum taken at the lowest temperature, the intensity of the first band is almost zero. It is also possible to observe two small bands, marked by (*), at about 100 and 170 cm^{-1} below 235 and 175 K, respectively. In spite of their very low intensities, the observation of these L-modes (Loh, 1975; Crowell & Chronister, 1993) shows a trend in which molecules of D-Ala seem to gain librational degrees of freedom. We point out that both modes belong to the B symmetry, see Fig. 3, and a possible explanation for their appearance is a break of the selection rules due to a subtle phase transition or configurational change in D-Ala. Even if one might consider this observation disputable, and that in reality these new bands are
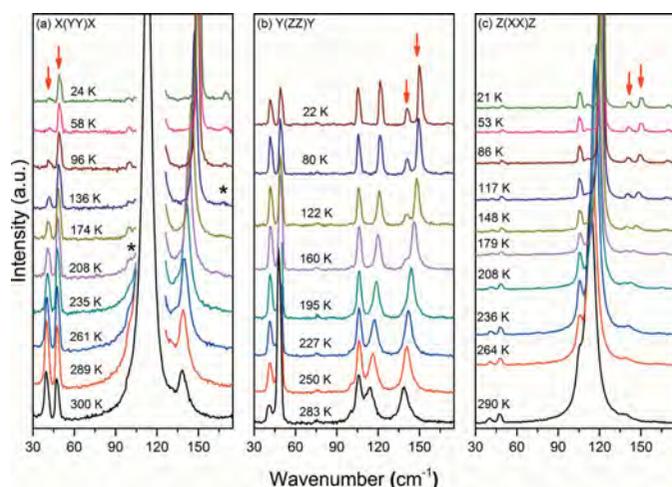

Figure 2
Raman spectra of hydrogenated D-Ala (C$_3$H$_7$NO$_2$) in the A-irreducible representation of the factor group D_2 for several temperatures between 20 and 300 K in the region from 30 to 175 cm^{-1}. New bands are marked by (*), while arrows indicate bands that split at lower temperature.

Figure 3
Raman spectra of hydrogenated D-Ala (C$_3$H$_7$NO$_2$) in the B-irreducible representation of the factor group D_2 for several temperatures between 20 and 300 K in the region from 30 to 175 cm^{-1}. New bands are marked by (*), while arrows indicate bands that split at lower temperature.
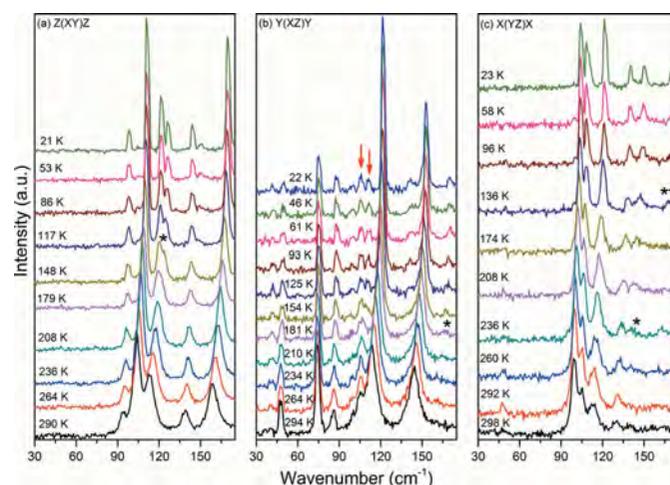
already present at 300 K, becoming visible on cooling due to their low intensities, other indictations of a configurational change in D-Ala are clear from the RS results.

Let us first consider Fig. 2(b), the spectra of D-Ala recorded in the $y(zz)y$ scattering geometry (also A irreducible representation). In this spectra we observe at 283 K the presence of a single band located at ~140 cm^{-1}, which clearly splits below 160 K in two modes located at 140 and 150 cm^{-1} (marked by arrows) at the lowest temperature. Now we turn to the $z(xx)z$ Raman spectra (also an A irreducible representation of the factor group D_2) depicted in Fig. 2(c). It is clear that the mode at 140 cm^{-1} also splits into two modes with wavenumbers 140 and 150 cm^{-1} (marked by arrows) at the lowest temperature.
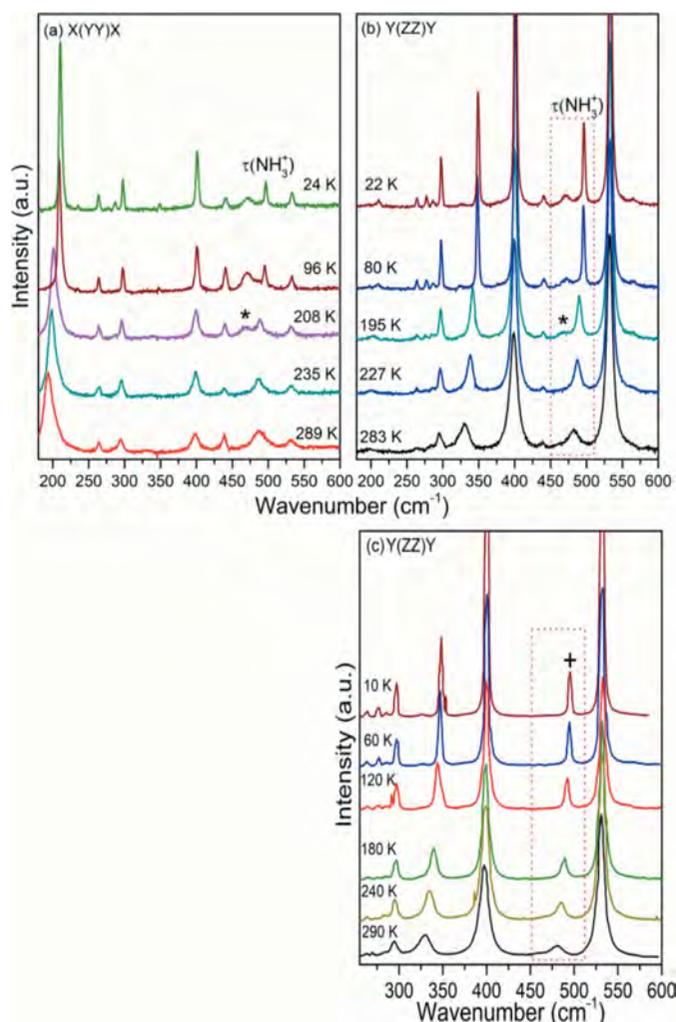

Figure 4
(a) and (b) Raman spectra of hydrogenated D-Ala (C$_3$H$_7$NO$_2$) in the A-irreducible representation of the factor group D_2 for several temperatures between 20 and 300 K in the region from 180 to 600 cm^{-1}. A temperature-dependent band at 468 cm^{-1} appears below 200 K and is marked by (*). (c) Raman spectra in the A-irreducible $y(zz)y$ representation of the factor group D_2 for selected temperatures between 10 and 290 K in the region from 250 to 600 cm^{-1} of hydrogenated L-Ala [C$_3$H$_7$NO$_2$, adapted from (Vik et al., 2005)]. Note that, differently from D-Ala, the τ(NH$_3^+$) mode indicated for clarity by (*) in (b), does not split in L-Ala on cooling, as indicated by (+). However, on heating a remarkable wavenumber decrease accompanied by the increase in the linewidth, attributed to the increase in anharmonicity of the torsional vibrations, is observed in both samples.

Finally, the disappearance of the lowest band at 41 cm^{-1} and the decrease in intensity of the vibration at 48 cm^{-1} on cooling, also seen in Fig. 2(a), further substantiate the idea that crystalline D-Ala undergoes a structural rearrangement at low temperatures.

Now we turn to the polar modes belonging to the B-irreducible representations of the factor group D_2, Fig. 3. Off diagonal Raman tensor components α_{xy}, α_{xz} and α_{yz} were measured in the following scattering geometries:, $z(xy)z$, $y(xz)y$ and $x(yz)x$. According to a group theory analysis, the modes observed in these configurations are both IR and Raman active. Moreover, due to their scattering geometry, i.e. longitudinal optical phonons that generate a macroscopic electric field producing additional scattering mechanism, it is expected that substantial deformation of the crystalline lattice will be distinctly reflected in their behaviour. At 290 K five modes, exactly as predicted, were observed in the $z(xy)z$ spectrum, Fig. 3(a), at 93, 103, 113, 138 and 159 cm^{-1}. However below 180 K the mode at 113 cm^{-1} splits, giving rise to a new peak marked by (*), and at the lowest temperature the modes are observed at 121 and 126 cm^{-1}. In Fig. 3(b) we present the $y(xz)y$ spectrum that shows six modes located at 47, 74, 86, 105, 113 and 144 cm^{-1} at room temperature. Even if in this geometry the signal-to-noise ratio is not top quality, it is possible to observe that the mode located at 105 cm^{-1} starts splitting below 180 K and becomes completely separated, 105 and 110 cm^{-1}, at the lowest temperatures (marked by arrows). In addition, an extremely weak mode at 165 cm^{-1}, marked by (*), can be observed below 210 K. Finally, in Fig. 3(c) the $x(yz)x$ Raman spectrum is presented, showing five modes at 99, 105, 114, 131 and 138 cm^{-1}. On cooling two new modes are observed. One is seen around 260 K [marked by (*)] and the other around 136 K [marked by (**)] located at 150 and 169 cm^{-1}, respectively, at the lowest temperature. Additionally, an inversion of the intensities of the modes located at 99, 105 and 114 cm^{-1} occurs. The mode at 47 cm^{-1}, which completely disappears on cooling, is most likely a leak of polarization due to imperfections on the crystal faces.

In the spectral range between 180 and 600 cm^{-1} (Fig. 4), we can observe four strong bands at 300, 400, 496 and 532 cm^{-1} (at 22 K) in the $y(zz)y$ configuration, which are attributed to the CH$_3$ torsion, skeletal rocking, NH$_3^+$ torsion (Wang & Storms, 1971; Barthès et al., 2002; Kolesov & Boldyreva, 2011; Zhang et al., 2015) [labelled in Fig. 4(b) as τ(NH$_3^+$)], and to a mix of intermolecular vibrations. Of more interest, however, is the appearance of a mode at 468 cm^{-1} below 220 K [marked by (*)], distinctively absent in the periodic DFT calculations, which find no mode at all in this region down to 420 cm^{-1} [Fig. 5(a), top lines] as well as in the Raman spectra of L-Ala (Vik et al., 2005), see Fig. 4(c). This vibration is, however, observed in L-alanine aluminium nitrate, LAAN (Hudson et al., 2009) at 454 cm^{-1}. In LAAN this unassigned vibration has an intensity roughly identical to that of the τ(NH$_3^+$) and is separated by approximately 30 cm^{-1} from the τ(NH$_3^+$) mode (Barthès et al., 2002; Lagaron, 2002), therefore its nature was related to an apparent structural change involving motion of a proton at low temperature.

A most noteworthy difference in the low-frequency dynamics of D- and L-alanine is apparent when comparing the calculated 10 K INS spectra for D-Ala *versus* L-Ala, Fig. 5(*b*). It is quite obvious that there are significant differences in the vibrational amplitudes (*i.e.* peak intensities) of the low-frequency modes below 350 cm^{-1}, while the high-frequency portion of the INS spectra for the two crystals are very similar. This result can be considered as a further indication that the intermolecular interactions in L- and D-Ala differ because the local symmetry of the enantiomers is not identical. In the VASP minimized structure, the positions of the atoms not involved in the chirality were found to be the same, while the three hydrogen-bond geometries differ between the enantiomers and were found to be similar to those reported in (Wilson *et al.*, 2005), see Table S1 in the supplementary information. We can, therefore, hypothesize on the basis of all these observations that in crystalline D-Ala a rearrangement of the hydrogen bonds, and in particular a change in the displacement potential for the NH$_3^+$ protons, may occur which leads to breaking of the selection rules by lowering the local symmetry. In order to better evaluate these spectral anomalies we now turn to the analysis of the neutron powder diffraction data.

3.2. Neutron powder diffraction: re-arrangement of the hydrogen bonds in D-Ala

Analysis of the NPD data has allowed us to precisely measure the evolution of bond lengths in D- and L-Ala as a function of temperature and draw correlations between their evolution and changes in the Raman data. The advantage of this approach is the self consistency in the data with respect to systematic errors that reveals this evolution of bond lengths as
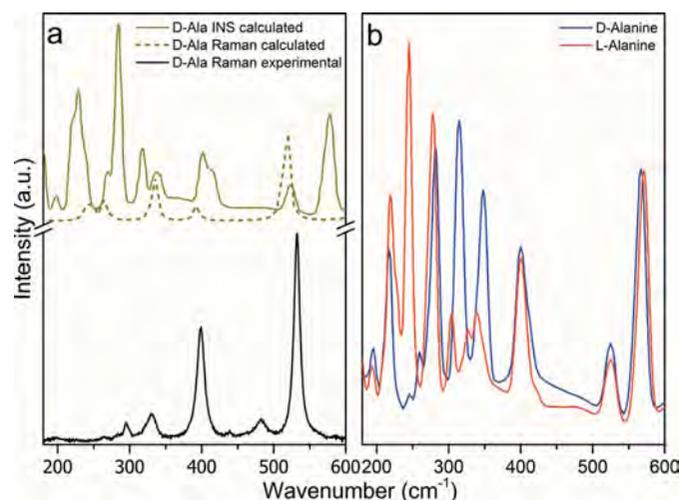

Figure 5
(*a*) Calculated and experimental Raman spectra of D-Ala (C$_3$D$_7$NO$_2$ and C$_3$H$_7$NO$_2$, respectively) between 150 and 600 cm^{-1} at 280 K. Comparison is also made with the calculated INS spectrum at 10 K for D-Ala (C$_3$H$_7$NO$_2$) from the periodic DFT calculations. Here we note that in DFT calculations (0 K) there is no internal mode between 420 cm^{-1} and 500 cm^{-1}. (*b*) Comparison of the periodic DFT calculations for fully hydrogenated L- and D-Ala at 10 K where significant differences in the intensities of some of the peaks, *i.e.* the attendant vibrational amplitudes, are evident between about 200 cm^{-1} and about 300 cm^{-1}.

opposed to precise comparisons of bond-length distances to past measurements at a limited number of temperatures made using a variety of instruments and radiations (Lehmann *et al.*, 1972; Destro *et al.*, 1988, 2008; Wilson *et al.*, 2005). Regardless, our results, Fig. 6, are in reasonable agreement with the previously reported single-crystal measurements at 300 K on hydrogenated D-Ala (Wilson *et al.*, 2005), where the NH$_3^+$ group presents two similar N—H distances at this temperature, see Fig. S1(*b*) in the supporting information. We note the agreement of our data with those of Wilson *et al.* (2005), between 160 and 240 K where also three different N—D distances were observed.

Firstly, turning our attention on the evolution of the N—D bonds as a function of temperature, for both enantiomers, we find a similar behaviour for the N—D1 and N—D3 bonds. While the N—D3 bond, which links the molecules into columns, remains relatively-temperature independent, in contrast we find that the N—D1 bond in both cases has the same value at 280 K and increases on cooling to 175 K, remaining at a relatively constant value below that temperature. The key difference between the N—D bonds of D-Ala and D-Ala resides in the evolution of the N—D2 bond. For D-Ala, we find that this bond length has a similar value to N—D3 at 280 K and on cooling it decreases in value until 175 K, remaining relatively constant in value on further cooling. We find an opposite behaviour in L-Ala, where N—D2 has a similar value to the N—D1 bond length at 270 K, while its value increases gradually on cooling. Overall, the low-temperature behaviour of these bonds in D-Ala and L-Ala is different in that for D-Ala we find that N—D1, N—D2 and N—D3 are dissimilar, while for L-Ala N—D1 and N—D3 are somewhat similar and N—D2 is smaller in value. These data suggest somewhat different conformations in D- and L-Ala both at high and low temperatures. Careful scrutiny of Fig. S1 will lead to this same conclusion.

Turning our attention to the D⋯O bonds, our measurements also indicate differences in the D⋯O bond lengths for D-Ala and L-Ala. In both enantiomers, we find the temperature dependence of D(1)⋯O(1) and D(3)⋯O(2) to be very similar, both decreasing linearly with temperature. For D(1)⋯O(1), more specifically, the decrease is linear until approximately 100 K, and then this bond length remains relatively constant with further cooling. The most striking difference in the temperature evolution of these bonds is found for the D(2)⋯O(2) bond length. For L-Ala, D(2)⋯O(2) is of similar value and tracks closely the evolution of D(1)⋯O(1), while in sharp contrast the same D(2)⋯O(2) bond in D-Ala shows a much smaller value at 280 K compared with its, isomer, increases in size on cooling to 160 K, and on further cooling follows a very similar evolution and value of the D(1)⋯O(1) bond length.

The dissimilarities in the temperature evolution of bond lengths that we have identified in the NPD data mirror the differences in the low-frequency Raman modes of L- and D-Ala, both reflecting conformational differences between the enantiomers. The differences in the higher temperature behaviour of the D(2)⋯O(2) and N—D2 bonds, in particular,

can be directly correlated with the appearance of the new peaks in the Raman data.

In order to understand these results we turn to previous infrared studies performed on isotopically labelled ND-Ala molecules in a hydrogenated L-Ala crystal (Rozenberg *et al.*, 2003), RS studies in fully hydrogenated L-Ala (Kolesov & Boldyreva, 2011) as well as to more recent studies on the twice methylated amino group of *N,N*-dimethylglycine (Kapustin *et al.*, 2014). While Rozenberg *et al.* (2003) hypothesize that the appearance of the new bands in the spectra of partially deuterated L-Ala reveals an intrinsic hydrogen-bond disorder resulting from different accessible proton positions, the other authors discuss how the N—H⋯O hydrogen bonds regulate the stability of the main structural unit in crystalline amino acids. Therefore and as a whole, we must consider that while structural methods probe long-range periodic order, RS sensitivity to short-range interactions allows probing hetero-geneous hydrogen-bonding systems. Thus, the appearance of the new mode at 468 cm^{-1} and the band splitting of the $\tau(NH_3^+)$ observed in the RS of D-Ala strongly suggest that the reported structural differences in the two enantiomers are related to dissimilar accessible weakly bounded protons.

4. Conclusion

We have investigated the influence of temperature in the structure of D-Ala combining polarized RS, NPD and DFT-based methods. We find that the reorientation of the NH_3^+

group in D-Ala also induces modification of the N—H⋯O hydrogen bonds between two neighbouring molecules simi-larly to L-Ala (Vik *et al.*, 2005). In addition, modes assigned to lattice vibrations (translations and librations of molecules) in the Raman spectrum split on cooling as in L-Ala (Kolesov & Boldyreva, 2011). What is more interesting and different from L-Ala, is the observation of new Raman active modes in the *A*- and in *B*-irreducible representations for D-Ala below 160 and 260 K, as well as the observation of a temperature-dependent feature at 468 cm^{-1} below 200 K. The temperature depen-dence of the Raman spectra and the coincidence of the new feature in the Raman spectra with anomalies in the bond lengths obtained from NPD in the deuterated D-Ala exclude the possibility of inclusions in the sample. Finally, from NPD one observes that the temperature dependence of the N—D covalent bonds in D-Ala and L-Ala are quite different in the following way:

(i) For 250 K < *T* < 270 K, the ND_3^+ group in L-Ala shows one long (N—D3) and two short (N—D1 and N—D2) cova-lent bonds, in agreement with Lehmann *et al.* (1972), while D-Ala has two long (N—D2 and N—D3) and one short (N—D1) covalent bond.

(ii) Between 175 K < *T* < 250 K we observe a transition region for both L- and D-Ala.

(iii) For 60 K < *T* < 175 K, L-Ala shows two long (N—D1 and N—D3) and one short (N—D2) covalent bonds. This is in agreement with Destro *et al.* (2008) data at 23 K. On the hand,
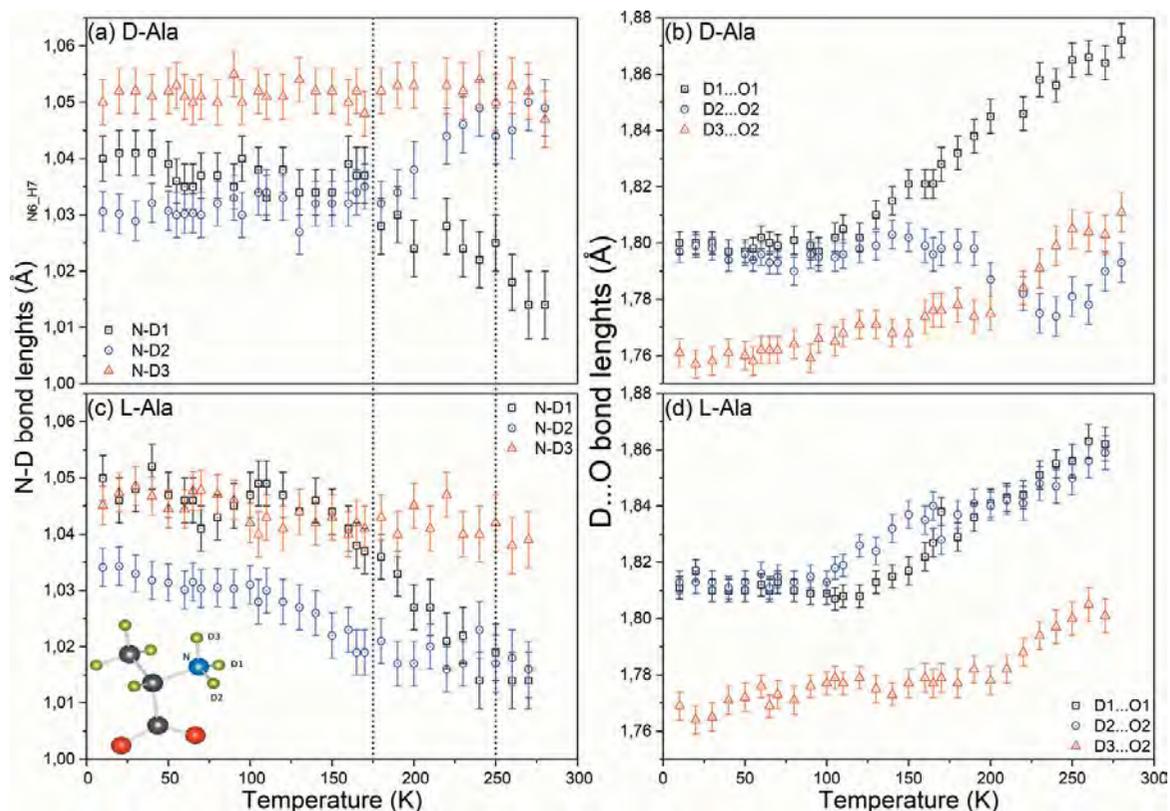

Figure 6
Temperature dependence of the N—D and D⋯O bond lengths in D-Ala (C$_3$D$_7$NO$_2$) are shown in panels (*a*) and (*b*). Temperature dependence of the N—D and D⋯O bond lengths in L-Ala reproduced from De Souza *et al.* (2007) and recalculated from the data used in De Souza *et al.* (2009), respectively, are shown in panels (*c*) and (*d*). The molecule is represented in the bottom left corner of the figure and labelled in agreement with Destro *et al.* (1988). The NPD data were collected on D2B (ILL) using λ = 1.594 Å.

and in agreement with Wilson *et al.* (2005), D-Ala shows two short (N—D1 and N—D2) and one long (N—D3) covalent bonds.

(iv) Differently from L-Ala, our data suggest the existence of three dissimilar N—D covalent bonds below 60 K in D-Ala. This is further supported by the variation in intensity of the vibration located at 41 cm^{-1} in the $x(yy)x$ representation; this intense peak observed in the spectrum recorded at room temperature basically vanishes on cooling.

Our work therefore leads to the conclusion that even if the crystal symmetry is maintained both L-Ala and D-Ala undergo micro-conformation transitions due to a subtle rearrangement of the hydrogen-bond network (Barthès *et al.*, 2003; Kolesov & Boldyreva, 2011), which is manifested by the evolution of the bond lengths revealed by NPD and the unexpected RS results. Additionally, a slight difference in crystal packing between the two alanine forms induces distinct dynamics for the hydrogen bonds in D-Ala, which culminates in the observation of extra Raman modes and dissimilar hydrogen-bond arrangements compared with L-Ala.

While D-Ala can be used as a biomarker for kidney disease, the presence of D-Ser is now thought to have an important function in the central nervous system, and D-Asp is reported to regulate the hormonal release in the endocrine glands, no comprehensive studies have been conducted to fully understand the solid-state properties of D-amino acids. Therefore, the results presented in this paper could have important clinical implications, since the reported changes in the hydrogen-bond strength of D-Ala when compared with L-Ala, will cause a direct impact on binding energy, consequently affect its affinity, and lead to disequilibrium between active and inactive conformational receptors (Kržan *et al.*, 2016).

References

Barthès, M., Dénoyer, F., Lorenzo, J.-E., Zaccaro, J., Robert, A., Zontone, F. & Bordallo, H. N. (2003). *Eur. Phys. J. B - Condens. Matter.* **37**, 375–382.

Barthès, M., Vik, A. F., Spire, A., Bordallo, H. N. & Eckert, J. (2002). *J. Phys. Chem. A*, **106**, 5230–5241.

Bordallo, H. N., Barthès, M. & Eckert, J. (1997). *Physica B*, **241–243**, 1138–1140.

Crowell, R. A. & Chronister, E. L. (1993). *Phys. Rev. B*, **48**, 172–177.

Dalton, J. B. & Schmidt, C. L. A. (1933). *J. Biol. Chem.* **103**, 549–578.

Destro, R., Marsh, R. E. & Bianchi, R. (1988). *J. Phys. Chem.* **92**, 966–973.

Destro, R., Soave, R. & Barzaghi, M. (2008). *J. Phys. Chem. B*, **112**, 5163–5174.

Frisch, M. J. *et al.* (2009). Gaussian 09, Revision A. Gaussian Inc., Wallingford, Connecticut, USA.

Ganesan, A., Brunger, M. J. & Wang, F. (2013). *Eur. Phys. J. D*, **67**, 229.

Hamase, K., Morikawa, A. & Zaitsu, K. (2002). *J. Chromatogr. B*, **781**, 73–91.

Hudson, M. R., Allis, D. G., Ouellette, W. & Hudson, B. S. (2009). *Phys. Chem. Chem. Phys.* **11**, 9474–9483.

Ishikawa, K., Terasawa, Y., Tanaka, M. & Asahi, T. (2017). *J. Phys. Chem. Solids*, **104**, 257–266.

Kapustin, E. A., Minkov, V. S., Stare, J. & Boldyreva, E. V. (2014). *Cryst. Growth Des.* **14**, 1851–1864.

Karakawa, S., Shimbo, K., Yamada, N., Mizukoshi, T., Miyano, H., Mita, M., Lindner, W. & Hamase, K. (2015). *J. Pharm. Biomed. Anal.* **115**, 123–129.

Kimura, T., Hamase, K., Miyoshi, Y., Yamamoto, R., Yasuda, K., Mita, M., Rakugi, H., Hayashi, T. & Isaka, Y. (2016). *Sci. Rep.* **6**, 26137.

Kolesov, B. A. & Boldyreva, E. V. (2011). *J. Raman Spectrosc.* **42**, 696–705.

Kresse, G. & Furthmüller, J. (1996). *Phys. Rev. B*, **54**, 11169–11186.

Kržan, M., Vianello, R., Maršavelski, A., Repič, M., Zakšek, M., Kotnik, K., Fijan, E. & Mavri, J. (2016). *PLoS One*, **11**, e0154002.

Lagaron, J.-M. (2002). *Macromol. Symp.* **184**, 19–36.

Larson, A. C. & Von Dreele, R. B. (1994). Los Alamos National Laboratory Report LAUR, 86-748.

Lehmann, M. S., Koetzle, T. F. & Hamilton, W. C. (1972). *J. Am. Chem. Soc.* **94**, 2657–2660.

Loh, E. (1975). *J. Chem. Phys.* **63**, 3192–3194.

Monkhorst, H. J. & Pack, J. D. (1976). *Phys. Rev. B*, **13**, 5188–5192.

Perdew, J. P., Burke, K. & Ernzerhof, M. (1996). *Phys. Rev. Lett.* **77**, 3865–3868.

Ramirez-Cuesta, A. J. (2004). *Comput. Phys. Commun.* **157**, 226–238.

Rozenberg, M., Shoham, G., Reva, I. & Fausto, R. (2003). *Spectrochim. Acta A Mol. Biomol. Spectrosc.* **59**, 3253–3266.

Salam, A. (1992). *Phys. Lett. B*, **288**, 153–160.

Souza, J. M. de, Freire, P. T. C., Argyriou, D. N., Stride, J. A., Barthès, M., Kalceff, W. & Bordallo, H. N. (2009). *Chem. Phys. Chem.*, **10**, 3337–3343.

Souza, J. M. de, Freire, P. T. C., Bordallo, H. N. & Argyriou, D. N. (2007). *J. Phys. Chem. B*, **111**, 5034–5039.

Sullivan, R., Pyda, M., Pak, J., Wunderlich, B., Thompson, J. R., Pagni, R., Pan, H., Barnes, C., Schwerdtfeger, P. & Compton, R. (2003). *J. Phys. Chem. A*, **107**, 6674–6680.

Susi, H. & Byler, D. M. (1980). *J. Mol. Struct.* **63**, 1–11.

Vik, A. F., Yuzyuk, Y. I., Barthès, M. & Sauvajol, J.-L. (2005). *J. Raman Spectrosc.* **36**, 749–754.

Wang, W., Min, W., Bai, F., Sun, L., Yi, F., Wang, Z., Yan, C., Ni, Y. & Zhao, Z. (2002). *Tetrahedron Asymmetry*, **13**, 2427–2432.

Wang, C. H. & Storms, R. D. (1971). *J. Chem. Phys.* **55**, 3291–3299.

Wang, W., Yi, F., Ni, Y., Zhao, Z., Jin, X. & Tang, Y. (2000). *J. Biol. Phys.* **26**, 51–65.

Wilson, C. C., Myles, D., Ghosh, M., Johnson, L. N. & Wang, W. (2005). *New J. Chem.* **29**, 1318.

Zhang, F., Wang, H.-W., Tominaga, K. & Hayashi, M. (2015). *J. Phys. Chem. A*, **119**, 3008–3022.

IUCrJ

Supporting information for article:

Hydrogen bonds in crystalline D-Alanine: Diffraction and spectroscopic evidence for differences between enantiomers

Ezequiel A. Belo, Jose E. M. Pereira, Paulo T. C. Freire, Dimitri N. Argyriou, Juergen Eckert and Heloisa N. Bordallo

Figure S1 summarizes the data reported for fully hydrogenated single crystals results from (Wilson *et al.*, 2005) The lines are meant as guides to the eye. The data at 60 and 295 K were collected using standard procedures on the SXD instrument at the ISIS spallation neutron source at the Rutherford Appleton Laboratory, while the structure refined at 240 K, 250 K, 260 K and 300 K was obtained from data collected on the VIVALDI instrument at the ILL. Data obtained using single crystal X-ray diffraction collected at 23 K (Destro *et al.*, 2008) and single crystal neutron diffration at 300 K (Lehmann *et al.*, 1972) for L-Ala are also reported for comparison.

Figure S2 shows a typical Rietveld analysis of neutron diffraction data measured from D-Ala using the neutron powder diffractometer D2B.

The three N-H bond geometries obtained for L-Ala and D-Ala after performing the VASP minimization of the crystalline structure are given in Table S1 together with the values reported in (Wilson *et al.*, 2005).

Lattice coordinates for D-Ala and L-Ala as a function of temperature obtained from the powder diffraction data analysed using the crystallographic model of Destro *et al.* (1988) as initial input with the GSAS suite of programs (Larson & Von Dreele, 1994) are also provided.
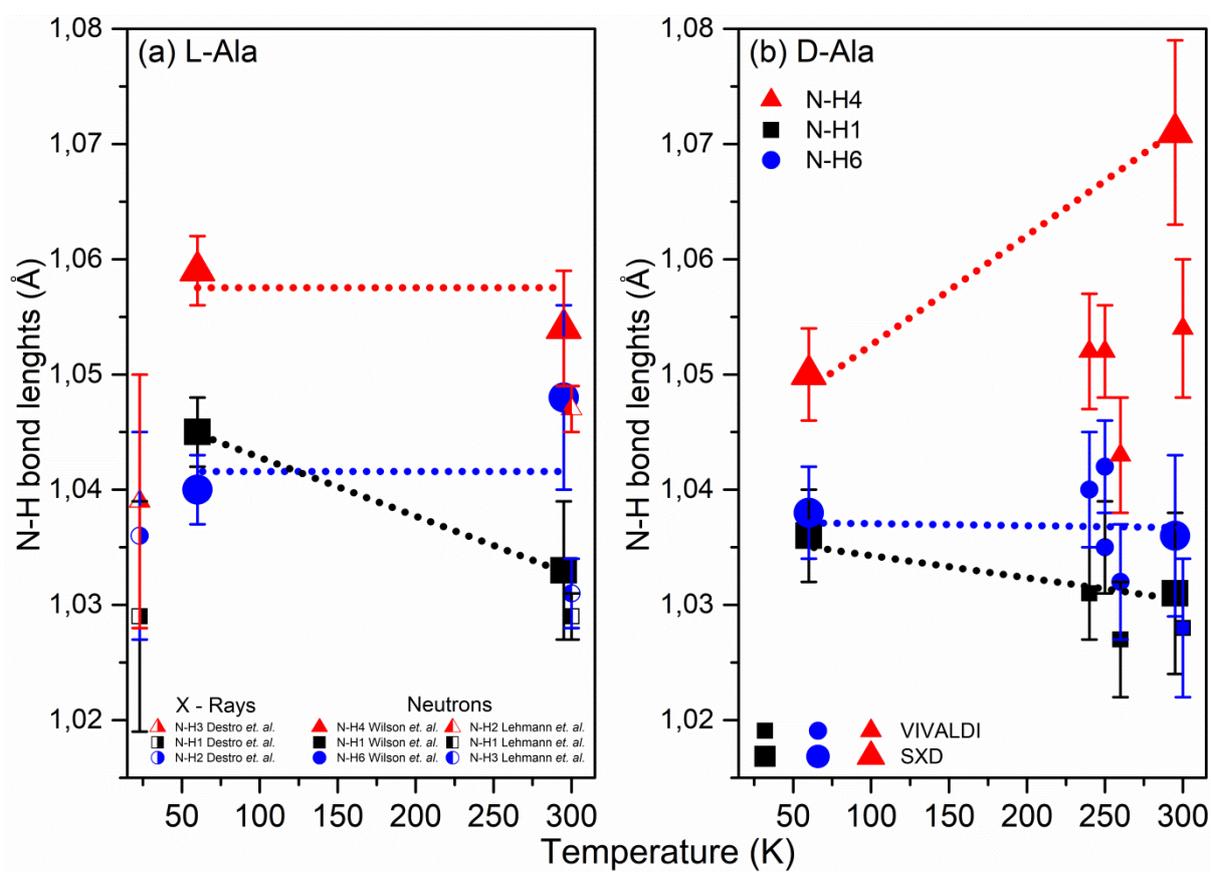
Figure S1   (a) Single crystal X-ray diffraction data reported by Destro *et al.* (2008) (right side half filled symbols) at 23K along with single crystal neutron diffraction data reported by Wilson *et al.* (2005) (closed symbols, data taken using SXD) at 295 and 60K and by Lehmann *et al.* (1972) (left side half filled symbols) at 300K for fully hydrogenated L-Ala. (b) Single crystal neutron diffraction data reported by Wilson *et al.* (2005) at various temperatures using VIVALDI (small closed symbols) and SXD (large closed symbols) for fully hydrogenated D-Ala. On this figure we have kept the bond length nomenclature used by the respective authors to facilitate comparison. Note that we have used the Destro *et al.* (1988 & 2008) nomenclature for labelling the bond lengths of deuterated L-Ala and D-Ala. Thus, square, circle and triangle symbols always correspond N-H$_1$, N-H$_2$ and N-H$_3$, respectively. The lines are meant as guides to the eye.
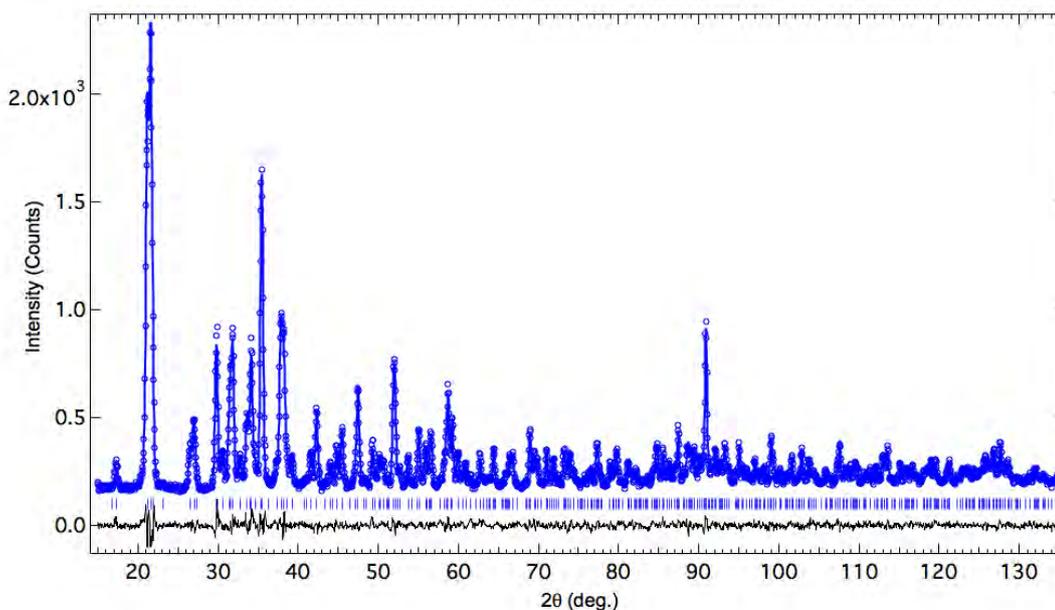
Figure S2 A typical Rietveld analysis of neutron diffraction data measured from D-Ala using the D2B powder diffractometer at the ILL. These data were collected at 270 K. Here the open circles represent the observations and the line through the data points the calculated profile. The difference (ons-calc) is plotted below the data together with the calculated position of Bragg reflections represented as vertical bars.

Table S1 N-H bond distances minimized in the DFT calculations compared to experimental values (Wilson *et al.*, 2005).

N-H distance (Å)	D-Ala DFT minimized structure	D-Ala at 60K Wilson *et al.*, 2005	L-Ala DFT minimized structure	L-Ala at 60K Wilson *et al.*, 2005
N-H$_1$	1.0434	1.036(4)	1.046	1.045(3)
N-H$_2$	1.0459	1.038(4)	1.0435	1.040(3)
N-H$_3$	1.0610	1.050(4)	1.0605	1.059(3)

D-Alanine-d7
Space group P 21 21 21
The lattice is acentric   primitive orthorhombic Laue symmetry mmm
Multiplicity of a general site is   4

 The equivalent positions are:

 (1)   X   Y   Z (2) 1/2+X 1/2-Y   -Z
 (3)   -X 1/2+Y 1/2-Z (4) 1/2-X   -Y 1/2+Z

   Lattice constants at 280 K are   6.01243 12.32675   5.78411 0.00000 0.00000
0.00000
     Standard deviations   0.00018   0.00035   0.00010 0.00000 0.00000 0.00000

        15584_280K_D2B

O1   0.2723(9)   -0.0855(4)   0.3709(9)
O2   0.5547(9)   -0.1858(5)   0.2411(8)
C3   0.4371(8)   -0.1445(4)   0.3982(7)
C2   0.5250(9)   -0.1631(4)   0.6456(7)
C1   0.7260(8)   -0.0886(4)   0.6988(8)
N   0.3467(5)   -0.137(32)   0.8140(6)
D1   0.2966(9)   -0.0588(4)   0.8000(9)
D2   0.2173(8)   -0.1935(4)   0.7968(8)
D3   0.4004(8)   -0.1480(5)   0.9846(8)
D4   0.5612(9)   -0.2485(4)   0.6590(9)
D6   0.8572(12)   -0.1046(6)   0.5796(11)
D7   0.6790(12)   -0.0032(6)   0.6967(12)
D5   0.7876(11)   -0.1075(5)   0.8723(12)

        15580_270K_D2B

O1   0.2734(9)   -0.0848(4)   0.3717(9)
O2   0.5558(9)   -0.1859(5)   0.2407(7)
C3   0.4372(7)   -0.1445(4)   0.3980(7)
C2   0.5260(8)   -0.1633(4)   0.6452(7)
C1   0.7270(8)   -0.08938(35)   0.6986(8)

N	0.3471(5)	-0.13696(31)	0.8143(6)
D1	0.2976(9)	-0.0586(4)	0.7999(9)
D2	0.2168(8)	-0.1932(4)	0.7976(8)
D3	0.4017(8)	-0.1485(5)	0.9854(8)
D4	0.5626(9)	-0.2492(4)	0.6606(8)
D6	0.7896(10)	-0.0848(6)	0.8723(10)
D7	0.8578(11)	-0.1048(6)	0.5791(11)
D5	0.6802(12)	-0.0040(5)	0.6961(12)

15576_260K_D2B

O1	0.2726(9)	-0.0852(4)	0.3716(9)
O2	0.5569(9)	-0.1871(5)	0.2405(7)
C3	0.4379(7)	-0.1439(4)	0.3987(7)
C2	0.5271(8)	-0.1629(4)	0.6451(7)
C1	0.7275(7)	-0.08886(34)	0.6983(8)
N	0.3478(5)	-0.13727(30)	0.8142(5)
D1	0.2973(9)	-0.0586(4)	0.8005(9)
D2	0.2172(8)	-0.1928(4)	0.7967(8)
D3	0.4034(8)	-0.1491(5)	0.9849(8)
D4	0.5639(8)	-0.2492(4)	0.6604(8)
D6	0.7904(11)	-0.1084(6)	0.8724(10)
D7	0.8575(11)	-0.1049(5)	0.5783(11)
D5	0.6810(10)	-0.0039(5)	0.6964(12)

15572_250K_D2B

O1	0.2734(9)	-0.0854(4)	0.3730(9)
O2	0.5565(9)	-0.1866(5)	0.2404(7)
C3	0.4384(7)	-0.1441(4)	0.3984(7)
C2	0.5266(8)	-0.1629(4)	0.6456(7)
C1	0.7284(7)	-0.08907(33)	0.6984(8)
N	0.3475(5)	-0.13742(30)	0.8139(5)
D1	0.2965(9)	-0.0582(4)	0.8004(9)
D2	0.2167(8)	-0.1928(4)	0.7965(8)
D3	0.4030(8)	-0.1488(5)	0.9842(8)
D4	0.5647(8)	-0.2490(4)	0.6605(8)
D6	0.7906(11)	-0.1088(6)	0.8721(10)
D7	0.8578(11)	-0.1043(5)	0.5771(11)
D5	0.6814(10)	-0.0037(5)	0.6953(11)

15568_240K_D2B

O1	0.2723(9)	-0.0849(4)	0.3723(8)
O2	0.5570(8)	-0.1867(5)	0.2403(7)
C3	0.4381(7)	-0.1436(4)	0.3985(7)
C2	0.5282(8)	-0.1625(4)	0.6448(7)
C1	0.7285(7)	-0.08908(33)	0.6980(8)
N	0.3477(5)	-0.13724(30)	0.8142(5)
D1	0.2964(8)	-0.0583(4)	0.8008(9)
D2	0.2167(7)	-0.1931(4)	0.7955(8)
D3	0.4041(7)	-0.1495(5)	0.9847(7)
D4	0.5658(8)	-0.2491(4)	0.6601(8)
D6	0.7917(11)	-0.1090(5)	0.8721(9)
D7	0.8590(11)	-0.1038(5)	0.5769(11)
D5	0.6805(10)	-0.0037(5)	0.6955(11)

15564_230K_D2B

O1	0.2729(8)	-0.0847(4)	0.3735(8)

O2	0.5564(8)	-0.1864(4)	0.2400(7)
C3	0.4387(7)	-0.1439(4)	0.3985(7)
C2	0.5287(8)	-0.1624(4)	0.6445(7)
C1	0.7295(7)	-0.08907(32)	0.6975(8)
N	0.3474(5)	-0.13777(30)	0.8150(5)
D1	0.2964(8)	-0.0586(4)	0.8016(9)
D2	0.2168(7)	-0.1934(4)	0.7950(8)
D3	0.4051(7)	-0.1492(5)	0.9850(7)
D4	0.5667(8)	-0.2489(4)	0.6597(8)
D6	0.7930(11)	-0.1091(5)	0.8711(9)
D7	0.8603(10)	-0.1045(5)	0.5789(10)
D5	0.6824(10)	-0.0038(5)	0.6955(11)

15560_220K_D2B

O1	0.2723(8)	-0.0845(4)	0.3744(8)
O2	0.5572(8)	-0.1861(4)	0.2390(7)
C3	0.4387(7)	-0.1433(4)	0.3992(6)
C2	0.5288(8)	-0.1627(4)	0.6456(6)
C1	0.7304(7)	-0.08946(32)	0.6975(7)
N	0.3480(4)	-0.13726(29)	0.8151(5)
D1	0.2961(8)	-0.0578(4)	0.8020(9)
D2	0.2174(7)	-0.1929(4)	0.7958(8)
D3	0.4063(7)	-0.1497(4)	0.9847(7)
D4	0.5678(8)	-0.2490(4)	0.6596(8)
D6	0.7947(10)	-0.1091(5)	0.8714(9)
D7	0.8601(10)	-0.1043(5)	0.5764(10)
D5	0.6828(9)	-0.0040(4)	0.6957(11)

15556_210K_D2B

O1	0.268(7)	-0.08328(32)	0.374(7)
O2	0.5578(7)	-0.1857(4)	0.2398(6)
C3	0.4417(6)	-0.14141(30)	0.3993(5)
C2	0.5317(6)	-0.16138(30)	0.6462(5)
C1	0.738(6)	-0.09085(28)	0.6964(6)
N	0.3505(4)	-0.13717(24)	0.8151(4)
D1	0.3009(7)	-0.05655(30)	0.8036(7)
D2	0.2215(6)	-0.19203(33)	0.7949(6)
D3	0.4131(6)	-0.15(4)	0.9832(6)
D4	0.5706(7)	-0.24825(33)	0.6605(7)
D6	0.8036(8)	-0.1088(4)	0.8728(7)
D7	0.8669(8)	-0.1045(4)	0.573(8)
D5	0.69(8)	-0.00448(35)	0.6925(8)

15552_200K_D2B

O1	0.2713(8)	-0.0846(4)	0.3747(8)
O2	0.5566(8)	-0.1864(4)	0.2389(7)
C3	0.4385(7)	-0.14294(35)	0.3994(6)
C2	0.5299(7)	-0.1623(4)	0.6452(6)
C1	0.7325(7)	-0.08959(31)	0.6976(7)
N	0.3488(4)	-0.13713(29)	0.8154(5)
D1	0.2965(8)	-0.058(4)	0.8032(9)
D2	0.2192(7)	-0.1927(4)	0.7955(7)
D3	0.4083(7)	-0.1496(4)	0.9847(7)
D4	0.5665(8)	-0.2487(4)	0.6593(7)
D6	0.796(10)	-0.1092(5)	0.8723(8)
D7	0.862(10)	-0.1046(5)	0.5757(10)
D5	0.6835(9)	-0.0044(4)	0.6939(10)

```
          15548_190K_D2B

O1          0.2715(8)            -0.0847(4)            0.3748(7)
O2          0.5555(8)            -0.1863(4)            0.2395(7)
C3          0.4386(7)            -0.1427(34)           0.3995(6)
C2          0.5294(7)            -0.16218(35)             0.6456(6)
C1          0.7341(7)            -0.0899(31)           0.6974(7)
N           0.349(4)             -0.13698(28)            0.8154(5)
D1          0.2976(8)            -0.0572(4)            0.8035(8)
D2          0.2193(7)            -0.192(4)             0.7953(7)
D3          0.4093(7)            -0.1498(4)            0.9841(7)
D4          0.5665(8)            -0.2489(4)            0.6593(7)
D6          0.7971(9)            -0.1093(5)            0.8723(8)
D7          0.863(9)             -0.1051(5)            0.575(9)
D5          0.6853(9)            -0.0048(4)            0.6929(10)


          15544_180K_D2B

O1          0.271(7)             -0.0842(4)            0.3754(7)
O2          0.5566(8)            -0.186(4)             0.2398(6)
C3          0.4394(7)            -0.14224(33)             0.3994(6)
C2          0.5303(7)            -0.16185(34)             0.6456(6)
C1          0.735(7)             -0.09027(30)             0.6973(7)
N           0.3494(4)            -0.13697(28)             0.8153(5)
D1          0.2982(7)            -0.05721(34)             0.8038(8)
D2          0.22(6)              -0.192(4)             0.7952(7)
D3          0.4101(7)            -0.1491(4)            0.984(7)
D4          0.5661(8)            -0.2484(4)            0.6604(7)
D6          0.7974(9)            -0.1088(5)            0.8727(8)
D7          0.8638(9)            -0.105(4)             0.5752(9)
D5          0.6859(9)            -0.005(4)             0.6923(9)


          15540_170K_D2B

O1          0.271(7)             -0.0841(4)            0.3756(7)
O2          0.5565(7)            -0.1857(4)            0.2397(6)
C3          0.4398(6)            -0.1418(32)           0.3993(6)
C2          0.5303(7)            -0.16194(33)             0.6461(6)
C1          0.7353(7)            -0.09004(29)             0.697(7)
N           0.3499(4)            -0.1373(27)           0.8158(5)
D1          0.2979(7)            -0.0569(34)           0.803(8)
D2          0.2198(6)            -0.1923(4)            0.795(7)
D3          0.41(7)              -0.1494(4)            0.9839(7)
D4          0.5676(8)            -0.2486(4)            0.6599(7)
D6          0.7985(9)            -0.1087(4)            0.8727(8)
D7          0.8647(9)            -0.105(4)             0.5747(9)
D5          0.6864(8)            -0.0046(4)            0.6924(9)


          15536_165K_D2B

O1          0.27(7)              -0.08398(35)             0.3753(7)
O2          0.5568(7)            -0.1858(4)            0.2402(6)
C3          0.4396(6)            -0.1421(32)           0.3994(6)
C2          0.5308(7)            -0.16146(33)             0.6456(6)
C1          0.7364(7)            -0.09032(29)             0.6967(7)
N           0.3497(4)            -0.13712(26)             0.8154(5)
D1          0.2985(7)            -0.05657(33)             0.8037(8)
D2          0.22(6)              -0.19228(35)             0.7953(7)
D3          0.4116(7)            -0.1492(4)            0.9836(6)
D4          0.5682(8)            -0.24817(35)             0.6599(7)
```

D6	0.7992(8)	-0.1086(4)	0.8724(7)
D7	0.8648(9)	-0.105(4)	0.5748(9)
D5	0.6869(8)	-0.0048(4)	0.6929(9)

15532_160K_D2B

O1	0.2695(7)	-0.08409(34)	0.3751(7)
O2	0.5566(7)	-0.1858(4)	0.2397(6)
C3	0.4395(6)	-0.14173(32)	0.3993(6)
C2	0.5313(7)	-0.1614(32)	0.6458(6)
C1	0.7366(7)	-0.09015(29)	0.6969(6)
N	0.3501(4)	-0.13722(26)	0.8153(5)
D1	0.2991(7)	-0.05648(33)	0.8037(8)
D2	0.2204(6)	-0.1921(4)	0.795(7)
D3	0.4111(7)	-0.1495(4)	0.9835(6)
D4	0.5688(8)	-0.24834(35)	0.6601(7)
D6	0.7996(8)	-0.1089(4)	0.8729(7)
D7	0.8649(9)	-0.1048(4)	0.5736(8)
D5	0.6877(8)	-0.0042(4)	0.6926(9)

15528_150K_D2B

O1	0.2692(7)	-0.08377(33)	0.3745(7)
O2	0.5573(7)	-0.1852(4)	0.2394(6)
C3	0.4404(6)	-0.14138(31)	0.3992(6)
C2	0.5311(7)	-0.16116(31)	0.6451(6)
C1	0.7371(7)	-0.09052(28)	0.6973(6)
N	0.3505(4)	-0.13733(25)	0.8154(5)
D1	0.2988(7)	-0.05702(31)	0.8042(8)
D2	0.2205(6)	-0.19211(34)	0.7947(6)
D3	0.4122(6)	-0.15(4)	0.9835(6)
D4	0.5695(7)	-0.24798(33)	0.6598(7)
D6	0.8012(8)	-0.109(4)	0.873(7)
D7	0.8657(8)	-0.1051(4)	0.5733(8)
D5	0.688(8)	-0.0046(4)	0.6923(9)

15524_140K_D2B

O1	0.2684(7)	-0.08377(33)	0.3734(7)
O2	0.5569(7)	-0.1852(4)	0.2397(6)
C3	0.442(6)	-0.1413(30)	0.3994(5)
C2	0.5314(6)	-0.16129(31)	0.6456(5)
C1	0.7375(7)	-0.09052(28)	0.697(6)
N	0.3506(4)	-0.13718(25)	0.8153(4)
D1	0.2998(7)	-0.05672(31)	0.8042(8)
D2	0.2212(6)	-0.19231(33)	0.7946(6)
D3	0.4128(6)	-0.1499(4)	0.9833(6)
D4	0.5708(7)	-0.2481(33)	0.6606(7)
D6	0.8027(8)	-0.1087(4)	0.8728(7)
D7	0.8673(8)	-0.1048(4)	0.5732(8)
D5	0.6883(8)	-0.0044(4)	0.6933(9)

15520_130K_D2B

O1	0.268(7)	-0.08328(32)	0.374(7)
O2	0.5578(7)	-0.1857(4)	0.2398(6)
C3	0.4417(6)	-0.14142(30)	0.3993(5)
C2	0.5317(6)	-0.16138(30)	0.6462(6)
C1	0.738(6)	-0.09086(28)	0.6964(6)
N	0.3505(4)	-0.13716(24)	0.8151(4)

```
D1          0.3009(7)        -0.05655(30)              0.8036(7)
D2          0.2215(6)        -0.19202(33)              0.7949(6)
D3          0.4131(6)        -0.15(4)          0.9832(6)
D4          0.5706(7)        -0.24825(33)              0.6605(7)
D6          0.8036(8)        -0.1088(4)         0.8728(7)
D7          0.8669(8)        -0.1045(4)         0.573(8)
D5          0.6899(8)        -0.00448(35)              0.6925(8)


      15516_120K_D2B

O1          0.2685(6)        -0.08316(31)              0.3736(6)
O2          0.5578(7)        -0.1856(4)         0.2401(6)
C3          0.4426(6)        -0.14094(29)              0.3993(5)
C2          0.5326(6)        -0.16129(29)              0.646(5)
C1          0.739(6)         -0.09062(27)              0.6967(6)
N           0.3513(4)        -0.13702(23)              0.8153(4)
D1          0.3004(6)        -0.05618(30)              0.8044(7)
D2          0.2214(6)        -0.19212(32)              0.7944(6)
D3          0.4139(6)        -0.1502(4)         0.9829(6)
D4          0.5724(7)        -0.24799(32)              0.6606(6)
D6          0.8044(8)        -0.109(4)          0.8731(7)
D7          0.8678(8)        -0.1046(4)         0.5728(7)
D5          0.6909(7)        -0.00415(34)              0.6927(8)


      15512_110K_D2B

O1          0.2686(6)        -0.08288(30)              0.3734(6)
O2          0.558(7)         -0.18523(34)              0.2401(6)
C3          0.4431(6)        -0.1411(28)        0.3998(5)
C2          0.5336(6)        -0.16079(29)              0.6466(5)
C1          0.7385(6)        -0.09033(27)              0.6964(6)
N           0.35142(35)      -0.13721(23)              0.8157(4)
D1          0.301(6)         -0.05672(29)              0.8051(7)
D2          0.222(5)         -0.19273(31)              0.7943(6)
D3          0.4143(6)        -0.15024(34)              0.9831(6)
D4          0.5721(7)        -0.24846(32)              0.6614(6)
D6          0.8057(7)        -0.1089(4)         0.8727(7)
D7          0.8697(8)        -0.1051(4)         0.5726(7)
D5          0.69(7)          -0.00361(34)              0.692(8)


      15508_105K_D2B

O1          0.2687(6)        -0.08322(30)              0.3735(6)
O2          0.5584(6)        -0.1853(33)        0.2396(6)
C3          0.443(6)         -0.14069(28)              0.3999(5)
C2          0.5337(6)        -0.16092(29)              0.6464(5)
C1          0.7395(6)        -0.09048(27)              0.6968(6)
N           0.35139(35)      -0.13706(22)              0.8158(4)
D1          0.3009(6)        -0.05618(29)              0.8054(7)
D2          0.2219(5)        -0.19256(31)              0.7942(6)
D3          0.4149(6)        -0.15022(34)              0.9831(6)
D4          0.5723(7)        -0.24819(32)              0.6617(6)
D6          0.8052(7)        -0.1091(4)         0.873(7)
D7          0.8692(8)        -0.1048(4)         0.5726(7)
D5          0.6907(7)        -0.00409(33)              0.6928(8)


      15504_100K_D2B

O1          0.2705(6)        -0.08255(29)              0.3748(6)
O2          0.5602(6)        -0.18495(29)              0.2395(5)
```

C3	0.445(5)	-0.1403(25)	0.3995(5)
C2	0.5358(6)	-0.16055(26)	0.6458(5)
C1	0.7434(5)	-0.09082(24)	0.6962(5)
N	0.35313(32)	-0.13739(20)	0.8161(4)
D1	0.3(6)	-0.05647(27)	0.8069(6)
D2	0.2233(5)	-0.19259(28)	0.7934(6)
D3	0.4164(5)	-0.14986(32)	0.9838(5)
D4	0.5748(6)	-0.24812(29)	0.6626(6)
D6	0.8091(7)	-0.10835(33)	0.8727(6)
D7	0.8721(7)	-0.10441(34)	0.5709(6)
D5	0.6929(6)	-0.00416(31)	0.6917(7)

15500_95K_D2B

O1	0.2694(6)	-0.08275(30)	0.3736(6)
O2	0.5582(6)	-0.18544(33)	0.2398(6)
C3	0.4438(6)	-0.14088(27)	0.3998(5)
C2	0.5337(6)	-0.1607(28)	0.6462(5)
C1	0.7399(6)	-0.09071(26)	0.6965(6)
N	0.35159(34)	-0.13732(22)	0.8157(4)
D1	0.3017(6)	-0.05615(28)	0.8059(7)
D2	0.2226(5)	-0.19266(30)	0.7939(6)
D3	0.4148(6)	-0.15059(34)	0.9828(6)
D4	0.5731(7)	-0.24852(31)	0.6613(6)
D6	0.8069(7)	-0.1088(4)	0.873(6)
D7	0.8702(7)	-0.1052(4)	0.5722(7)
D5	0.6909(7)	-0.00415(33)	0.6922(8)

15496_90K_D2B

O1	0.2687(6)	-0.08274(30)	0.3733(6)
O2	0.5586(6)	-0.18503(33)	0.2396(6)
C3	0.4438(6)	-0.14035(27)	0.3994(5)
C2	0.5343(6)	-0.16058(28)	0.6459(5)
C1	0.7404(6)	-0.09087(26)	0.6967(6)
N	0.35164(34)	-0.13716(22)	0.8157(4)
D1	0.3015(6)	-0.0564(28)	0.8053(7)
D2	0.2225(5)	-0.19278(30)	0.7939(6)
D3	0.4155(6)	-0.15061(34)	0.9835(6)
D4	0.5738(7)	-0.2484(32)	0.6615(6)
D6	0.8068(7)	-0.1086(4)	0.8728(6)
D7	0.8706(7)	-0.1048(4)	0.5716(7)
D5	0.6907(7)	-0.00403(33)	0.6916(8)

15492_80K_D2B

O1	0.269(6)	-0.08261(29)	0.3734(6)
O2	0.5593(6)	-0.18538(31)	0.2397(5)
C3	0.4441(6)	-0.14027(26)	0.3994(5)
C2	0.5347(6)	-0.16064(27)	0.6458(5)
C1	0.741(6)	-0.09054(25)	0.6971(5)
N	0.35206(33)	-0.13748(21)	0.8164(4)
D1	0.3009(6)	-0.05675(28)	0.8055(7)
D2	0.2227(5)	-0.19275(29)	0.7933(6)
D3	0.4153(6)	-0.15055(33)	0.9835(6)
D4	0.5737(7)	-0.24844(31)	0.6615(6)
D6	0.8069(7)	-0.1085(4)	0.8734(6)
D7	0.8703(7)	-0.105(4)	0.5723(7)
D5	0.6909(7)	-0.00411(32)	0.6919(8)

```
      15488_70K_D2B

O1           0.2693(6)           -0.08265(29)           0.3744(6)
O2           0.5598(6)           -0.18527(31)           0.2391(5)
C3           0.4439(5)           -0.14031(26)           0.3998(5)
C2           0.5351(6)           -0.1607(27)        0.646(5)
C1           0.7417(6)           -0.09069(25)           0.6961(5)
N            0.35229(33)         -0.13717(21)        0.816(4)
D1           0.3007(6)           -0.05648(27)           0.8055(7)
D2           0.2236(5)           -0.19271(29)           0.7936(6)
D3           0.4158(6)           -0.15065(33)           0.983(6)
D4           0.574(7)            -0.24809(30)           0.6618(6)
D6           0.8072(7)           -0.1084(35)         0.8733(6)
D7           0.8712(7)           -0.1047(4)          0.5718(7)
D5           0.6922(7)           -0.00398(32)           0.6921(8)


      15484_65K_D2B

O1           0.2692(6)           -0.08255(29)           0.3738(6)
O2           0.5597(6)           -0.18511(30)           0.2392(5)
C3           0.4443(5)           -0.14008(26)           0.3997(5)
C2           0.5356(6)           -0.16065(26)           0.6459(5)
C1           0.7424(5)           -0.0906(25)         0.6961(5)
N            0.35241(33)         -0.13737(20)           0.816(4)
D1           0.3014(6)           -0.0567(27)         0.8057(7)
D2           0.2234(5)           -0.19274(29)           0.7934(6)
D3           0.4157(5)           -0.15049(32)           0.9832(6)
D4           0.5744(7)           -0.2483(30)         0.6617(6)
D6           0.8076(7)           -0.10849(34)           0.8732(6)
D7           0.8712(7)           -0.10465(35)           0.5715(6)
D5           0.6917(7)           -0.00383(31)           0.692(8)


      15480_60K_D2B

O1           0.2698(6)           -0.08256(29)           0.374(6)
O2           0.5597(6)           -0.18494(30)           0.2396(5)
C3           0.4443(5)           -0.14003(26)           0.3995(5)
C2           0.536(6)            -0.16067(26)           0.6458(5)
C1           0.7423(5)           -0.09078(25)           0.6965(5)
N            0.35271(33)         -0.13741(20)           0.8159(4)
D1           0.3004(6)           -0.0569(27)         0.8059(6)
D2           0.2236(5)           -0.19276(29)           0.7935(6)
D3           0.4158(5)           -0.15044(32)           0.9833(5)
D4           0.5736(7)           -0.24831(30)           0.6625(6)
D6           0.8083(7)           -0.10806(34)           0.8732(6)
D7           0.8707(7)           -0.10469(35)           0.5713(6)
D5           0.6921(7)           -0.00359(31)           0.6916(7)


      15476_55K_D2B

O1           0.2696(6)           -0.0824(29)         0.374(6)
O2           0.5597(6)           -0.18515(30)           0.2393(5)
C3           0.4444(5)           -0.14(26)           0.3998(5)
C2           0.5361(6)           -0.16057(26)           0.6462(5)
C1           0.7422(5)           -0.09068(25)           0.6964(5)
N            0.35275(33)         -0.13732(20)           0.8161(4)
D1           0.3009(6)           -0.0567(27)         0.8061(7)
D2           0.2237(5)           -0.19268(29)           0.7936(6)
D3           0.4167(5)           -0.15046(32)           0.9836(6)
D4           0.5742(7)           -0.24854(29)           0.6621(6)
D6           0.8084(7)           -0.10799(34)           0.8732(6)
```

D7	0.872(7)	-0.10472(35)	0.5709(6)
D5	0.6925(7)	-0.00404(31)	0.6912(8)

15472_50K_D2B

O1	0.2699(6)	-0.08251(29)	0.3744(6)
O2	0.5599(6)	-0.18491(30)	0.2394(5)
C3	0.4446(5)	-0.14007(26)	0.3996(5)
C2	0.5361(6)	-0.16037(26)	0.6459(5)
C1	0.7428(5)	-0.09053(25)	0.6965(5)
N	0.35291(33)	-0.13736(20)	0.8160(4)
D1	0.3006(6)	-0.05657(27)	0.8066(7)
D2	0.2236(5)	-0.19271(29)	0.7935(6)
D3	0.4165(5)	-0.15034(32)	0.9834(6)
D4	0.5741(7)	-0.24821(29)	0.6623(6)
D6	0.8081(7)	-0.10825(34)	0.8730(6)
D7	0.872(7)	-0.10469(35)	0.5714(6)
D5	0.6922(7)	-0.00391(31)	0.6914(7)

15468_40K_D2B

O1	0.2705(6)	-0.08255(29)	0.3748(6)
O2	0.5602(6)	-0.18495(29)	0.2395(5)
C3	0.445(5)	-0.14030(26)	0.3995(5)
C2	0.5358(6)	-0.16055(26)	0.6458(5)
C1	0.7434(5)	-0.09082(24)	0.6962(5)
N	0.35313(32)	-0.13739(20)	0.8161(4)
D1	0.3000(6)	-0.05647(27)	0.8069(6)
D2	0.2233(5)	-0.19259(28)	0.7934(6)
D3	0.4164(5)	-0.14986(32)	0.9838(5)
D4	0.5748(6)	-0.24812(29)	0.6626(6)
D6	0.8091(7)	-0.10835(33)	0.8727(6)
D7	0.8721(7)	-0.10441(34)	0.5709(6)
D5	0.6929(6)	-0.00416(31)	0.6916(7)

15464_30K_D2B

O1	0.2701(6)	-0.0827(28)	0.3750(6)
O2	0.5608(6)	-0.18462(29)	0.2390(5)
C3	0.4443(5)	-0.14005(25)	0.3994(5)
C2	0.5361(6)	-0.16059(26)	0.6458(5)
C1	0.7443(5)	-0.09066(24)	0.6965(5)
N	0.35306(32)	-0.13755(20)	0.8161(4)
D1	0.3001(6)	-0.05659(27)	0.8070(6)
D2	0.2231(5)	-0.19228(29)	0.7931(6)
D3	0.4165(5)	-0.15015(32)	0.9838(5)
D4	0.5742(6)	-0.24801(29)	0.6627(6)
D6	0.8091(7)	-0.10853(33)	0.8729(6)
D7	0.8726(7)	-0.10431(34)	0.5707(6)
D5	0.6934(6)	-0.00423(31)	0.6911(7)

15460_20K_D2B

O1	0.2707(6)	-0.08292(29)	0.3744(6)
O2	0.5604(6)	-0.18473(29)	0.2393(5)
C3	0.4447(5)	-0.14020(25)	0.4000(5)
C2	0.5359(6)	-0.16074(26)	0.6456(5)
C1	0.7439(5)	-0.09074(24)	0.6968(5)
N	0.3532(32)	-0.13733(20)	0.8164(4)
D1	0.2998(6)	-0.05648(27)	0.8073(6)

```
D2        0.2234(5)        -0.19228(29)           0.7928(6)
D3        0.4168(5)        -0.14975(32)           0.9840(5)
D4        0.5745(6)        -0.24814(28)           0.6631(6)
D6        0.8093(7)        -0.10822(33)           0.8727(6)
D7        0.8724(7)        -0.10453(34)           0.5711(6)
D5        0.6939(6)        -0.00419(31)           0.6915(7)


      15456_10K_D2B

O1        0.2704(6)        -0.08275(29)           0.3750(6)
O2        0.5605(6)        -0.18483(29)           0.2394(5)
C3        0.4445(5)        -0.14017(25)           0.3995(5)
C2        0.5369(6)        -0.16069(25)           0.6460(5)
C1        0.7441(5)        -0.09078(24)           0.6963(5)
N         0.35296(32)      -0.13733(20)           0.8163(4)
D1        0.2997(6)        -0.05655(27)           0.8066(7)
D2        0.2230(5)        -0.19222(28)           0.7926(6)
D3        0.4172(5)        -0.14967(32)           0.9834(5)
D4        0.5749(6)        -0.24813(28)           0.6637(6)
D6        0.8095(7)        -0.10835(33)           0.8727(6)
D7        0.8722(7)        -0.10452(34)           0.5711(6)
D5        0.6939(6)        -0.00419(30)           0.6914(7)


      15452_4K_D2B

O1        0.2697(8)        -0.0823(4)          0.3740(8)
O2        0.5589(8)        -0.1834(4)          0.2382(7)
C3        0.4435(7)        -0.13785(33)           0.3994(6)
C2        0.5386(8)        -0.16093(34)           0.6449(6)
C1        0.7446(7)        -0.09075(32)           0.6952(7)
N         0.3522(4)        -0.13745(28)           0.8167(5)
D1        0.2961(8)        -0.0572(4)          0.8050(8)
D2        0.2251(7)        -0.1916(4)          0.7913(7)
D3        0.4156(7)        -0.1516(4)          0.9838(7)
D4        0.5734(9)        -0.2479(4)          0.6605(8)
D6        0.8060(9)        -0.1067(5)          0.8726(8)
D7        0.8712(9)        -0.1050(4)          0.5726(8)
D5        0.6900(9)        -0.0050(4)          0.6900(9)
```

L-Alanine-d7
Space group P 21 21 21
The lattice is acentric   primitive orthorhombic Laue symmetry mmm
Multiplicity of a general site is   4

 The equivalent positions are:

 (1)   X   Y   Z (2) 1/2+X 1/2-Y   -Z
 (3)   -X 1/2+Y 1/2-Z (4) 1/2-X   -Y 1/2+Z

  Lattice constants at 270 K are   6.02156 12.35167   5.79806 0.00000 0.00000
0.00000
  Standard deviations   0.00014   0.00027   0.00012 0.00000 0.00000 0.00000

      15444_270K_D2B

  O1   0.7278(7)   0.08475(33)   0.6268(8)
  O2   0.4498(7)   0.1850(4)   0.7594(7)
  C3   0.5606(7)   0.14466(32)   0.6017(6)
  C4   0.4738(7)   0.16441(31)   0.3534(7)
  C5   0.2732(6)   0.08951(30)   0.3023(7)
  N6   0.6555(4)   0.13634(24)   0.1845(5)
  D7   0.7039(8)   0.05812(33)   0.2008(9)
  D8   0.7821(7)   0.1897(4)   0.2074(7)
  D9   0.5989(7)   0.1487(4)   0.0173(7)
  D10   0.4347(7)   0.24766(33)   0.3407(8)
  D11   0.2081(9)   0.1120(4)   0.1307(9)
  D12   0.1469(9)   0.1048(5)   0.4187(10)
  D13   0.3212(9)   0.0049(4)   0.3025(10)

      15440_260K_D2B

  O1   0.7268(7)   0.08473(33)   0.6269(7)
  O2   0.4491(7)   0.1847(4)   0.7589(7)
  C3   0.5613(7)   0.14450(31)   0.6022(6)
  C4   0.4732(7)   0.16456(30)   0.3546(7)
  C5   0.2737(6)   0.08950(30)   0.3024(7)

```
N6        0.6551(4)      0.13656(24)     0.1847(5)
D7        0.7040(8)      0.05827(33)     0.2002(8)
D8        0.7822(6)      0.1899(4)       0.2087(7)
D9        0.5988(7)      0.1489(4)       0.0176(7)
D10       0.4335(7)      0.24778(33)     0.3404(8)
D11       0.2073(9)      0.1114(4)       0.1314(9)
D12       0.1462(9)      0.1046(5)       0.4185(9)
D13       0.3195(8)      0.0050(4)       0.3036(10)


      15436_250K_D2B

O1        0.7269(7)      0.08436(32)     0.6264(7)
O2        0.4483(7)      0.1849(4)       0.7590(7)
C3        0.5610(7)      0.14439(31)     0.6016(6)
C4        0.4730(7)      0.16450(30)     0.3546(6)
C5        0.2726(6)      0.09012(30)     0.3030(7)
N6        0.6550(4)      0.13675(23)     0.1846(5)
D7        0.7033(8)      0.05798(33)     0.2003(8)
D8        0.7822(6)      0.1898(4)       0.2087(7)
D9        0.5977(7)      0.1491(4)       0.0171(7)
D10       0.4327(7)      0.24760(32)     0.3399(8)
D11       0.2059(9)      0.1113(4)       0.1309(9)
D12       0.1455(9)      0.1047(5)       0.4187(9)
D13       0.3177(8)      0.0052(4)       0.3041(10)


      15432_240K_D2B

O1        0.7275(6)      0.08435(31)     0.6265(7)
O2        0.4496(7)      0.1847(4)       0.7589(7)
C3        0.5614(6)      0.14422(30)     0.6011(6)
C4        0.4721(6)      0.16414(29)     0.3547(6)
C5        0.2726(6)      0.09012(29)     0.3028(7)
N6        0.6551(4)      0.13652(23)     0.1843(4)
D7        0.7028(7)      0.05801(31)     0.1999(8)
D8        0.7816(6)      0.19073(34)     0.2100(7)
D9        0.5973(6)      0.1489(4)       0.0174(7)
D10       0.4325(7)      0.24754(31)     0.3402(7)
D11       0.2054(8)      0.1113(4)       0.1309(8)
D12       0.1447(8)      0.1043(4)       0.4203(9)
D13       0.3181(8)      0.0048(4)       0.3044(9)


      15428_230K_D2B

O1        0.7282(6)      0.08457(30)     0.6254(7)
O2        0.4495(7)      0.18500(34)     0.7587(6)
C3        0.5611(6)      0.14353(29)     0.6010(6)
C4        0.4708(6)      0.16428(28)     0.3539(6)
C5        0.2712(6)      0.08999(28)     0.3039(6)
N6        0.6549(4)      0.13671(22)     0.1840(4)
D7        0.7036(7)      0.05760(30)     0.1991(8)
D8        0.7811(6)      0.19038(33)     0.2103(7)
D9        0.5958(6)      0.1489(4)       0.0173(6)
D10       0.4319(7)      0.24762(30)     0.3400(7)
D11       0.2046(8)      0.1107(4)       0.1316(8)
D12       0.1430(8)      0.1043(4)       0.4208(9)
D13       0.3180(8)      0.0049(4)       0.3045(9)


      15424_220K_D2B

O1        0.7280(6)      0.08420(30)     0.6249(7)
```

O2	0.4489(7)	0.18557(34)	0.7594(6)
C3	0.5613(6)	0.14367(29)	0.6013(6)
C4	0.4703(6)	0.16374(29)	0.3541(6)
C5	0.2709(6)	0.09035(28)	0.3037(7)
N6	0.6547(4)	0.13643(22)	0.1843(4)
D7	0.7026(7)	0.05728(31)	0.1995(8)
D8	0.7803(6)	0.19050(33)	0.2091(7)
D9	0.5941(6)	0.1490(4)	0.0172(7)
D10	0.4314(7)	0.24810(31)	0.3397(7)
D11	0.2038(8)	0.1106(4)	0.1317(8)
D12	0.1431(8)	0.1044(4)	0.4208(9)
D13	0.3167(8)	0.0050(4)	0.3065(9)

15420_210K_D2B

O1	0.7284(6)	0.08455(30)	0.6236(7)
O2	0.4492(7)	0.18539(33)	0.7597(6)
C3	0.5619(6)	0.14381(28)	0.6009(6)
C4	0.4704(6)	0.16387(28)	0.3535(6)
C5	0.2693(6)	0.09026(27)	0.3038(6)
N6	0.6542(4)	0.13633(22)	0.1830(4)
D7	0.7027(7)	0.05681(30)	0.1992(8)
D8	0.7799(6)	0.19064(32)	0.2101(7)
D9	0.5933(6)	0.1489(4)	0.0170(6)
D10	0.4323(7)	0.24821(30)	0.3398(7)
D11	0.2035(8)	0.1107(4)	0.1317(8)
D12	0.1416(8)	0.1050(4)	0.4215(8)
D13	0.3165(8)	0.00523(35)	0.3059(9)

15416_200K_D2B

O1	0.7279(6)	0.08433(29)	0.6235(7)
O2	0.4483(6)	0.18539(33)	0.7600(6)
C3	0.5617(6)	0.14346(28)	0.6009(6)
C4	0.4699(6)	0.16374(28)	0.3529(6)
C5	0.2684(6)	0.09057(27)	0.3041(6)
N6	0.6540(4)	0.13637(22)	0.1829(4)
D7	0.7020(7)	0.05670(29)	0.1994(8)
D8	0.7793(6)	0.19073(32)	0.2096(7)
D9	0.5927(6)	0.1490(4)	0.0164(6)
D10	0.4321(7)	0.24795(30)	0.3404(7)
D11	0.2024(8)	0.1102(4)	0.1316(8)
D12	0.1410(8)	0.1043(4)	0.4217(8)
D13	0.3154(8)	0.00539(35)	0.3071(9)

15412_190K_D2B

O1	0.7284(6)	0.08421(28)	0.6232(6)
O2	0.4479(6)	0.18527(31)	0.7598(6)
C3	0.5612(6)	0.14333(26)	0.6010(5)
C4	0.4696(6)	0.16377(27)	0.3535(6)
C5	0.2678(5)	0.09084(26)	0.3049(6)
N6	0.65316(34)	0.13652(21)	0.1832(4)
D7	0.7023(7)	0.05651(28)	0.1994(7)
D8	0.7794(5)	0.19046(30)	0.2095(6)
D9	0.5920(6)	0.14904(35)	0.0175(6)
D10	0.4316(7)	0.24828(29)	0.3406(7)
D11	0.2017(7)	0.1100(4)	0.1317(7)
D12	0.1393(7)	0.1047(4)	0.4225(8)
D13	0.3142(7)	0.00560(33)	0.3074(8)

```
15408_180K_D2B

O1      0.7282(6)     0.08404(28)   0.6228(6)
O2      0.4464(6)     0.18506(31)   0.7601(6)
C3      0.5610(6)     0.14299(26)   0.6008(5)
C4      0.4699(6)     0.16380(26)   0.3536(5)
C5      0.2672(5)     0.09073(26)   0.3044(6)
N6      0.65277(33)   0.13632(21)   0.1825(4)
D7      0.7029(6)     0.05615(27)   0.1992(7)
D8      0.7792(5)     0.19055(29)   0.2091(6)
D9      0.5913(6)     0.14919(34)   0.0165(6)
D10     0.4320(7)     0.24799(29)   0.3399(7)
D11     0.2016(7)     0.1098(4)     0.1311(7)
D12     0.1395(7)     0.1047(4)     0.4231(8)
D13     0.3130(7)     0.00598(32)   0.3085(8)


15404_170K_D2B

O1      0.7278(5)     0.08382(27)   0.6227(6)
O2      0.4466(6)     0.18523(30)   0.7597(6)
C3      0.5609(5)     0.14236(25)   0.6004(5)
C4      0.4696(5)     0.16345(26)   0.3542(5)
C5      0.2664(5)     0.09076(25)   0.3050(6)
N6      0.65239(32)   0.13651(20)   0.1825(4)
D7      0.7034(6)     0.05634(26)   0.1992(7)
D8      0.7796(5)     0.19022(29)   0.2093(6)
D9      0.5905(6)     0.14919(33)   0.0170(6)
D10     0.4312(6)     0.24796(28)   0.3403(6)
D11     0.2006(7)     0.10952(35)   0.1309(7)
D12     0.1386(7)     0.1047(4)     0.4227(7)
D13     0.3121(7)     0.00592(31)   0.3090(8)



15400_165K_D2B

O1      0.7275(5)     0.08390(27)   0.6227(6)
O2      0.4461(6)     0.18487(30)   0.7596(6)
C3      0.5605(5)     0.14275(25)   0.6008(5)
C4      0.4695(5)     0.16337(26)   0.3537(5)
C5      0.2661(5)     0.09092(25)   0.3044(6)
N6      0.65217(32)   0.13639(20)   0.1823(4)
D7      0.7023(6)     0.05599(26)   0.1990(7)
D8      0.7789(5)     0.19042(29)   0.2089(6)
D9      0.5908(6)     0.14934(33)   0.0164(6)
D10     0.4307(6)     0.24825(28)   0.3402(7)
D11     0.1992(7)     0.10938(35)   0.1312(7)
D12     0.1381(7)     0.1051(4)     0.4229(7)
D13     0.3127(7)     0.00559(31)   0.3081(8)


15396_160K_D2B

O1      0.7287(5)     0.08392(26)   0.6228(6)
O2      0.4460(6)     0.18505(29)   0.7598(5)
C3      0.5607(5)     0.14232(25)   0.6004(5)
C4      0.4688(5)     0.16330(25)   0.3538(5)
C5      0.2654(5)     0.09073(24)   0.3050(6)
N6      0.65197(32)   0.13633(20)   0.1824(4)
D7      0.7023(6)     0.05572(26)   0.1995(7)
D8      0.7792(5)     0.19054(28)   0.2093(6)
D9      0.5901(5)     0.14912(32)   0.0171(6)
D10     0.4309(6)     0.24834(28)   0.3398(6)
D11     0.1990(7)     0.10949(34)   0.1308(7)
```

```
D12      0.1379(7)      0.10450(34)     0.4228(7)
D13      0.3124(7)      0.00553(30)     0.3088(8)

    15392_150K_D2B

O1       0.7283(5)      0.08380(26)     0.6226(6)
O2       0.4450(6)      0.18462(29)     0.7599(5)
C3       0.5602(5)      0.14241(25)     0.6010(5)
C4       0.4688(5)      0.16328(25)     0.3534(5)
C5       0.2650(5)      0.09105(24)     0.3048(6)
N6       0.65160(32)    0.13628(20)     0.1827(4)
D7       0.7029(6)      0.05552(25)     0.1986(7)
D8       0.7784(5)      0.19072(27)     0.2089(6)
D9       0.5894(5)      0.14933(31)     0.0170(6)
D10      0.4303(6)      0.24831(28)     0.3399(6)
D11      0.1984(7)      0.10937(34)     0.1315(7)
D12      0.1368(7)      0.10488(34)     0.4238(7)
D13      0.3110(7)      0.00535(30)     0.3089(8)

    15388_140K_D2B

O1       0.7285(5)      0.08379(25)     0.6224(6)
O2       0.4448(6)      0.18461(28)     0.7601(5)
C3       0.5601(5)      0.14211(24)     0.6009(5)
C4       0.4682(5)      0.16291(24)     0.3530(5)
C5       0.2640(5)      0.09079(23)     0.3045(5)
N6       0.65107(30)    0.13626(19)     0.1823(4)
D7       0.7024(6)      0.05529(24)     0.1989(6)
D8       0.7780(5)      0.19118(26)     0.2091(6)
D9       0.5885(5)      0.14928(30)     0.0169(5)
D10      0.4299(6)      0.24826(26)     0.3409(6)
D11      0.1982(6)      0.10903(32)     0.1310(6)
D12      0.1360(6)      0.10492(32)     0.4242(7)
D13      0.3100(6)      0.00508(29)     0.3077(7)

    15384_130K_D2B

O1       0.7283(5)      0.08351(26)     0.6225(6)
O2       0.4440(6)      0.18500(28)     0.7600(5)
C3       0.5592(5)      0.14210(24)     0.6008(5)
C4       0.4677(5)      0.16293(24)     0.3530(5)
C5       0.2632(5)      0.09115(24)     0.3049(5)
N6       0.65071(31)    0.13630(19)     0.1827(4)
D7       0.7015(6)      0.05537(25)     0.1991(7)
D8       0.7779(5)      0.19131(27)     0.2089(6)
D9       0.5879(5)      0.14938(31)     0.0171(6)
D10      0.4291(6)      0.24854(27)     0.3396(6)
D11      0.1976(6)      0.10912(33)     0.1312(6)
D12      0.1347(7)      0.10532(33)     0.4248(7)
D13      0.3100(6)      0.00488(29)     0.3087(7)

    15380_120K_D2B

O1       0.7286(5)      0.08322(25)     0.6233(6)
O2       0.4435(5)      0.18452(27)     0.7593(5)
C3       0.5585(5)      0.14176(24)     0.6005(5)
C4       0.4673(5)      0.16245(24)     0.3532(5)
C5       0.2629(5)      0.09101(23)     0.3044(5)
N6       0.65007(30)    0.13653(19)     0.1827(4)
D7       0.7019(6)      0.05547(24)     0.1988(6)
D8       0.7779(5)      0.19139(26)     0.2089(6)
D9       0.5878(5)      0.14930(30)     0.0171(5)
D10      0.4287(6)      0.24830(27)     0.3392(6)
D11      0.1961(6)      0.10886(32)     0.1312(6)
```

D12	0.1336(6)	0.10534(32)	0.4254(7)
D13	0.3088(6)	0.00483(29)	0.3085(7)

15376_110K_D2B

O1	0.7284(5)	0.08328(25)	0.6233(6)
O2	0.4427(6)	0.18491(28)	0.7595(5)
C3	0.5583(5)	0.14161(24)	0.6007(5)
C4	0.4670(5)	0.16246(24)	0.3534(5)
C5	0.2621(5)	0.09116(23)	0.3053(5)
N6	0.64978(31)	0.13640(19)	0.1823(4)
D7	0.7017(6)	0.05525(25)	0.1996(6)
D8	0.7779(5)	0.19135(27)	0.2082(6)
D9	0.5873(5)	0.14936(30)	0.0166(5)
D10	0.4282(6)	0.24855(27)	0.3395(6)
D11	0.1952(6)	0.10882(32)	0.1321(6)
D12	0.1328(7)	0.10534(32)	0.4263(7)
D13	0.3085(6)	0.00470(29)	0.3081(7)

15372_105K_D2B

O1	0.7284(5)	0.08335(25)	0.6231(6)
O2	0.4428(6)	0.18511(28)	0.7594(5)
C3	0.5578(5)	0.14165(24)	0.6007(5)
C4	0.4669(5)	0.16225(24)	0.3533(5)
C5	0.2615(5)	0.09113(23)	0.3054(5)
N6	0.64975(31)	0.13644(19)	0.1822(4)
D7	0.7017(6)	0.05520(25)	0.1987(6)
D8	0.7776(5)	0.19139(26)	0.2081(6)
D9	0.5871(5)	0.14909(30)	0.0170(5)
D10	0.4280(6)	0.24874(28)	0.3392(6)
D11	0.1949(6)	0.10879(32)	0.1323(6)
D12	0.1326(7)	0.10571(32)	0.4261(7)
D13	0.3082(6)	0.00479(29)	0.3080(7)

15368_100K_D2B

O1	0.7285(5)	0.08332(25)	0.6237(6)
O2	0.4417(5)	0.18503(27)	0.7600(5)
C3	0.5581(5)	0.14152(23)	0.6009(5)
C4	0.4665(5)	0.16239(23)	0.3534(5)
C5	0.2611(5)	0.09100(23)	0.3052(5)
N6	0.64937(30)	0.13654(19)	0.1823(4)
D7	0.7012(6)	0.05547(24)	0.1990(6)
D8	0.7778(5)	0.19149(26)	0.2083(6)
D9	0.5865(5)	0.14915(29)	0.0168(5)
D10	0.4283(6)	0.24853(27)	0.3389(6)
D11	0.1955(6)	0.10896(31)	0.1318(6)
D12	0.1326(6)	0.10578(31)	0.4266(6)
D13	0.3085(6)	0.00437(28)	0.3084(7)

15364_90K_D2B

O1	0.7282(5)	0.08345(25)	0.6236(6)
O2	0.4418(5)	0.18494(27)	0.7598(5)
C3	0.5568(5)	0.14150(24)	0.6010(5)
C4	0.4661(5)	0.16207(24)	0.3539(5)
C5	0.2607(5)	0.09105(23)	0.3053(5)
N6	0.64930(30)	0.13634(19)	0.1828(4)
D7	0.7014(6)	0.05546(25)	0.1980(6)
D8	0.7774(5)	0.19158(27)	0.2079(6)
D9	0.5864(5)	0.14932(30)	0.0167(5)
D10	0.4279(6)	0.24866(28)	0.3386(6)
D11	0.1938(6)	0.10889(31)	0.1319(6)

```
D12      0.1316(6)      0.10521(32)      0.4266(6)
D13      0.3085(6)      0.00439(28)      0.3083(7)

    15360_80K_D2B

O1       0.7282(5)      0.08331(26)      0.6235(6)
O2       0.4414(6)      0.18492(28)      0.7602(5)
C3       0.5567(5)      0.14131(24)      0.6008(5)
C4       0.4653(5)      0.16202(24)      0.3540(5)
C5       0.2595(5)      0.09087(23)      0.3054(5)
N6       0.64884(31)    0.13647(19)      0.1826(4)
D7       0.7011(6)      0.05571(25)      0.1976(7)
D8       0.7770(5)      0.19166(27)      0.2084(6)
D9       0.5858(5)      0.14933(30)      0.0163(6)
D10      0.4272(6)      0.24850(29)      0.3383(6)
D11      0.1932(6)      0.10888(32)      0.1324(6)
D12      0.1315(7)      0.10526(33)      0.4272(6)
D13      0.3082(6)      0.00434(29)      0.3079(7)

    15356_70K_D2B

O1       0.7284(5)      0.08357(26)      0.6237(6)
O2       0.4417(6)      0.18478(28)      0.7596(5)
C3       0.5565(5)      0.14138(24)      0.6009(5)
C4       0.4647(5)      0.16190(24)      0.3543(5)
C5       0.2595(5)      0.09099(24)      0.3052(5)
N6       0.64910(31)    0.13640(19)      0.1828(4)
D7       0.7017(6)      0.05582(26)      0.1979(7)
D8       0.7775(5)      0.19152(28)      0.2083(6)
D9       0.5856(5)      0.14926(30)      0.0166(6)
D10      0.4271(6)      0.24848(29)      0.3382(6)
D11      0.1925(6)      0.10895(32)      0.1318(6)
D12      0.1316(7)      0.10511(33)      0.4269(6)
D13      0.3076(6)      0.00416(29)      0.3080(7)

    15352_65K_D2B

O1       0.7282(5)      0.08349(25)      0.6238(6)
O2       0.4418(5)      0.18518(27)      0.7601(5)
C3       0.5559(5)      0.14133(24)      0.6007(5)
C4       0.4649(5)      0.16167(23)      0.3544(5)
C5       0.2587(5)      0.09099(23)      0.3053(5)
N6       0.64859(30)    0.13655(19)      0.1825(4)
D7       0.7017(6)      0.05563(25)      0.1976(6)
D8       0.7776(5)      0.19150(27)      0.2081(6)
D9       0.5847(5)      0.14919(29)      0.0163(5)
D10      0.4261(6)      0.24850(28)      0.3379(6)
D11      0.1925(6)      0.10907(31)      0.1321(6)
D12      0.1310(6)      0.10514(32)      0.4278(6)
D13      0.3077(6)      0.00459(28)      0.3078(7)


    15348_60K_D2B

O1       0.7276(5)      0.08359(26)      0.6240(6)
O2       0.4414(5)      0.18477(27)      0.7597(5)
C3       0.5562(5)      0.14124(24)      0.6007(5)
C4       0.4650(5)      0.16200(24)      0.3544(5)
C5       0.2585(5)      0.09094(23)      0.3049(5)
N6       0.64832(30)    0.13648(19)      0.1830(4)
D7       0.7017(6)      0.05564(25)      0.1978(6)
D8       0.7768(5)      0.19151(27)      0.2086(6)
D9       0.5851(5)      0.14895(29)      0.0171(5)
D10      0.4270(6)      0.24840(28)      0.3381(6)
```

```
D11        0.1920(6)       0.10891(31)     0.1319(6)
D12        0.1306(6)       0.10529(32)     0.4278(6)
D13        0.3074(6)       0.00424(28)     0.3090(7)


     15344_50K_D2B

O1         0.7280(5)       0.08354(26)     0.6239(6)
O2         0.4415(5)       0.18484(27)     0.7599(5)
C3         0.5559(5)       0.14116(24)     0.6008(5)
C4         0.4640(5)       0.16185(23)     0.3547(5)
C5         0.2582(5)       0.09085(23)     0.3051(5)
N6         0.64827(30)     0.13666(19)     0.1827(4)
D7         0.7018(6)       0.05570(25)     0.1971(7)
D8         0.7774(5)       0.19151(27)     0.2086(6)
D9         0.5841(5)       0.14910(30)     0.0172(5)
D10        0.4266(6)       0.24833(28)     0.3379(6)
D11        0.1924(6)       0.10900(31)     0.1319(6)
D12        0.1303(7)       0.10510(32)     0.4275(6)
D13        0.3070(6)       0.00450(29)     0.3087(7)


     15340_40K_D2B

O1         0.7275(5)       0.08363(26)     0.6233(6)
O2         0.4413(6)       0.18493(27)     0.7597(5)
C3         0.5553(5)       0.14133(24)     0.6007(5)
C4         0.4641(5)       0.16172(24)     0.3547(5)
C5         0.2577(5)       0.09090(23)     0.3055(5)
N6         0.64799(31)     0.13671(19)     0.1829(4)
D7         0.7021(6)       0.05546(25)     0.1978(7)
D8         0.7772(5)       0.19158(28)     0.2087(6)
D9         0.5836(5)       0.14877(30)     0.0169(6)
D10        0.4263(6)       0.24838(28)     0.3372(6)
D11        0.1916(6)       0.10902(31)     0.1320(6)
D12        0.1301(7)       0.10504(32)     0.4280(6)
D13        0.3070(6)       0.00440(29)     0.3083(7)



     15336_30K_D2B

O1         0.7280(5)       0.08360(26)     0.6234(6)
O2         0.4410(5)       0.18451(27)     0.7600(5)
C3         0.5556(5)       0.14122(24)     0.6008(5)
C4         0.4638(5)       0.16164(24)     0.3546(5)
C5         0.2572(5)       0.09086(23)     0.3048(5)
N6         0.64806(30)     0.13657(19)     0.1825(4)
D7         0.7024(5)       0.05566(25)     0.1971(7)
D8         0.7769(5)       0.19182(27)     0.2086(6)
D9         0.5834(5)       0.14906(30)     0.0164(5)
D10        0.4266(6)       0.24818(28)     0.3377(6)
D11        0.1920(6)       0.10909(31)     0.1318(6)
D12        0.1303(7)       0.10500(32)     0.4284(6)
D13        0.3068(6)       0.00437(29)     0.3073(7)


     15332_20K_D2B

O1         0.7273(5)       0.08367(26)     0.6231(6)
O2         0.4411(5)       0.18463(27)     0.7602(5)
C3         0.5553(5)       0.14108(24)     0.6013(5)
C4         0.4633(5)       0.16181(24)     0.3546(5)
C5         0.2573(5)       0.09071(23)     0.3049(5)
N6         0.64776(30)     0.13663(19)     0.1822(4)
D7         0.7025(5)       0.05601(25)     0.1972(7)
D8         0.7773(5)       0.19159(28)     0.2089(6)
D9         0.5831(5)       0.14871(30)     0.0162(5)
```

```
D10       0.4264(6)     0.24798(27)    0.3376(6)
D11       0.1916(6)     0.10909(31)    0.1317(6)
D12       0.1303(6)     0.10479(32)    0.4284(6)
D13       0.3066(6)     0.00430(29)    0.3073(7)

     15328_10K_D2B

O1        0.7269(5)     0.08376(26)    0.6234(6)
O2        0.4408(5)     0.18461(27)    0.7603(5)
C3        0.5553(5)     0.14115(24)    0.6010(5)
C4        0.4638(5)     0.16164(24)    0.3546(5)
C5        0.2567(5)     0.09100(23)    0.3050(5)
N6        0.64777(31)   0.13649(19)    0.1825(4)
D7        0.7032(5)     0.05554(25)    0.1969(7)
D8        0.7773(5)     0.19146(28)    0.2090(6)
D9        0.5837(5)     0.14883(30)    0.0168(5)
D10       0.4259(6)     0.24798(28)    0.3376(6)
D11       0.1909(6)     0.10895(31)    0.1322(6)
D12       0.1298(7)     0.10485(32)    0.4282(6)
D13       0.3067(6)     0.00463(29)    0.3081(7)

     15324_4K_D2B

O1        0.7273(5)     0.08410(26)    0.6228(6)
O2        0.4407(5)     0.18467(27)    0.7597(5)
C3        0.5556(5)     0.14140(24)    0.6008(5)
C4        0.4630(5)     0.16157(23)    0.3545(5)
C5        0.2576(5)     0.09065(23)    0.3042(5)
N6        0.64767(30)   0.13637(19)    0.1826(4)
D7        0.7026(5)     0.05599(25)    0.1967(7)
D8        0.7773(5)     0.19163(27)    0.2089(6)
D9        0.5832(5)     0.14862(30)    0.0162(5)
D10       0.4256(6)     0.24823(27)    0.3371(6)
D11       0.1911(6)     0.10900(30)    0.1327(6)
D12       0.1301(6)     0.10463(32)    0.4287(6)
D13       0.3063(6)     0.00433(28)    0.3074(7)
```

Paper 2

J. E. M. Pereira, Juergen Eckert, Svemir Rudić, Dehong Yu, Richard Mole, Nikolaos Tsapatsaris and Heloisa N. Bordallo. Hydrogen bond dynamics and conformational flexibility in antipsychotics.

Hydrogen bond dynamics and conformational flexibility in antipsychotics

José E. M. Pereira,*,[†] Juergen Eckert,[‡] Svemir Rudic,[¶] Dehong Yu,[§] Richard Mole,[§] Nikolaos Tsapatsaris[†,‖], and Heloisa N. Bordallo[†,‖].

[†]The Niels Bohr Institute, University of Copenhagen, DK-2100, Copenhagen, Denmark
[‡]Department of Chemistry, University of South Florida, Florida 33620, United States
[¶]ISIS Facility, STFC, Rutherford Appleton Laboratory, Chilton, Didcot OX11 0QX, United Kingdom

[§] Australian Center for Neutron Scattering, Australian Nuclear Science and Technology Organization, Lucas Heights, 2233 NSW, Australia
[‖] European Spallation Source ESS AB, PO Box 176, SE-221 00 Lund, Sweden

Abstract

The complex nature of disorders of the central nervous system and the related difficulties in clinical research creates many barriers for developing novel therapeutic approaches using different mechanisms. Effective treatment is generally obtained when using drugs of similar moiety when these are known to be effective. A better understanding of the way a drug functions could conceivably create new opportunities for the clinical development of treatments for neuropsychiatric disorders. We have therefore investigated three different antipsychotic drugs: haloperidol ($C_{21}H_{23}ClFNO_2$), aripiprazole ($C_{23}H_{27}Cl_2N_3O_2$) and quetiapine hemifumarate ($C_{21}H_{25}N_3O_2S \cdot 0.5C_4H_4O_4$) based on similarities in their structures and their function. Our aims are to explore any relationship between the crystalline stability and dynamics of these molecules and to add such information to molecular dynamics simulations, which currently only account for flexibility of the receptor. To this end, the assignment of selected vibrational modes observed in the inelastic neutron scattering data was supported by theoretical calculations provided by density functional theory. Crystal structures were verified by X-ray diffraction, while conformational transformations and the purity of the samples were determined from calorimetric studies.

Introduction

The market for antipsychotic drugs is one of the largest in the pharmaceutical industry, valued at USD 11.7 billion in 2015[1]. These drugs, however, have a wide range of undesirable side effects, which are related to their function and delivery method. Pharmaceutical companies appear to have withheld significant information on these types of drugs because of their commercial significance. In fact, even the X-ray data of the structures of the polymorphs are generally patented, and very few papers can be found in the open literature [2]. The same holds true for the characterization of their

vibrational spectra [3]. As it is apparent that there is a general lack of understanding of the conformational habit of these molecules, we have initiated an investigation of three different antipsychotics, Haloperidol (HAL), Aripiprazole (APZ) and Quetiapine hemifumarate (QTP), which crystalline structures are represented in Figure 1. They have been selected because they represent different generations of antipsychotics drugs, and because their function has been broadly discussed, and structural details reported in the literature [4–6].

HAL is a typical antipsychotic agent frequently used to treat schizophrenia, which works by blocking receptors for the chemical dopamine in the brain causing neuron apoptosis. APZ and QTP, on the other hand, are atypical antipsychotics which bind to several different neurotransmitter receptors[7,8]. From the clinical point of view there is no clear evidence that these atypical antipsychotics are more effective or are better tolerated than typical ones [9]. In any case, the function of HAL, APZ and QTP in clinical treatment is unknown as it is for all antipsychotics. It is believed that the effectiveness of APZ is mediated by a combination of partial agonist activity at D2 and 5-HT1A receptors and antagonist activity at 5-HT2A receptors[10], while in the case of the older, traditional antipsychotic HAL and the atypical QTP, binding is thought to occur mainly to the dopamine D2 receptor. The main difference is the strength of the binding that in turn changes the dissociation constant, which is lower than that of dopamine in HAL but higher in QTP[11]. This idea agrees with the fact that protein-ligand interactions are mainly based on docking and binding affinity in forming a protein-ligand complex, and some studies have shown that even weak binding to multiple targets may have a pronounced impact on biological systems[12]. Another important factor to take into account is the flexibility of the protein-ligand complex, which is a crucial aspect of protein structure and function[13].

The nonexistence of a predictive animal model for complex psychiatric disorders is a major hindrance to research progress. The use of computational quantum chemistry methods is therefore becoming increasingly widespread in drug design and development as a result of the relatively high accuracy of estimates of binding energies[14,15], additionally, recent publications of experimental and predicted crystal structures of some receptors have made it possible for molecular dynamics simulations to characterize binding properties of these specific receptors[16–18].

The combination of vibrational spectroscopy by inelastic neutron scattering (INS) and density functional theory (DFT) calculations offers a stringent test of the molecular structure, which we aim to test as a way to connect conformational flexibility to the manner in which these molecules function. To this end the crystal structures of the three antipsychotic molecules were first confirmed by X-rays powder diffraction (XRPD), while polymorphic transformations and purity were determined using differential scanning calorimetry (DSC) and thermogravimetric analysis coupled with

Fourier transform infrared spectroscopy (TGA-FTIR). Subsequently, information on the dynamics of the systems was obtained by INS and assignment of the vibrational modes derived from theoretical spectra provided by DFT calculations.

Experimental details

Antipsychotic samples. Powder samples of APZ ($C_{23}H_{27}Cl_2N_3O_2$) and QTP ($C_{21}H_{25}N_3O_2S \cdot 0.5C_4H_4O_4$) were purchased from CHEMOS GmbH, while HAL ($C_{21}H_{23}ClFNO_2$) was acquired from Sigma Aldrich. All samples were used without further purification. XRPD was performed using a Bruker D8 Advance diffractometer with Cu Kα radiation (1.5418 Å) in θ/θ geometry to confirm the purity as well as the polymorphic structure of each sample. Our results (Figure S1) show that the diffraction patterns for APZ and HAL agree with previous results from the Cambridge Crystallographic Data Centre (CCDC) files 690585, 150416, respectively. The data for QTP are consistent with those previously reported (file number 2206876 Crystallography Open Database).

Calorimetric studies. The purity of each sample was further checked by the thermogravimetric analysis instrument, PERSEUS TG 209 F1 Libra from NETZSCH coupled with a Fourier transform infrared spectrometer by BRUKER Optics Inc. (TGA-FTIR). Changes in the mass of the sample as a function of temperature observed by TGA gives insight in the sample decomposition, while the slope of the mass loss indicates how rapidly the decomposition occurs. The gases released during the heating process for each sample are characterized by the attached Fourier Transform Infrared Spectrometer to determine the nature of the decomposition products. When combined with differential scanning calorimetry (DSC) (NETZSCH DSC 214 *Polyma*) these measurements give a complete picture of thermal effects on the crystalline stability of these drugs.

Samples were placed in an alumina crucible for the TGA experiments and heated from room temperature (RT) to 300°C at a constant heating rate of 10°C/min. A stream of nitrogen flowing at 20 ml/min was used throughout the experiment. FTIR spectra of the evolved gases were recorded every 3 °C to facilitate the understanding of the decomposition process.

DSC data were collected on samples sealed in aluminum crucibles, placed in a nitrogen atmosphere purged at 40 ml/min. An empty crucible was used as reference material. The instrument was calibrated with indium as a standard. Heating rates between 2 and 15°C/min were used for all samples. HAL and APZ were measured between RT (25 °C) and 180 °C, while data for QTP were collected up to a temperature of 300 °C.

Inelastic neutron scattering (INS). The dynamics of polycrystalline antipsychotic compounds were studied by INS vibrational spectroscopy using the spectrometers

PELICAN[19] at the Australian Nuclear Science and Technology Organisation - ANSTO (Australia) and TOSCA[20] at the ISIS Neutron and Muon Source at the Rutherford Appleton Laboratory (United Kingdom). The INS data were compared and interpreted using simulated spectra obtained from DFT calculations described below.

PELICAN is a cold neutron time-of-flight spectrometer that gives access to vibrational motions in the antipsychotic molecules in the energy range $0 - 40$ meV. With an incident wavelength of 4.72 Å, corresponding to an incident energy of 3.61 meV, excitations are measured by energy gain of the neutron, or the energy loss of the sample, i.e. on the anti-Stokes side of the spectra.

The data were collected at temperatures of 60K, 100K, 150K, 200K, 250K and 300K and processed using the Large Array Manipulation Program (LAMP)[21] as follows. The spectra were first normalized to a vanadium standard, followed by subtraction of the spectrum of an empty sample holder to correct for background, and finally, the spectra were converted to the incoherent dynamic structure factor, S(Q, ω), where Q is the magnitude of the scattering wave vector and ω is the energy transfer. This scattering function is dominated by vibrational motions of the hydrogen atoms and it can be correlated to the generalized density of state (GDOS) and in turn to the thermal populations of the excitations. S(Q, ω), is also correlated the generalized density of state GDOS, $G(\hat{\theta}, \omega)$, thus, the information contained in S(Q, ω) was converted as follows:

$$G(\hat{\theta}, \omega) = \frac{S(\hat{\theta}, \omega)}{Q^2(\hat{\theta}, \omega)} B(\omega, T), \qquad (1.2)$$

where $\hat{\theta}$ refers to the averaged scattering angle and $S(\hat{\theta}, \omega)$ is the scattering vector, which is calculated at each energy transfer for the averaged scattering angle as:

$$S(\hat{\theta}, \omega) = \frac{1}{N_D} \sum_i S_i(\theta_i, \omega), \qquad (1.2)$$

obtained by summing the signal from the first to the last detector considered, with θ_i being the angle corresponding to each detector. N_D is the total number of detectors.

$$B(\omega, T) = \hbar\omega(1 - e^{-\hbar\omega/kT}), \qquad (1.3)$$

is a function accounting for the population of the vibrational modes with temperature, T [22]. The temperature dependence of the GDOS will give rise to broadening in the harmonic motions of the molecular groups in HAL, APZ and QTP.

TOSCA is an inverse geometry time-of-flight spectrometer with a fixed final energy of the neutrons for observing vibrational spectra in neutron energy loss, or energy gain of the sample, i.e. the Stokes side of the spectra. The instrument covers the entire

frequency range for molecular vibrations. INS spectra for all samples were recorded at 10 K and converted to the scattering law, $S(Q, \omega)$ using standard programs.

DFT computational details. *Ab initio* calculations on the gas-phase molecules were carried out using the published atomic coordinates from the crystal structures of the antipsychotic molecules[23–25]. The INS spectra were generated with periodic calculations on crystalline antipsychotics using the Vienna *Ab initio* Simulation Package (VASP) with the Perdew–Burke–Ernzerhof (PBE) functional along with Vanderbilt ultrasoft pseudopotentials[26] with a plane wave kinetic energy cutoff of 450 meV. Additional periodic calculations were carried with a 4 x 4 x 4 Monkhorst-Pack mesh of k-points[27] to improve agreement at lower frequencies. The atomic coordinates were optimized with the unit cell fixed at the experimental values, followed by harmonic frequency calculations. The resulting vibrational amplitudes and frequencies were used to derive a simulated INS spectrum with the aCLIMAX software[28]

Results and discussion (in progress)

Calorimetric studies. DSC and TGA results for HAL, APZ and QTP are shown in Figures 2a, 2c and 2e. Clear and sharp endothermic events related to the melting points at 155, 150 and 178 °C, respectively, are observed in the DSC. Weak endothermic events between 120 and 140 °C for APZ are related to the loss of hydration water and evidently correlate with the weak mass loss observed in the TGA curve below 90 °C, indicated by the black arrow in Figure 2c.

Gases evolved during the decomposition steps, which indicated by arrows in the TGA curves, give rise to absorption peaks in the infrared spectra (Figures 2b, 2d and 2f). For example, the strong bands observed between 1450 and 1600 cm^{-1}, and between 2700 and 3100 cm^{-1} may be assigned to modes from the aromatic rings and a mix of C – H and C – N vibrations from groups which are present in these samples.

A second endothermic transition in QTP at about 235 °C is the result of a degradation of the hemifumarate salt ($C_4H_2O_4$). This is confirmed by the observation of the strong CO_2 vibration at 2300 cm^{-1} in the infrared spectra at 255 °C (Figure 2f).

Additional detailed DSC measurements, using different heating rates, are presented in the supplementary information. From these data, conclude that after a series of heating processes HAL maintains its stable crystalline form, while APZ undergoes a polymorphic transformation from form III to form II [29] and QTP degrades. Our calorimetric data also agree with previous reports [30–32], and in conjunction with the XRPD results (see supplementary information) confirm the polymorphic form for each sample.

Vibrational spectra of HAL, APZ and QTP as function of temperature. The most fundamental difference between optical spectroscopy techniques, such as Raman scattering, and Infrared spectroscopy compared to INS, lies in the nature of the interaction between the probe and the sample. Whereas photons interact with the electron density, neutrons are scattered by the atomic nuclei, so that there are no symmetry-based selection rules for INS spectra. Moreover, neutrons have mass and consequently the scattering process also involves momentum transfer. Neutrons can be scattered with our without a change in their energy, i.e. inelastically, or elastically, and this process can be coherent or incoherent. The coherent part of the inelastic scattering gives information about collective lattice vibrations, typically at energies less than 40 meV, while internal molecular vibrations at higher frequency are mainly observed in incoherent inelastic scattering involving motions of H atoms. INS intensities of vibrational bands can be quite a sensitive test for validation of force fields in MD simulations, and of methodology used in DFT calculations[33].

Spectra collected on PELICAN (Figure 4) were found to be considerably broadened at higher temperatures as a result of the Debye–Waller factor, which is particularly noticeable in APZ between 200 and 300 K. Furthermore, the observed experimental intensities of some bands are found to increase strongly upon cooling in all the samples (Figures 3, 4 and 5), and as in some orientationally disordered crystals[34,35]. We note that the INS spectra collected using TOSCA at 10 K are quite well reproduced by the theoretical results above 20 meV, while the spectra at 100 K (cooling cycle on PELICAN) appear to correspond to the calculated results below 20 meV.

Comparisons of the experimental INS spectra for HAL, APZ and QTP with those calculated by DFT were intended to provide information about the flexibility of the molecular groups in each sample and to connect this flexibility to the stability of the crystalline structures. The assignment of the main vibrational bands in the INS was achieved by visualizing the molecular vibrations of the modes obtained by VASP using Jmol software [36]. Considering that the spectra have a relatively complex and structureless nature resulting from the low symmetry of this molecule, between 0 to 40 meV (0 to 322 cm^{-1}) interestingly the calculation does not seem to miss any observed feature. From the performed analyzes, we conclude that most of the intensity in this analyzed region is due to mixed external motions of the molecule in the lattice, making the disentanglement of the low-frequency modes very difficult. Thus, even if the agreement between calculated and experimental data is sufficiently good, only few vibrational features can be unambiguously assigned.

Taking in consideration only all the most intense modes obtained in the calculated spectra for each molecule, we observe that in HAL, the main mode at 8 meV can be described as displacements of the H in to rings, while some of the low frequencies modes result from deformations of the alkyl group connecting the hydrophobic and

hydrophilic heads. In the case of APZ, in the range analysed, the modes can be described as collective motions dominated by displacements of the piperazine and quinoline rings, while for QTP the main mode at 7, 16 and 20 meV can be described as deformation from the aromatic structure.

Conclusions (in progress)

Our results provide a new benchmark for the characterization of the dynamical behavior of the bioactive molecules HAL, APZ and QTP, antipsychotics from different generations (typical and atypical) which function in different ways.

Antipsychotics drugs, due their amphipathic and amphiphilic properties, present high affinity for bio membranes and cause structural reorganization in the lipid bilayer[37,38]. Our results, obtained using INS and DFT calculations, add a different aspect to the analysis process of binding affinity and docking between protein and ligand, as knowledge on the flexibility of these molecules can be used as input for new approaches in computational modeling. Thus, opening a perspective into the understanding in how drug flexibility affects the interaction process between the drug itself and the receptor as well as the drug's ability to bind to other molecules. All these factors will affect the drug function.
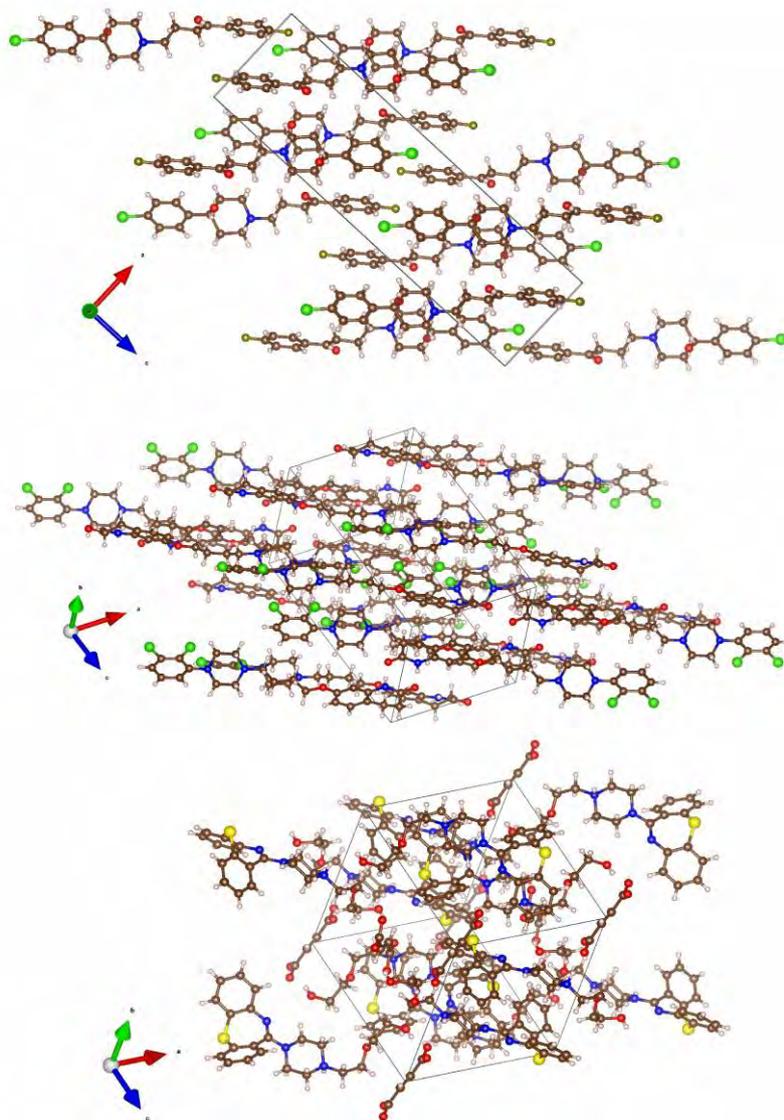
Figure 1 Crystal structure for HAL (C$_{21}$H$_{23}$ClFNO$_2$), APZ (C$_{23}$H$_{27}$Cl$_2$N$_3$O$_2$) and QTP (C$_{21}$H$_{25}$N$_3$O$_2$S · 0.5C$_4$H$_4$O$_4$).
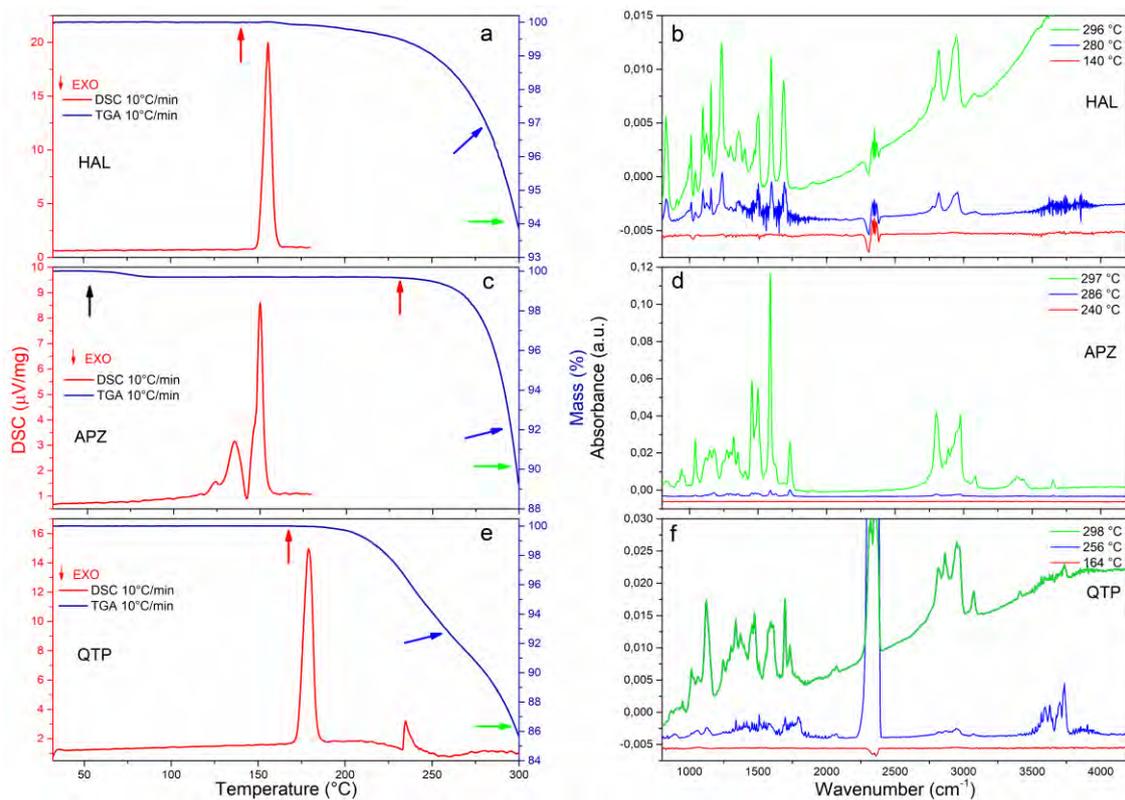
Figure 2 TGA-FTIR and DSC results. The left side of the figure shows the TGA and DSC curves while in the right side shows the FTIR collected during the heating process in the TGA. The arrows in the right side correspond the specific temperature present in the respective FTIR data. The black arrow in (b) indicates the dehydration process described in the text and associated to vibrational modes observed between 120 to 140 °C.
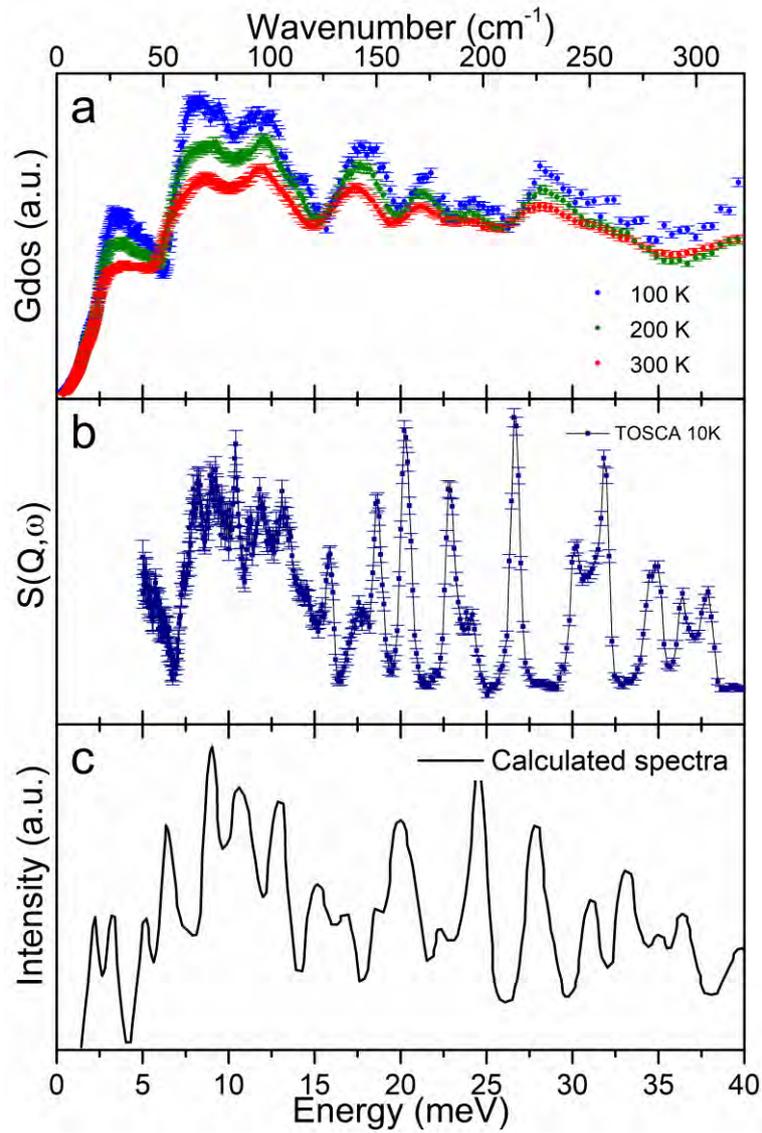
Figure 3 Experimental and calculated INS data for HAL ($C_{21}H_{23}ClFNO_2$), (a) Experimental INS data from spectrometer PELICAN collected at different temperatures, (b) Experimental INS data from spectrometer TOSCA obtained at 10 K and (c) Calculated INS using the VASP software.
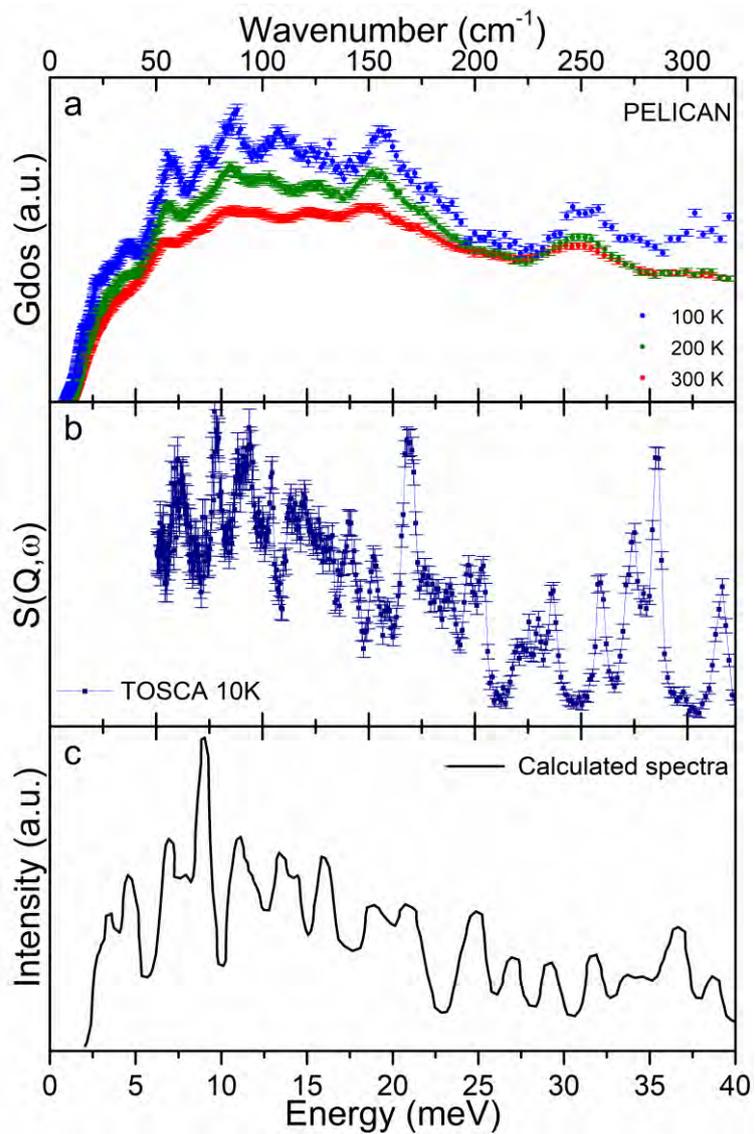
Figure 4 Experimental and calculated INS data for APZ ($C_{23}H_{27}Cl_2N_3O_2$) (a) Experimental INS data from spectrometer PELICAN collected at different temperatures, (b) Experimental INS data from spectrometer TOSCA obtained at 10 K and (c) Calculated INS using the VASP software.

Figure 5 Experimental and calculated INS data for QTP ($C_{21}H_{25}N_3O_2S \cdot 0.5C_4H_4O_4$) (a) Experimental INS data from spectrometer PELICAN collected at different temperatures, (b) Experimental INS data from spectrometer TOSCA obtained at 10 K and (c) Calculated INS using the VASP software.

References

1.   Antipsychotic Drugs Market Size & Share | Industry Report, 2014-2025. Available at: http://www.grandviewresearch.com/industry-analysis/antipsychotic-drugs-market. (Accessed: 20th November 2017)

2.   Robbins, B. D., Higgins, M., Fisher, M. & Over, K. Conflicts of interest in research on antipsychotic treatment of pediatric bipolar disorder, temper dysregulation disorder, and attenuated psychotic symptoms syndrome: Exploring the unholy alliance between big pharma and psychiatry. *J. Psychol. Issues Organ. Cult.* **1,** 32–49 (2011).

3.   Ayala, A. P. *et al.* Thermal stability of aripiprazole monohydrate investigated by Raman spectroscopy. *Vib. Spectrosc.* **54,** 169–173 (2010).

4.   Ravikumar, K. *et al.* Quetiapine hemifumarate. *Acta Crystallogr. Sect. E Struct. Reports Online* **61,** o3245–o3248 (2005).

5.   Nanubolu, J. B. *et al.* Sixth polymorph of aripiprazole - an antipsychotic drug. *CrystEngComm* **14,** 4677 (2012).

6.   Destri, G. L., Marrazzo, A., Rescifina, A. & Punzo, F. How molecular interactions affect crystal morphology: The case of haloperidol. *J. Pharm. Sci.* **100,** 4896–4906 (2011).

7.   Al Jurdi, K., Dixit, L. A. & Sajatovic, M. Neuropsychiatric Disease and Treatment role of extended release quetiapine in the management of bipolar disorders. *Neuropsychiatr. Dis. Treat.* **6,** 29–35 (2010).

8.   Bartolomeis, A. De, Tomasetti, C. & Iasevoli, F. Update on the Mechanism of Action of Aripiprazole : Translational Insights into Antipsychotic Strategies Beyond Dopamine Receptor Antagonism. *CNS Drugs* **29,** 773–799 (2015).

9.   Geddes, J., Freemantle, N. & Harrison, P. Atypical antipsychotics in the treatment of schizophrenia: systematic overview and meta-regression analysis.

10.   Mailman, R. B. & Murthy, V. Third generation antipsychotic drugs: partial agonism or receptor functional selectivity? *Curr. Pharm. Des.* **16,** 488–501

(2010).

11.   Seeman, P. Atypical antipsychotics: mechanism of action. *Can. J. Psychiatry.* **47,** 27–38 (2002).

12.   Xie, L., Evangelidis, T., Xie, L. & Bourne, P. E. Drug Discovery Using Chemical Systems Biology: Weak Inhibition of Multiple Kinases May Contribute to the Anti-Cancer Effect of Nelfinavir. *PLoS Comput Biol* **7,** (2011).

13.   Teodoro, M. L., Phillips, G. N. & Kavraki, L. E. Understanding Protein Flexibility through Dimensionality Reduction. *J. Comput. Biol.* **10,** 3–4 (2003).

14.   Selvam, B., Porter, S. L. & Tikhonova, I. G. Addressing Selective Polypharmacology of Antipsychotic Drugs Targeting the Bioaminergic Receptors through Receptor Dynamic Conformational Ensembles. *J. Chem. Inf. Model.* **53,** 1761–1774 (2013).

15.   Zanatta, G. *et al.* Antipsychotic Haloperidol Binding to the Human Dopamine D3 Receptor: Beyond Docking Through QM/MM Refinement Toward the Design of Improved Schizophrenia Medicines. *ACS Chem. Neurosci.* **5,** 1041–1054 (2014).

16.   Chien, E. Y. T. *et al.* Structure of the Human Dopamine D3 Receptor in Complex with a D2/D3 Selective Antagonist. *Science (80-.).* **330,** 1091–1095 (2010).

17.   Kalani, M. Y. S. *et al.* The predicted 3D structure of the human D2 dopamine receptor and the binding site and binding affinities for agonists and antagonists. *Proc. Natl. Acad. Sci.* **101,** 3815–3820 (2004).

18.   McCorvy, J. D. & Roth, B. L. Structure and function of serotonin G protein-coupled receptors. *Pharmacol. Ther.* **150,** 129–42 (2015).

19.   Yu, D., Mole, R., Noakes, T., Kennedy, S. & Robinson, R. Pelican – a Time of Flight Cold Neutron Polarization Analysis Spectrometer at OPAL. *J. Phys. Soc. Jpn* **82,** (2012).

20.   Colognesi, D. *et al.* TOSCA neutron spectrometer: The final configuration. *Appl. Phys. A Mater. Sci. Process.* **74,** s64–s66 (2002).

21.   Richard, D., Ferrand, M. & Kearley, G. J. Analysis and visualisation of neutron-scattering data. *J. Neutron Res.* **4,** 33–39 (1996).

22.   Rols, S., Jobic, H. & Schober, H. Monitoring molecular motion in nano-porous solids. *Comptes Rendus Phys.* **8,** 777–788 (2007).

23.   Braun, D. E. *et al.* Conformational polymorphism in aripiprazole: Preparation, stability and structure of five modifications. *J. Pharm. Sci.* **98,** 2010–2026 (2009).

24.   Ravikumar, K. & Sridhar, B. Quetiapine hemifumarate. *Acta Crystallogr. Sect. E Struct. Reports Online* **61,** o3245–o3248 (2005).

25.   Prasanna, M. D. & Row, T. N. G. Weak interactions involving organic fluorine: analysis of structural motifs in Flunazirine and Haloperidol. *J. Mol. Struct.* **562,**

55–61 (2001).

26. Perdew, J. P., Burke, K. & Ernzerhof, M. Generalized Gradient Approximation Made Simple. *Phys. Rev. Lett.* **77,** 3865–3868 (1996).

27. Monkhorst, H. J. & Pack, J. D. Special points for Brillouin-zone integrations. *Phys. Rev. B* **13,** 5188–5192 (1976).

28. Ramirez-Cuesta, A. J. aCLIMAX 4.0.1, the new version of the software for analyzing and interpreting INS spectra. *Comput. Phys. Commun.* **157,** 226–238 (2004).

29. Braun, D. E. *et al.* Conformational polymorphism in aripiprazole: Preparation, stability and structure of five modifications. *J. Pharm. Sci.* **98,** 2010–2026 (2009).

30. Dolitzky, B., Kovalevski-Ishai, E., Wizel, S. & Lidor-Hadas, R. Crystalline forms of quetiapine hemifumarate. **1,** (2003).

31. Braun, D. E. *et al.* Aripiprazole. *J. Pharm. Sci.* **6,** 35–85 (2013).

32. Épshtein, N. a. Test of the pharmaceutical compatibility of drug substances and pharmaceutical ingredients in drug dosage forms of a specified composition under development. *Pharm. Chem. J.* **29,** 211–213 (1995).

33. Kearley, G. J. The application of normal coordinate analysis to INS spectra. *Spectrochim. Acta Part A Mol. Spectrosc.* **48,** 349–362 (1992).

34. Bordallo, H. N. *et al.* Application of Incoherent Inelastic Neutron Scattering in Pharmaceutical Analysis: Relaxation Dynamics in Phenacetin. doi:10.1021/mp2006032

35. Plazanet, M., Geis, A., Johnson, M. R. & Trommsdorff, H. P. Tunneling systems in molecular crystals: studies by optical spectroscopy and neutron scattering. *J. Lumin.* **98,** 197–205 (2002).

36. Jmol: an open-source Java viewer for chemical structures in 3D. http://www.jmol.org/.

37. Tessier, C., Nuss, P., Staneva, G. & Wolf, C. Modification of membrane heterogeneity by antipsychotic drugs: An X-ray diffraction comparative study. *J. Colloid Interface Sci.* **320,** 469–475 (2008).

38. Alves, I., Staneva, G., Tessier, C., Salgado, G. F. & Nuss, P. The interaction of antipsychotic drugs with lipids and subsequent lipid reorganization investigated using biophysical methods. *Biochim. Biophys. Acta - Biomembr.* **1808,** 2009–2018 (2011).

Supporting information

The XRPD pattern collected are shown in the figure S1. DSC measurements using different heating rates for HAL, APZ and QTP are presented in figure S2. However, with the objective to confirm the structure stability for each sample when submitted to a cyclic process, heating and cooling in cycles, using the same sample in order to verify the stability of the structure our findings show that HAL, figure S3, presents a reversible process upon to thermal effects, while APZ changes the structure form a polymorphic form. See figure S4. QTP was submitted at the same process, however, due the degradation of the hemifumarate salt, the sample change for a amorphous form after the first heating process.
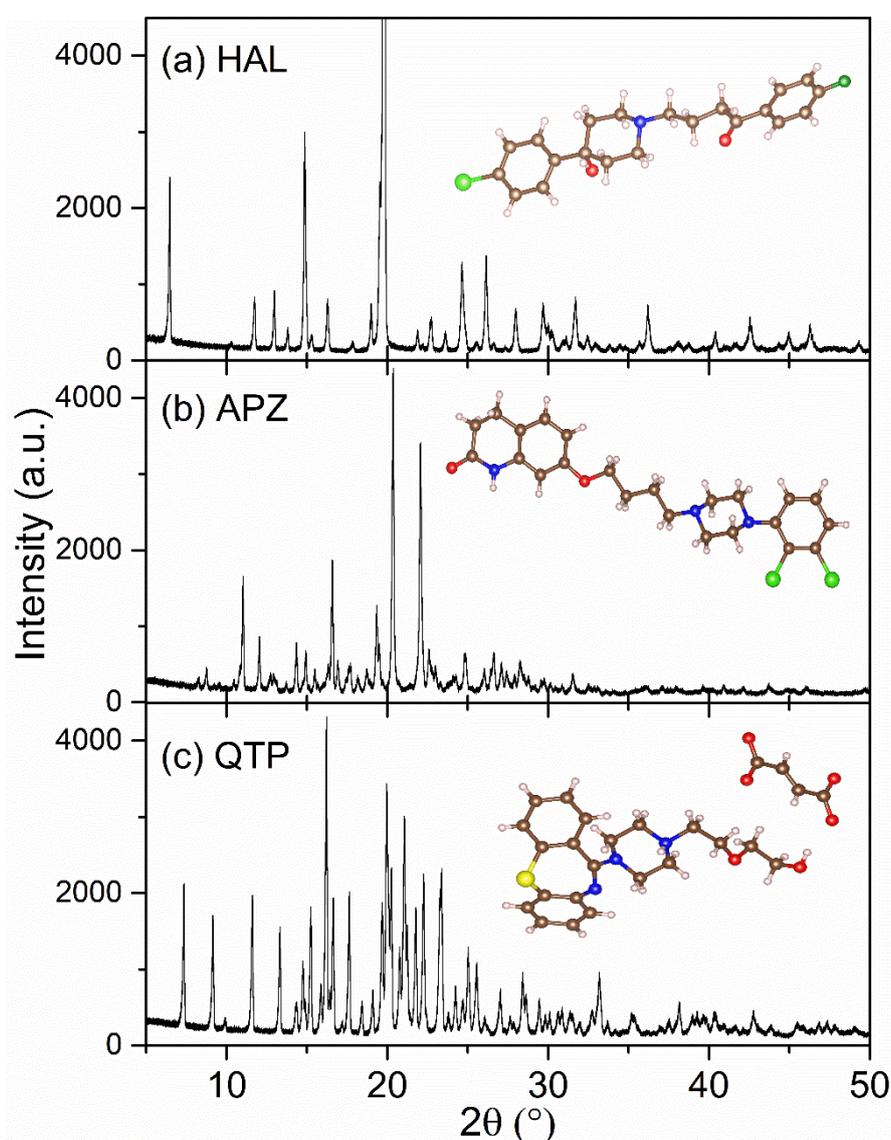
Figure S1 XRPD pattern (a) HAL, (b)APZ and (c) QTP using λ=1,5418 Å.
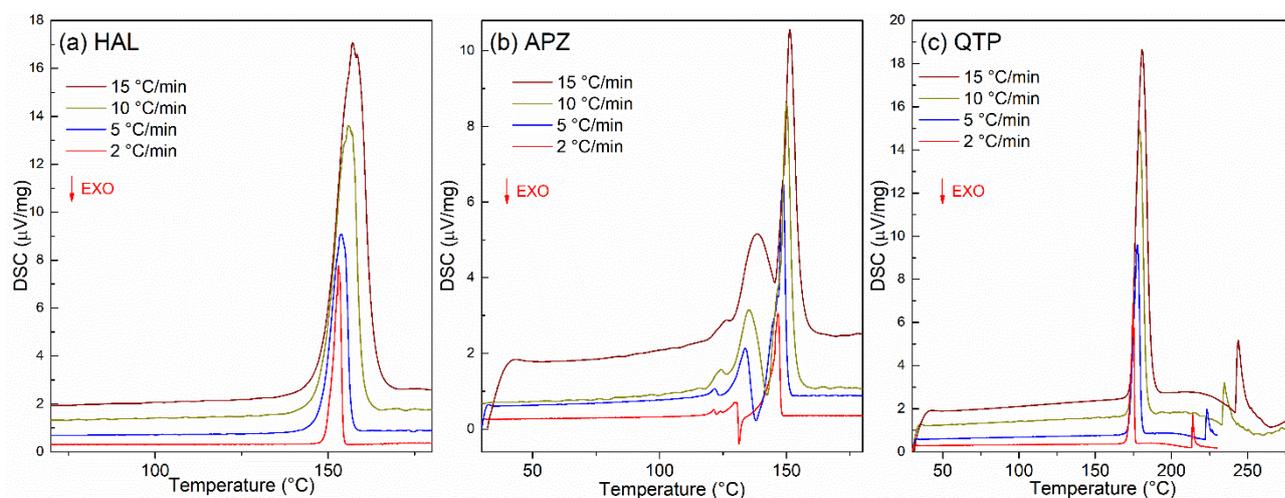
Figure S2 DSC thermograms of HAL, APZ and QTP subject to different heating rates using a new sample in each process.
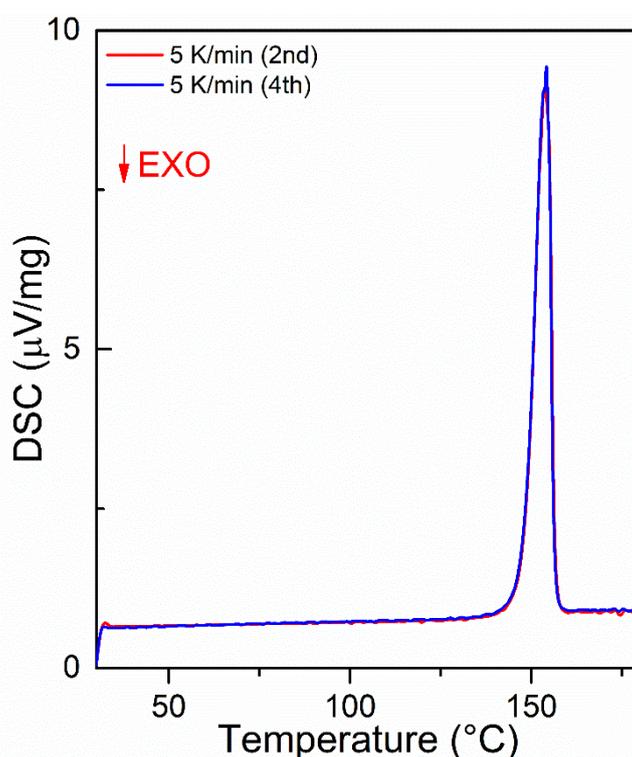
Figure S3 DSC thermograms of HAL submitted to cycling process; the heating was followed by cooling using the same rates and the same sample in each process. The curve in red, shows the crucible with a sample of HAL that was submitted to heating for the second time while in the curve in blue shows the one that was submitted to heating for the fourth time. The exact coincidences in the curves demonstrate that HAL undergoes reversible process upon exposure to thermal effects.
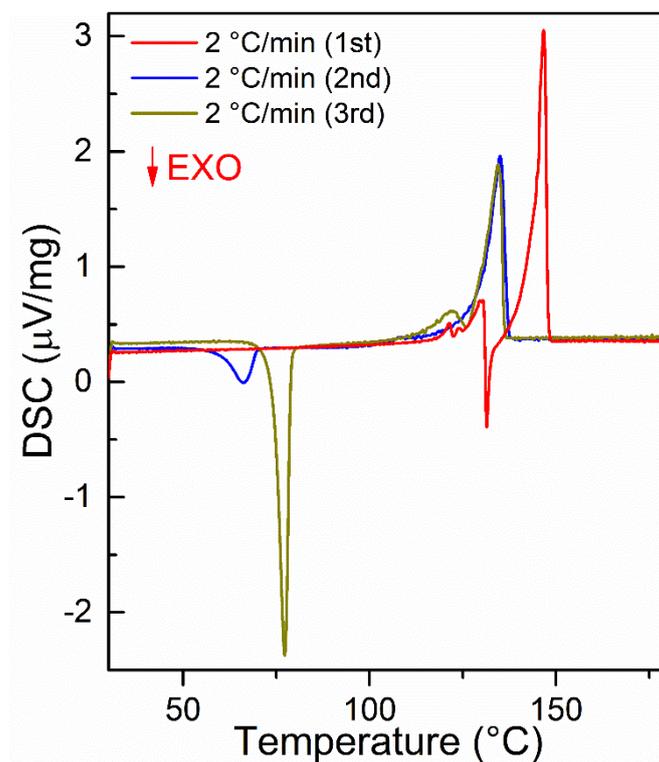
Figure S4 DSC thermograms of APZ submitted to cycling process; the heating was followed by cooling using the same rate and the same sample in each process. The different pattern collected in each round indicate that APZ changes the structure upon heating process. After the first process, appear a new exothermic peak appears, which was also observed in the third process.

Paper 3

Probing water mobility in human dentine using neutron spectroscopy

Journal:	*Journal of Dental Research*
Manuscript ID	JDR-17-0993.R1
Manuscript Type:	Research Reports
Date Submitted by the Author:	17-Jan-2018
Complete List of Authors:	Lauritsen, Alexander ; Faculty of Science, University of Copenhagen, Niels Bohr Institute Pereira, José; Faculty of Science, University of Copenhagen, Niels Bohr Institute Juranyi, Fanny; Paul Scherrer Institut Bordallo, Heloisa; Faculty of Science, University of Copenhagen, Niels Bohr Institute Larsen, Liselotte; Faculty of Health and Medical Sciences, University of Copenhagen, Department of Odontology Benetti, Ana Raquel; Kobenhavns Universitet, Department of Odontology
Keywords:	Dentin, Thermal analysis, Infrared spectroscopy
Abstract:	The aim of this study was to investigate hydrogen mobility within innate and demineralized human dentine. Dentine sections from extracted human molars, demineralized or not, were analyzed by combining neutron spectroscopy with thermal analysis. For the thermal analysis of the samples, differential scanning calorimetry and thermal gravimetric analysis coupled with Fourier transform infrared spectroscopy were performed. The hydrogen dynamics of water, collagen and hydroxyl groups present in the samples were investigated using neutron spectroscopy. From the mass loss observed from the TGA curves up to 600 $^{\circ}$C, the same amount of organic content is identified in the samples. From the DSC curves, a higher change in enthalpy associated to the denaturation of collagen is registered in the demineralized dentine, i.e. a structural change occurs in the collagen subsequent to demineralization. Since the intensity measured by neutron spectroscopy is dominated by the signal from hydrogen, in our samples coming mostly from the bulk-like and loosely bound water as well as from the collagen itself, higher proton mobility within the demineralized dentine was detected when compared to innate dentine. In the demineralized dentine, this proton mobility amounts to 80%, while the remaining hydrogen accounts for a combination of structural hydroxyls, as a result of the incomplete dissolution of the mineral phase by acid-etching, and hydrogen tightly bound present in the collagen structure. By combining neutron spectroscopy with the calorimetry data, our findings support the idea that hydroxyapatite protects the collagen in innate dentine. Demineralized dentine, on the other hand, acts as a sponge where free, bulk-like water is trapped.

1
2
3
4
5
6
7
8
9
10
11
12
13
14
15
16
17
18
19
20
21
22
23
24
25
26
27
28
29
30
31
32
33
34
35
36
37
38
39
40
41
42
43
44
45
46
47
48
49
50
51
52
53
54
55
56
57
58
59
60

SCHOLARONE™
Manuscripts

Probing water mobility in human dentine using neutron spectroscopy

A. K. Lauritsen[1], J. E. M. Pereira[1], F. Juranyi[2], H. N. Bordallo[1,3], L. Larsen[4], A. R. Benetti[4]

[1] Niels Bohr Institute, Faculty of Science, University of Copenhagen, Denmark

[2] Paul Scherrer Institute, Switzerland

[3] European Spallation Source, Sweden

[4] Department of Odontology, Faculty of Health and Medical Sciences, University of Copenhagen, Denmark

A supplemental appendix to this article is published electronically only at http://jdr.sagepub.com/supplemental.

Abstract word count: 257

Total word count (Abstract to Acknowledgments): 3194

Total number of tables: 1

Total number of figures: 4

Number of references: 29

Keywords: Dentin, Hydrogen, Neutrons, Thermal Analysis, Infrared Spectroscopy

Corresponding Author:

A. R. Benetti

Department of Odontology, Faculty of Health and Medical Sciences, University of Copenhagen, Denmark

Nørre Allé 20, DK-2200, Copenhagen, Denmark

Phone: +45 35 32 68 00

Email: arbe@sund.ku.dk

1

Probing water mobility in human dentine using neutron spectroscopy

Abstract

The aim of this study was to investigate hydrogen mobility within innate and demineralized human dentine. Dentine sections from extracted human molars, demineralized or not, were analyzed by combining neutron spectroscopy with thermal analysis. For the thermal analysis of the samples, differential scanning calorimetry and thermal gravimetric analysis coupled with Fourier transform infrared spectroscopy were performed. The hydrogen dynamics of water, collagen and hydroxyl groups present in the samples were investigated using neutron spectroscopy. From the mass loss observed from the TGA curves up to 600 °C, the same amount of organic content is identified in the samples. From the DSC curves, a higher change in enthalpy associated to the denaturation of collagen is registered in the demineralized dentine, i.e. a structural change occurs in the collagen subsequent to demineralization. Since the intensity measured by neutron spectroscopy is dominated by the signal from hydrogen, in our samples coming mostly from the bulk-like and loosely bound water as well as from the collagen itself, higher proton mobility within the demineralized dentine was detected when compared to innate dentine. In the demineralized dentine, this proton mobility amounts to 80%, while the remaining hydrogen accounts for a combination of structural hydroxyls, as a result of the incomplete dissolution of the mineral phase by acid-etching, and hydrogen tightly bound present in the collagen structure. By combining neutron spectroscopy with the calorimetry data, our findings support the idea that hydroxyapatite protects the collagen in innate dentine. Demineralized dentine, on the other hand, acts as a sponge where free, bulk-like water is trapped.

2

Introduction

Water plays an important role in bonding adhesive dental materials to the human dentine (Perdigão 2010). Within dentine, water is present inside the dentine tubules surrounding the extensions of the odontoblast cells (Pashley 1996, Van der Graaf and Ten Bosch 1990). Additionally, water is an essential component of the cellular matter encountered inside the tubular structure. On the molecular level, moreover, water hydrates collagen, one of the main components of dentine (Xu and Wang 2012, Traore et al. 2000, Fullerton et al. 2006).

Considering these distinct locations and roles, water within dentine may exist in different states: 1) in a free state, also known as bulk-like water; 2) adsorbed to the surface, known as loosely bound water; and 3) as structural water, also called tightly bound water. This explains variations in mass loss from dentine on varying the temperature, pressure (Lim and Liboff 1972) or dehydration methods (Agee et al. 2015). Furthermore, water dynamics is likely to be influenced by acid-etching dentine prior to bonding, a pretreatment required for traditional adhesive dental materials. Therefore, understanding the changing states of water within demineralized dentine may help optimize bonding to this tissue. These water states have been earlier investigated in demineralized human dentine using gravimetric analysis (Agee et al. 2015) and differential scanning calorimetry (Sakae et al. 1995, Armstrong et al. 2006). However, gathering this information by gravimetric methods alone is complicated due to the tubular structure of dentine, whereby water can easily enter or evaporate. The difficulty is to exactly maintain the native humidity of dentine during specimen preparation and storage, which is even more challenging for demineralized dentine. In a recent study, the amount of unbound water in demineralized human dentine accounted for 75-79 % wt. of the total matrix water (Agee et al. 2015). In order to investigate the states of water within dental hard tissues, combinations of other techniques such as X-ray diffraction or infrared absorption (LeGeros et al. 1978), the analysis of evolved gases during heating (Holcomb and Young 1980), nuclear magnetic resonance (^{1}H NMR) (Kishen and Rafique 2006) and multipulse spectroscopy (^{1}H CRAMPS) (Vyalikh et al. 2013) have been successfully employed.

Among the mentioned methods, infrared spectroscopy and X-ray diffraction techniques can only gather surface information from the samples, allowing limited quantification. While the analysis of hydrogen by NMR provides dynamic information, the complexity of the

3

dental hard tissues may result in a ^{1}H NMR spectrum that is not well resolved. This is particularly aggravated when the sample is not highly crystalline (Vyalikh et al. 2013), such as dentine. Conversely, the higher resolution provided by ^{1}H CRAMPS allows a better decomposition of the OH^{-} signal. For instance, a previous study demonstrated that the apatite in human dental tissues is poorly hydroxylated: while the hydroxyl content in enamel is 40% of the total spectral intensity, it accounts for only 9-14% in dentine (Vyalikh et al. 2013). The remaining hydrogen present in dentine is therefore attributed to collagen. The study of collagen hydration, among other properties, has been of wide interest for understanding protein folding as well as the strength and structural integrity of diverse body tissues. For instance, in collagen obtained from mammalian tendons subjected to sequential dehydration (Fullerton et al. 2006) or rehydrated collagen obtained from mammalian connective tissue (Traore et al. 2000) mainly bound water and very little, if any, bulk-like water were found using the NMR titration method. Furthermore, NMR titration combined with molecular structure calculations confirmed the existence of three distinct hydration fractions, in addition to bulk water, binding to the collagen (Fullerton et al. 2006). Under specific conditions, *viz.* when the tissue contains enough water, a fast exchange of protons between these hydration fractions occurs.

In native human dentine, collagen is involved with hydroxyapatite, whereby water fractions are less mobile (Van der Graaf and Ten Bosch 1990). On the contrary, a recent study demonstrated that the loss of mineral due to etching increases water mobility within the tissue (Agee et al. 2015). A major drawback of the latter study, however, is the need to dehydrate and subsequently rehydrate the samples for the gravimetric experiment. Considering that distinct transition temperatures are observed during thermal degradation of dry and hydrated collagen (Bozec and Odlyha, 2011), it can be concluded that changes in the structure of collagen during dehydration hinder full recovery of the water content.

Thus, a method that does not require previous dehydration of the samples would be better suited to probe the distinct states of hydrogen dynamics in demineralized dentine. Despite the significant contribution of ^{1}H NMR, invaluable information about water mobility can be obtained using neutron scattering. Due to the high attenuation of hydrogen by neutrons, neutron scattering is optimal to assess the states of water in biological samples (Lakey 2009). Therefore, the aim of this study was to investigate hydrogen mobility within human

4

dentine and demineralized dentine, by combining neutron spectroscopy with thermal analysis.

Materials and Methods

Human molars (n=16) from anonymous donors and exempt from notification to the Danish National Research Ethics Committee (Act on Research Ethics Review of Health Research Projects, section 14, paragraph 3) were used in this study. The teeth were sectioned using a diamond disc refrigerated by water (Accutom, Struers, Denmark). Coronal dentine of dimensions 5.5 mm x 5.5 mm (± 1 mm) was then sliced to thicknesses of 0.4 mm (± 0.1 mm). All slices were stored in 0.5% chloramine and rinsed in deionized water immediately before the experiments.

Two dentine slices were obtained from each tooth (see Appendix, Figure 1). To get information from the same, but demineralized, biological material, one slice from each tooth was immersed in 10% phosphoric acid (pH 1.0) under mechanical agitation at 300 rpm (KS 125 Basic, IKA Labortechnik, Jane & Kunkel GmbH & Co., Germany) for 4 days and is henceforth referred to as demineralized dentine (n=16). The acid solution was not changed during this period. The demineralized dentine was then rinsed in deionized water for 24 h under mechanical agitation. The remaining dentine slices (n=16) were left untreated and are henceforth referred to as dentine. For each sample, 14 slices were analyzed using neutron spectroscopy, while 2 slices were used for thermal analysis.

Thermal analysis

Differential scanning calorimetry (DSC) was used to observe enthalpy changes in the samples. By slowly heating the sample and a reference and measuring the supplied heat, the calorimeter measures the heat capacity as a function of temperature. A sudden change in heat capacity indicates a phase transition, as these require large amounts of energy for a relatively small change in temperature.

Thermogravimetric analysis (TGA) was used to determine the decomposition of the sample as a function of temperature. In TGA, the sample is slowly heated with the registered mass loss as a function of temperature indicating changes in the sample composition. The rate of mass loss with temperature gives an insight into how rapidly the decomposition occurs, thus indicating the strength of the bonds between different

5

molecular groups. If a Fourier transform infrared spectrometer is attached to the TGA (TGA-FTIR), a characterization of the decomposing substances upon heating is readily available.

The samples were rinsed immediately prior to thermal analysis. In order to obtain quadruplicate DSC and TGA-FTIR measurements from the same biological material, two slices from the same tooth were divided into 4 equal parts (see Appendix, Figure 1). The samples remained immersed in water and were blot-dried on absorbent paper towels immediately before the experiments.

Differential scanning calorimetry

Each sample was placed in an aluminum pan, sealed and then placed in the DSC device (Netzsch DSC 214 Polyma, Germany). The samples were heated from 20 °C to 500 °C at a rate of 5 K/min under nitrogen gas flow (40 mL/min).

Thermal gravimetric analysis coupled with Fourier Transform Infrared Spectrometer

The samples were placed in an aluminum oxide crucible into the TGA equipment (PERSEUS TG 209 F1 Libra, Netzsch, Germany) coupled with a Fourier transform infrared spectrometer (BRUKER Optics Inc., Germany). To stabilize the initial environment, the samples were kept at 20 °C for 5 min. Afterwards they were heated at a rate of 5 K/min to 600 °C under nitrogen gas flow (20 mL/min). A FTIR spectrum of the evolved gases was recorded for every 3 degrees of data collection.

Neutron spectroscopy

Neutron spectroscopy allows investigating molecular motion on a range of timescales as well as probing bound and unbound molecules confined in different environments. In dentine, the signal from hydrogen dominates the measured intensity of neutron scattering in water and collagen ($C_{57}H_{91}N_{19}O_{16}$): the so-called incoherent neutron scattering length for hydrogen is 80 barns, while it is close to zero for the other elements in dentine (C, N, O, Ca, P) (Dianoux and Lander 2003). Mobility in the complex dentine system was probed using the elastic fixed window approach (EFW) by measuring the number of elastically scattered neutrons from the sample as a function of temperature (Benetti et al. 2015), within a specific timescale, given by the elastic energy resolution of the instrument. When

no energy exchange between the neutrons and the sample is observed, i.e. no motion is detected within the observation time (or instrument resolution), the signal is seen as elastic and referred to as elastic intensity. However, changes in the dynamics of a system result in changes in the number of the elastically scattered neutrons, and an increase in temperature will result in activation of molecular vibrations. Using this approach, it is possible to differentiate hydrogen mobility in different environments, because its response differs during thermal activation. The present study focused on the hydrogen dynamics of water, collagen and hydroxyl groups within the samples. In the case of water, specific dynamics are clearly detected by sudden drops in the elastic intensity as a function of temperature: while bulk water mobility is activated at 273 K (or 0 ºC), for confined water this is observed at lower temperatures (Ridi et al. 2009, Berg et al. 2016).

In this study, the dentine samples were investigated using the inverted geometry time-of-flight backscattering spectrometer MARS (Mica Analyser high-Resolution Spectrometer) at the Paul Scherrer Institute (PSI), SINQ spallation source (Switzerland), between 2 K (He temperature) and 300 K (27 °C). Using a wavelength of 6.66 Å (Tregenna-Piggott et al. 2008) a resolution of ~13 µeV is achieved, allowing hydrogen mobility to be probed in the nanosecond timescale. In this timescale, molecular vibrations from bulk-like and loosely bound water present in the collagen will give rise to decay in the elastic intensity, while tightly bound water also present in the collagen structure and the hydrogen atoms from the structural hydroxyl groups are seen as immobile and contribute to the elastic intensity. Finally, bulk water contributes only to the background.

Results

1. Two-stage decomposition related to the evaporation of dentine water and hydroxyl from apatite lattice

The combined results from DSC and TGA-FTIR for dentine and demineralized dentine are shown in Figures 1, 2(a). From these results, the mass loss observed at temperatures < 120 ºC is attributed to the evaporation of bulk-like water. Denaturation of collagen observed in the samples is characterized by a clear endothermic transition in the DSC curve around T_{den} = 150 ºC (Table 1). On further heating, denaturation of collagen is observed as a slight decline in the TGA curves for dentine, but occurs at a lower temperature in the demineralized dentine (Table 1). For demineralized dentine the TGA

curve, rather than a gradual mass loss, shows instead a plateau in the interval between approximately 100 °C and 300 °C (Figure 2 (a)). As the temperature increases further, a second mass loss corresponding to the onset of the mineral phase degradation is indicated by a peak in the dTGA curve at T_{deg} = 330 ºC. Analysis of the FTIR-TGA spectrum from the decomposed gases (Figure 2(b)) shows the appearance of a vibration at 960 cm^{-1}, ascribed to a symmetric stretch of P-O (Wieliczka et al. 1996), and a second vibrational mode at ~940 cm^{-1}, related to phosphonate bands (Daasch and Smith 1951), thus confirming the mineral phase degradation. To follow the behavior of the 960 cm^{-1} stretch mode as a function of temperature, the relative absorbance (defined as the ratio of the maximum peak intensity at 960 cm^{-1} to the mean value of the spectral background, calculated between 600 cm^{-1} and 4400 cm^{-1}) is shown as the FTIR curves (Figures 1, 2(a)).

2. Higher energy is released from collagen denaturation in demineralized dentine

In demineralized dentine, there is a large change in enthalpy with a slight decrease in denaturation temperature (T_{den}), see Table 1. Considering that the integrated area beneath the peak in the DSC endotherm gives information about the change of calorimetric enthalpy (ΔH) during denaturation, independent of any model assumption, the higher enthalpy observed for the demineralized sample shows that more chemical bonds are broken in this sample at T_{den}.

3. Relating mineralization degree to proton mobility within dentine

The evolution of the normalized neutron scattering signal to the lowest temperature from dentine and demineralized dentine using the EFW approach (Figure 3) shows a very distinct pattern related to hydrogen motions. For the demineralized dentine, a sudden drop in the intensity of elastically scattered neutrons is noticed and shows a phase transformation of water from the solid to the liquid state at 0 °C. On the contrary, for dentine, only a slight deviation from the linear intensity decay is observed above 200 K. From Figure 3, the percentage of mobile hydrogen was calculated by taking the ratios of the neutron scattering elastic intensities at 300 K for each sample to the maximum intensity at 2 K. Thus, the intensity accounts for a 25 % fraction of mobile hydrogen in dentine and 80 % in demineralized dentine. These correspond, respectively, to an

immobile hydrogen fraction of 75 % in dentine and 20 % in demineralized dentine. The mean square displacement (MSD) of the hydrogen motion as a function of temperature (Figure 4) was extracted from the evolution of the EFW as described in details elsewhere (Martins et al. 2017). The higher MSD values highlight the greater proton mobility of demineralized dentine when compared with innate dentine.

Discussion

In dentine (Figure 1), the initial mass loss observed at temperatures <120 ºC is attributed to bulk-like water. In demineralized dentine, the very early onset of this mass loss makes it difficult to quantify the amount of evaporated water using TGA only (Figure 2(a)). Further heating sets the stage for collagen denaturation. At temperatures >120 ºC, the free water is removed. The remaining water admix (less free than bulk-like water) plays an important role in maintaining the conformation (Traore et al. 2000) and stability of collagen (Bozec and Odlyha 2011). In our study, the denaturation temperature of collagen was lower in dentine than in demineralized dentine. These results are in agreement with those reported by Armstrong et al. (2006) and imply the protection of collagen by the mineral matrix, which makes denaturation more difficult.

This idea is further supported by the significant increase in enthalpy recorded for demineralized dentine, which denotes a structural change in the triple helical domains of the collagen from a restrained structure within the mineral phase to a freer state, in which the decomposition is less complicated. An increase in enthalpy of collagen denaturation in various conditions was reported previously (Sakae et al. 1995, Miles et al. 1995, Schroepfer and Meyer 2017). In the study of Miles et al. (1995), the enthalpy of collagen denaturation was found to be 2.5 times higher after swelling in acetic acid. These authors suggested that intact collagen fibrils in water were more tightly packed – and thus the number of co-operative units that contribute to the enthalpy smaller – while swelling in acid caused the collagen molecules to act independently and establish new molecular bonds. Furthermore, the enthalpy of collagen is influenced by its hydration state (Schroepfer and Meyer 2017).

The TGA-FTIR experiments show a clear difference in the shape of the relative absorbance when comparing mineralized and demineralized dentine. The half-width at half-maximum of the relative FTIR absorbance peaks from each sample involve different

9

temperature ranges (Figures 1-2(a)). In the demineralized dentine, the temperature range is the narrowest and thus in agreement with the abrupt drop observed in the TGA curve for this sample (Figure 2(a)). The second mass loss in the TGA curves of both samples is ascribed to the breaking of lattice water within the mineral phase (LeGeros et al. 1978) in combination with water within the collagen (Sakae et al. 2005), and consequent combustion of the inorganic phase of dentine. Additionally, the presence of P-O stretching in the FTIR-TGA spectra obtained from the demineralized dentine shows that the adopted etching protocol does not completely solubilize all hydroxyapatite crystals.

Neutron scattering shows increased water mobility in demineralized dentine. This is reflected by the sudden drop at 273 K seen for the demineralized dentine in Figure 3, and fully agrees with previous work, in which the largest fraction of water hydrating mammalian collagen – similarly to demineralized dentine – is loosely bound (Traore et al. 2000, Fullerton et al. 2006). As the elastic scattered intensity does not reach zero at room temperature, the demineralized dentine still possesses 20% of immobile hydrogen in the probed timescale. This accounts for a combination of structural hydroxyls, as a result of the incomplete dissolution of the mineral phase by etching, and hydrogen with slower mobility than the observation time provided by the instrument, tightly bond in the altered collagen structure. Our data does not allow quantification of each contribution separately.

For dentine, in contrast, the deviation from the linear decay observed in the neutron scattering intensity at 200 K is caused by thermal activation of the OH-groups present in the hydroxyapatite and collagen, as well as from surface and/or confined water (Berg et al. 2016, Ridi et al. 2009). This slight, but continuous, drop of intensity accounts for approximately 25 % of mobile hydrogen within dentine at 300 K. This agrees with previous gravimetric experiments interpreted using the longitudinal diffusion model, which found that water in the mineral matrix of dentine has a diffusion coefficient approximately 10 times slower than bulk water (Van der Graaf and Ten Bosch 1990).

Despite the progress from ongoing research to make bonding to dentine stronger, more durable (Peumans et al. 2014), and less sensitive to moisture (Loguercio et al. 2015), complete insight on the nanostructural organization of dentine collagen and their structural dependence on water molecules is missing. This paper demonstrated the ability of combining thermal analysis to neutron spectroscopy in the study of water dynamics in dentine. While innate dentine maintains water to some extent at a loosely bound state, our

data confirms that demineralized dentine acts as a sponge where water is found with less restriction. Complementing earlier mathematical modeling, neutron scattering allowed a realistic account of the proportions of bound and unbound water within human dentine.

In conclusion, our work shows that the structural rearrangement of the collagen fibrils subsequent to acid etching deeply influences the hydrogenous moieties in dentine. By understanding the intricate hydrated nanostructure of dentine, new possibilities for interaction between this tissue and the current dental restorative materials emerge, and consequently future opportunities for optimizing bonding.

11

Table

Table 1. Mean and standard deviation of denaturation temperature (T_{den}) and the energy involved in this phase transition (ΔH: enthalpy, expressed as the area under the peak in the DSC endotherm). Mean and standard deviation of degradation temperature (T_{deg}) obtained from TGA.

	Dentine	Demineralized dentine
T_{den} (°C)	150 ± 12	132 ± 17
ΔH (µVs/mg)	818 ± 50	5679 ± 553
T_{deg} (°C)	326 ± 1	304± 5

12

Figure legends

Figure 1. Representative curves from a dentine sample plotted as a function of temperature. 1) Results from the TGA are expressed as percentage mass; the dTGA, is defined as the negative of the differential of the TGA curve and is expressed as percentage mass per degree of temperature increase; and the FTIR curve represents the relative absorbance, defined as the ratio of the maximum peak intensity at 960 cm^{-1} to the mean value of the spectral background, calculated between 600 cm^{-1} and 4400 cm^{-1}, in arbitrary units. 2) Calorimetry (DSC) data is expressed as enthalpy change in voltage per mass.

Figure 2. (a) Representative curves from demineralized dentine plotted as a function of temperature. 1) Results from the TGA are expressed as percentage mass; the dTGA, is defined as the negative of the differential of the TGA curve and is expressed as percentage mass per degree of temperature increase; and the FTIR curve represents the relative absorbance, defined as the ratio of the maximum peak intensity at 960 cm^{-1} to the mean value of the spectral background, calculated between 600 cm^{-1} and 4400 cm^{-1}, in arbitrary units. 2) Calorimetry (DSC) data is expressed as enthalpy change in voltage per mass. (b) Absorbance spectrum from a demineralized dentine sample at 330 ºC between 800 and 1100 cm^{-1}. Note here the peaks associated with the vibration of phosphorous.

Figure 3. Intensity of elastic scattering from dentine and demineralized dentine as a function of temperature, employing the EFW approach normalized to the intensity at the lowest temperature. The mass of both samples was similar, ~1g. The vertical line marks the transition of water from the solid to the liquid state at 0°C.

Figure 4. Mean square displacement from dentine and demineralized dentine as a function of temperature. The mass of both samples was similar, ~1g. Molecular motions are activated when the curves deviate from the x-axis. The values were obtained from elastic fixed window (EFW) scans normalized to the intensity at the lowest temperature.

13

References

Agee KA, Prakki A, Abu-Haimed T, Naguib GH, Nawareg MA, Tezvergil-Mutluay A, Scheffel DL, Chen C, Jang SS, Hwang H et al. 2015. Water distribution in dentin matrices: bound vs. unbound water. Dent Mater. 31(3):205-216.

Armstrong SR, Jessop JLP, Winn E, Tay FR, Pashley DH. 2006. Denaturation temperatures of dentin matrices. I. Effect of demineralization and dehydration. J Endod. 32(7):638-641.

Benetti AR, Jacobsen J, Lehnhoff B, Momsen NC, Okhrimenko DV, Telling MT, Kardjilov N, Strobl M, Seydel T, Manke I, Bordallo HN. 2015. How mobile are protons in the structure of dental glass ionomer cements? Sci Rep. 10;5:8972. doi: 10.1038/srep08972.

Berg MC, Jacobsen J, Momsen NCR, Benetti AR, Telling MTF, Seydel T, Bordallo HN. 2016. Water dynamics in glass ionomer cements. Eur Phys J Special Topics. 225(4): 775–779.

Bozec L, Odlyha M. 2011. Thermal denaturation studies of collagen by microthermal analysis and atomic force microscopy. Biophys J. 101(1):228-236.

Daasch L, Smith D. 1951. Infrared spectra of phosphorus compounds Anal Chem 23(6): 853-868.

Dianoux A J, Lander G. (eds.). 2003. Neutron data booklet. 2 ed. Philadelphia: Old City Publishing. ISBN: 0-9704143-7-4. https://www.ill.eu/fileadmin/users_files/documents/links/documentation/NeutronDataBooklet.pdf

Fullerton GD, Nes E, Amurao M, Rahal A, Krasnosselskaia L, Cameron I. 2006. An NMR method to characterize multiple water compartments on mammalian collagen. Cell Biol Int. 30(1):66-73.

Holcomb DW, Young RA. 1980. Thermal decomposition of human tooth enamel. Calcif Tissue Int. 31(3):189-201.

Kishen A, Rafique A. 2006. Investigations on the dynamics of water in the macrostructural dentine. J Biomed Opt. 11(5):054018.

Lakey, JH. 2009. Neutrons for biologists: a beginner's guide, or why you should consider using neutrons. J R Soc Interface. 6 (Suppl 5): S567–S573.

LeGeros RZ, Bonel G, Legros R. 1978. Types of "H_2O" in human enamel and in precipitated apatites. Calcif Tiss Res. 26(2):111-118.

Lim JJ, Liboff AR. 1972. Thermogravimetric analysis of dentin. J Dent Res. 51(2):509-514.

Loguercio AD, de Paula EA, Hass V, Luque-Martinez I, Reis A, Perdigão J. 2015. A new universal simplified adhesive: 36-month randomized double-blind clinical trial. J Dent. 43(9):1083-1092.

Martins ML, Eckert J, Jacobsen H, dos Santos EC, Ignazzi R, de Araujo DR, Bellissent-Funel MC, Natali F, Koza MM, Matic A et al. 2017. Probing the dynamics of complexed local anesthetics via neutron scattering spectroscopy and DFT calculations. Int J Pharm 524(1-2):397-406.

Miles CA, Burjanadze TV, Baile AJ. 1995. The kinetics of the thermal denaturation of collagen in unrestrained rat tail tendon determined by differential scanning calorimetry. J Mol Biol. 245(4):437-446.

Pashley DH. 1996. Dynamics of the pulpo-dentin complex. Crit Rev Oral Biol Med. 7(2):104-133.

Perdigão J. 2010. Dentin bonding - variables related to the clinical situation and the substrate treatment. Dent Mater. 26(2):e24–e37.

Peumans M, De Munck J, Mine A, Van Meerbeek B. 2014. Clinical effectiveness of contemporary adhesives for the restoration of non-carious cervical lesions. A systematic review. Dent Mater. 30(10):1089-1103.

Ridi F, Luciani P, Fratini E, Baglioni P. 2009. Water confined in cement pastes as a probe of cement microstructure evolution. J Phys Chem B. 113(10):3080–3087.

Sakae T, Mishima H, Kosawa Y, LeGeros RZ. 1995. Thermal stability of mineralized and demineralized dentin: a differential scanning calorimetric study. Connec Tiss Res. 33(1-3):193-196.

Sakae T, Oinuma H, Higa M, Kozawa Y. 2005. X-ray diffraction and FTIR study on heating effects of dentin from mammoth tusk. J Oral Biosci. 47(1):83-88.

Schroepfer M, Meyer M. 2017. DSC investigation of bovine hide collagen at varying degrees of crosslinking and humidities. Int J Biol Macromol. 103:120-128.

Traore A, Foucat L, Renou JP. 2000. 1N NMR study of water dynamics in hydrated collagen: transverse relaxation-time and diffusion analysis. Biopolymers. 53(6):476-483.

Tregenna-Piggott PLW, Juranyi F, Allenspach P. 2008. Introducing the inverted-geometry time-of-flight backscattering instrument, MARS at SINQ. J Neutron Res. 16(1-2):1-12.

Van der Graaf ER, Ten Bosch JJ. 1990. The uptake of water by freeze-dried human dentine sections. Arch Oral Biol. 35(9):731-739.

Vyalikh A, Mai R, Scheler U. 2013. OH^{-} deficiency in dental enamel, crown and root dentine as studied by ^{1}H CRAMPS. Bio Med Mater Engineer. 23(6):507-512.

Wieliczka DM, Spencer P, Kruger MB. 1996. Raman mapping of the dentin adhesive interface. Appl Spec. 50 (12): 1500-1504.

Xu C, Wang Y. 2012. Chemical composition and structure of peritubular and intertubular human dentine revisited. Arch Oral Biol. 57(4):383-391.

16

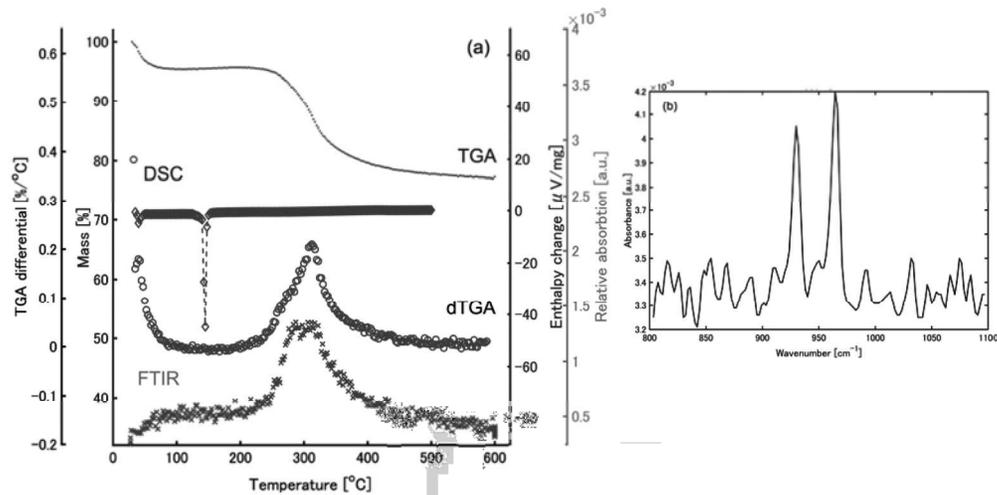Figure 1. Representative curves from a dentine sample plotted as a function of temperature. 1) Results from the TGA are expressed as percentage mass; the dTGA, is defined as the negative of the differential of the TGA curve and is expressed as percentage mass per degree of temperature increase; and the FTIR curve represents the relative absorbance, defined as the ratio between the maximum peak intensity and the mean value of the spectral background, in arbitrary units. 2) Calorimetry (DSC) data is expressed as enthalpy change in voltage per mass.

285x217mm (300 x 300 DPI)

Figure 2. (a) Representative curves from demineralized dentine plotted as a function of temperature. 1) Results from the TGA are expressed as percentage mass; the dTGA, is defined as the negative of the differential of the TGA curve and is expressed as percentage mass per degree of temperature increase; and the FTIR curve represents the relative absorbance, defined as the ratio of the maximum peak intensity at 960 cm-1 to the mean value of the spectral background, calculated between 600 cm-1 and 4400 cm-1, in arbitrary units. 2) Calorimetry (DSC) data is expressed as enthalpy change in voltage per mass. (b) Absorbance spectrum from a demineralized dentine sample at 330 ºC between 800 and 1100 cm-1. Note here the peaks associated with the vibration of phosphorous.
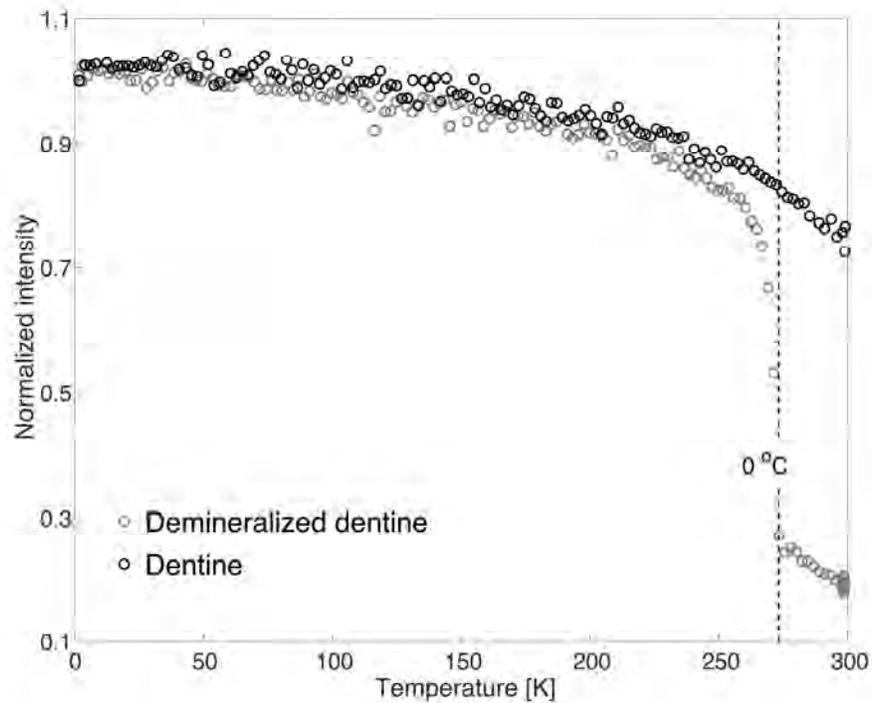
177x88mm (300 x 300 DPI)

Figure 3. Intensity of elastic scattering from dentine and demineralized dentine as a function of temperature, employing the EFW approach normalized to the intensity at the lowest temperature. The mass of both samples was similar, ~1g.The vertical line marks the transition of water from the solid to the liquid state at 0°C.
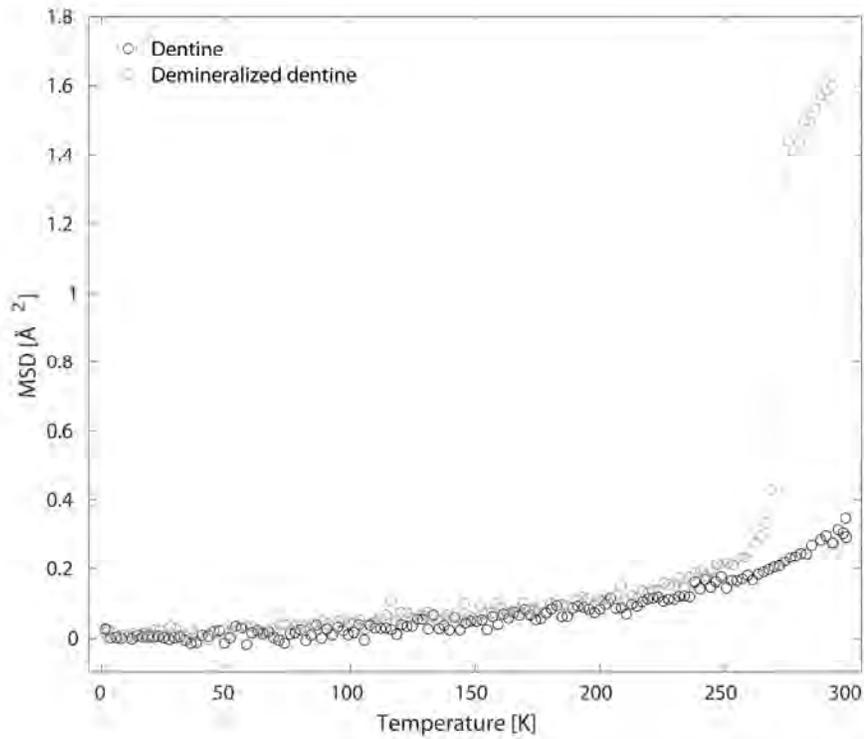
285x219mm (300 x 300 DPI)

1
2
3
4
5
6
7
8
9
10
11
12
13
14
15
16
17
18
19
20
21
22
23
24
25
26
27
28
29
30
31
32

Figure 4. Mean square displacement from dentine and demineralized dentine as a function of temperature. The mass of both samples was similar, ~1g. Molecular motions are activated when the curves deviate from the x-axis. The values were obtained from elastic fixed window (EFW) scans normalized to the intensity at the lowest temperature.

171x139mm (300 x 300 DPI)

33
34
35
36
37
38
39
40
41
42
43
44
45
46
47
48
49
50
51
52
53
54
55
56
57
58
59
60

Supplemental appendix

Probing water mobility in human dentine using neutron spectroscopy

A. K. Lauritsen, J. E. M. Pereira, F. Juranyi, H. N. Bordallo, L. Larsen, A. R. Benetti

Sample preparation

This appendix includes a schematic drawing of cutting the teeth for sample preparation (Appendix, Figure 1).
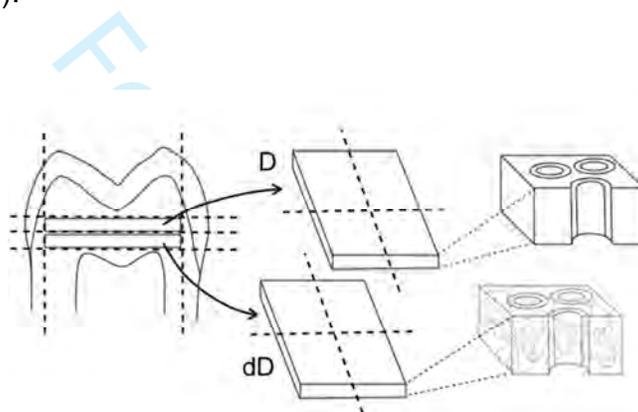
Appendix Figure 1. Schematic of the sample preparation. From each tooth 2 dentine slices were obtained, one namely innate dentine (D) and the other was immersed in 10% phosphoric acid (pH 1.0) and is henceforth referred to as demineralized dentine (dD). To the right are enlarged cuts of the dentine showing the schematic tubular structure in the samples, including the exposed collagen in dD.
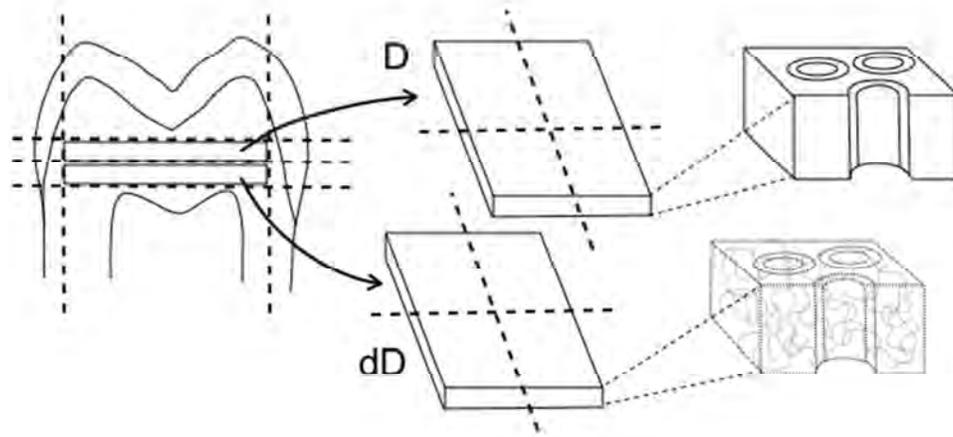
Thermal analysis of hypermineralized dentine

An additional tooth showing significant wear and loss of occlusal enamel, as well as exposed dentine on the top of the cusps - which are signs compatible with parafunctional habits – was sliced and subjected only to thermal analysis. After slicing the tooth, a higher degree of dentine mineralization was visible. Two slices obtained from this sample, henceforth referred to as hypermineralized dentine, were analyzed. The methods are described in details in the main manuscript.

1

Representative curves from the thermal analysis of the hypermineralized dentine - differential scanning calorimetry (DSC) and thermogravimetric analysis attached to a Fourier transform infrared spectrometer (TGA-FTIR) - can be visualized in Appendix, Figure 2. These curves are very similar to the curves obtained for innate dentine. In our study, the denaturation temperature (T_{den} = 154 ± 19 °C) of collagen and change in enthalpy (ΔH = 753 ± 57 µVs/mg), as well as the degradation temperature (331 ± 5 °C), in hypermineralized dentine was similar to dentine. This reinforces the idea that collagen is protected by the mineral matrix.
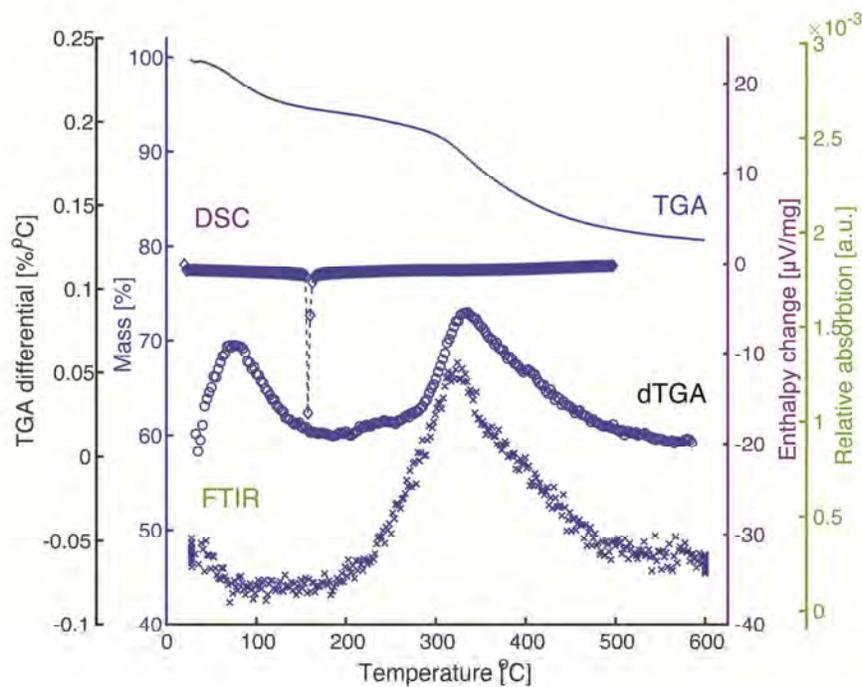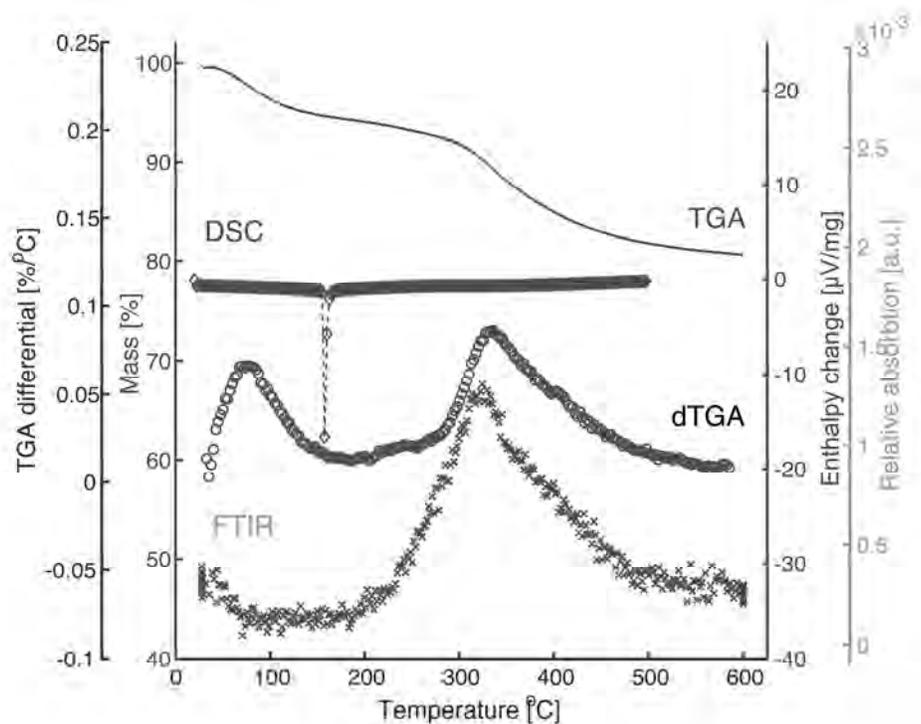

Appendix Figure 2. Representative curves from hypermineralized dentine plotted as a function of temperature. 1) Results from the TGA are expressed as percentage mass; the dTGA, is defined as the negative of the differential of the TGA curve and is expressed as percentage mass per degree of temperature increase; and the FTIR curve represents the relative absorbance, defined as the ratio of the maximum peak intensity at 960 cm-1 to the mean value of the spectral background, calculated between 600 cm-1 and 4400 cm-1, in arbitrary units. 2) Calorimetry data (DSC) is expressed as enthalpy change in voltage per mass.

Appendix Figure 1. Schematic of the sample preparation. From each tooth 2 dentine slices were obtained, one namely innate dentine (D) and the other was immersed in 10% phosphoric acid (pH 1.0) and is henceforth referred to as demineralized dentine (dD). To the right are enlarged cuts of the dentine showing the schematic tubular structure in the samples, including the exposed collagen in dD.

218x116mm (72 x 72 DPI)

Appendix, Figure 2. Representative curves from hypermineralized dentine plotted as a function of temperature. 1) Results from the TGA are expressed as percentage mass; the dTGA, is defined as the negative of the differential of the TGA curve and is expressed as percentage mass per degree of temperature increase; and the FTIR curve represents the relative absorbance, defined as the ratio between the maximum peak intensity and the mean value of the spectral background, in arbitrary units. 2) Calorimetry data (DSC) is expressed as enthalpy change in voltage per mass.

285x217mm (300 x 300 DPI)

Paper 4

M. K. Rasmussen, J. E. M. Pereira, M.C. Berg, G. N. Iles, N. H. Jalarvo, V. F. Botosso, O. A. Sant'Anna, M. C. A. Fantini, H. N. Bordallo. Dynamics of encapsulated hepatitis B surface antigen: A combined neutron spectroscopy and thermo-analysis study. *Under review*.

Dynamics of encapsulated Hepatitis B surface Antigen

A combined neutron spectroscopy and thermo-analysis study

Martin K. Rasmussen[1,a], José E. M. Pereira[1], Marcella C. Berg[1,2], Gail N. Iles[3,4], Nicolas R. de Souza[4], Niina H. Jalarvo[5,6], Viviane F. Botosso[7], Osvaldo A. Sant'Anna[8], Marcia C. A. Fantini[9], and Heloisa N. Bordallo[1,2]

[1] Niels Bohr Institute, University of Copenhagen, Copenhagen, Denmark
[2] European Spallation Source (ESS), Lund, Sweden
[3] Department of Physics, Royal Melbourne Institute of Technology, Melbourne, Australia
[4] Australian Nuclear Science and Technology Organisation, Lucas Heights, Australia
[5] Neutron Scattering Division, Oak Ridge National Laboratory, Oak Ridge, TN, USA
[6] Jülich Centre for Neutron Science (JCNS-1), Forschungszentrum Jülich, Jülich, Germany
[7] Virology Laboratory, Butantan Institute, São Paulo, Brazil
[8] Immunochemistry Laboratory, Butantan Institute, São Paulo, Brazil
[9] Institute of Physics, São Paulo University, São Paulo, Brazil

Abstract. As a result of its well-arranged pore architecture mesoporous SBA-15 offers new possibilities for incorporating biological agents. Considering its applicability in oral vaccination, which shows attractive features when compared with parenteral vaccines, SBA-15 is seen as a very promising adjuvant to carry, protect, and deliver entrapped antigens. Recent studies have shown several remarkable features in the immunisation of hepatitis B, a viral disease transmitted mainly through blood or serum transfer. However, the surface antigen of the hepatitis B virus, HBsAg, is too large to fit inside the SBA-15 matrix with mean pore diameter around 10 nm, thus raising the question of how SBA-15 can protect the antigen. In this work, thermal analysis combined with neutron spectroscopy allowed us to shed light on the interactions between HBsAg and SBA-15 as well as on the role these interactions play in the efficiency of this promising oral vaccination method. This information was obtained by verifying how the dynamics of the antigen is modified under confinement in SBA-15 thus also establishing an experimental method for verification of molecular dynamics simulation.

1 Introduction

Vaccination is a powerful and cost-effective form of preventing infectious diseases. However, most vaccines are delivered by injection, which makes mass immunisation

costly and less safe, particularly in resource-poor developing countries. Oral delivery of vaccines has many benefits, and is becoming a preferred means for effective vaccination of many diseases. Unfortunately, often the vaccine-active proteins are unable to produce an immune response when encountering the digestive tract. However there are clear evidences that oral immunisation is a feasible alternative for preventing infections transmitted through non-mucosal routes[1]. Under these lines and as a result of its structural stability and low toxicity, mesoporous silica SBA-15 has been shown to be a promising adjuvant for the oral delivery of hepatitis B[2], a viral disease which attacks the liver and infects about 2 billion people[3].

The pore structure of SBA-15 is bi-modal, having hexagonal ordered 10 nm mesopores, together with disordered macropores larger than 50 nm. This bimodal porosity is therefore expected to protect the vaccine from the gastric acid of the stomach before initiating their release in the intestine. However, the release behaviour will depend on both the physical properties of the carried vaccine (antigen) and the morphology of the carrier SBA-15 (adjuvant). In this work loaded SBA-15 was characterised by using thermogravimetric Fourier Transform Infrared spectroscopy and inelastic neutron scattering to obtain a better understanding of the dynamics of the Hepatitis B surface antigen (HBsAg) encapsulated in SBA-15. Neutron scattering is a well suited method for probing the dynamics of HBsAg inside SBA-15 due to neutrons ability to penetrate and their large interaction with the hydrogen atoms[4].

2 Experimental details

2.1 Sample preparation

SBA-15 with encapsulated HBsAg was prepared by adding 250 mg commercially produced SBA-15 , synthesized as described in[5], to a solution consisting 110 mL 0.45 mg/mL HBsAg solution supplied with phosphate buffered solution (PBS, 10 mM Na_2HPO_4) to obtain a final volume of 500 mL and then dried at 35 °C following the most optimal encapsulation method reported in[6]. Thus obtaining a powder with HBsAg to SBA-15 mass ratio of 1:5. This sample is hereafter labelled SBA-15+HBsAg. A sample containing 500 mL of PBS solution was also prepared to be used as a reference. This sample is labelled SBA-15+PBS.

2.2 Thermogravimetric analysis and Fourier-transform infrared spectroscopy

To determine and characterise the decomposing substances upon heating of the samples, the mass loss and the chemical composition of the released gases from SBA-15+PBS and SBA-15+HBsAg were measured by thermogravimetric analysis (TGA) and Fourier-transform infrared spectroscopy (FTIR) using a Perseus TG 209 F1 Libra (Netzsch, Germany) with an attached ALPHA FTIR spectrometer (Bruker Optics Inc., Germany). About 10 mg of each sample were placed in an aluminum oxide crucible and the temperature was varied from 30 °C to 1050 °C with at heating rate of 10 °C/min under nitrogen gas flow. A new FTIR spectrum of the evolved gases was recorded for every 3 degrees of data collection. An empty crucible were measured as background correction.

2.3 Neutron spectroscopy

Incoherent inelastic neutron scattering (IINS) along with molecular dynamics (MD) simulations offers real possibilities of investigating the dynamics associated with

a molecule biological function(s). Using the large incoherent scattering cross section intrinsic to naturally abundant hydrogen atoms, information on the elastic (E), quasielastic (QENS), and inelastic (IINS) neutron scattering response of a molecule can be obtained. This experimental information when combined to MD simulations offers unique information on the dynamics of biological molecules in confinement, thus deepening our understanding of the relationship between a molecules dynamics and its function.

In this work, quasi elastic neutron scattering (QENS) combined to the elastic fixed window (EFW) method were performed on both samples in order to disentangle the dynamics of the protein confined within the different pore sizes of SBA-15. This approach was used because the degree of confinement will shift the onset of the local protein dynamics to different time-scales and/or temperatures[7]. The EFW method gives information on the evolution of the elastic scattering intensity as a function of temperature, thus allowing us to find the onset of proton mobility by points of inflexion[8]. On the other hand, by analysing the variation of the line width obtained from the analysis of the QENS signal changes in the diffusion coefficient mainly related to the water in the PBS can be readily obtained[9]. This information is crucial in elucidating how the dynamical properties of the salt and antigen are modified when confined in the carrier.

EFW scans were performed during heating from 20 K to 300 K using the EMU high-resolution backscattering spectrometer at the Australian Centre for Neutron Scattering[10]. EMU is a Si (111) crystal backscattering spectrometer characterised by an energy resolution in the order of 1.2 μeV (FWHM) and a wavelength of $\lambda = 6.27$ Å. To probe the confined water dynamics, we performed another set of QENS experiments on the same samples at 310 K, corresponding to body temperature using the backscattering spectrometer BASIS with wavelength centered at $\lambda = 6.4$ Å and an elastic energy resolution of 3.5 μeV (FWHM)[11]. This corresponds to a time scale in the nanosecond (ns) range. For both experiments the sample was placed in annular cylindrical sample holders.

3 Results and discussion

Comparing the TGA curves presented in Fig. 1(a), no observable mass loss was detected for pure SBA-15, indicating that the percentage of polymeric template left in the structure after washing was negligible[12,13]. On the other hand, we observe a mass loss of ~ 8 % for SBA-15+HBsAg starting at 250 °C, which is not present for the SBA-15+PBS sample. The peaks observed in the FTIR signal obtained from the gases released at 300 °C can be assigned to stretching of C-H, C-O and C=O bonds, Fig. 1.(b). Thus, considering that encapsulated HBsAg is a protein consisting of more than 389 amino acids, we can attribute this mass loss to initial stages of protein degradation[14]. The mass remain constant between 500 °C and 800 °C, while on further heating a second mass loss, corresponding to ~ 25 % and ~ 20 % for SBA-15+HBsAg and SBA-15+PBS, respectively, starts at 800 °C. We attribute these to degradation of the strongly hydrogen binding to the surface silanol groups formed during the incorporation of PBS salt[13]. Furthermore, from the FTIR spectrums obtained at 880 °C, Fig. 1.(a), we also observe a weak C-O signal for SBA-15+HBsAg, indicating further degradation of strongly bound antigen.
The combined TGA and FTIR results seem to indicate that the surface antigen HBsAg is confined in two different environments. The majority, which degrades at 300 °C, is present in the larger macropores of SBA-15 and a smaller amount is most likely attached to the entrance of mesopores that starts degrading at 800 °C.
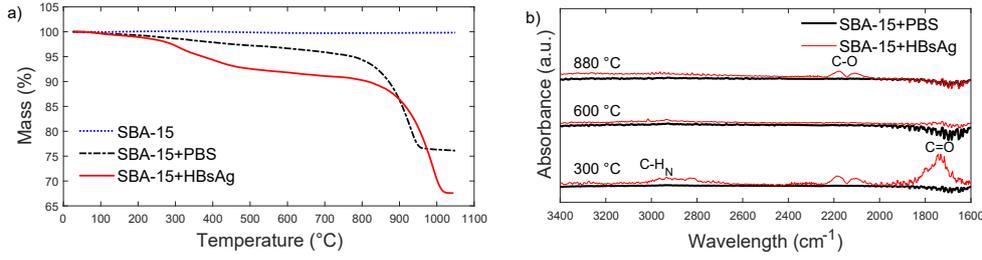
Fig. 1. Comparison of TGA curves (a) and FTIR spectrums at temperatures of interest (b) for SBA-15+PBS containing only PBS salt and SBA-15+HBsAg with encapsulated antigen. Organic material is observed to be released at both 300 °C and 880 °C from SBA-15+HBsAg indicating two different configurations of HBsAg encapsulation. No mass loss was detected for pure SBA-15.
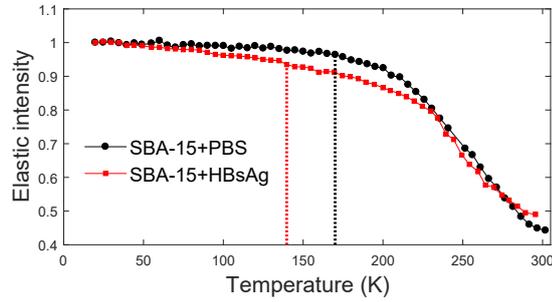

Fig. 2. EFW scans during heating obtained using the backscattering spectrometer EMU for SBA-15+PBS and SBA-15+HBsAg. The inflexion points, indicating the activation of diffusive motions, are marked by dashed lines.

Now we turn to the analysis of the neutron spectroscopy results. By comparing the EFW scans of the two samples in Fig. 2, we observe a faster decrease of the elastic scattering response for SBA-15+HBsAg. Furthermore, the lower temperature of the inflexion point (120 K, marked with a red dashed line), when compared to that for SBA-15+PBS (160 K, marked with a black dashed line) indicates that the presence of the antigen facilitates the activation of hydrogen dynamics as a result of changes in the hydrogen bond network caused by the HBsAg[15]. The second inflection point, around 240 K can be assigned to bulk water confined in pores of tenths of nm[16]. The slightly higher value of immobile hydrogen observed for SBA-15+HBsAg indicates stronger confinement for this sample in the observable time window of EMU.

By focusing on the analysis of the quasi-elastic (QE) region of the inelastic incoherent neutron scattering spectrum obtained on BASIS, we accessed unique information on the dynamical process occurring on the two samples. To this end, we have used the simplest analytical model to describe the hydrogen mobility assuming decoupled translational and rotational motions. Details for the data analysis approach can be found in[17]. Under these lines, all samples were fitted to a delta function, one Lorentzian and a background. For all samples the background was restricted based on the signal recorded at 20 K signal, however the slope of the background was free to vary.

By plotting the half-width at half-maximum (HWHM) as a function of Q^2, Fig. 3, one may check that Fick's law applies if a straight line is obtained. The slope gives directly the self- diffusion coefficient. In the present case, while a linear variation of
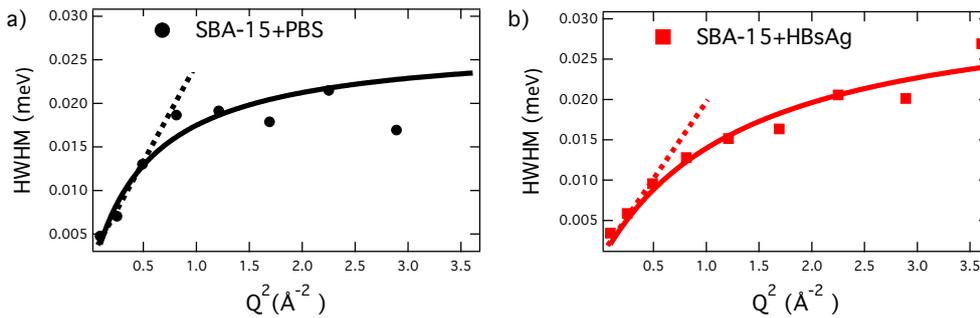
Fig. 3. Evolution of the half-width at half maximum of the quasi-elastic line calculated as a function of Q^2 modelled using the Singwi-Sjölander model from the data obtained using the backscattering spectrometer BASIS for SBA-15+PBS and SBA-15+HBsAg. Dotted lines depict the straight line dependence expected for Fick's diffusion. The errorbars are within the size of the markers.

Table 1. Diffusion coefficient (D_t) and residence time (τ_0) obtained using the Singwi-Sjölander model for the confined water in SBA-15+PBS and SBA-15+HBsAg using an observation time of ns.

Sample	D_t (10^{-9}m^2/s)	τ_0 (ps)
SBA-15+PBS	0.8 ± 0.3	24 ± 3
SBA-15+HBsAg	0.37 ± 0.06	20 ± 2

the broadening is found at small Q values, the width deviates from a straight line at larger Q values. This indicates that the continuous diffusion model is no more valid at small distances and that the details of the elementary diffusive steps have to be taken into account. Therefore, the interpretation of the QENS spectra at larger Q values requires a model which contains as parameters the characteristic lengths and times of the mobility steps. Considering the progressive convergence to an asymptotic value, the data were analysed using the Singwi-Sjöander model[18]. The results are given on Table 1. It is well known that under confinement water mobility will shift to longer relaxation times with respect to the bulk water processes (D_t=2.3 10^{-9}m^2/s). Thus our results indicate that while the diffusion of the water in the PBS solution is slowed down by a factor close to 3, when the antigen is introduced the diffusion coefficient is slower by a factor 6. The latter indicates that in the ns time scale indeed PBS+HBsAg are immobilised (or protected) by the inner structure of the SBA-15.

4 Conclusion

Molecular dynamics simulations would be a powerful tool to understand and predict the release mechanics of HBsAg from SBA-15 both under relevant biological environments and for various loading degrees of vaccine in the porous silica. Such simulation methods would also be very useful for predicting the behaviour of antigens used in other types of vaccines, with different physical properties including the antigens small enough to enter the 10 nm mesopores. In order to develop such models, however, a variant of state of the art experimental methods are required to verify the simulated dynamics. In this work we have presented results obtained using thermal analysis and incoherent inelastic neutron scattering that reveal properties of the antigen HBsAg encapsulated in the mesoporous silica SBA-15. Through analysis of the neutron data

we were able to probe the dynamics of the hydrogen atoms from the confined HBsAg. In the future we expect that comparison between experimental IINS data and molecular dynamics simulation can be used improving vaccine-active proteins encapsulation in SBA-15.

References

1. L. Wang and Ross L Coppel, Expert Rev Vaccines **7**, (2008) 729-738.
2. K. Scaramuzzi, G. D. Tanaka, F. Mariano Neto, P.R.A.F. Garcia, J.J.M. Gabrili, D.C.A. Oliveira, D.V. Tambourgi, J.S. Mussalem, D. Paixo-Cavalcante, M.T. DAzeredo Orlando, V.F. Botosso, C.L.P. Oliveira, M.C.A. Fantini, O.A. Sant'Anna. Nanomedicine: Nanotechnology, Biology and Medicine, **12**, (2016) 2241-2250.
3. World Health Organization. http://www.who.int/mediacentre/factsheets/fs204/en/.
4. J.H. Lakey. J R Soc Interface. **6**, (2009) S567S573.
5. J.R. Matos, L.P. Mercuri, M. Kruk and M. Jaroniec, Chem. Mater. **13** (2001) 1726-31
6. F. Mariano-Neto, J.R. Matos, L.C. Carvalho, K. Scaramuzzi, O.A. Sant'Anna, C.P. Oliveira and M.C.A. Fantini. Journal of Physics D: Applied Physics **47**, (2014) 425402.
7. J. D. Nickles, S. Perticaroli, H. ONeill, Q. Zhang, G. Ehlers and A.P. Sokolov. Biophys. J. **103**, (2012) 1566-1575.
8. M.C. Berg, J. Jacobsen, N.C.R. Momsen, A.R. Benetti, M.T.F. Telling, T. Seydel and H.N. Bordallo. Eur. Phys. J. Special Topics **225**, (2016) 775779.
9. J. Jacobsen, M.S. Rodrigues, M.T.F. Telling, A.L.Beraldo, S.F. Santos, L.P. Aldridge and H.N. Bordallo. Sci. Rep. **3**, (2013) 2667.
10. N.R. de Souza, A. Klapproth and G.N. Iles. Neutron News **27**, (2016) 20-21.
11. E. Mamontov and K.W. Herwig. Rev. Sci. Instrum. **82** (2011) 85109.
12. L.V. Carvalho, R.C. Ruiz, K. Scaramuzzi, E.B. Marengo, J.R. Matos, D.V. Tambourgi, M.C.A. Fantini, O.A. Sant'Anna. Vaccine **28** (2010) 78297836.
13. M. Kruk, M. Jaroniec,C.H.Ko and R. Ryoo. Chemistry of Materials **12**, (2000) 1961-1968.
14. V. Schmidt, C. Giacomelli and V. Soldi. Polymer Degradation and Stability **87**, (2005) 25e31
15. J.D. Nickels, Chemical Physics 424 (2013) 7-11.
16. T. Takamuku, M. Yamagami, H. Wakita, Y. Masuda and T. Yamaguchi, J. Phys. Chem. B **101**, (1997) 57305739.
17. R.E. Lechner, J. Fitter, T. Gutberlet and J. Katsaras. Springer-Verlag Berlin Heidelberg, Germany, (2006) 355-392.
18. K. S. Singwi and A. Sjölander , Phys. Rev. **119**, (1960) 863871.

Book Chapter

Application of Neutron Scattering in Amino Acid Crystals – Structural and Dynamical Information

Paulo T.C. Freire, José E.M. Pereira and Heloisa N. Bordallo

Additional information is available at the end of the chapter

Abstract

In this work results of neutron powder diffraction and inelastic neutron scattering on aliphatic amino acid (L-alanine, L-valine and L-leucine) crystals are presented. The study allows inferring important informations about both the stability of the structures and the dynamics of phase transitions. In particular, it was possible to compare the behavior of different amino acids and to infer that changes in the mean-square displacements observed for two deuterated forms of L-alanine $ND_3^+ - C_2H_4 - CO_2^-$ and $NH_3^+ - C_2D_4 - CO_2^-$ are due to a structural rearrangement related to thermally activated amplitude reorientation of NH_3^+ and CO_2^-. Conformation changes in L-valine and L-leucine related to the phase transition are also discussed.

Keywords: Amino acid crystal, neutron diffraction, inelastic neutron scattering

1. Introduction

Amino acids are the basic blocks of proteins of all living beings, but are also found alone in the cytoplasm of several cells. They were produced and selected since the beginning of life in the Earth, although it is not possible to rule out an extraterrestrial origin. Due to the fact that they appear forming zwitterion structure (involving simultaneously the NH_3^+ and the CO_2^- groups) in both aqueous environment and in solid state phase, amino acids have been extensively studied in the last years. The researches deal mainly with spectroscopic and structural properties, giving special attention to the hydrogen bonds between the amino acid and the water molecules in the aqueous solution and among amino acids, when the material is found in crystalline structures [1 – 4].

From the spectroscopic point of view, amino acids have been investigated using mainly Raman spectroscopy [4 – 6], where information about optical phonons is readily obtained. Based on

INTECH
open science | open minds

such studies it has been suggested that amino acid crystals can present structural instabilities at low temperatures or high pressures. Regarding their structural properties, X-rays [7, 8] and neutron scattering diffraction data [5] have been useful in providing a picture of the origin of the stabilities of their crystal structures as well as the role played by the hydrogen bonds.

In particular, it was possible to gain information on the modifications of the hydrogen bonds studying different deuterated of amino acids samples using inelastic neutron scattering [9 – 11]. From these data the elastic intensity can be expressed as a function of temperature such as $I(T) = I(0).exp[-Q^2 u(T)^2]$, where Q is the scattering vector and $u(T)$ represents the mean-square displacement of the scattering nuclei. Additionally, if a dynamic transition occurs, one can observe a change in the slope of the observed $u(T)^2$. Furthermore, selective deuteration allows tackling changes in the mean-square displacements of particular groups, such as the torsion vibration of CH_3^+ or the torsion of NH_3^+ group. Inelastic neutron scattering combined to selective deuteration can also be used to highlight the modes of particular molecular groups by comparing the spectra of the selected deuterated groups [12].

The objective of this chapter is to present a quick review of neutron powder diffraction and inelastic neutron scattering results on various aliphatic amino acid crystals. These investigations allowed to compare the behavior of different aliphatic amino acids (alanine, valine and leucine), in particular, looking at their vibrational and dynamical properties. For L-alanine, for example, combining neutron diffraction to incoherent elastic neutron scattering measurements allowed us to infer that changes in the mean-square displacements observed for two deuterated forms of L-alanine: (i) $ND_3^+ - C_2H_4 - CO_2^-$ and (ii) $NH_3^+ - C_2D_4 - CO_2^-$ are due to a structural rearrangement related to thermally activated amplitude reorientation of NH_3^+ and CO_2^-.

2. Structural and vibrational anomalies observed in selected amino acids

Many results on the vibrational properties of amino acid crystals are known. From these studies one has constructed an interesting picture about the behavior of the crystals in a huge range of temperature and/or pressure. L-alanine, the simplest chiral amino acid, is an example where surprising aspects of the vibrational properties stand. Among these aspects it is possible to cite some: the intriguing step-wise evolution of the wavenumber of some bands [13], the unconventional increasing of the c lattice parameter when L-alanine is cooled [14], and the localization of vibrational states as revealed by the variation of intensities of the low wavenumber modes at 41 and 49 cm^{-1} [15]. Simultaneously to the increasing of the c lattice parameter a progressive conformational change of the NH_3^+ zwitterion, as well as a strong dynamic Jahn-Teller-like effect due the coupling between NH_3^+ charge and the lattice were observed [13]. These results can be interpreted as consequence of the N – H stretching self-trapped states related to the N – H...O hydrogen bonds directed along the head-to-tail chains of the zwitterions. According to Ref. [16] these self-trapped states should be associated with some of the anomalies reported for L-alanine. The behavior of the intensity of one lattice mode was realized as consequence of the response of one N – H...O hydrogen bond to respond to the changes in the interaction of the nitrogen and oxygen atoms with other atoms forming different hydrogen

bonds. In fact, it is believed that one can assume that hydrogen bonds in chains of zwitterion have diverse properties from those between the chains and the variation of temperature should produce subtle rearrangement of the hydrogen bond network, explaining the existence of anomalies at low temperature [16]. Under high pressure, L-alanine also shows intriguing aspects. For instance, Raman spectroscopy studies have indicated the occurrence of a phase transition at ~ 2.3 GPa [17], which was later confirmed by X-ray diffraction measurements [18]. A new interpretation, however, has indicated that the modifications about 2 GPa might also be understood as a conformation change of the NH_3^+ group [19, 20].

The above considerations for the chiral L-alanine can be extended to encompass the racemic material. DL-alanine seems to be stable at low temperature, presenting no evidence of a solid-solid phase transition from room temperature down to 15 K [21]. However, although no modification in the spectral region of the lattice modes – normally between 30 and 200 cm^{-1} – was detected, certain changes in the internal mode region of the spectrum were noted. These changes can be understood as slight conformational modification of the molecule on cooling. In fact, the rocking vibration of CO_2^- presents an unconventional behavior, *i.e.*, variation of the wavenumber in step-like shape at specific temperatures. In relation to this, it is important to mention that the data obtained using polarized Raman shows that the main change associated with hydrogen bonds take place along the x-axis direction, instead of the bonds along the z-axis. This behavior was also simultaneously reported in the work presented in Ref. [16] for the chiral partner of alanine crystal.

Crystalline L-leucine, another aliphatic amino acid, presents an interesting behavior when submitted to temperature variation between 300 and 400 K. As shown by Raman spectroscopic measurements, the material undergoes a phase transition at ~ 353 K. One possible explanation for the occurrence of such a modification is the appearance of transverse optical (TO) modes at high temperature. Such a vibrational aspect can be translated to the structural language if one assumes that the room temperature monoclinic structure C_2 change to a monoclinic C_s structure [22]. In other words, from the point of view of the spectroscopic scrutiny the $C_2 \rightarrow C_s$ phase transition is a viable path.

Obviously, other questions are relevant as the interaction of amino acid molecules with metal ions. Ions can be present in the living beings as participating of biochemistry processes or nosy hazard agents. Additionally, from a technological point of view it is important to know the influence of metal doping on several crystals with the objective to modify some of their properties, including modification of the crystal habit, thermal conductivity, etc. Analysis of Raman spectroscopy and X-ray diffraction measurements suggested, for example, Ni ions occupy interstitial crystallographic sites in the lattice of L-histidine hydrochloride monohydrate crystal [23]. This specific position is the same occupied by Cu ions in the L-histidine.$HCl.H_2O$ crystal; the stabilization of the ion – amino acid molecule could be achieved by the interaction between the metal ion and the NH_3^+ group. On cooling, due to the packing of structure, the interaction ion – amino acid is intensified. To understand the interaction of metal ion and amino acid (representing active part of proteins and peptides) is a task with relevance to biochemistry science.

From this résumé one realizes that many changes might occur when crystalline amino acids are submitted to different pressure and/or temperature conditions. Therefore, one question comes to mind: how the hydrogen bonds connecting the molecules in the solid state phase adapt themselves to the new phases in these amino acids? This question will be addressed in the next sections, where it is explained how neutron diffraction and inelastic neutron scattering experiments can bring unique information to this problem.

3. Basic theory

Postulated by Rutherford in 1920 and discovered by J. Chadwick in 1932, neutrons are non-charged subatomic particles with mass rather close to that of the proton m_n = $1.675.10^{-27}$ kg, magnetic moment equals to - 1.913 μ_b and a nuclear spin s = ½, which are important and unique properties for developing the theory of neutron scattering [24].

Since neutrons are non-charged particles, their interactions with matter, both nuclear and magnetic, are short range; therefore neutrons can penetrate deeply into matter. This enables us to study the structure and dynamics of materials under very precise environmental conditions. Neutrons can be described using either classical mechanics, with momentum $\vec{p} = m\vec{v}$, where m is the neutron mass and $\vec{v}$ is its velocity, or quantum mechanics, with momentum $\vec{p} = \hbar\vec{k}$, with $|\vec{k}| = \frac{2\pi}{\lambda}$ defining the wave vector of the neutron and λ its associated wavelength.

This also implies that neutron scattering processes are based on the analysis of momentum and energy transfer, which may occur due to the interactions between neutrons and matter. The momentum transfer vector or the scattering vector, $\vec{Q}$, is defined as the vector difference between the incoming and scattered wave vectors as in Eq. (1).

$$\vec{Q} = \vec{k_i} - \vec{k_f}, \tag{1}$$

while the variation in the neutron momentum is given by Eq. (2):

$$\hbar\vec{Q} = \hbar(\vec{k_i} - \vec{k_f}), \tag{2}$$

The corresponding neutron energy E can be described as described by Eq. (3):

$$E = \frac{p^2}{2m} = \frac{1}{2}mv^2 = \frac{\hbar^2}{2m\lambda} = \frac{\hbar^2 k^2}{2m}, \tag{3}$$

where $h = 2\pi\hbar$ = $6.626.10^{-34}$J.s is the Planck's constant. Thus, variation of the energy ($\hbar\omega$) measured in a neutron scattering experiment is given by Eq. (4):

$$\hbar\omega = E_i - E_f = \frac{\hbar^2}{2m}\left(k_i^2 - k_f^2\right). \tag{4}$$

During the scattering process, elastic scattering occurs when the variation of energy between neutron and the sample is zero. On the other hand, when this variation is different from zero, the scattering processes is called inelastic.

In a typical neutron experiment the collected information is related to the partial differential cross-section, $d^2\sigma/(dEd\Omega)$, given by Eq. (5), according to Ref. [25]:

$$\frac{d^2\sigma}{d\Omega dE_f} = \frac{k_f}{k_i}\frac{1}{\hbar}\left[b_{coh}^2 S_{coh}\left(\vec{Q},\omega\right) + b_{inc}^2 S_{inc}\left(\vec{Q},\omega\right)\right], \tag{5}$$

where $S_{coh}(\vec{Q},\,\omega)$ and $S_{inc}(\vec{Q},\,\omega)$ are the so-called coherent and incoherent scattering functions. These functions are Fourier transformations of the van Hove correlation functions $G(\vec{r},\,t)$, which can be described as the probability for an atom at the origin at time 0, to also be found within the unit volume at a position $\vec{r}$ at a time t.

The probability of interactions between the neutrons and the atoms is a characteristic of each isotope and described by two terms: coherent and incoherent cross sections (σ_{coh} and σ_{inc}), as shown in Table 1. The cross section is related to the coherent (b_{coh}) and incoherent (b_{inc}) scattering length by the following relation: $\sigma = 4\pi b^2$. The high σ_{inc} value of ^1H in comparison to the other elements allows the assignment of the vibrations related to hydrogen atoms. On the other, the high value of the coherent cross section of ^2D when compared to ^1H allows to locate the hydrogen atom by using deuteration.

	^1H	^2D	C	O	N	Cl
σ_{coh}	1.76	5.59	5.55	4.23	11.0	11.5
σ_{inc}	80.27	2.05	<0.01	<0.01	0.50	5.30

Table 1. Coherent (σ_{coh}) and incoherent (σ_{inc}) cross-sections in 10^{-24} cm^2 for selected elements and isotopes [26].

For crystalline matrices, the coherent scattering function in Eq. (5) is written as given in Eq. (6):

$$S_{coh} = \left|F(\vec{Q})\right|^2 \delta(\omega)\sum_{\frac{\vec{G}}{2\pi}}\delta\left(\vec{Q}-\vec{G}\right)$$

$$+\sum_{s,\vec{q}}\left|F\left(s,\vec{q}\right)\right|^2 \frac{\left\langle n(\omega)\left|+\frac{1}{2}\pm\frac{1}{2}\right.\right\rangle}{\omega}\delta(\omega\mp\omega_{s,\vec{q}})\sum_{\frac{\vec{G}}{2\pi}}\delta\left(\vec{Q}+\vec{q}-\vec{G}\right), \tag{6}$$

where the first term represents Bragg scattering and in a diffraction experiment the Bragg's Law is satisfied:

$$n\lambda = 2d\sin\theta, \tag{7}$$

here n is a positive integer and λ is the wavelength of incident wave and the angle θ is defined as the angle between the incoming ray and the diffraction atomic plane.

The second term in Eq. (6) describes collective atomic motions (phonons), where $\vec{q}$ is the wave vector of the collective atomic motion and s an index that specifies the various modes of such collective motions.

Contributions from single particle motion are described by $S_{inc}(\vec{Q}, \omega)$ as given by Eq. (8):

$$S_{inc}\left(\vec{Q},\omega\right) = S_{inc}^{trans}\left(\vec{Q},\omega\right) \otimes S_{inc}^{rot}\left(\vec{Q},\omega\right) \otimes S_{inc}^{vib}\left(\vec{Q},\omega\right), \tag{8}$$

In Eq. (8) the terms describe contributions from the translational, rotational and vibrational modes, respectively.

4. Experimental details

In order to obtain the results presented in this chapter, a series of facilities were utilized. Neutron powder diffraction (NPD) experiments were carried out using the powder diffrac‐ tometers E9 located at the Helmholtz-Zentrum Berlin für Materialien und Energie (Berlin, Germany) and D2b at the Institut Laue-Langevin (Grenoble, France). Such equipments allowed the determination and refinement of crystal structures with very high resolution, furnishing lattice constants and internal atomic coordinates with great precision. Through the experi‐ ments with temperature variation the data were analyzed using a crystallographic model from Ref. [27] Due to the thermal diffuse scattering contribution, attention was paid to the modeling of the background.

Incoherent elastic neutron scattering measurements were carried out using the time-of-flight spectrometer NEAT at the Helmholtz-Zentrum Berlin für Materialien und Energie as well as the backscattering instrument IN10 located at the Institut Laue-Langevin.

The analysis of the evolution of the elastic line centered around $E = 0$, (energy resolution, ΔE = 100 μeV (NEAT) or 1 μeV (IN10)) as a function of temperature gives information about the mean square displacement of the atoms around their equilibrium positions or, in very broad terms, describes the crystal flexibility. On the other hand, the inelastic part of the spectra gives information on the lattice phonons as well as on the inter-molecular vibrations of the samples. The obtained information is complementary to infrared (IR) and Raman scattering (RS).

5. Looking inside amino acid crystals

In relation to amino acid crystals there is a pivotal point to be considered when using neutron spectroscopy or neutron diffraction: the hydrogen bonds that connect the various molecules together in the crystal structure. In this chapter results on crystals of the amino acids L-alanine, L-valine and L-leucine are discussed.

The first discussion will furnish a picture on the simplest chiral amino acid, L-alanine. Selective deuteration of L-alanine were analyzed: (i) C_2H_4-(ND_3^+)-CO_2^-, Ala-ND3; (ii) C_2D_4-(NH_3^+)-CO_2^-, Ala-CD4; (iii) C_2D_4-(ND_3^+)-CO_2^-, Ala-D7. L-alanine crystallizes in an orthorhombic structure with four molecules per unit cell in a $P2_12_12_1$ space group. The molecules are distributed spatially as head-to-tail chains along the crystallographic c-axis, presenting a complex three dimensional network of hydrogen bonds. Here we recall that the c-axis a stepwise change of the size parameter on cooling. Combining inelastic neutron scattering (INS) and neutron powder diffraction (NPD) is possible to study the relationship between the local dynamics of NH_3, CO_2 and CH_3 and to gain insights about the behavior of hydrogen bonds.

Figure 1 presents the inelastic neutron scattering spectra of (a) Ala-ND3 and (b) Ala-CD4 for several temperatures in the energy range from 0 to 70 meV. Data were obtained using the NEAT spectrometer. It is possible to observe several normal modes: lattice modes below 20 meV and other modes such as torsion of CO_2 group, $\tau(CO_2^-)$, torsion of NH_3, $\tau(NH_3^+)$, and torsion of CH_3, $\tau(CH_3)$, as specified in the figure. It is interesting to observe the peak located ~ 60 meV that is associated with $\tau(NH_3^+)$. The width of this peak can be understood as consequence of the anharmonicity of the hydrogen bonds because all three protons participate of N–H...O hydrogen bonds. The influence of anharmonicity is not restrict to the torsion of the ammonia group; as it can be noted in Figure 1 the large peaks associated with the lattice modes that involves bending and stretching of hydrogen bonds can be ascribed to the same effect. Additionally, if one plots the energy of $\tau(CO_2^-)$ mode in Ala-ND3 (not shown in Figure 1) as a function of temperature, one notes a discontinuity between 150 and 200 K. Such a discontinuity coincides with a discontinuity of the wavenumber of a band associated with $\tau(CO_2^-)$ in the Raman spectrum at temperatures in the same interval.

Figure 2 presents the neutron diffraction patterns of Ala-CD4 for two different temperatures. The measurements were obtained with a neutron wavelength of 2.8060 Å. Impressively, at T = 100 K, it is observed a Bragg peak at ~ 2θ = 78° that does not belong to the $P2_12_12_1$ orthorhombic structure. In the attempt to index this peak authors were guided to assume a primitive orthorhombic cell with the a-axis with double size [11]. It is remembered that the non-deuterated L-alanine presents any strong modification in its lattice parameter, although the crystal itself shows a series of anomalies at low temperatures. As a consequence, the result presented in Figure 2 suggests that the partial deuteration of L-alanine induces a solid-solid phase transition. Interestingly such a phase transition can be seen as an enhancement of an anomaly observed in the non-deuterated partner at T ~ 260 K [13]. The doubling of the a-lattice parameter involves changes in the two hydrogen bonds represented in Figure 3 and a rearrangement of the whole molecule. Between 270 and 250 K, a decreasing in the D(2)...O(2)
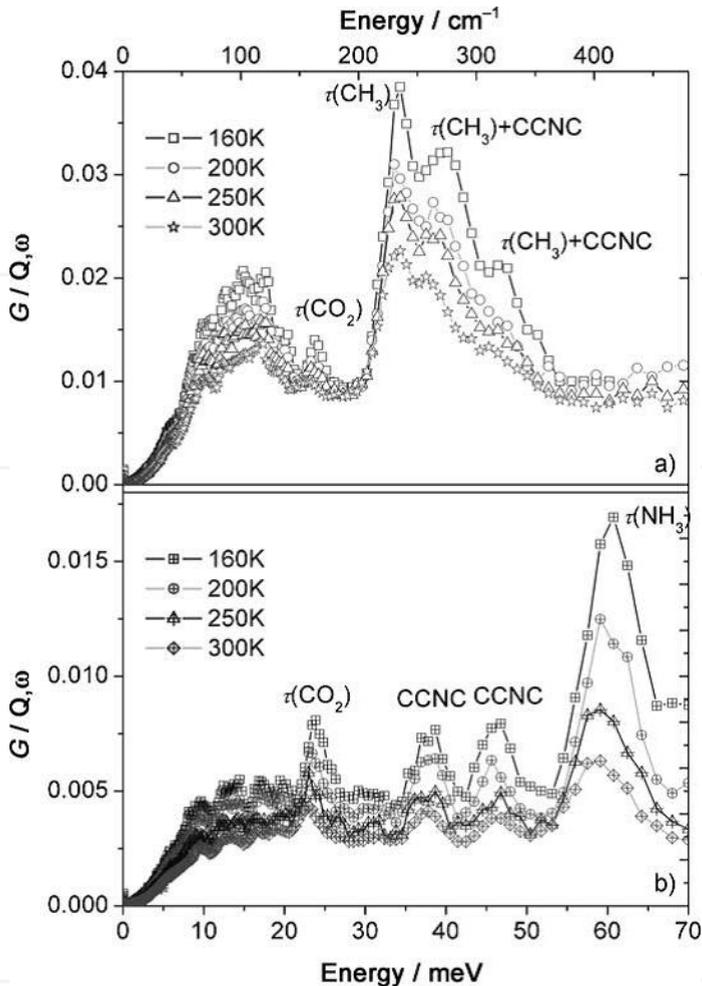
Figure 1. Inelastic neutron scattering spectra at various temperatures for (a) Ala-ND3 and (b) Ala-CD4. The assignment of the main modes is given [11].

bond is observed and an impressive anomaly between 250 and 100 K. On the other hand, the D(1)...O(1) bond becomes longer when temperature is lower than 100 K.

Figure 4 presents $<u_H(T)^2>$ of C_2H_4-(ND_3^+)-CO_2^- and C_2D_4-(NH_3^+)-CO_2^-, where $u_H(T)$ represents the mean-square displacement of the scattering nuclei. Here, as specified previously, $I(T) = I(0).exp[-Q^2\,u(T)^2]$ is the elastic intensity expressed as a function of temperature (the tempera-ture dependence is embedded in u_H). In fact, once the elastic intensity has been experimentally determined, one obtain $u(T)^2$. As it is expected, due the large incoherent cross section of the hydrogen, $u(T)$ is supposed originated only the motion of H atoms. Another aspect to be
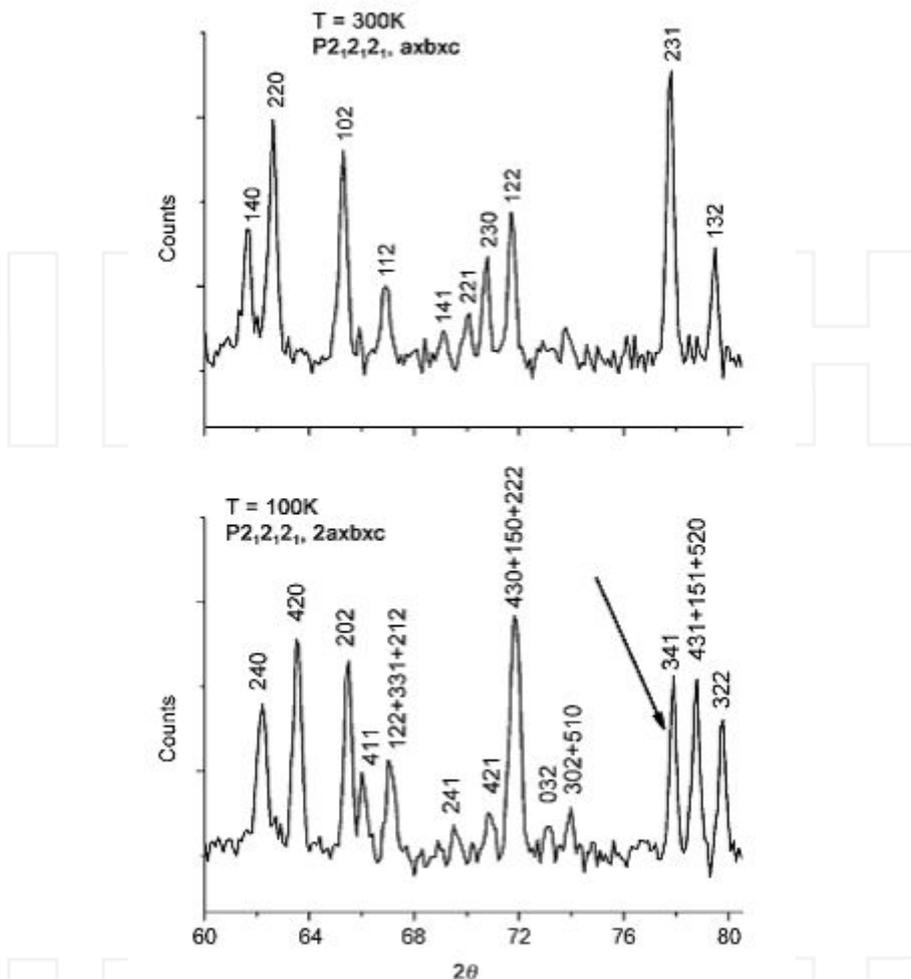
Figure 2. Neutron diffraction patterns of $C_2D_4\text{-}(NH_3^+)\text{-}CO_2^-$ at T=300 K and T=100 K measured with the E9 diffractometer at Hahn-Meitner-Institut. The arrow indicates the peak that could not be indexed with the original $P2_12_12_1$ structure [11].

considered is the following: change in the slope of $u(T)^2$ indicates a dynamical transition in the material. From the Figure 4 one observe that at 160 K and at 220 K there are clear changes in the slop, that can be interpreted as a phase transition or, at least, to a structural rearrangement. Such rearrangement should be probably related to thermally activated large-amplitude reorientations of both CH_3 and NH_3 smithereens of the L-alanine molecule.

The previous paragraphs showed that in the study of partially deuterated L-alanine crystal, the H(1)...O(1) hydrogen bond length increases below 100 K on decreasing temperature and
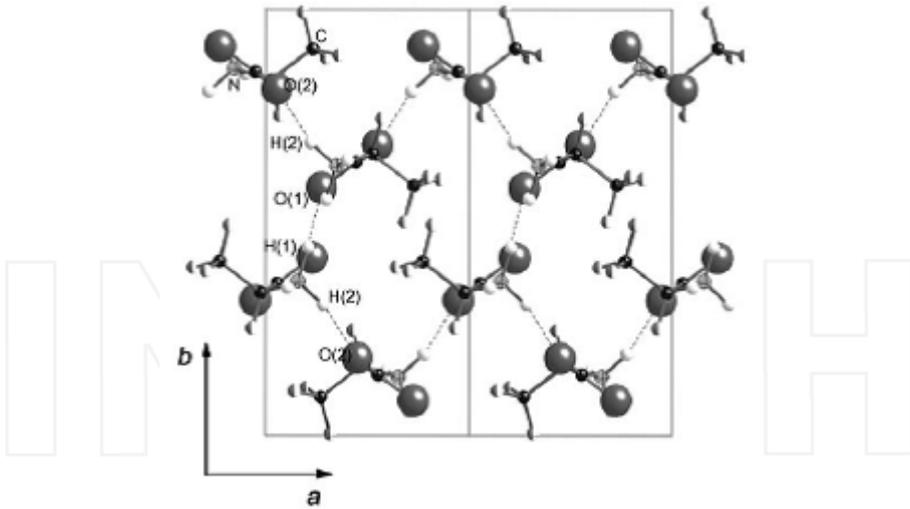
Figure 3. Representation of the crystal structure of L-alanine showing the *ab*-plane. The two hydrogen bonds modifies at low temperature are shown [11].
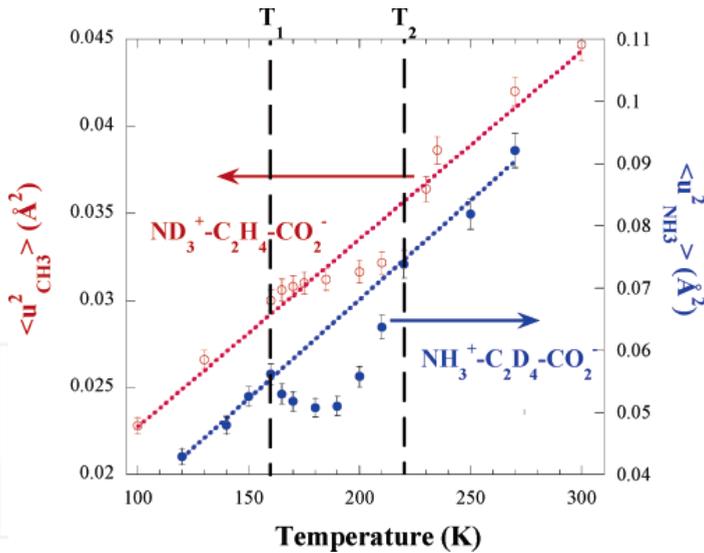

Figure 4. Mean-square dependence from the normalized elastic intensity as a function of temperature. The left scale and open circles represent data for C_2H_4-(ND_3^+)-CO_2^- and the right scale and full circles represent data for C_2D_4-(NH_3^+)-CO_2^- [10].

the H(2)...O(2) length presents an anomaly between 100 and 250 K. What about the behavior of fully deuterated L-alanine under the scrutiny of INS and NPD techniques? Roughly

speaking, deuteration, or isotopic substitution, D → H, produces strong modification in the length of the hydrogen bond. This change generally affects the tunneling rates and the motional properties of the molecules, an effect known as Ubbelohde effect; it is observed in crystals with complex network of hydrogen bonds and even in isolated pair of this type of bond.

Figure 5 presents the temperature dependence of several parameters related to the hydrogen bonds for the fully deuterated L-alanine crystal, C_2D_4-(ND_3^+)-CO_2^-, Ala-D7. Several anomalies are described in the next paragraphs.

From the measurement it is possible to realize that the N-D(3) distance remains almost constant between 10 and 270 K. On the other hand, the N-D(1) distance remains constant only between 10 and 130 K, and diminishes for temperatures higher than 130 K (Figure 5a). Also interesting is the dramatic increase of the D(3)...O(2) hydrogen bond responsible for connecting the molecules into columns (see Figure 5b). This last point is in complete accordance with the fact that torsion of NH_3 group presents important anharmonicity, as depicted during the discussion of Figure 1. So, one can understand the anharmonicity of $\tau(NH_3^+)$ as consequence of the modification of one specific hydrogen bond during the temperature variation [10]. Looking at the average C–D lengths one notes anomalies at low temperatures as presented in Figure 5c. From the Figure 5d one also notes an anomaly in the C–C–C bond angle that extends from about 160 K up to 225 K. In this point is important to emphasize that Raman spectroscopy studies showed splitting of bands associated with lattice modes at T ~ 170 K. This means evidence of a phase transition. Additionally, it was observed anomalies in the Debye-Waller factor, confirming the phase transition at about 170 K in the fully deuterated L-alanine [10].

L-valine was the second aliphatic amino acid crystal studied through neutron techniques. Investigations so performed revealed aspects related to hydrogen bonds, ultimately, respon‐ sible for the structural stability of the material. L-valine crystallizes in a monoclinic structure with $P2_1$ space group and four molecules per unit cell. From these molecules, two assumes *gauche I* conformation and two others *trans* conformation. Previous work using Raman spectroscopy suggested L-valine should undergo a solid-solid phase transition because impressive modifications of the bands associated with lattice modes were observed at low temperatures [28].

Figure 6 presents the dynamical susceptibility ($\chi''(E)$) of both L-valine hydrogenated [$(CH_3)_2CHCH(NH_2)CO_2H$] and deuterated [$(CD_3)_2CDCD(NH_2)CO_2H$] (synthesized by Dr. Ehrenstorfer GmbH from Augsburg, Germany). The comparison of the INS spectra of L-valine and deuterated L-valine (L-valine-d_8) shows differences that can be understood as follows. At first, an intense band at 480 cm^{-1} in the spectrum of L-valine-d_8 points to the accuracy of the assignment of the vibrations involving the N–H...O hydrogen bonds. Also, a decrease of the signal for energy lower than 450 cm^{-1} indicates they are associated with the CH_3 and CO_2 groups and the N–C–C units [9]. It is impressive in the room temperature INS spectrum of L-valine the presence of a mode at ~ 120 cm^{-1}. It is remembered that such a band not visible at T= 300 K appeared in the Raman spectra of L-valine for temperatures lower than 120 K. In other words, this band could be associated with a mode not active in the Raman spectrum of the monoclinic room temperature structure, being active only in the infrared. During the phase transition the mode should become Raman active and the phase transition should be realized as consequence
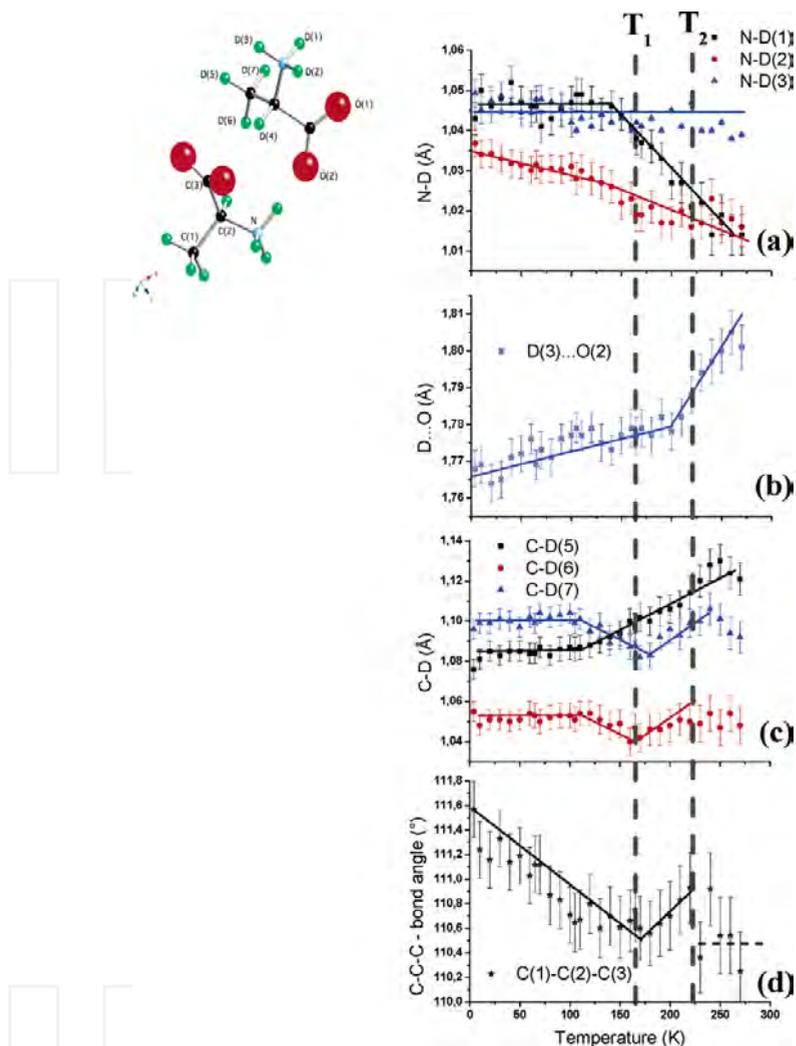
Figure 5. Temperature dependence of (a) N–D, (b) D...O, (c) average C–D length, (d) avergage C–C–C bond angles for fully deuterated L-alanine. The molecule is represented in the top left side of the figure an dashed lines are guides to the eyes [10].

of the activation of an infrared mode. An additional aspect of the study is to show (Figure 6b) the splitting of the band at ~ 15 meV at low temperature when compared with the spectrum recorded at 300 K, reinforcing the idea of a phase transition, as supported by the Raman spectroscopic study [28].

Up to now the present authors have seen several aspects of the bonds on L-alanine and an explanation for the phase transition undergone by L-valine using neutrons. It can be noted
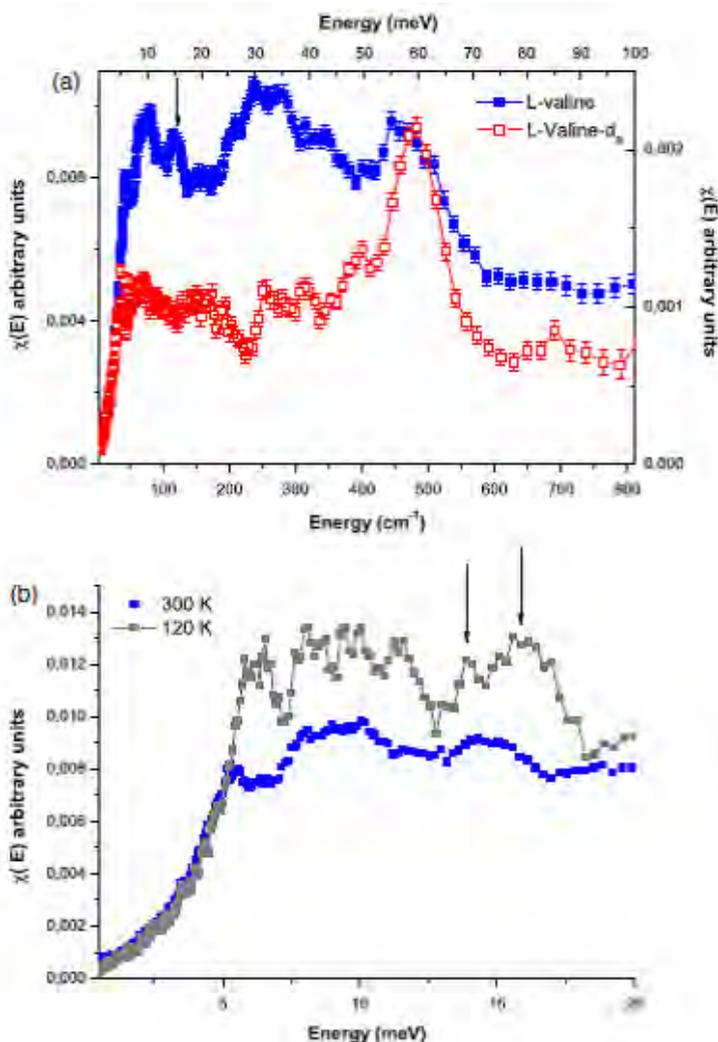
Figure 6. (a) Dynamical susceptibility [$\chi''(E)$] for both L-valine (full squares) and L-valine-d_8 (open squares) using a 5.1 Å incident wavelength at the NEAT spectrometer. (b) $\chi''(E)$ of L-valine for two temperatures, 300 K and 120 K. The arrow in part (a) corresponds to the mode at 120 cm^{-1}, observed in the low temperature range by Raman spectroscopy [12].

that subtle conformational change can lead to impressive modifications in the structural and vibrational properties of these two members of the amino acid family. Now, the discussion deals about another aliphatic amino acid. L-leucine, NH_3-CH-CO_2-CH_2-CH-$(CH_3)_2$, crystallizes in a monoclinic structure $P2_1$ with four molecules per unit cell. The carboxyl and amino groups are hydrogen bonded in a double layer, forming the crystal structure. The van der Waals interaction plays its role by connecting neighboring layers [1]. Due the existence of an addi-

tional CH_2 group in its chain, L-leucine is slightly more hydrophobic than L-valine. A previous research demonstrated the occurrence of a phase transition in L-leucine at ~ 353 K possibly maintaining the crystal with a monoclinic structure [22].

Figure 7 presents the dynamical susceptibility function χ'' obtained from calculations based on the inelastic data from NEAT. It is perceived that below 280 K the mode at 30 meV (approximately at 240 cm^{-1}) presents a red shift down to 190 K and below this, presents a blue shift; also, the intensity increases on cooling. Interesting enough is the occurrence of a redistribution of intensity of the bands between 300 and 375 K that can be correlated with the phase transition observed at 353 K. The phase transition can also be glimpsed by the intensities of most modes located below 30 meV, associated with lattice modes, that show pronounced changes in the interval 300 – 375 K.
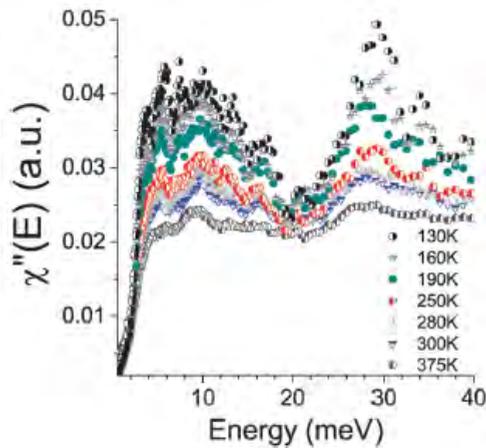

Figure 7. (a) Dynamical susceptibility [$\chi''(E)$] for L-leucine in the temperature range from 130 and 375 K measured in the energy interval from 1 to 30 meV. The mode at ~ 30 meV is associated with an out-of-plane vibration of CH_2 [29].

Supposing $S(Q,\omega)$ the scattering function, with Q being the magnitude of the scattering wave vector and ω being the energy transfer, it is possible to decompose it in three different components: $S_E(Q, \omega = 0)$, the elastic; $S_E(Q, \omega \sim 0)$, quasi-elastic; $S_E(Q, \omega > 0)$, inelastic. The study of the elastic scattering decay can furnish information about transitions because it appears as changes in the temperature dependence of the elastic intensity. Figure 8a shows the elastically scattered intensity as a function of temperature for L-leucine. The main contribution to S_E comes from the hydrogen atoms. Within the time scale of ~ 10 ps originated from the resolution of the equipment one can argue that the transition at ~ 150 K is a consequence of CH_3 groups. Such an anomaly confirms differential scanning calorimetry (DSC), as well as X-ray diffraction measurements [29].

In addition, one notes the broadening of the quasi-elastic response apparently disappears in the temperature range 220 – 250 K and the peak height decreases. It was possible to derive a
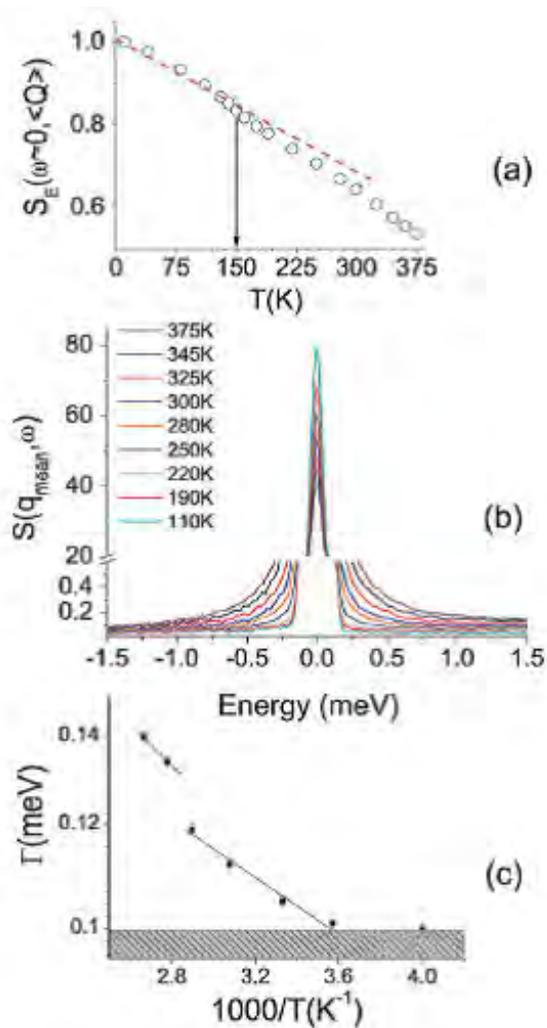
Figure 8. (a) Elastically scattered intensity as a function of temperature for L-leucine. An anomaly in the temperature evolution is marked by an arrow. (b) Dynamic structure factors obtained for AE = 98 μeV for several temperatures averaged over the whole range of Q. (c) Lorentzian half width at half maximum (HWHM), G, obtained using an Arrenhius-like relation [29].

qualitative description by fitting the quasi-elastic S_{QE}, using a Dirac function and a Lorentzian linewidth, which could describe, respectively, the elastic and quasi-elastic signals. In this approach it is possible to correlate the quasi-elastic broadening (Γ) with the activation energy, E_{act}, by the relation $\Gamma = \Gamma_0 \cdot \exp[-E_{act}/kT]$. The most important point derived from this relation is presented in Figure 8c, where a discontinuity, associated with the high temperature phase transition is observed between 345 and 360 K.

6. Conclusions

Neutron diffraction and inelastic neutron scattering are powerful techniques to investigate several materials, among them, amino acid crystals, as it was shown in this chapter. From these studies it was presented the possibilty to correlate small variations of the network of hydrogen bonds to conformation changes in the amino acid molecules.

L-leucine, that presents only one polymorph at room temperature, was shown to undergo phase transitions at low and high temperatures. The new phases were analyzed and insights about the conformation of the molecules were attained.

In the case of L-valine it was possible through comparison between Raman spectroscopy and inelastic neutron scattering to identify infrared active modes responsible for the phase transition undergone by the crystal at approximately 120 K.

Finally, a series of information was obtained for the simplest proteic amino acid crystal, L-alanine. In the case of the fully deuterated sample, L-alanine-d_7, our results showed a clear evidence of a structural phase transition at ~ 170 K. Such fact can be related to the Ubbelohde effect, or in other words different dimensions of the hydrogen bonds stabilize differently the deuterated and the non-deuterated crystals. Consequently, although the deuterated sister presents a phase transition, the non-deuterated structure, even if a series of structural and vibrational anomalies are observed, is stable at low temperatures. Our investigations point to the fact that the Ubbelohde effect can be significant, even if only small changes of hydrogen bond dimensions occur.

Acknowledgements

Author details

Paulo T.C. Freire[1], José E.M. Pereira[2] and Heloisa N. Bordallo[2]

*Address all correspondence to: tarso@fisica.ufc.br

1 Departamento de Física – Universidade Federal do Ceará, Fortaleza, Brazil

2 Niels Bohr Institute – University of Copenhagen, Copenhagen, Denmark

References

[1] Fleck M, Petrosyan AM, Salts of amino acids: Crystallization, structure and properties. Heidelberg: Springer; 2011. 574 p. DOI: 10.1007/978-3-319-06299-0_1.

[2] Görbitz CH. Crystal structures of amino acids: from bond lengths in glycine to metal complexes and high-pressure polymorphs. Crystallography Reviews. 2015; 21: 160–212, DOI: 10.1080/0889311X.2014.964229.

[3] Boldyreva E, Cristalline Amino Acids: A Link between Chemistry, Materials Science and Biology, In: Boyens JCA, Ogilvie JF, editors. Models, Mysteries, and Magic of Molecules. Netherlands: Springer; 2007. p. 167-192. DOI: 10.1007/978-1-4020-5941-4.

[4] Freire PTC, JA Lima Jr, BTO Abagaro, GS Pinheiro, JAF Silva, JM. Filho, FEA Melo. High Pressure Raman spectra of amino acid crystals. In: Dominique de Caro, editor. Vibrational Spectroscopy. Rijeka: InTech; 2012. p. 37 – 58. DOI: 10.5772/1345. ch2

[5] Bordallo HN, Kolesov BA, Boldyreva EV, Juranyi F. Different Dynamics of Chiral and Racemic (L- and DL-) Serine Crystals: Evidenced by Incoherent Inelastic Neutron and Raman Scattering, Journal of the American Chemistry Society. 2007; 129: 10984–10985. DOI: 10.1021/ja073351n.

[6] Freire PTC, Pressure-Induced Phase Transitions in Crystalline Amino Acids, In: Boldyreva E, Dera P, editors, High Pressure Crystallography – From Fundamental Phenomena to Technological Applications. New York: Springer; 2010. p. 559-572. DOI: 10.1007/978-90-481-9258-8.

[7] Moggach SA, Allan DR, Clark SJ, Gutmann MJ, Parsons S, Pulham CR, Sawyer L. High-pressure polymorphism in L-cysteine: the crystal structure of L-cysteine-III and L-cysteine-IV. Acta Crystallographica B. 2006; 62: 296 – 309. DOI: 10.1107/S0108768105038802.

[8] Kistenmacher TJ, Rand GA, Marsh RE. Refinements of the crystal structures of DL-serine and anhydrous L-serine, Acta Crysttalographica B. 1974; 30: 2573 – 2578. DOI: 10.1107/S0567740874007618.

[9] Pawlukojc A, Borrowicz L, Natkaniec I, Leciejewicz J. The IINS spectroscopy of amino acids: L- and DL-valine. Spectrochimica Acta A. 1995. 51: 303-308. DOI: 10.1016/0584-8539(94)00812-P.

[10] Souza JM, Freire PTC, Bordallo HN, Argyriou DN. Structural isotopic effects in the smallest chiral amino acid: observation of a structural phase transition in fully deuterated alanine. Journal of Physical Chemistry B. 2007; 111: 5034 – 5039. DOI: 10.1021/jp070366z.

[11] Souza JM, Freire PTC, Argyriou DN, Stride JA, Barthès M, Kalceff W, Bordallo HN. Raman and neutron scattering study of partially deuterated L-alanine: evidence of a

solid-solid phase transition. ChemPhysChem. 2009; 10 3337- 3343. DOI: 10.1002/cphc. 200900482.

[12] Silva JH, Lima Jr, JA, Freire PTC, Lemos V, Mendes Filho J, Melo FEA, Pizani PS, Fischer J, Klemke B, Kemner E, Bordallo HN. Raman spectroscopy and inelastic neutron scattering study of crystalline L-valine., Journal of Physics: Condensed Matter. 2009; 21: 415404. DOI: 10.1088/0953-8984/21/41/415404.

[13] Barthes M, Bordallo HN, Dénoyer F, Lorenzo J-E, Zaccaro J, Robert A, Zontone F. Micro-transitions or breathers in L-alanine? The European Physical Journal B. 2004; 37: 375-382. DOI: 10.1140/epjb/e2004-00069-1.

[14] Destro R, Marsh RE, Bianchi R. A low-temperature (23K) study of L-alanine. The Journal of Physical Chemistry. 1988; 92: 966-973 DOI: 10.1021/j100315a022.

[15] Migliori A, Maxton PM, Clogston AM, Zirngiebl E, Lowe M. Anomalous temperature dependence in the Raman spectra of l-alanine: Evidence for dynamic localization. Physical Review B. 1988; 38: 13464-13467. DOI: 10.1103/PhysRevB.38.13464.

[16] Kolesov BA, Boldyreva EV. Micro-conformational transition in L-alanine single crystals revisited by low wavenumber Raman spectroscopy. Journal of Raman Spectroscopy. 2010; 42: 696-705. DOI: 10.1002/JRS.2768.

[17] Teixeira AMR, Freire PTC, Moreno AJD, Sasaki JM, Ayala AP, Mendes Filho J, Melo FEA. High-pressure Raman study of l-alanine crystal. Solid State Communications. 2000; 116: 405-409. DOI: 10.1016/S0038-1098(00)00342-2.

[18] Olsen JS, Gerward L, Freire PTC, Mendes Filho J, Melo FEA, Souza Filho AG. Pressure-induced phase transitions in L-alanine crystals. Journal of Physics and Chemistry of Solids. 2008; 69: 1641-1645. DOI: 10.1016/j.jpcs.2007.12.005.

[19] Funnel NP, Dawson A, Francis D, Lennie DR, Marshall WG, Moggach SA, Warren JE, Parsons S. The effect of pressure on the crystal structure of l-alanine. CrystEngComm. 2010; 12: 2573-2583. DOI: 10.1039/C001296C.

[20] Tumanov NA, Boldyreva EV, Kolesov BA, Kurnosov AV, Quesada Cabrera R. Pressure-induced phase transitions in L-alanine, revisited. Acta Crystallographica Section B. 2010; 66: 358-371. DOI: 10.1107/s010876811001983X.

[21] Lima Jr. JÁ, Melo FEA, Mendes Filho J, De Sousa G.P, Lima RJC, Façanha Filho PF, Bordallo HN. Low-temperature Raman spectra of racemate DL-Alanine crystals. Journal of Raman Spectroscopy. 2010; 41: 808-813. DOI: 10.1002/jrs.2507.

[22] Façanha Filho PF, Freire PTC, Lima KCV, Mendes Filho J, Melo FEA, Pizani PS. High temperature Raman spectra of L-leucine crystals. Brazilian Journal of Physics. 2008; 38: 131-137. DOI: 10.1590/S0103-97332008000100024.

[23] Remédios CMR, Paraguassu W, Lima Jr. JÁ, Freire PTC, Mendes Filho J, Melo FEA, Menezes AS, dos Santos AO, Cardoso LP, Miranda MAR. Effect of Ni(II) doping on

the structure of L-histidine hydrochloride monohydrate, crystals, Journal of Physics: Condensed Matter. 2008; 20: 275209. DOI: 10.1088/0953-8984/20/27/275209.

[24] Lovesey SW. Neutron Scattering Theory. Oxford: Oxford Science Publications; 1986. 317 p. DOI: 10.1088/0953-8984/5/34/016.

[25] Squires GL. Introduction to the Theory of Thermal Neutron Scattering. New York: Cambridge University Press; 1978. DOI: 10.1080/00107514.2012.745613.

[26] Dianoux AJ, Lander G, editors (2003). Neutron data booklet. 2nd. Edition, ISBN: 0-9704143-7-4.

[27] Lehnman MS, Koetzle TF, Hamilton WC. Precision neutron diffraction structure determination of protein and nucleic acid components. I. Crystal and molecular structure of the amino acid L-alanine. Journal of the American Chemistry Society. 1972; 94: 2657 – 2660. DOI: 10.1021/ja00763a700.

[28] Lima Jr. JA, Freire PTC, Lima RJC, Moreno AJD, Mendes Filho J, Melo FEA. Raman scattering of L-valine crystals. Journal of Raman Spectroscopy. 2005; 36: 1076-1081. DOI: 10.1002/jrs.1410.

[29] Façanha Filho PF, Jiao X, Freire PTC, Lima Jr. JA, Dos Santos AO, Henry PF, Yokaichiya F, Kremner E, Bordallo HN. Structure-property relations in crystalline L-leucine obtained from calorimetry, X-rays, neutron and Raman scattering. Physical Chemistry Chemical Physics. 2011; 13: 6576-6583. DOI: 10.1039/C0CP02278K.